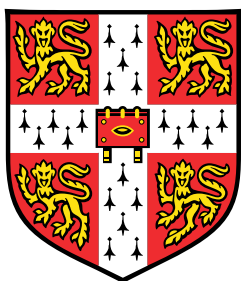


A Unified Turbine Preliminary Design Study



Shaun Michael Kaufmann

Department of Engineering
University of Cambridge

This dissertation is submitted for the degree of
Doctor of Philosophy

November 2020

I dedicate my dissertation work to the memory of my Grandfather, Jolyon Beerstecher and my partner in crime, Oona Beerstecher. I miss you both.

Declaration

I hereby declare that except where specific reference is made to the work of others, the contents of this dissertation are original and have not been submitted in whole or in part for consideration for any other degree or qualification in this, or any other university. This dissertation is my own work and contains nothing which is the outcome of work done in collaboration with others, except as specified in the text and Acknowledgements. This dissertation contains fewer than 65,000 words including appendices, bibliography, footnotes, tables and equations and has fewer than 150 figures.

Shaun Michael Kaufmann

November 2020

Abstract

A Unified Turbine Preliminary Design Study

Shaun Michael Kaufmann

During the preliminary stages of design, designers must make decisions concerning size, speed and machine type. Misinformed choices in design parameters and architecture can lock in suboptimal performance. Design charts leveraging similitude are powerful tools that can help designers make better decisions at this point in the design process. The design charts used up until now are either partially or entirely based on lost correlations and do not include mixed flow architectures. On top of this many of the current charts contain little to no information about the various loss mechanisms, turbine characteristics and how both change through out the design parameter space. This thesis builds on the pre existing work by mapping out design parameter spaces using computation methods, more specifically using a Reynolds averaged Navier Stokes Equation Solver. This also allowed for the partial decoupling of loss mechanisms.

This thesis includes a unified design methodology built around a unified set of design flow parameters. This was used to generate design charts for all architecture types, including radially fibred mixed flow architectures with fixed cone angle and radius ratio. Both total to static and total to total efficiency was presented as a function of loading coefficient and duty flow coefficient instead of the typically used non dimensional speed and diameter. This was done in order to help aid in the aerodynamic interpretation of the data.

Results showed the shapes of the design spaces in the present framework can largely be explained by surface dissipation. That is, entropy generated at the surface is proportional to the surface velocity cubed with a fixed dissipation coefficient. A universal trend across all architectures was found. Turbines with high duty flow coefficient have characteristically high surface velocities and turbines with lower values of duty flow coefficient are characterised by high surface area. However, the balance between area and surface velocity of the different architectures differed significantly. Axial turbines have characteristically high surface velocities. Whereas radial turbines have characteristically high surface area and lower surface velocities. The lower surface velocities of the radial turbine was in part due to the centrifugal loading. It was shown that shifting loading from the relative acceleration term to the centrifugal term decreases relative passage velocities.

It was shown that axial turbines have the broadest range across the design space, both the constrained mixed flow and radial turbines sit inside the axial space. In addition to this, axial architectures did not show a performance boundary at lower duty flow coefficients. This was attributed to the aspect ratio being fixed and other tolerances based geometric features scaling with the passage. The mixed and radial architectures were shown to suffer high losses at lower duty flow coefficients, this was attributed to the high end wall surface area, characteristic of designs in this region of the Balje chart.

All turbines suffer a drop off in performance at high duty flow with all mechanisms contributing to this. The characteristically high velocities of these designs result in high profile and end wall surface dissipation loss. In addition the leakage loss increases in part due to the high velocity with which the leakage flow is mixing and the high over tip driving pressure. Radial architectures show a sharper drop in performance with increasing duty flow. This was attributed to flow separation at the casing due to reducing radius of curvature. By virtue of having a lower cone angle, the mixed flow architecture have a significantly larger radius of curvature and did not exhibit any signs of flow separation. As expected the (radially fibred) mixed flow architectures have lower performance loss with increasing loading coefficients than the (radially fibred) radial architectures due to the inlet metal angle not being constrained. However axial architectures outperform both. When comparing the mixed and axial flow architectures the mixed flow architectures showed a sharper increase in surface area with increasing loading.

Acknowledgements

Throughout the writing of this dissertation I have received a great deal of support and assistance. I would first like to thank my supervisor, Dr. Liping Xu, whose expertise was invaluable in the formulating of the research topic and methodology in particular.

I would like to acknowledge my colleagues from The Whittle lab, for their wonderful collaboration, in particular Jonathan Smyth. What we worked on has been neglected for so long, it was good to have a team mate through this process.

In addition, I wish to express my deepest gratitude to my parents and partner for their support. To my mother, you helped me push past learning difficulties, allowing me to get this far. you believed in me when many did not. To my father you taught me personal skills and financially supported my early engineering studies when no institution would. To my step father, you helped foster my creative engineering skills that I use today. To my partner Sophie Shapter, you supported me through some of the most challenging times, helping me in more way that you can imagine.

Finally, there are my friends, who were of great support, in particular Joe Cooper who spent many hours proofreading my dyslexic thesis.

Table of contents

List of figures	xi
List of tables	xvii
Nomenclature	xviii
1 Introduction and Literature Review	1
1.1 Introduction	1
1.2 Turbine Flow Features	1
1.3 Loss Mechanisms	11
1.3.1 Secondary/Endwall Flow Loss	14
1.3.2 Passage losses	15
1.3.3 Tip Leakage loss	16
1.3.4 Exit loss	16
1.4 Radial blade fibre	17
1.5 Architecture Selection	18
1.5.1 Similarity Methods	18
1.5.2 Balje, Cordier and Rholik Diagrams	20
1.5.3 Alternative duty similarity parameters	23
1.6 Numerical Methods	26
1.6.1 Overview of methods	26
1.6.2 Limitations	28
1.7 Problem statement	29
2 Design Methodology	32
2.1 Unified Design Parameters	33
2.2 Geometry Generation	41
3 Low Order Model And Numerical Method	55
3.1 Low Order Model	55
3.1.1 Profile Loss	56

3.1.2	Secondary/End wall loss	66
3.1.3	Tip leakage	72
3.2	Numerical Method	75
3.2.1	Choice of tool	76
4	Axial Turbine Design Space	92
4.1	Chapter Objectives	92
4.2	Axial Total-Total Smith Chart	93
4.2.1	Profile loss	98
4.2.2	Endwall/Secondary loss	99
4.2.3	Tip leakage loss	101
4.3	Axial Total-Static Smith Chart	103
4.4	Meridional Velocity Ratio	104
4.5	Interstage swirl & Circulation coefficient	107
4.6	Loading and Duty Flow Coefficient Based Balje Diagram	109
4.7	Axial Total-Total Balje Chart	110
4.7.1	Profile loss	112
4.7.2	Endwall loss	113
4.7.3	Tip Leakage loss	114
4.8	Axial Total-Static Balje Chart	115
4.9	Optimal local flow coefficient	117
4.10	Chapter Conclusions	121
5	Radial Turbine Design Space	124
5.1	Chapter Objectives	124
5.2	Radial Smith Chart	124
5.3	Total to Total Isentropic Efficiency	125
5.3.1	End Wall & Incidence Loss	129
5.4	Total - Static Isentropic Efficiency	130
5.5	Radial Turbine Balje/Rohlik Diagrams	131
5.6	Total to Total Balje Diagram	133
5.6.1	Profile loss	135
5.6.2	Endwall/Secondary loss	136
5.6.3	Tip clearance loss	138
5.7	Total to Static Balje Diagram	139
5.8	Optimal Local Flow Coefficient	141
5.9	Radius ratio	144
5.10	Meridional velocity ratio	147
5.11	Chapter Conclusions	148

6 Mixed Turbine Design Space	151
6.1 Chapter Objectives	151
6.2 Mixed Turbine Hub Flow Separation	152
6.3 Hub Fillet for Mixed Flow Turbines	158
6.4 Mixed Flow Turbine Smith Chart	162
6.4.1 Profile loss	165
6.4.2 Endwall/Secondary loss	166
6.4.3 Tip leakage loss	169
6.5 Mixed Flow Turbine Balje Chart	170
6.6 Mixed Turbine Total-Total Balje Chart	170
6.6.1 Profile loss	172
6.6.2 Secondary/Endwall loss	173
6.6.3 Tip Leakage loss	174
6.6.4 Mixed Turbine Total-Static Balje Chart	175
6.7 Radius Ratio vs Cone Angle	176
6.8 Chapter Conclusions	179
7 Unified Designs And Conclusions	183
7.1 Chapter Objectives	183
7.2 Total to Total Efficiency	184
7.3 Total to static	192
7.3.1 Power Density, Inertia & Cost trends	196
7.4 Combined diffuser turbine performance	200
7.5 Conclusion	202
References	211
Appendix A Additional Table Data	215
Appendix B Additional plots	221
B.1 numerical error axial	221
B.2 Axial Smith	222
B.3 Axial Balje	223
B.4 Radial total to static	224
B.5 Radial total to static	225
B.6 Radial total to static Chen and Baines	226
B.7 Radial total to static	227
B.8 Mixed turbine profile surface area and velocity distribution	227
B.9 Mixed turbine secondary and surface end wall dissipation loss	230

Appendix C Method for calculating reduced static pressure(compressible) and isentropic velocity	231
Appendix D Vorticity Amplification Factor For A Curved Rectangular Duct	233
Appendix E Curvature pressure gradient Factor	237
Appendix F Circulation vs Flow angles	239
Appendix G Velocity difference equation	242
Appendix H Velocity Triangle	244

List of figures

1.1	Axial turbine Flow regions (meridional projection)	4
1.2	schematic of secondary flow patterns in an axial turbine, from [29]	5
1.3	schematic of tip leakage flow in an axial turbine [Denton [26]]	6
1.4	Radial turbine Flow regions (meridional projection)	7
1.5	A: Coriolis force directions. B: counter vortex	8
1.6	Predicted flow in meridional plane, from Zangeneh [58]	9
1.7	<i>A:</i> Movement of low momentum fluid on two cross-flow surfaces , from Zangeneh [58]. <i>B:</i> Contours of relative stagnation pressure at the exit of a radial turbine , from Huntsman [35].	10
1.8	Dissipation coefficient for laminar and turbulent boundary layers Denton [26] / Cebeci and Carr [10]	12
1.9	Diagram illustrating radial blade fibre design	17
1.10	Diagram illustrating how changing the inlet metal angle effects the shape of a mixed flow turbine passage for radially fibrered architectures	18
1.11	Cordier diagrams from [30]	21
1.12	$N_s D_s$ Diagram for single disk turbines Balje [3]	22
1.13	Loss distribution, Rohlik [46]	23
1.14	illustration of effects of using different local flow coefficients has on flow and geometry, for a fixed duty flow coefficient	25
1.15	Diagram illustrating radial blade fibre design	26
2.1	Turbine parameter flow chart	34
2.2	Illustrating effect of radius ratio on passage geometry	37
2.3	Illustrating effect of meridional velocity ratio on passage geometry (incompressible flow)	38
2.4	Inlet angle vs Blade count reconstructed from Whitfield and Baines [54]	40
2.5	design methodology flow chart	41
2.6	<i>A:</i> Diagram of axial the meridional geometry. <i>B:</i> Diagram of radial/mixed the meridional geometry	44
2.7	Illustration of the effects of increasing inlet area has on casing radius of curvature	45

2.8	Diagram of the meridional geometry including blade section defined by leading end blade angle distribution	45
2.9	Diagrams illustrating Design limitations	46
2.10	<i>A:</i> Diagram of radial/mixed blade angle distribution. <i>B:</i> Diagram of axial blade angle distribution	47
2.11	<i>A:</i> Shape Function construction. <i>B:</i> Example Thickness Distribution of Mixed Flow turbine	49
2.12	Fillet construction factors	51
2.13	Spoon fill construction	51
2.14	Spoon fill construction	53
2.15	Hub pressure surface fill	54
3.1	Velocity distribution modelled from numerical solution mass averaged quantities.	58
3.2	Illustration of how the area distribution is approximated from geometry.	60
3.3	Various passage velocities for an axial: numerical solution, uncorrected model, model with mass average and smoothing corrections.	61
3.4	Comparison of different loading terms to the numerical solution for a mixed flow turbine.	62
3.5	Comparison of velocity distribution models with numerical solution.	65
3.6	Variation of total to total efficiency with shroud radius of curvature.	69
3.7	<i>A:</i> Variation of total to total efficiency with casing radius of curvature. <i>B:</i> Variation of total to total efficiency with shroud radius of curvature.	71
3.8	Tip flow and driving pressure, Dambach [23]	73
3.9	Over tip driving pressure from Coull and Atkins[19]	74
3.10	Illustration of competing stream tube model.	75
3.11	Comparison of effective discharge coefficient with measured values from Dambach [23]	75
3.12	<i>A:</i> Comparison of contours of stagnation pressure loss coefficient, Contour interval 0.05 [25]. <i>B:</i> Growth of the stagnation pressure loss coefficient through the cascade [25]	78
3.13	<i>A:</i> Radial turbine steady state turbine efficiency vs velocity ratio [9]. <i>B:</i> Mixed flow turbine steady state turbine performance vs velocity ratio [41]	79
3.14	<i>A:</i> Index directions. <i>B:</i> Variation of point density with surface coordinate	81
3.15	H mesh grids for various architectures.	83
4.1	<i>A:</i> Total-total Smith chart with fixed $\frac{A}{r_m^2}$. <i>B:</i> Inlet and exit meanline relative flow angles.	94
4.2	Contours of blade profile surface area and surface-area averaged cubic velocity.	95
4.3	Sample of smith chart velocity profiles.	97

4.4	Lost efficiency due to profile loss.	99
4.5	A:Lost efficiency due to secondary/endwall loss. <i>B</i> decoupled endwall losses. . .	100
4.6	Lost efficiency due to tip leakage loss.	101
4.7	Contour plot of lost work for 1% and 0.1% tip clearance [$\psi = 2$, $\phi_L = 0.6$]. . .	103
4.8	Total-static Smith chart with fixed $\frac{A}{r_m^2}$	104
4.9	Partial derivatives of total to total and static efficiencies with respect to meridional velocity ratio.	105
4.10	Variation of efficiencies (A), Variation surface area and velocity (B) and loss components (C) with changes in R_{vm} at $\phi_L = 0.7$, $\psi = 1.9$	105
4.11	A:Partial derivatives of total to total and static efficiencies with respect to interstage swirl. <i>B</i> Partial derivatives of total to total efficiency with respect to circulation coefficient.	108
4.12	<i>A</i> :Contours of total to total efficiency for axial turbines with varying loading and duty flow coefficients. <i>B</i> Contours of blade profile surface area and surface-area averaged cubic velocity.	111
4.13	Contours of loss in efficiency of axial turbines due to profile loss.	112
4.14	Contours of loss in efficiency of axial turbines due to secondary/endwall loss. .	113
4.15	Contours of loss in efficiency of axial turbines due to Tip Leakage loss. . . .	115
4.16	<i>A</i> :Contours of total to static efficiency for axial turbines with varying loading and duty flow coefficients. <i>B</i> Contours of lost efficiency due to exit loss	116
4.17	Contours of optimised local flow coefficient for axial turbines with varying loading and duty flow coefficient.	117
4.18	Comparison of optimal design local flow coefficient with a fixed loading coefficient $\Psi = 1.6$ and different duty flow coefficients.	118
4.19	<i>A</i> :Area and cubic velocity for turbines with different duty flow coefficient. <i>B</i> : Non-dimensional inlet area for turbines with different duty flow coefficient. . .	120
5.1	<i>A</i> :Total to total Smith chart with fixed $R_r = 0.7$ and $\frac{A}{r_n^2} = 2$. <i>B</i> : Inlet and exit meanline flow angles.	127
5.2	Radial turbine isentropic velocity distributions for different levels of loading, $\phi_L = 0.3$	128
5.3	Contours of blade surface area and surface area averaged cubic velocity	128
5.4	Inlet and exit meanline flow angles	129
5.5	Comparison of exit flow conditions at two different points on a Smith chart. . .	130
5.6	Total-static Smith chart with fixed $R_r = 0.7$ and $\frac{A}{r_n^2} = 2$	131
5.7	Non-dimensional meridional geometry.	132
5.8	<i>A</i> :Total to total Balje diagram with optimised local flow coefficient and hub $R_{rhub} = 0.2$. <i>B</i> : Blade surface area and surface-area averaged cubic velocity. . .	134
5.9	Estimated loss in isentropic efficiency as a result of profile loss.	135

5.10 <i>A</i> :Variation of endwall loss with duty flow. <i>B</i> : Variation of shroud meridional curvature, end-wall to profile surface area ratio and exit shroud blade angle with duty flow coefficient.	137
5.11 Comparison of exit flow conditions at different points on a Balje chart.	138
5.12 Estimated loss in isentropic efficiency as a result of tip clearance.	139
5.13 Total to static Balje diagram with optimised local flow coefficient and hub $R_r = 0.2140$	
5.14 Exit loss variation across design space.	141
5.15 Optimised local flow coefficient corresponding to Figure 5.8.	141
5.16 Comparison of exit flow conditions at different points on a Balje chart.	143
5.17 Non dimensional Area and cubic velocity for turbines with different duty flow coefficient.	144
5.18 Effect of radius ratio on performance and optimal flow coefficient.	145
5.19 Effect of radius ratio on profile surface area and area averaged cubic velocity. .	146
5.20 Effect of Meridional velocity ratio on performance and optimal flow coefficient.	147
6.1 Total-total Mixed flow Smith chart featuring detrimental flow separation	152
6.2 <i>A&B</i> : Meridional projections (near suction surface) of entropy contours	153
6.3 Surface contour plot of reduced static pressure (Turbine A), L and H denotes regions of low and high pressure respectively	154
6.4 Variation in Mixed flow blade geometry with Loading	155
6.5 Comparison of static pressure variations for radial and non radial blade fibre designs, contour spacing equal	156
6.6 <i>A</i> :Zoomed in section of the inviscid solution of the turbine in figure 6.3 Including contours of Coriolis force, where H denotes region of high magnitude. <i>B</i> :Difference in the reduced static pressure field with Coriolis terms switch on or off (same contour spacing of $\Delta C_p = 0.05$, $L_{on} < L_{off}$).	158
6.7 Surface contour plot of reduced static pressure (Turbine A), L and H denotes regions of low and high pressure respectively	160
6.8 Comparison of a mixed flow turbine with and without a hub fillet and spoon, Contours are of reduced static pressure where L denotes low pressure regions .	161
6.9 Total-total mixed flow turbine Smith chart with fixed $R_r = 0.7$, $\frac{A}{r_m^2} = 2$ and $\lambda = 45^\circ$	163
6.10 <i>A</i> :Variation of non dimensional surface area and isentropic surface velocity cubed. <i>B</i> :Inlet and exit meanline flow angles and blade geometry at various points through out the design space.	164
6.11 Estimated profile loss	165
6.12 Comparison of exit flow conditions at $\phi_L = 0.4$, A $\psi = 1.0$ and B $\psi = 1.8$. .	166
6.13 <i>A</i> :Estimated secondary loss. <i>B</i> : Estimated components of end wall loss.	168
6.14 leakage loss	169

6.15 A:Contours of total to total efficiency for mixed flow turbines with varying loading and duty flow coefficients. <i>B</i> : Contours of Surface Area and surface area averaged velocity cubed, varying loading and duty flow coefficients.	171
6.16 Contours of loss in efficiency of Mixed turbines due to profile loss	173
6.17 Contours of loss in efficiency of Mixed turbines due to endwall loss	173
6.18 Contours of loss in efficiency of Mixed turbines due to Tip Leakage loss	174
6.19 Contours of total to static efficiency for mixed flow turbines with varying loading and duty flow coefficients	175
6.20 Contours of Total to Total efficiency with varying Radius Ratio and Cone Angle, $\psi = 1.0$ and $\Phi_D = 0.2$	176
6.21 Contours of Total to Total efficiency with varying Radius Ratio and Cone Angle, $\psi = 1.6$ and $\Phi_D = 0.2$	178
6.22 Contours of surface area with varying Radius Ratio and Cone Angle, $\psi = 1.6$ and $\Phi_D = 0.2$	179
7.1 Contours of total to total efficiency for Axial, Mixed and Radial flow turbines with varying loading and duty flow coefficients	184
7.2 Contours of total to static efficiency for Axial, Mixed and Radial flow turbines with varying loading and duty flow coefficients	192
7.3 A: Contours of non-dimensional second moment of volume for Axial, Mixed and Radial flow turbines with varying loading and duty flow coefficients. <i>B</i> : Contours of non-dimensional Power density for Axial, Mixed and Radial flow turbines with varying loading and duty flow coefficients.	197
7.4 Illustration of how parallelization and staging shifts duty flow parameters across a (Φ_D, Ψ) style Balje chart	200
7.5 Illustrating effects that varying diffuser recovery factor has on combined turbine-diffuser efficiency for various design flow coefficients. The red line marks the track of the optimal design flow coefficients	202
7.6 Combined total to total Balje diagram	203
7.7 Combined total to static Balje diagram	204
B.1 lost efficiency due to numerical error and cusp	221
B.2 Change in area and average surface velocity cube with - 10 degrees exit swirl .	222
B.3 Change in surface dissipation with - 10 degrees exit swirl	223
B.4 End wall dissipation and secondary flow components of loss	224
B.5 Radial Total to static with $C_d = 0.006$	225
B.6 Radial Total to static with $C_d = 0.006$	226
B.7 Comparison of Model and numerical solution with varying radius ratio and local flow coefficient	228

B.8	profile surface area and velocity distribution	229
B.9	Mixed turbine secondary and end wall surface dissipation loss	230
D.1	Model diagram	233
D.2	total to total efficiency vs Non dimensional radius of curvature	235
D.3	Change in total to total efficiency vs curvature amplification factor	236
E.1	total to total efficiency vs Non dimensional radius of curvature	238
E.2	Change in total to total efficiency vs curvature pressure gradient factor	238
H.1	Velocity triangles	244

List of tables

3.1	turbines duty and boundary conditions	85
4.1	Axial Smith chart parameters	93
4.2	Axial Balje chart parameters	110
5.1	Radial Smith chart parameters	125
5.2	Radial Balje/Rohlik chart parameters	132
6.1	Mixed flow Smith chart parameters	162
6.2	Mixed flow Balje chart parameters	170
7.1	Turbine comparison for point A	187
7.2	turbine comparison for point B	189
7.3	turbine comparison for point C	191
7.4	turbine comparison for point A	194
7.5	turbine comparison for point B	196
A.1	turbine comparison for point D	216
A.2	turbine comparison for point E	217
A.3	turbine comparison for point F	218
A.4	turbine comparison for point C	219
A.5	turbine comparison for point D	220

Nomenclature

Roman Symbols

$\overline{V^3}^*$ Non dimensional area averaged surface velocity, $\frac{\overline{V^3}}{\Delta h_0^2}$

A Area

A^* Non dimensional Area, $\frac{A}{\Delta h_0^{-\frac{1}{2}} Q}$

D_s Specific Diameter

DF Velocity diffusion Factor $\frac{W_{peak}}{W_2}$

h Specific Enthalpy, span(height)

N_s Specific Speed

P Pressure

p Pressure, Pitch

R_r Radius Ratio

R_{vm} Meridional Velocity Ratio

S Entropy

s Specific Entropy

T Temperature

V Velocity absolute or relative

W Velocity relative only

Greek Symbols

α absolute flow angle

β	relative flow angle
δ^*	displacement thickness
η	Efficiency
γ	Ratio of specific heats
λ	cone angle
Ω	Vorticity
ω	Angular velocity
ϕ_D	Duty Flow Coefficient
ϕ_L	Local Flow Coefficient
ψ	Loading coefficient
σ	Camber, rake angle
θ	momentum thickness, circumferential coordinate

Subscripts

θ	Circumferential Component
$*$	Non-dimensional, Rescaled
1	Rotor inlet
0	Total
2	Rotor exit
a	Area
ake	Absolute kinetic energy
bp	Base pressure
cen	Centrifugal
cori	Coriolis
cur	Curvature (Casing)
d	Dissipation

dis	Discharge
eke	Exit kinetic Energy
end	End wall
in	Inertial
is	Isentropic
m	Meridional
n	Mean line (centre of area)
C_o	Circulation coefficient, $\frac{\text{actual circulation}}{\text{ideal circulation}} = \frac{\oint V_{surf} ds}{V_2 S_{tot}}$
p	pressure
pres	Pressure Surface
pro	Profile
rac	Relative acceleration
r	Radial, reduced
sec	secondary flow
s	Surface, suction
suc	Suction Surface
te	Trailing edge
tip	Tip leakage
tot	Total
ts	Total to Static
tt	Total to Total
Q	Volume
x	Axial

Chapter 1

Introduction and Literature Review

1.1 Introduction

There are hundreds of millions of turbines currently in use throughout the world, and therefore small improvements in performances can lead to massive savings in global energy production and considering the current climate crisis, increasing efficiency is of paramount importance. During the early stages of turbine design, poorly informed decisions about the architecture type and design parameters can lock designers into suboptimally performing regions of the design parameter spaces.

There are generally two main philosophies by which designers go about preliminary design and architecture selection; Company heritage (i.e go with what you know) or by the use of design charts, such as those developed by Cordier 1953 [14], Balje 1962 [3] and Rohlik 1968 [46]. These authors leveraged the power of similarity, which stems from the inherent scaling symmetries in the Navier Stokes equations, to construct design spaces by empirical, semi-empirical and analytical approaches. Balje considered the design charts, which are still used today as preliminary, due to the lack of understanding of the interrelation between loss and geometry. This thesis aims to build on the work done by these authors and to use contemporary knowledge and modern computational tools to further expand the understanding of these design spaces.

1.2 Turbine Flow Features

Before discussing architecture selection, it is important first to appreciate the differing nature of axial, radial and mixed flow turbines. A good starting point is the Euler turbine equation.

$$\Delta h_0 = \underbrace{\frac{1}{2}(V_1^2 - V_2^2)}_{\Delta h_{absolute KE}} + \underbrace{\frac{1}{2}(W_2^2 - W_1^2)}_{\Delta h_{relative acceleration}} + \underbrace{\frac{1}{2}\omega(r_1^2 - r_2^2)}_{\Delta h_{Centrifugal}} \quad (1.1)$$

This equation was taken from Casey [12] which the following discussion is based on. The first term on the RHS of equation 1.1 represents the change in absolute kinetic energy through the turbine. The stator or scroll/volute provides high amounts of kinetic energy, which is then extracted by the rotor. The second term represents the change in relative flow velocities in the rotor. In compressors this would be a deceleration, which if too high can lead to stability issues and high losses due to flow separation. For turbines operating at low Mach numbers, this is an acceleration, which has no physical limit associated with separation, hence turbines can achieve higher work transfers than compressors. The third term is known as the centrifugal term/effect which generally differentiates radial and mixed from axial architectures, where this term is zero or close to zero. It will later be shown that changes in ratio of the exit to inlet radius redistributes work between the centrifugal and relative acceleration term (for a case of zero interstage swirl).

Apparent Forces And Reduced Static Pressure

In order to be able to interpret the differing nature of flow for axial, radial and mixed turbines within the rotating reference frame, one must first have an appreciation of the additional apparent force terms. These terms arise from the variant transformation to a rotating reference frame. The incompressible Euler flow equation in a rotating reference frame is as follows

$$\frac{\nabla p}{\rho} = -(\vec{w} \cdot \nabla) \vec{w} - 2\vec{\omega} \times \vec{w} - \vec{\omega} \times (\vec{\omega} \times \vec{r}) \quad (1.2)$$

Note $\vec{\omega}$ is angular velocity and later $\vec{\Omega}$ will be used for vorticity. The first term on the RHS of equation 1.2 is the inertial term which was present before transformation and represents the relative acceleration due to stream line curvature. The second term is the Coriolis acceleration and the third term is the centrifugal term. Johnson [36] combines the centrifugal term with the pressure term to form a reduced static pressure (see equation 1.3). This is particularly useful in interpreting the effects of the pressure field on low momentum fluid in a rotating reference frame.

$$p_{in} + p_{cori} = p^* = p - \frac{1}{2}\rho\omega^2r^2 \quad (1.3)$$

$$\frac{1}{\rho} \nabla [p_{in} + p_{cori}] = -(\vec{w} \cdot \nabla) \vec{w} - 2\vec{\omega} \times \vec{w}$$

Johnson [36] showed that the direction of the secondary flow was in the direction of the reduced static pressure gradient. This is because the centrifugal component of the pressure field is independent of velocity and is in balance regardless of the momentum of the fluid. Therefore this component of the pressure field will not drive over turning of low momentum flow or drive boundary layer separation. It is for this reason centrifugal compressors can operate at higher pressure ratios than those of axial ones. Essentially the centrifugal loading component does not affect the boundary layer.

Zangeneh [58] showed that the generation of stream wise vorticity ($\vec{w} \cdot \Omega$; also known as helicity) in the relative frame, may be expressed as

$$\vec{w} \cdot \nabla (\vec{w} \cdot \vec{\Omega}) = 2\vec{\Omega} \cdot (\vec{w} \cdot \nabla) \vec{w} + \vec{\omega} \cdot (2\vec{\omega} \times \vec{w}) = \frac{1}{\rho} (\vec{\omega} \cdot \nabla p_{in} + \vec{\omega} \cdot \nabla p_{cori}) \quad (1.4)$$

Stream wise vorticity is generated when there is a reduced static pressure gradient in the direction of the vorticity vector (i.e vortex stretching or compression). This will be used to explain the nature of the secondary flow in the various architectural types.

Flow Development In Axial Turbines

In order to analyse the sources of loss within a turbine stage, it is first important to understand aerodynamic features that drive these losses. To aid in the description of the flow features, the axial turbine blade will be broken into 3 regions: the core region or 2D region, the hub region and the casing region.

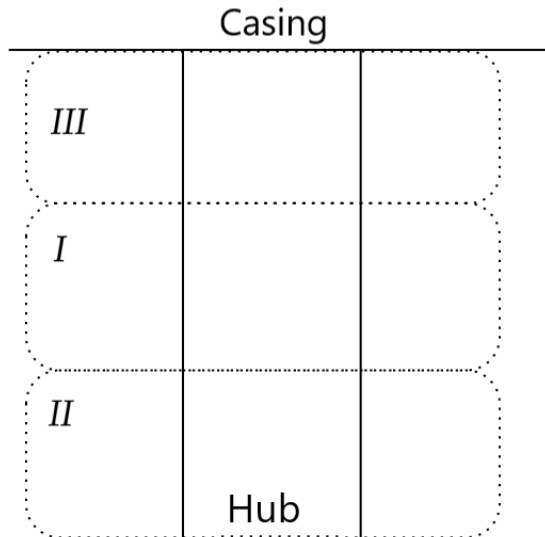


Fig. 1.1 Axial turbine Flow regions (meridional projection)

Core Flow *I*

This is considered to be the region of flow that is minimally influenced by the end walls and tends to be two dimensional in nature (for high aspect ratios). The loss measured in this region during cascade testing is generally known as profile loss, which is a result of entropy generation within the boundary layer, forming over the blade surface and trailing edge effects. Important features which govern the behaviour of the boundary layer in this region is the velocity level and distribution, as well as the state of the boundary layer and trailing edge thickness.

Hub and Casing Regions *II&III*

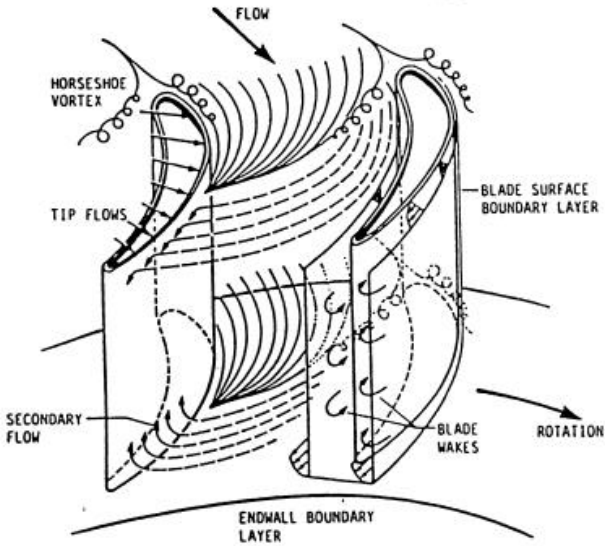


Fig. 1.2 schematic of secondary flow patterns in an axial turbine, from [29]

Secondary Flow

The “bulk” flow establishes the pressure field which arises primarily due to the blade to blade pressure gradient and any associated swirl. Any low momentum flow (e.g. boundary layer fluid) will be strongly influenced by the pressure field and will overturn. Additionally, the vorticity of the inlet end wall boundary layer is in a similar direction to the cross passage pressure gradient and hence vortex stretching will occur. Flow patterns are illustrated in Figure 2 and the description is based on that given by ref:Denton [26],Miller and Denton [29] and Coull [16].

The end wall boundary layer starts to be influenced by the blade pressure field. This happens roughly a blade pitch upstream of the leading edge. The boundary layer thickens and starts to overturn towards the suction surface. As the low momentum fluid approaches the leading edge, it is forced to separate. This occurs before reaching the leading edge region as it has a lower stagnation pressure than the bulk flow. The separated boundary layer roles up into the commonly known horse shoe vortex. The inlet end wall boundary layer is then funnelled between the lift off lines. The pressure leg of the horse shoe vortex is driven across the passage towards the suction surface of the adjacent blade, growing as it sweeps up the end wall boundary layer fluid. Some of this fluid is driven slightly up the span of the blade. The suction surface leg of the horse shoe vortex forms a small counter rotating vortex in the suction surface end wall corner. A new thin boundary layer forms behind the lift off line and is subjected to the scoring effect of the passage vortex and skewing from the pressure to suction surface pressure gradient. As a result of the formation of this secondary flow, a large loss core is present at the trailing edge, displaced slightly away from the end wall. This loss core contains mostly fluid from the inlet end wall boundary layer, as well as some new end wall boundary layer fluid, and fluid from the suction surface boundary layer. The secondary vorticity associated with this loss core causes

rotating flow with a velocity component normal to the primary flow direction. The vorticity transfers kinetic energy from the bulk flow to secondary kinetic energy (SKE). The SKE is then dissipated down stream by mixing.

Leakage Flow Over Un-shrouded Blades

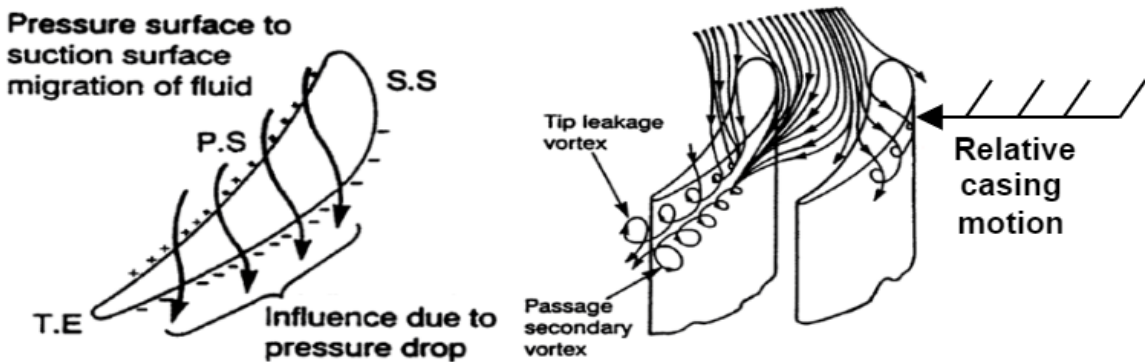


Fig. 1.3 schematic of tip leakage flow in an axial turbine [Denton [26]]

This thesis primarily concerned with un-shrouded blades as most mixed and radial turbines are un-shrouded. For obvious mechanical reasons, tip clearance is required between the rotor and the casing. This clearance allows flow to leak over the blade tip from the pressure surface to the suction surface. The leakage flow is driven from the pressure surface through the tip gap to the suction surface, due to the over tip pressure gradient. Flow enters the tip gap from the pressure side and separates at the blade edge, contracting into a jet with a typical contraction ratio of 0.6. This contraction ratio is a function of the edge radius and Reynolds number as shown by Moore & Tilton [39] and Heyes et al [34]. If the blade thickness is about 4 times the clearance gap, then the flow will completely mix out in the gap. If the blade thickness is significantly thinner, then the contracted jet will not mix in the gap. The leakage flow then proceeds to enter the suction side region. Since the flow velocity on the suction side and the leakage flow both differ in magnitude and direction, a vortex sheet is set up. This will then roll up forming a tip leakage vortex, rotating in the opposite direction to the secondary flow. This vortex is then convected down the passage. The effect of the relative casing motion (RCM) generally reduces the strength of tip leakage flow for turbines. This is likely to be dependent on a range of parameters such as end wall boundary layer thickness, and so on. Yaras and Sjolander [57] found that the discharge coefficient was approximately halved [4]. Denton [26] attributed this to a modification of the driving pressure and not necessarily to a change of the velocity profile in the tip gap. A computational study by Coull and Atkins [19] showed that the leakage mass flow changed markedly when introducing RCM and a stage calculated inlet condition,

which fully resolved the end wall boundary layers and effects of the upstream stator. For the case where only RCM was used, Coull and Atkins attributed the reduced leakage flow to a reduced driving pressure as a result of the relative dynamic head $\frac{1}{2}\rho(\omega r)^2 \cos^2 \beta$ which was first introduced by Dambach [23].

Flow Development In Radial & and Mixed Turbine Rotors

As with the axial turbine, the radial turbine blade will be broken into 3 regions: the inlet Section, radial to axial bend and axial section/exducer, see figure 1.4. This subsection draws from the work done by Zangeneh [58].

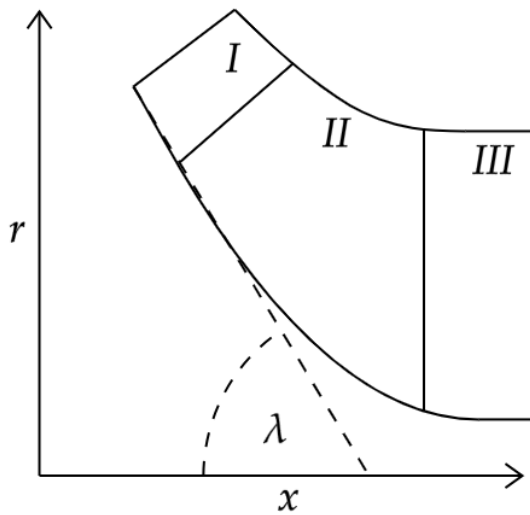


Fig. 1.4 Radial turbine Flow regions (meridional projection)

Inlet Section I

For radial turbines, the flow in the inlet section is predominantly radial, and therefore the circumferential component of the Coriolis term is large. This sets up a high reduced static pressure gradient from blade to blade. This in turn initiates secondary flow on the hub and casing walls which flows towards the suction surface. Decreasing the cone angle λ shifts the architecture to a mixed flow design and for a constant meridional velocity this reduces the radial component and hence the associated component of the Coriolis force. This is illustrated in figure 1.5 A. However increases in the inlet angle, typically associated with the use of mixed flow turbines, results in higher circumferential components of velocity, this in turn, increases Coriolis force associated with this component of velocity. In axial turbine the Coriolis force vector is orientated up the span and does not have a significant influence on the blade to blade loading. As with radial turbines, mixed flow turbines have a component of the Coriolis force away from

the blade surface, which must be balanced by the pressure field and therefore contributes to the blades pressure distribution.

In radial turbines, the effect of high Coriolis at the inlet gives rise to the incidence effect in which the flow is turned into the blade increasing the effective flow angle. An alternative description of the incidence effect was described by Whitfield et al [54]. The author attributes the incidence effect to the existence of the so called relative eddy. This eddy arises as a result of an initially irrotational fluid entering a rotating reference frame, maintaining its angular momentum. Thus in the rotating frame, a counter vortex is set up as illustrated in Figure 1.5 B. The circulation tends to turn the stream lines into the rotor and as a result, must be compensated for in order to avoid separation on the thin leading edges of turbine rotor blades.

Dambach [23] showed that the inlet section experiences reduced leakage mass flow in comparison with the rest of the turbine, due to a high component of relative casing motion perpendicular to the local blade surface.

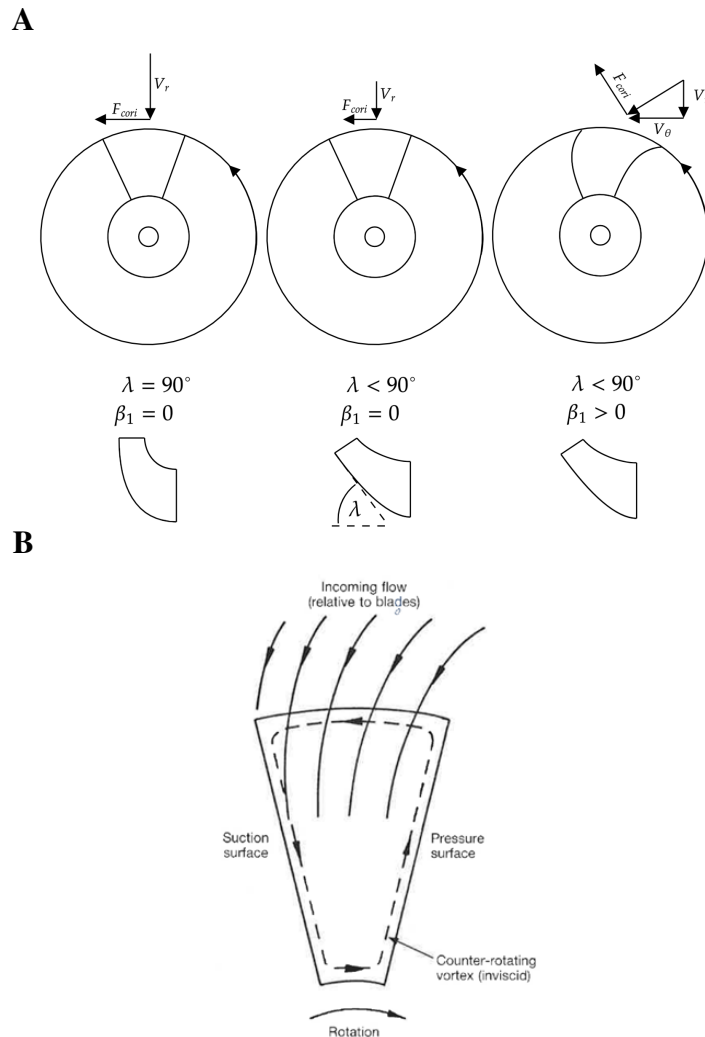


Fig. 1.5 A: Coriolis force directions. B: counter vortex

Radial to Axial Bend II

The flow in the radial to axial bend is more complex in nature, as it is influenced by streamline curvature and rotational effects as pointed out by Zangeneh [58]. Due to the meridional curvature in the radial to axial bend, there is a spanwise acceleration (and therefore an associated pressure gradient) with a component in the direction of the blade boundary layer vorticity. This results in the formation of secondary flow which is driven to the casing surface (the position of minimum p^* in that plane). This can be seen in Figure 1.6 where according to Zangeneh [58] the relative Mach number contours are equivalent to p^* contours. The Coriolis term reduces in strength as this section bends towards the axial direction, reducing the $2\omega V_r$ component. Huntsman[35] reported the existence of a lift off line in this region as a result of the secondary flow. The magnitude and component of relative casing motion perpendicular to the blade is lower in this region as a result of the reduced radius and increased blade angle. This results in a stronger leakage flow in comparison to the radial section. Reducing the cone angle reduces the radius of curvature at the casing which can help reduce the cross passage driving pressure, as well as help prevent casing separation.

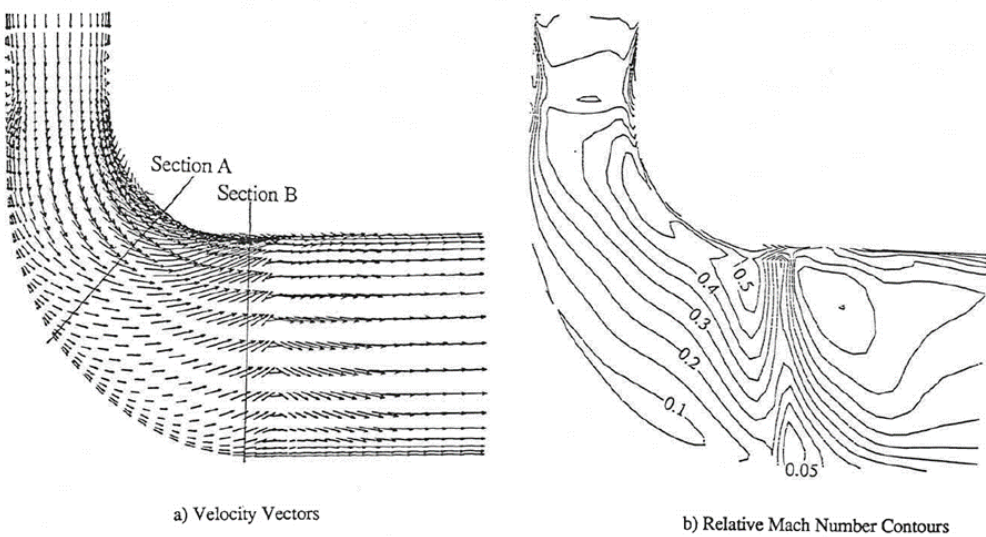


Fig. 1.6 Predicted flow in meridional plane, from Zangeneh [58]

Axial Section/ Exducer II

The secondary flow in the exducer is also a result of both curvature and Coriolis acceleration. However, $2\omega V_\theta$ is dominated by the Coriolis term. This term is in the direction of the blade surface boundary layers and drives secondary flow from the hub to the casing. The blade curvature in this section also drives low momentum fluid from pressure to suction surface. The leakage flow in the axial section is further increased due to the now small effect of the

relative casing motion is negligible. This is because the relative casing motion is low in this region. Figure 1.7 A, gives an overview of the secondary flow with directions and strengths. The resulting secondary flow forms a loss core close to the suction surface casing corner. Similarly, the leakage flow forms a loss core rotating in the opposite sense to the secondary flow vortex as shown in figure 1.7 B.

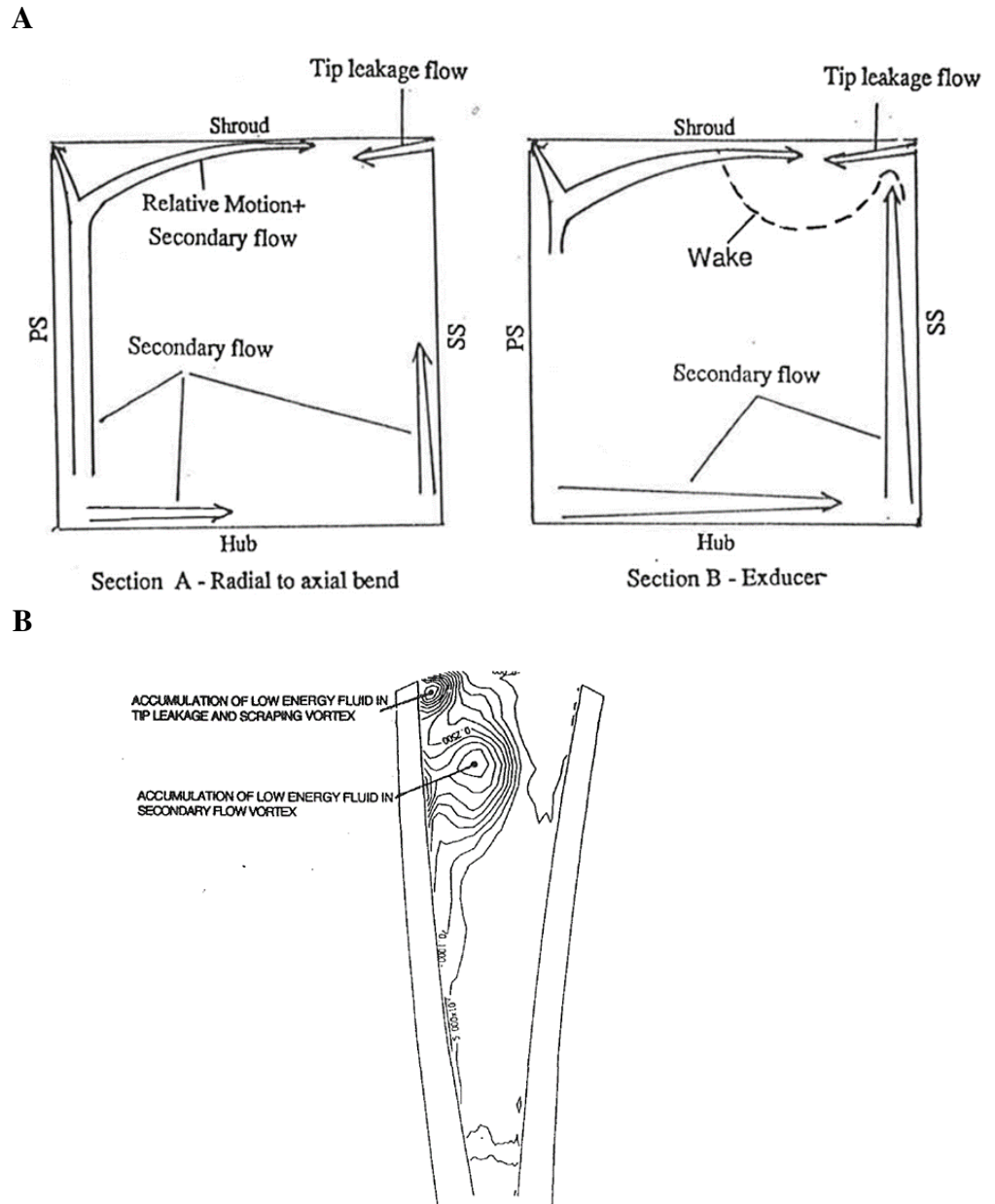


Fig. 1.7 A: Movement of low momentum fluid on two cross-flow surfaces , from Zangeneh [58].
B: Contours of relative stagnation pressure at the exit of a radial turbine , from Huntsman [35].

1.3 Loss Mechanisms

Understanding the mechanisms which drive loss are key to understanding the shape of the design space. This section discusses these loss mechanism and is largely drawn from Denton [26].

Entropy generation in fluid flows can arise from the following processes:

- Viscous friction in either boundary layers or free shear layers (mixing processes).
- Heat transfer across finite temperature differences.
- Non equilibrium processes-such as shock waves.

The focus of this section is on describing how the first of these entropy generation mechanism processes arise in axial radial and mixed flow machines.

Entropy Generation In Boundary Layers

Boundary Layers are a primary sources of loss in turbines. Within a 2D boundary layer, at a given height from the surface, the local generation of entropy per unit volume due to viscous dissipation is given by:

$$\dot{S}_v = \frac{1}{T} \tau \frac{dv}{dy} \quad (1.5)$$

Here $\tau \frac{dv}{dy}$ is the viscous shear work which is being converted to heat at temperature T . At the molecular level (From a kinetic theory point of view) the "bulk" or average kinetic energy of the molecules, is being transferred via diffusion (a mixing process which gives rise to viscosity), to thermal kinetic energy.

For most boundary layers, the change in velocity occurs in the lower regions close to the surface and hence this is where most of the entropy is produced. This is especially true for equilibrium turbulent boundary layers due to their universal velocity profile nature. Only the outer layer is strongly affected by pressure gradients leaving the viscous and inertial sublayer largely unaffected, as these regions are dominated by the force terms after which they are named. Dawes [24] showed that 90% of the entropy is produced in this inner region, which would imply that the entropy produced by the equilibrium boundary layer is largely insensitive to the detailed state. The entropy production per unit surface area can be turned into a dimensionless coefficient.

$$C_d = \frac{T \dot{S}_a}{\rho V_\delta^3} \quad (1.6)$$

Where S_a is the entropy produced per unit surface area and V_δ is the velocity at the edge of the boundary layer. Dawes [24] pointed out that for turbulent flows the dissipation coefficient like the coefficient of friction only varies weakly ($Re_\theta^{-\frac{1}{6}}$) but unlike the coefficient of friction, is nearly independent of the shape factor at least in the range 1.2 to 2.0. Figure 1.8 suggest that, above momentum based Reynolds number of 500, the dissipation coefficient remains largely unchanged.

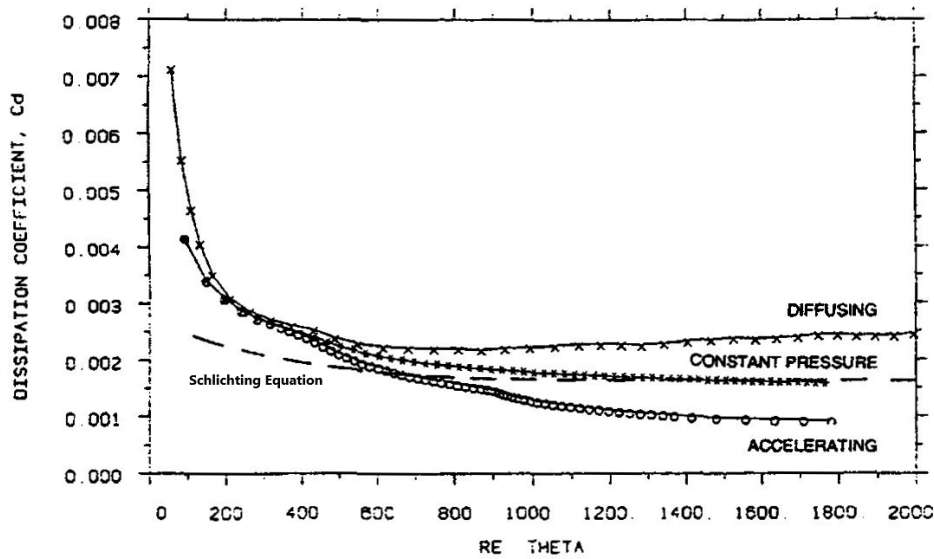


Fig. 1.8 Dissipation coefficient for laminar and turbulent boundary layers Denton [26] / Cebeci and Carr [10]

Considering that the dissipation coefficient is relative insensitive, equation 1.6 shows that surface dissipation is most sensitive to changes in velocity. Assuming incompressibility and a constant dissipation coefficient, the total entropy generated can be written as an integral over the entire surface area.

$$\dot{S} = \frac{C_d \rho}{T} \int^{A_t} V^3 da. \quad (1.7)$$

Then defining an area average of the surface velocity cubed.

$$\overline{V^3}_s = \frac{\int^A V^3 da.}{A} \quad (1.8)$$

Combine 1.7 and 1.8

$$\dot{S} = \frac{C_d \rho}{T} \overline{V^3} A \quad (1.9)$$

Equation 1.9 will be important later on as it can be used to characterise the lossy nature of a turbomachine since it can be used to illustrate the contributions from area and velocity to the overall surface dissipation. It is useful to non dimensionalise these with machine duty (incompressible form), this allows for the comparison with machines with differing duty.

$$\overline{V^3}^* = \frac{\overline{V^3}}{\Delta h_0^{\frac{3}{2}}} \quad (1.10)$$

$$A^* = \frac{A}{\Delta h_0^{-\frac{1}{2}} Q} \quad (1.11)$$

Entropy Generation in Mixing Processes

Entropy generation occurs wherever flow shear is present and as such is not only confined to boundary layers. High amounts of shear occur in free shear layers such as leakage jets, wakes, and at the edge of separated regions. Although these are all complex in nature, the overall entropy can be approximated from simple control volume analysis. This is because the mixing will occur until the flow has become uniform and therefore conservation laws can be used to calculate uniform state at the exit of the volume.

Mixing processes can take place in regions of increasing or decreasing static pressure which will alter the overall amount of entropy created. When the shear layer is within a favourable pressure gradient, the transverse velocity gradient driving mixing is reduced. This is because the slow moving fluid remains within the favourable pressure gradient for longer and is accelerated, which reduces the difference in velocity. Since the transverse velocity gradient is reduced, the overall entropy produced is lower. Conversely deceleration increases mixing loss.

Profile and Trailing Edge Loss

Profile loss is considered to be the loss produced by the blade itself over a region that is not influenced by the end walls. The following analytical expression derived by Denton [26] is for the mixed out total pressure loss (at constant area) downstream of a two-dimensional blade row.

$$\zeta = \frac{C_{pb} t}{p \cos \beta_2} + \frac{2\theta}{p \cos \beta_2} + \left(\frac{t + \delta}{p \cos \beta_2} \right)^2 \quad (1.12)$$

The first term on the RHS is due to the base pressure at the trailing edge being lower than that of the free stream value. The second term is the boundary layer loss of the blade mixed out. The final term represents the combination of the blockages of the trailing edge and boundary layers.

Isolating the profile loss is harder to establish in radial devices as the average aspect ratio is low and the flow along the mean line is heavily influenced by the end walls and meridional curvature. End-wall loss is grouped together with profile (or blade surface) loss to form what is called passage loss, which accounts for all the loss in the passage, excluding leakage loss.

As previously shown, the loss generated by an attached boundary layer is proportional to the dissipation coefficient multiplied by the local surface velocity cubed. The dissipation coefficient varies greatly between laminar and turbulent boundary layers highlighting the importance of predicting transition in turbo machines. Huntsman's [35] turbine stator had a profile loss as low as 1.2 % which was attributed to the boundary layer being laminar over most of the stator as a result of the zero suction surface diffusion. However, this rig is not representative of all radial device inlet conditions for example turbochargers tend to operate with high inlet turbulence intensity which would likely result in transition.

Trailing edge loss is another major source of profile loss. This is a result of pressure at the base of the trailing edge being under the free stream value. For turbines with blockage around 6%, a third of the profile loss is attributed to the trailing edge as confirmed by Roberts and Denton [44]. The loss attributed to trailing edge can be approximated:

$$\zeta_{te} = \frac{C_{pb}t}{p \cos \beta_2} + \left(\frac{t}{p \cos \beta_2} \right)^2 \quad (1.13)$$

The first term on RHS of equation 1.13 represents the effects of the base pressure and second term is the mixed out loss due to trailing edge blockage.

1.3.1 Secondary/Endwall Flow Loss

The flow structure of the end wall loss was describe in section 1.2. This loss is function of the blade loading and aspect ratio but very roughly is considered to be around a third of the total loss of an typical axial turbine.

The factors causing end wall loss are complex in nature; however, Miller and Denton [29] have described the interrelating components that cause this loss as follows:

- There is a component of entropy generation from the end wall boundary layer upstream of rotor which can be high for shroud-less rotors
- A further source of entropy generation is from the end wall boundary layer within the passage, which is likely to be high due to a thin dissipative laminar boundary layer formed behind lift off line
- A third aspect of end wall boundary layer loss is entropy generation in the end wall boundary layer down stream of rotor which is reduced in shroud-less rotors

- The loss associated with the end wall boundary layer upstream, in the passage and downstream of the passage is considered by Denton to contribute to $\frac{2}{3}$ of the total end wall loss
- Entropy is generated as a result of mixing out of upstream end wall boundary layer
- An additional source of entropy generation is due to mixing out of kinetic energy of the secondary vortex system which is in order of 30% of total end wall loss in turbines
- There are further factors influencing end wall such as early transition, separation and boundary layer skews etc.
- A final factor influencing end wall loss is the complex interaction between the secondary flow and tip leakage flow and hence end wall loss and tip leakage loss cannot completely decoupled

1.3.2 Passage losses

Due to the inherently complex nature of the flow within radial turbines the profile and secondary loss/end wall are not decoupled during mean line prediction and are grouped together as a passage loss. The current state of the art for passage models available in open literature is that given by Baines [2].

$$\Delta h_{pass} = K_p \frac{1}{2} (W_1^2 + W_2^2) \left(\left(\frac{L_h}{D_h} \right) + 0.68 \left[1 - \left(\frac{r_1}{r_2} \right)^2 \right] \cos(\beta_2) \right) \quad (1.14)$$

Within this model the passage loss comprises of two components: the friction on the blade and end wall, and secondary flow loss. The first term of the equation in the large brackets represents the frictional losses on the blade and end walls where $\frac{L_h}{D_h}$ is the ratio of mean hydraulic length to mean hydraulic diameter which can be approximated from initial geometry. The second term in the large brackets accounts for the secondary flow loss excluding the end wall friction. This comprises of two factors: one for blade loading as a result of mean radius change and one for turning the flow in tangential plane where c is the rotor blade chord and b is the blade height. The value for K_p generally takes values of $K_p = 0.1$. However, for turbines with high exducer to inlet tip radius ratio, the passage loss is multiplied by 2 when

$$\frac{r_{1c} - r_{2c}}{h_2} < 0.2$$

Baines stated that this accounts for the large increase in secondary loss and probable separation on the shroud as a result of a small radius of curvature. It must be pointed out that the criterion presented above for a sharp increase in passage loss does not explicitly include the

axial length which would govern the radius of curvature of the casing line. If casing line were to take circular form this would correspond to a non dimensional radius of curvature limit of $r_c/h_2 = 0.2$.

1.3.3 Tip Leakage loss

Leakage is a form of mixing loss. To help better understand how the loss is driven, an equation is taken from Denton's [26], "Simple theory for tip leakage loss of unshrouded blades".

$$T\Delta S = \int V_2^2 \left(1 - \frac{V_p}{V_s}\right) dm \quad (1.15)$$

From this, the loss is shown to scale with the exit velocity, the ratio of the local pressure to suction surface velocities and the mass flow which can be estimated from.

$$dm = C_{dis} t \sqrt{2\rho\Delta p} ds$$

Which shows that the mass flow is proportional to the tip gap, over tip driving pressure which itself is a function the difference in suction and pressure surface velocities and the discharge coefficient C_{dis} . As previously mentioned Dambach [23] showed that the inlet section experiences a reduced leakage mass flow in comparison with the rest of the turbine due to the "scraping effect" of the relative casing boundary layer. This was presented as a reduced discharge coefficient in the inlet section. Following this Dambach [22] used Dentons model to compare tip leakage of radial and axial turbines used as micro-turbine generators. The author showed in that specific comparison, that due to the scraping effect, the radial turbine had significantly lower leakage loss.

1.3.4 Exit loss

If the kinetic energy exiting a stage is completely un-utilised, it is considered a loss in performance. However, it does not result in a rise in entropy. This loss is the measure of the difference between the total to total and total to static isentropic efficiency. It can be calculated from the absolute exit dynamic head which can be written as:

$$\Delta\eta_{eke} = \frac{(R_{vm} \phi_L)^2}{2\psi \cos^2(\alpha_2)^2} \quad (1.16)$$

Where R_{vm} is the ratio of exit to inlet meridional velocity. The exit loss is a strong function of flow coefficient and exit swirl angle and as such, most single stage machines (without exit diffusers) are designed with low flow coefficient and zero exit swirl.

1.4 Radial blade fibre

Nearly all radial and mixed flow architecture turbines are design with radial blade fibres. This produces high strength blades because no centrifugal bending moments are generated due to the alignment of the blade fibres and centrifugal stress. Also for machined blades this allows for easy access of cutting bit.

A radially fibred turbine is characterised by a single camberline $\theta(x)$ line which defines the entire blade surface. In other words for a give axial location the value for θ is equal for all value of radius, see figure 1.9.

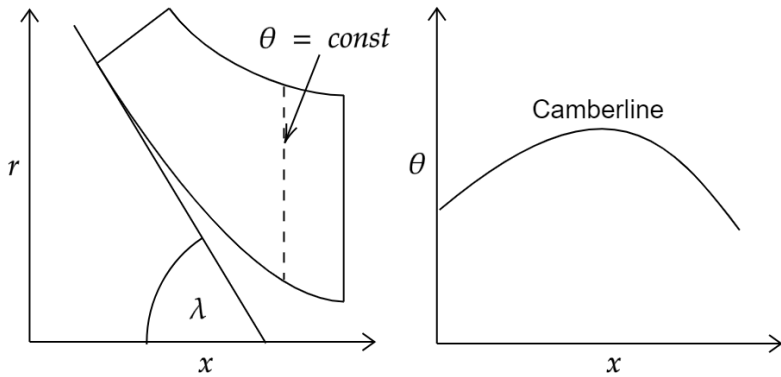


Fig. 1.9 Diagram illustrating radial blade fibre design

A relationship between the blade, camber/rake and cone angle, taken from Whitfield and Baines [54], is as follows:

$$\tan \beta = \tan \sigma \cos \lambda \quad (1.17)$$

Where the camber angle/rake is defined as

$$\tan \sigma = r \frac{d\theta}{dx} \quad (1.18)$$

A consequence of this design approach for radial turbines is that the blade inlet metal angle has to be zero in order to maintain a finite rake/camber angle. Equation 1.17 can be used to explain the predominate reason designers use mixed flow architectures. For cone angles $\lambda = 90^\circ$ The blade angle β has to be zero which in turn limits radial architectures loading ability. Using mixed flow architectures ($\lambda < 90^\circ$) relaxes this constraint and hence radial fibred mixed flow architectures can be designed for higher loading than radial architectures. For maximum possible energy extraction turbochargers need to operate efficiently at the peak of the exhaust pulse, this occurs at higher loading coefficients(lower speed ratios). Since mixed flow turbines can be designed at higher loading coefficients than radial architectures, the use of these architectures

can lead to better energy extraction. However this come with an addition geometric effect, a form of blade lean sometimes called rake. This is different to tangential lean used in axial architectures which is from stacking on a non radial axis. Instead this lean/rake forms an angle between the span wise and circumferential direction. Under standing how this comes about is best done by considering a projection of a mixed flow turbine onto a cylinder of constant radius which is illustrated in figure 1.10. From equation 1.17, increasing blade angle or cone angle increases the camber/rake angle this increases the difference in θ between the hub and casing. From inlet perspective the passage leant over. One very noticeable consequence of this lean is a significant increase in passage surface area.

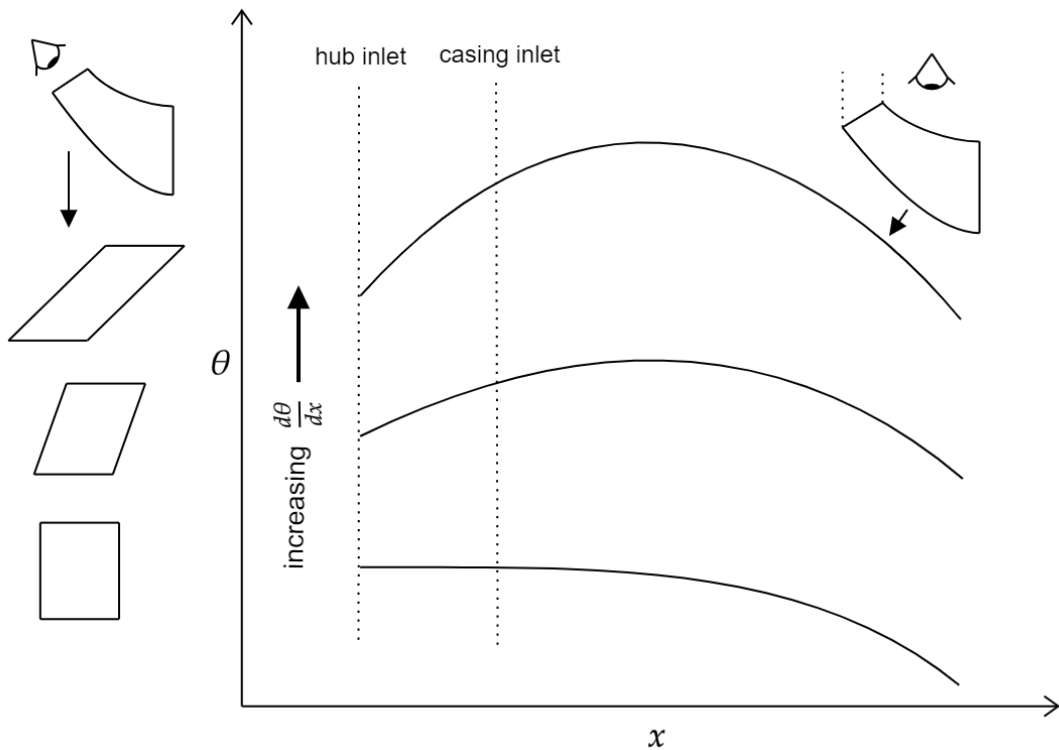


Fig. 1.10 Diagram illustrating how changing the inlet metal angle effects the shape of a mixed flow turbine passage for radially fibrerred architectures

1.5 Architecture Selection

1.5.1 Similarity Methods

The following subsection draw from Casey [12] and Balje[4]. Similarity in fluid mechanics arises from an inherent scaling symmetry present in the governing equations which dictate the behaviour of fluid devises such as turbomachines. Taking advantage of this symmetry (more specifically a scaling invariance) is indispensable for the design and comparison of

turbomachines. This is achieved through the use of non-dimensional parameters to rescale the machines. This rescaling allows the comparison of machines with different rotational speeds, sizes, fluids and flow conditions.

The different forms of similarity conditions include:

- Geometric similarity – the machines only differ in size with a single scaling parameter.
- Fluid dynamic similarity – the kinematic and dynamic description of the fluid flow through the machines need to be similar
- Thermodynamic similarity – the changes in the thermodynamic properties of the fluid through the system need to be similar.

If say a turbine being developed were to meet all of these similarity condition, when compared to an existing turbine, the turbine being developed will have exactly the same efficiency as the pre-existing machine. This is the power of similarity. In practise however not all of these conditions need to be met for similarity to be useful.

Similarity parameters

Non-dimensional parameters are a powerful means of utilising similitude. These parameters can be used to characterise machines and allows for the comparison of efficiencies, independent of the absolute measurements of a turbine. For adiabatic compressible flow, four types of similarity parameters are required to describe a fluid machine (operating with the same fluid). These are:

- A Newton number- which represents kinematic similarity e.g. head rise coefficient
- Strouhal number-additional kinematic similarity e.g. flow coefficient
- Reynolds number- which represents dynamic similarity in the form of the ratio of the viscous to inertial forces.
- Mach number- represents thermodynamic similarity. If different compressible perfect gases are used for comparisons, the ratio of the specific heats is also required, of which the speed of sound is a function.

These four types of non-dimensional parameters essentially represent the gross/duty characteristics of the machine and are derived using dimensional analysis. In functional form these typical would be.

$$\eta(N_s, D_s, Re_{rot}, M_{rot}, \gamma) \quad (1.19)$$

Where N_s is known as the specific speed, D_s the specific diameter and RE_{rot} and M_{rot} are rotational Reynolds and Mach numbers.

The Reynolds and Mach numbers, where possible are typically omitted during machine selection, leaving just the specific speed and diameter.

Typically these are defined as:

$$N_s = N \frac{Q^{\frac{1}{2}}}{H^{\frac{3}{4}}} \text{ or } \omega \frac{Q^{\frac{1}{2}}}{\Delta h_{0s}^{\frac{3}{4}}} \quad (1.20)$$

$$D_s = D \frac{H^{\frac{1}{4}}}{Q^{\frac{1}{2}}} \text{ or } 2r \frac{\Delta h_{0s}^{\frac{1}{4}}}{Q^{\frac{1}{2}}} \quad (1.21)$$

Where H is the total Hydraulic head. Note That this uses the isentropic change in stagnation enthalpy. Using isentropic conditions means that architectures can easily be selected independent of the efficiencies.

1.5.2 Balje, Cordier and Rholik Diagrams

Cordier [14] introduced the use of similarity parameters for Turbo-machinery, more specifically for "arbeitsmaschinen" (i.e compressors, pumps and fans). Cordier plotted the locations of "speed and diameter numbers" (N_s and D_s) of high performing machines on a logarithmic graph. Forming a curve which is now known as a Cordier line, as shown in figure 1.11 A. Cordier went on to show that Axial machines best operate in the high speed number region, radials in the lower speed number region and diagonal machines (mixed flow) in the intermediate region. It must be noted that this does not apply to turbines, Balje [3] showed that radial turbines sit within the axial turbines design space. While the Cordier diagram dose not give detailed information about the exact blade shape, it is a powerful for helping the designer make decision about machine type and sizing.

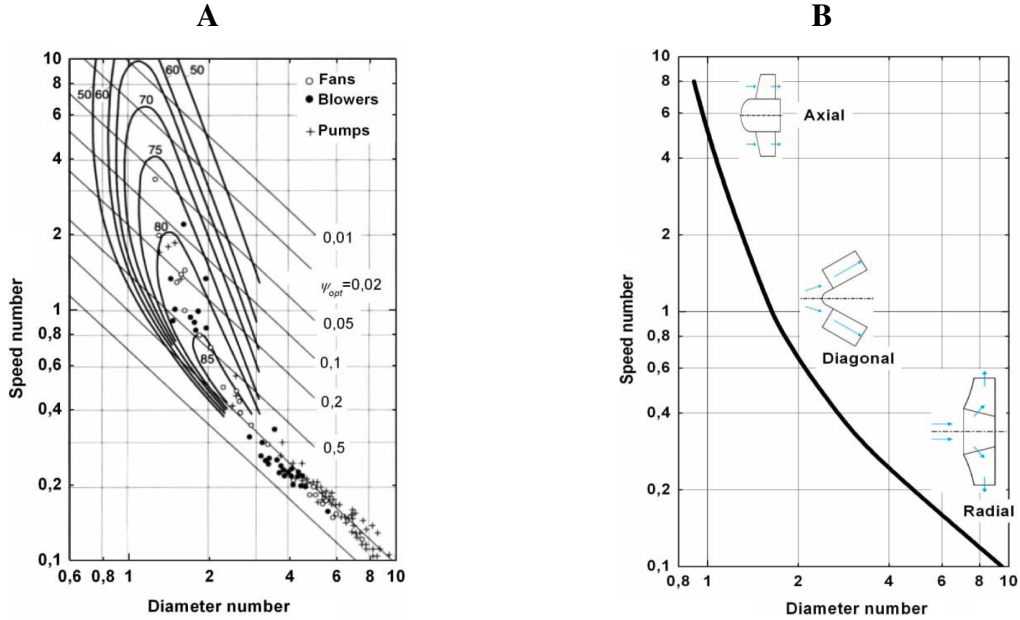


Fig. 1.11 Cordier diagrams from [30]

Balje [3] further developed on the similarity methods of Cordier. Balje created design charts for both compressors and turbines and for each of these machine types, studied a large variety of machines such as: partial admission, full admission, impulse and reaction type axial turbines and finally radial turbines (no mixed flow machines).

Balje mapped the design spaces using a hydraulic-turbine efficiency equation (derived from the Euler turbine equation) in conjunction with loss correlations, or via extrapolation of pre existing designs, using observed trends. Figure 1.12 is a composite N_s, D_s -diagram produced by Balje. The low specific speed region was produced using the loss correlations with the hydraulic-turbine efficiency equation and the high specific speed region was produced via extrapolation of pre existing designs. Balje notes that "the data for high specific speed designs are considerably more tentative than the data for low specific speed designs". The figure presented is for a total to static like efficiency, Balje does produce a design chart for a total to total like efficiency but states that the designs are optimised for total to static performance. In a later chapter, it will be shown that designs optimised for total to static efficiency differ significantly from those optimised for total to total efficiency.

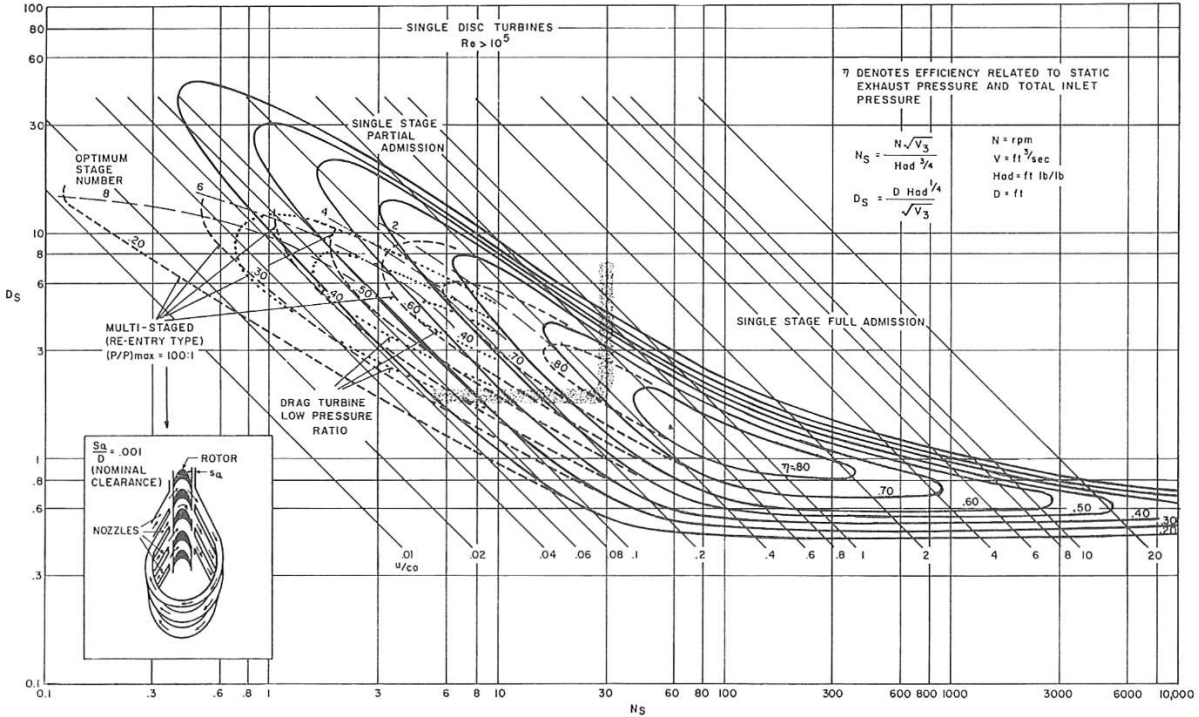


Fig. 1.12 $N_s D_s$ Diagram for single disk turbines Balje [3]

The design chart typically used by radial designers is one produced by Rohlik [46]. Rohlik examined the radial design space analytical (i.e using loss correlations) to determine the optimum geometry. This was done over a wide range of specific speeds and different design parameters. Amongst these were diameter ratio, stator exit flow angle and rotor exit hub to tip ratio. The optimum value for these parameters were determined which allows for rapid preliminary design. Figure 1.13 shows the design space produced by Rohlik, particularly useful is that the loss breakdown is shown. Some key points about the loss correlations are that the rotor and stator loss use the same correlation, which interestingly enough was developed for axial turbines. In addition to this, the leakage loss model only scales with the ratio of clearance height to span.

The key main conclusions stated by Rohlik are:

- The maximum total to static and total to total efficiencies can be found at 0.58 and 0.93 respectively
- The efficiency drops rapidly with decreasing specific speed. Due to high rotor, leakage and windage loss. Which is a result of high ratios of loss generating area to flow area.
- The optimum geometry features are basically the same for both optimum total and static efficiency.

- Using an exit diffuser with effectiveness of $C_r = 0.6$ shifted the optimum static efficiency to a specific speed of 0.72

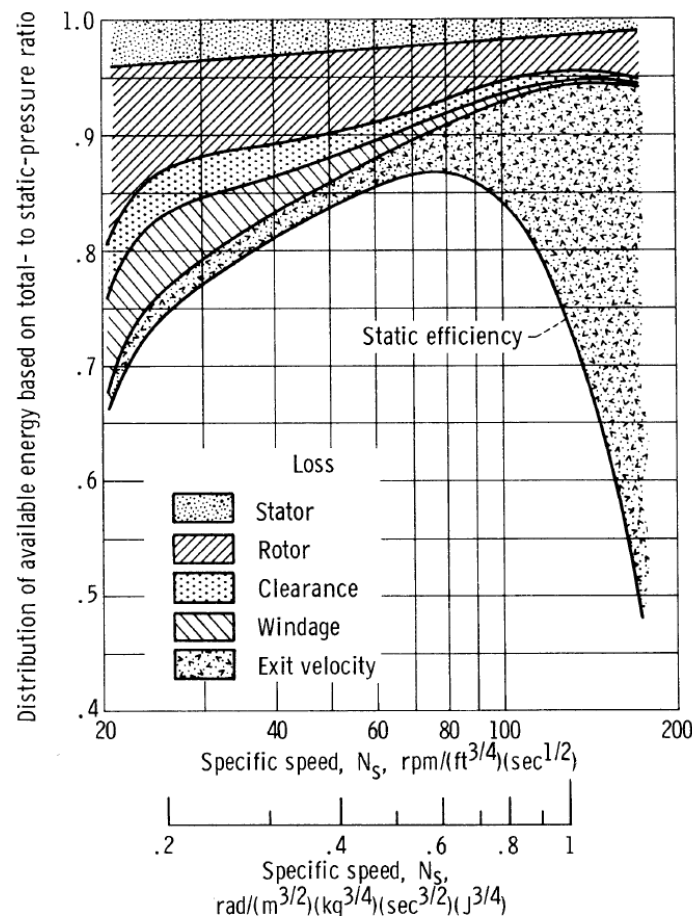


Fig. 1.13 Loss distribution, Rohlik [46]

1.5.3 Alternative duty similarity parameters

Another duty parameter sometimes used by radial turbine aerodynamicists, is the global flow coefficient. This parameter represents the ratio of the actual mass flow to hypothetical mass flow that would result from the "stagnation flow" passing through a reference area at the velocity of the reference blade speed. Typically the virtual area used is the reference diameter or radius square, then:

$$\Phi_D = \frac{\dot{m}}{\rho_0 r_n^3 \omega} \text{ or } \frac{Q}{r_n^3 \omega} \quad (1.22)$$

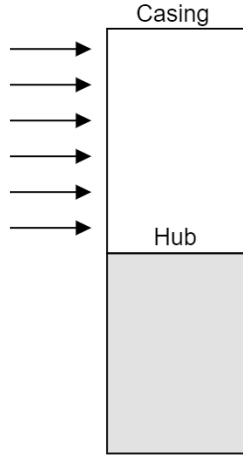
Where the second version is for incompressible flows. The subscript D stands for duty and from here on the parameter will be called the duty flow coefficient. This decision came about from discussion with members of the Whittle lab and it is believed this better represents the use of the parameter. In this form the duty flow coefficient essentially characterises the volumetric swallowing capacity of a machine and therefore is interrelated with the typical flow coefficient. For incompressible flow the duty flow coefficient can be written as

$$\Phi_D = \Phi_L \frac{A_{in}}{r_n^2} \quad (1.23)$$

Where $\phi_L = \frac{V_{m1}}{r_n \omega}$ which will be called the local flow coefficient to distinguish it from the duty flow coefficient. A_{in} is the annulus/through flow area at the inlet of the rotor (area normal to meridional direction). The ratio $\frac{A_{in}}{r_n^2}$ is functionally related to the hub to tip ratio, low values represent a hub to tip ratio closing in on one and high value represent a low hub to tip ratio. Equation 1.23 illustrates the two degrees of freedom which determines the mass flow capability of a machine. A machine can pass mass/volume flow by high through flow velocity and high through flow area. This is best explained with an example. Say, given two axial turbines (incompressible) with the same duty flow coefficient but differing local flow coefficient, see figure 1.14. The turbine with the higher local flow coefficient will have higher meridional velocities and lower through flow/annulus area. The turbine with the lower local flow coefficient will have lower meridional velocity and higher area, The latter results in a lower hub to tip ratio which would make it more "3D". The duty flow coefficient, in a sense, links the non-dimensional flow area(hub to tip ratio for axial architectures) to the meanline velocity triangles.

Axial turbine:

- * Same duty flow coefficient
- * Lower local flow coefficient
- * Lower meridional velocity
- * Higher annulus/through flow area
- * Lower hub to tip ratio



Axial turbine:

- * Same duty flow coefficient
- * Higher local flow coefficient
- * Higher meridional velocity
- * Lower annulus/through flow area
- * Hub to tip ratio closer to one

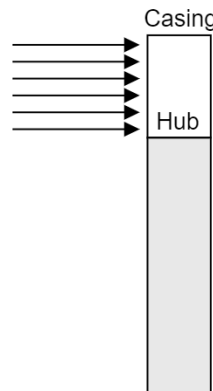


Fig. 1.14 illustration of effects of using different local flow coefficients has on flow and geometry, for a fixed duty flow coefficient

Casey [12] suggested the use of the duty flow coefficient as an alternative to specific speed, for aerodynamicists. Amongst other advantages, Casey found the parameter more straight forward to interpret across the design space. In the context of Buckingham Pi Theorem, any combination of non dimensional parameters are themselves valid non-dimensional parameters. As shown below the specific speed and diameter can be expressed in terms of the loading and duty flow coefficients and hence these parameters can serve as possible replacements for specific speed and diameter.

$$N_s = \frac{\phi_D^{\frac{1}{2}}}{\psi_s^{\frac{3}{4}}} \quad (1.24)$$

$$D_s = \frac{\psi_s^{\frac{1}{4}}}{\dot{\phi}_D^{\frac{1}{2}}} \quad (1.25)$$

1.6 Numerical Methods

As shown in the preceding sections, the flow field inside a turbine passage is highly complex, with a variety of flow features and loss mechanisms. Using an experimental trial and error approach to design and analysis is particularly slow and challenging. Therefore numerical methods are currently heavily relied upon for turbomachinery development.

Due to decades of development there exists a extensive hierarchy of tools, trading off accuracy for runtime. Miss use of these tools can lead to highly inaccurate results and poor design. The art behind the use of numerical methods, is finding the correct balance of runtime verses accuracy for the given problem, while understanding the short comings of the tool being used.

1.6.1 Overview of methods

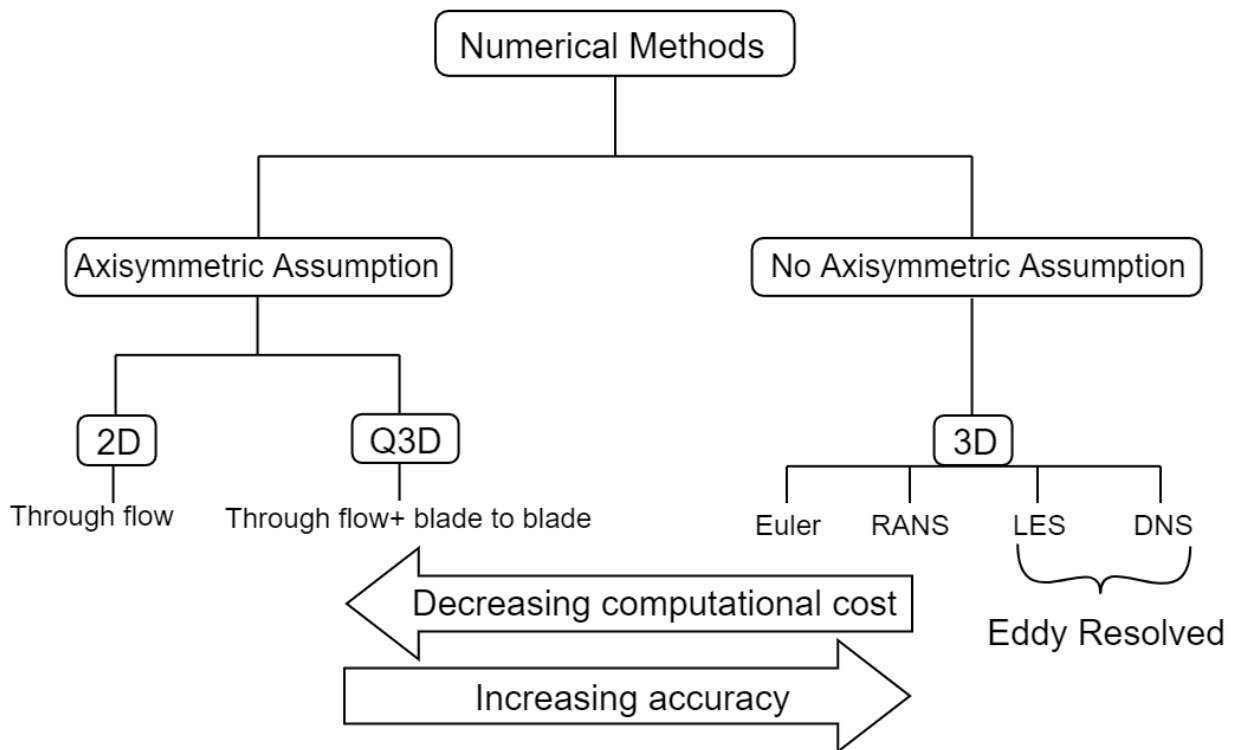


Fig. 1.15 Diagram illustrating radial blade fibre design

Figure 1.15 shows an ordered clustering of available tools. The numerical approaches can at first, be grouped under two broad classes; methods that make an Axisymmetric flow field assumption and methods that do not. Methods that do so, are 2-dimensional and quasi 3-dimensional, such as through flow and the combination of through flow with a blade to blade method respectively.

Through Flow is considered by many as the "backbone" of turbomachinery design, primary due to its high speed. The method typically involves solving streamline curvature (less often stream function) equations on axisymmetric stream surfaces. As the method is inviscid, loss correlations are required and this is the main weakness. The loss correlations determine the accuracy which can be severely compromised if applied to geometries that are significantly different to the geometries that were used to derive the correlations in first place.

Blade to Blade can be combined with through flow to form a quasi 3-dimensional method. This allows designers to determine the shape of the blade, and with this information the reliance on correlations is reduced. The goal of this work relies on a tool that is, for the most part, consistent across all architectures. Due to large differences in the geometries and the highly 3-dimensional nature of some of the architecture (e.g mixed flow turbines) these methods won't be used in this work. A fully 3-dimensional method is a primary requirement of the work presented in this thesis.

Solutions to the **Euler** equations fulfil the 3-dimensional requirement. However, since these equations do not contain the viscous terms of the full Navier-Stokes equations, no viscous loss occurs and the only loss that is generated is from the numerical method itself (e.g numerical viscosity). Therefore, this approach will not be useable to predict efficiency and thus will not be used.

RANS Method are solutions to the Reynolds averaged Navier-Stokes equations. These equations are derived by averaging a decomposition of the primary flow variables into mean and fluctuating terms. This process results in an under determined system. Additional apparent terms are introduced known as Reynolds stresses, which need to be modelled in order to close the equations. These models are both the strength and weakness of this approach. On the one hand, misuse of one of the many available turbulence models (say for a flow field for which it was not developed) can result in considerably inaccurate quantitative results and even qualitatively very different flow fields. On the other hand, the models allow for the use of relatively coarse grids, which does not need to resolve all the length scales of turbulence. This significantly reduces runtime. This is particularly important where multiple designs are being compared say for geometric optimisation or in the context of this work, mapping design spaces.

LES, (large eddy simulation) attempts to resolve (on grid) the larger scales of turbulence, where most of the turbulent kinetic energy resides. The method then accounts for the remaining smaller scales using a sub grid model. There are parallels between LES and RANS, as they both represent a decomposition of the primary flow variables. However, with LES these variables are decomposed into the resolvable scales (mean in RANS) and the sub-grid scales (perturbation in RANS). In other words, LES represents a filtering out of scales, as opposed to an averaging process. The accuracy of this approach is less dependent on the sub-grid model as users attempt to resolve scales containing around 90 % of the turbulent kinetic energy. This method is however significantly more computationally expensive.

DNS (direct numerical simulation) are solutions to the Navier-Stokes equations, where all spacial and temporal scales of turbulence are resolved (all the way down to the Kolmogorov scale) and hence no models are required. Currently, this would require unrealistic amounts of computation resources to resolve even a single passage, let alone an entire design space.

1.6.2 Limitations

Understanding the limitation of computational fluid dynamics is crucial to interpreting results and to some extent, avoiding, or where this is not possible, quantifying potential sources of error. Denton [27] (which this section primary draws from) lists some of the main potential sources of error as:

- Numerical errors due to the finite difference approximation and numerical smoothing.
- Modelling errors, where the true physics is not known - e.g turbulence modelling, steady flow assumption
- Unknown boundary conditions such as inlet pressure or temperature profile
- Unknown geometry such as tip clearance or leading edge shapes.

Numerical errors arise as a result of the finite difference approximation of numerical methods and also from the use of artificial viscosity or smoothing to maintain stability. These errors are high in regions where the second derivatives of the flow properties are high (e.g leading edge) and the grid spacings are large. The error behaves as if there was an additional viscous term in the equations causing false entropy production, which is convected down stream. These errors can be reduced by increasing the number of grid points, which is how this error was kept to a minimum for the numerical work done in this thesis. The loss was partially estimated by running inviscid solutions and tracking the entropy production for sample cases, the results of which can be found in the results sections.

Modelling errors come from a wide variety of sources such as: turbulence modelling, transition modelling, mixing planes and steady flow assumptions. As previously mentioned, the choice of turbulence model or constants within that model can lead to differing quantitative and qualitative results. These errors can stem from a number of different source and are dependent on the choice of model. For example, the mixing length model (eddy viscosity type) which works well for thin shear flow, can produce poor results for separated and recirculating flow. Luckily for turbines this is generally not the case. The mixing length model was the choice for the work presented in this thesis due to its: simplicity (and cheap in terms of computing resource), availability (one of two available in the solver) and it is well established. In addition, the mixing length model is well calibrated for use in the solver used (TBLOCK).

The trailing edge is a potential source of significant modelling errors. It is widely known that under certain circumstances (well resolved thick trailing edge) can lead to delayed separation from the trailing edge. This in turn can result in high streamline curvature and an associated low pressure region, which can lead to negative blade loading. This was remedied by the use of a trailing edge cusp which does not carry load. Denton [27] noted that this is unlikely to give the correct base pressure acting on the trailing edge and so will not predict the correct loss. The correct base pressure can be potentially determined by the use of detailed unsteady calculations. However, this would require significantly more computational resources.

Tip-leakage is a significant feature of turbo-machinery and plays a key role in determining levels of loss, and has a significant effect on the qualitative nature of the flow field. The turbines in this study are un-shrouded and hence over tip-leakage must be captured. Of the many approaches used to model the tip clearance, a gridded tip was used as it is more realistic than a pitch tip or periodic tip. That being said, the use of the mixing length turbulence model in this block is questionable, due to the complex flow in the gap. Denton [27] points out that flow acceleration into the gap dampens turbulence, possibly even leading to laminar flow. The only probable way to overcome these issues is to use numerical methods, which are less dependent (LES) or independent (DNS) of turbulence models.

Unknown geometry as a modelling error is not intrinsic to CFD itself, but can represent a large error when comparing numerical results to real world geometries. Since no specific real world designs are being recreated here, this does not represent a source of error.

1.7 Problem statement

Design charts leveraging similitude are powerful tools during the early stages of design. The use of similarity was first introduced by Cordier [14] and then significantly expanded upon by Balje [3] and Rohlik [46]. These authors mapped out the design space using a combination of empirical and analytical methods. Cordier formed the "Cordier line" by plotting the location of high performing pumps, compressors and fans on a logarithmic N_s - D_s chart. From this designers can find the optimal rotational speed for a given diameter and vice versa. On top of this Cordier also showed that machine types/architectures (i.e axial, radial, mixed) were grouped along specific ranges of N_s or D_s and therefore the Cordier's diagram could be used for architectures selection. Rohlik used an entirely correlation/analytical based approach to map out the radial turbine design space, where as Balje used a combination of correlations, the hydraulic efficiency equation and observed trends to form design charts for a diverse array of machines.

This thesis aims to build upon the past research of the above authors, using the now readily available computational resources and an alternative framework. There are a number of limitations of the past work which this thesis aims to address:

- The previous design charts were either partially(Balje) or entirely(Rohlik) based on loss correlations and in some cases on observed trends (high N_s region of axial Balje Diagram). Balje stated that "the accuracy of the loss coefficient relations which necessarily are based on the present available experimental evidence, determine the validity of the N_s - D_s chart". Ignoring for now the errors in the exact levels of loss predicted, some correlation do not even capture the correct trend across the design space, as shown by Coull [20] for axial Smith charts. On top of this, loss correlations can have particularly poor performance outside of the parameter range in which they were developed. The rotor loss correlation used by Rohlik(radial space) was in fact developed for use in axial flow machines.

This thesis aims to map design spaces using Computational Fluid Dynamics (CFD) simulations, more specifically using Reynolds Averaged Navier-Stokes Equation Solvers. While this approach also come with inherent limitation, for example due to the necessity of turbulence models, it will be more robust in capturing the physics than loss correlations. The thesis will aim to use CFD as a comparative tool as suggested by Denton [27]. In other words, will be more concerned with trends in changes across the design space than the exact levels of efficiency themselves. That being said the uncertainty margin for levels of efficiency are likely to sit comfortably within those of produced by Balje, who quoted a 8% percent variability in efficiency and Rohliks does not specify any uncertainty.

- The design spaces produced by Balje do not contain any information about the various loss mechanisms and the changes in these through out the space. Rohlik on the other hand does provide this (radial turbines only) but these variation have not been validated experimental or even numerically.

This thesis aim to decouple the loss mechanism as best as possible to help gain an understanding of the variations across the design space, according to the CFD. This will allow designs to make more informed decision on there choices of architecture, speed and sizing.

- To aid in the aerodynamic understanding, the Balje type spaces will be reproduced based on the use of duty flow coefficient (global flow) and loading coefficient instead of the specific speed and diameter, as suggested by Casey [12]. The author believes that these parameters are easier to use when interpreting the aerodynamic nature of turbines at different points in the design space. That being said the maps can easily be converted back into specific speed and diameter.
- For the current turbine design spaces produced by Rohlik and Balje, mixed flow turbines are not present. This thesis aims to include these architectures as well. For simplicity the cone angle and radius ratio will be fixed which limits the flexibility of which could be considered the most generalized turbine. Therefore a limited further study on radius ratio and cone angle will be done to further explore these design parameters.

- Balje pointed out, that there was no understanding about the interrelation of the radius ratio (which controls the centrifugal component of loading) and loss. This thesis will explore variation in this parameter and others such as meridional velocity ratio to help further understand there effects on loss and components of loading.
- There is a significant divide within the turbomachinery community when it comes to architecture types. Radial and axial turbine designers use different design philosophies and parameters. In order to produce a coherent set of design charts a unified preliminary design approach will be implemented including a set of unified design parameters. On top of this a set of unified loss models will be tested against the numerical results.

This will form an architecturally unified preliminary design methodology. However, due to the vast nature of the design space there are necessary limitations to the work presented in this thesis. To produce an idealised parameter space requires all parameters, other than the parameters being explored, to be optimised. This can be problematic, not only does this result in a high dimension problem requiring an incredible amount of time and resources to achieve, optimisers are also known to exploit any short comings in the simulation tool. Instead, to reduce the design parameters varied, many will be fixed to sensible values. To further reduce the scope of the analysis, this thesis will focus on rotor only simulations as this is the key differentiating component. Therefore the design spaces produced in this thesis are far from perfect.

That being said, computational resources available to engineers are ever increasing and with it, the ability to continuously produce design charts with fewer design limitations and better modelling. Therefore the author of this thesis does not want engineers to heavily rely on the charts themselves, but should use them for building understanding, motivation and a framework to produce more detailed versions of their own.

Chapter 2

Design Methodology

Introduction

The following chapter presents the design methodology used to map the design spaces. This includes the set of unified design parameters used and method by which the geometer was generated.

Mapping a design space, including all architecture types, is a challenging task. The method itself will have an impact on the resulting space. Ideally these design spaces should be constructed with fully optimised designs such that they represent the best possible performance that can be achieved by the specific combination of design parameters being studied. But what is meant by fully optimised? Increasing the degrees of freedom defining the geometry will increase flexibility, allowing a design system to access higher, maximum efficiency designs. However the number geometric parameters used can be arbitrarily long, hence this problem can very quickly become intractable. In addition to this, increases in the degrees of freedom likely comes with diminishing returns. Due to broad nature of designs in this work, a simplistic direct design methodology was used.

The requirements deemed important for this work:

- Need to be able to design all architectures (radial, axial, mixed)
- Due to the vast number of possible designs, across three architecture types, the methodology needs to be simple, straight forward and relatively fast.
- As radial and mixed flow turbine architectures are nearly universally radially blade fibred, the methodology needs to be able to design for this and explore potentials if some deviations are allowed for.
- The methodology needs to be consistent as possible across the different architecture types. i.e should not favour one over the other, except for the radial blade fibred of radial and mixed flow architectures, which does constrain these designs.

In order to meet these rather specific requirements the author opted for a self-developed blade geometry generator written in Matlab. One of the additional benefits of this choice is that the process allowed the author to gain insight and understanding of the blade design process which in turn helped interpreting the results. Another additional benefit of having access to the source code is that custom geometric features can be added in, which later proved useful.

The designs produced from this approach, by no means represent the state of the art. However, considering that this thesis is concerned with the general shape of the design spaces and not the maximum achievable efficiencies, the method proved to be robust enough and capable of mapping the spaces.

The first section of the chapter focus on the unified set of design parameters, followed then by the details of geometry generation.

2.1 Unified Design Parameters

In order to unify all architectures under a single design methodology, a set of unified design parameters is required. In the proceeding section, the choice of parameters will be outlined and discussed. This will be done in the order in which they are introduced into the preliminary design process. Figure 2.1 illustrates and outlines this in the form of a flow chart.

Duty parameters *I*

The starting point of preliminary design, duty parameters essentially specify the gross characteristics of a machine. As previously discussed these parameters are derived using dimensional analysis. This is done by forming a functional relationship of the duty flow, machine radius and rotational speed.

$$f(r_n, \omega, \dot{m}, \Delta h_0, T_0, \rho_0, \gamma, R_{gas}, \mu) = 0 \quad (2.1)$$

Then using Buckingham Pi theorem (using $\rho_0 T_0 r \omega$ to non-dimensionalise) a new non dimensional function can be formed.

$$f_2(\Phi_D, \psi, M_{rot}, Re_{rot}, \gamma) = 0 \quad (2.2)$$

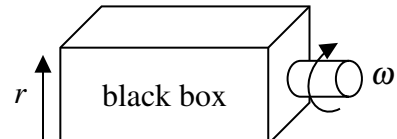
$$\Phi_D = \frac{\dot{m}}{\rho_0 r_n^3 \omega}$$

Duty

$$\dot{m}, \Delta h_o, R_{gass}, \gamma, \mu, T_0, P_0$$

$\omega, r \longrightarrow$
↓
Duty level parameters I

$$\Phi_D, \Psi, (N_s, D_s) M, Re$$



Balje Diagram or Company Heritage
(Go with what you know)

Architecture Selection II



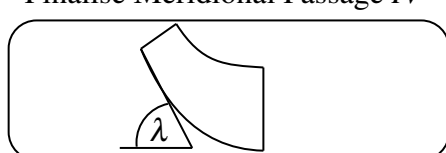
Increasing Level Of Detail

Euler turbine equation \longrightarrow $\phi_L, R_r, R_{vm}, \alpha_1, \alpha_2$ or Reaction

Mean line flow III

velocity triangle	turbine inflow area	work split
	$\frac{A_{in}}{r_n^2} = \frac{\Phi_D}{\phi_L}$	$\Psi_{total} = \Psi_{cent} + \Psi_{RKE} + \Psi_{KE}$

λC_x or AR \longrightarrow
Finalise Meridional Passage IV



C_o or Zweifel

Blade Count V

Vortex Design VI

Detailed Design
34

Fig. 2.1 Turbine parameter flow chart

$$\Psi = \frac{\Delta h_0}{(r_n \omega)^2}$$

$$M_{rot} = \frac{r_n \omega}{\sqrt{\gamma R_{gas} T_0}}$$

$$RE_{rot} = \frac{\rho_0 r^2 \omega}{\mu}$$

Note Φ_D and Ψ have replaced specific speed and diameter. ϕ_D . The Duty flow and loading coefficient were chosen as these parameters are better at characterising the aerodynamic nature of the turbines throughout the design space. Casey [11] regraded the duty flow (global) coefficient as a more simple to understand than the specific speed. Note that in this thesis, the author has chosen to use the non-isentropic stagnation enthalpy change. This is typically done by axial turbine design, as this form of the loading coefficient ties directly to the flow angles. That being said since the efficiencies are known, all design charts can be converted to isentropic form. Once these parameters have been specified, the machine at this points represents a black box, were only the size, flow going into the box and the rotor shaft speed is know. The architecture type has yet to be specified.

Architecture selection II

This is the point in preliminary design where the black box machine becomes a turbine of a specific architecture or if out of the turbine parameter range, another machine type e.g rotary-displacement machines. If a turbine is to be used, the designer will have to chooses whether to use an axial, radial or mixed flow turbine. This is typically done in one of two ways, using an architecture based on company heritage or using a design chart such as those produced by Balje [4]. If the designer has some flexibility in rotor radius and or rotational speed, they can use a Balje diagram to readjust the duty parameters to sit in a region of high performance for a given architecture. Note that at this point in the preliminary design process the velocity triangle has yet to be specified.

Mean line flow /Velocity triangles III

In order to specify the rotor meanline velocity triangle, the Euler equation is used in conjunction with additional design parameters which are:

$$\phi_L, R_r, R_{vm}, \alpha_0, \alpha_2 \text{ or Reaction}$$

By specifying these parameters and therefore a velocity triangle, the work split between the different loading terms in equation 1.1 is determined. The non dimensional form which (derived by Smyth [52]) can be written as:

$$\psi = \underbrace{\frac{\phi_L^2}{2}(\sec^2 \alpha_1 - R_{vm}^2 \sec^2 \alpha_2)}_{\Psi_{absolute\ KE}} + \underbrace{\frac{\phi_L^2}{2}(R_{vm}^2 \sec^2 \beta_2 - \sec^2 \beta_1)}_{\Psi_{relative\ acceleration}} + \underbrace{\frac{1}{2}(1 - R_r^2)}_{\Psi_{Centrifugal}} \quad (2.3)$$

Where $R_r = \frac{r_{n_2}}{r_{n_1}}$ is called the radius ratio and $R_{vm} = \frac{V_{m_2}}{V_{m_1}}$ is known as the meridional velocity ratio. As in section 1.2, the first term on the right, is the change in absolute kinetic energy through the turbine. The seconded term is relative acceleration through the passage and the last term is known as the centrifugal effect. Equation 2.3 is useful in showing how certain parameters effect the work split. For zero interstage swirl case the individual loading terms of this equation can be written as follows:

$$\psi_{ke} = \frac{1}{2}[\phi_L^2(1 - R_{vm}^2) + \psi^2] \quad (2.4)$$

$$\psi_{rac} = \frac{1}{2}[R_r^2 + \phi_L^2(R_{vm}^2 - 1) - (\psi - 1)^2] \quad (2.5)$$

$$\psi_{cent} = \frac{1}{2}(1 - R_r^2) \quad (2.6)$$

Local flow coefficient

As mention in section 1.5.3, choices in the selection of local flow coefficient for a given duty flow coefficient, set the manner in which the mass flow through the turbine is achieved. A high local flow coefficient results in high meridional velocity and reduced inlet through flow area. From equation 2.3 the local flow coefficient also serves to scale the relative acceleration and change in kinetic energy components of loading.

Radius ratio

The radius ratio sets the components of centrifugal loading (equation 2.6) by setting the change in radius of the mean streamline, see figure 2.2. This term is positive for a radius ratio less than one and hence most turbines with a centrifugal component are radial inflow turbines, with some exceptions used in organic Rankine cycles [50]. For axial turbines this term is generally equal to one or very close to it. From equation 2.3, it clear that there is a limit to the amount of centrifugal loading that can be achieved. For a meanline radius ratio of zero, which is unphysical, the maximum amount of centrifugal loading that can achieved is $\psi_{cent} = \frac{1}{2}$.

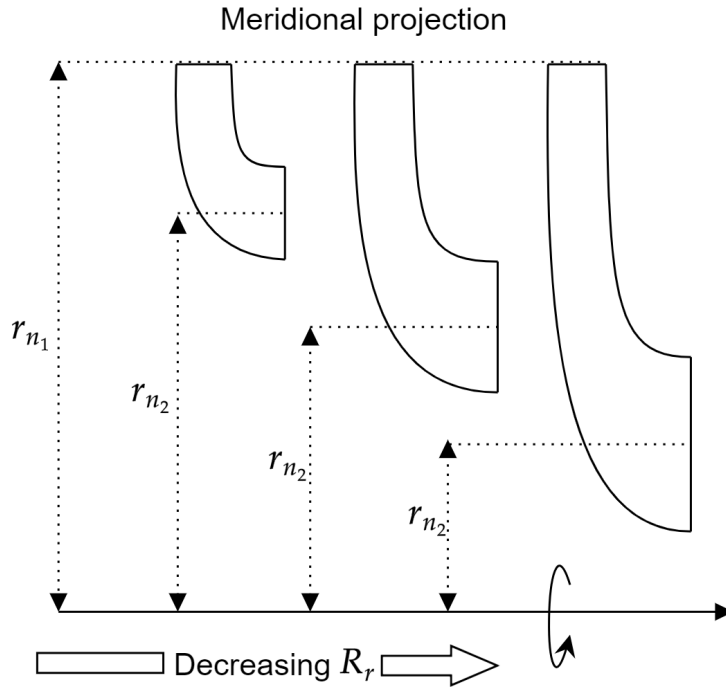


Fig. 2.2 Illustrating effect of radius ratio on passage geometry

Meridional velocity ratio

The meridional velocity ratio sets the amount of meridional diffusion. For values under one the exit meridional velocity is lower and as a result of continuity the exit area must increase. This is illustrated in figure 2.3 for an incompressible machine. From equations 2.4 and 2.5, the meridional velocity ratio exchanges loading between the relative acceleration and change in absolute kinetic energy terms. The exit loss of a turbine is particularly sensitive to changes in meridional velocity ratio, this can be seen in equation 1.16. Decreasing this parameter can significantly improve the total to static efficiency.

Setting all of the above parameters fixes the meanline velocity triangle.

Meridional Passage IV

Up until this point only the inlet area, exit area and the change in radius has been specified. To complete the preliminary design of the meridional geometry an axial length is required for all architectures. Axial designers tend to set this by specifying an aspect ratio which the author has chosen to do here. Radial and mixed flow turbine designers typical set this based on considerations of meridional curvature, blade loading and inertial requirements. In conjunction with specifying an axial length mixed flow architectures require a cone angle to be specified. The way in which the axial length was set for the radial and mixed flow architectures can be found in

Meridional projection

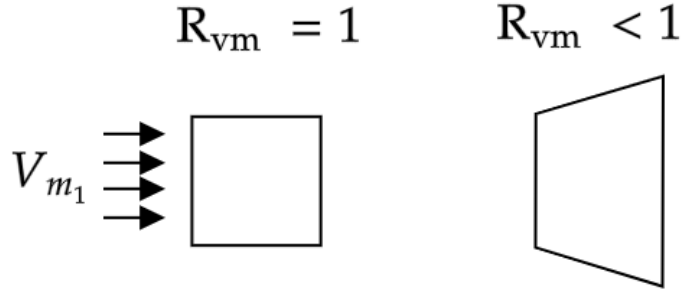


Fig. 2.3 Illustrating effect of meridional velocity ratio on passage geometry (incompressible flow)

detail in section 2.2, but in short, this was set by specifying a minimum non dimensional radius of curvature.

Blade count V

A number of blades needs to be specified. For axial turbines this was done using a circulation coefficient which is a parameter similar to the Zwiefel coefficient. Coull[20] defined circulation coefficient as "Circulation Coefficient Co is defined as the ratio of the blade circulation to an ideal circulation, with $V_{surf} = V_2$ on the suction surface and stagnated flow ($V_{surf} = 0$) on the pressure surface".

$$Co = \frac{\text{actual circulation}}{\text{ideal circulation}} = \frac{\oint V_{surf} ds}{V_2 S_{tot}} \quad (2.7)$$

From this definition a relationship for the pitch to suction surface length was derived using thin aerofoil theory, see appendix F. This extended the equation to be used for radial and mixed flow architectures.

$$Co = \frac{p_1}{S_{tot}} \frac{\cos \beta_2}{R_{vm}} \left(\overbrace{(1 - R_r^2)(\tan \alpha_1 - \tan \beta_1)}^{\text{Centrifugal}} + \overbrace{\tan \beta_1 - R_r R_{vm} \tan \beta_2}^{\text{Tangential}} \right) \quad (2.8)$$

Which can be decomposed into two terms. The first, is the contribution to circulation from the centrifugal loading which is zero for axial architectures, note the decomposition is slightly

different to equation 2.3 and the second term will be called the tangential term. A value of $C_o = 0.7$ will be used for axial architectures, see Coull[20].

As put by Whitfield and Baines [54] "No rigorous method is available (for radial architectures) for determining the optimum number of blades but a criteria based on avoiding zero blade surface velocities in the inlet region of the rotor". The inlet of a radial turbine is subject to strong Coriolis forces as discussed in 1.2. If the blade count is to low this can lead to stagnation of the flow on the pressure surface. There exists a number equations based on this criteria in the literature see figure 2.4. These will not be discussed in detail here, see Whitfield and Baines [54] for a review. Instead the circulation coefficient will be used to determine blade count for both radial and mixed flow turbines as well.

A value of $C_o = 0.7$ was tested for a large sample of radial turbines (from this thesis) and is shown in figure 2.4. For the most part, these turbines meets the zero blade surface velocity criteria. All designs are above that of Glassman's [32] widely used criteria (which is a semi empirical relationship) and most of the turbines sit above Whitfield equation (analytical derivation). Additionally, Whitfield and Baines, in their comparison of the different blade number equation, suggest that a modest about of stagnation can be tolerated without a significant detriment to efficiency.

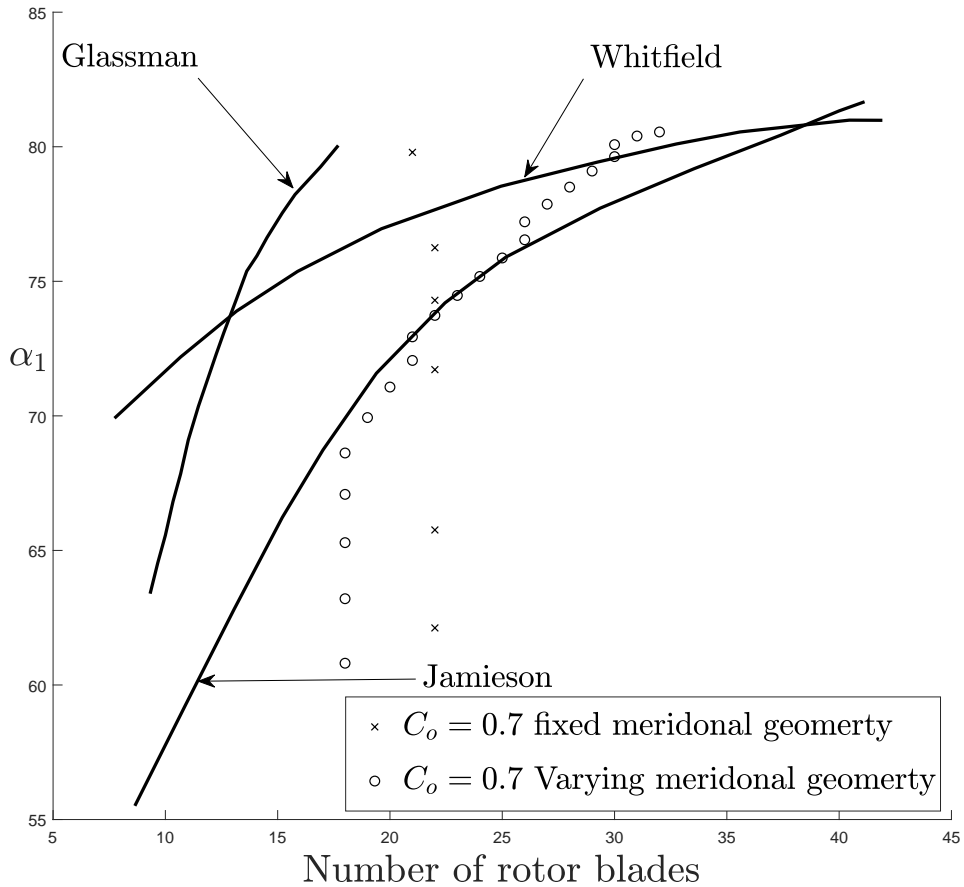


Fig. 2.4 Inlet angle vs Blade count reconstructed from Whitfield and Baines [54]

Vortex design VI

To finalise the preliminary design a vortex distribution needs to be specified. Radial architectures tend to be designed with zero exit swirl for high total to static efficiency. Interestingly this coincides with the distribution due to a radial blade fibred design, see Whitfield and Baines [54]. Since the radius is a constant at the inlet, there is no metal angle variation at the inlet of radial turbine.

For mixed flow architectures, Abidat [1] used conservation of angular momentum to specify the flow at the inlet which coincides with a free vortex approach. Since free vortex can be used for all the architectures(often used in axial turbines) and is relatively simple to implement it will be used here.

$$V_\theta r = \text{constant}$$

This concludes the preliminary design phase.

2.2 Geometry Generation

An outline for the design flow is shown in figure 2.5 and will be discussed in the sub sections.

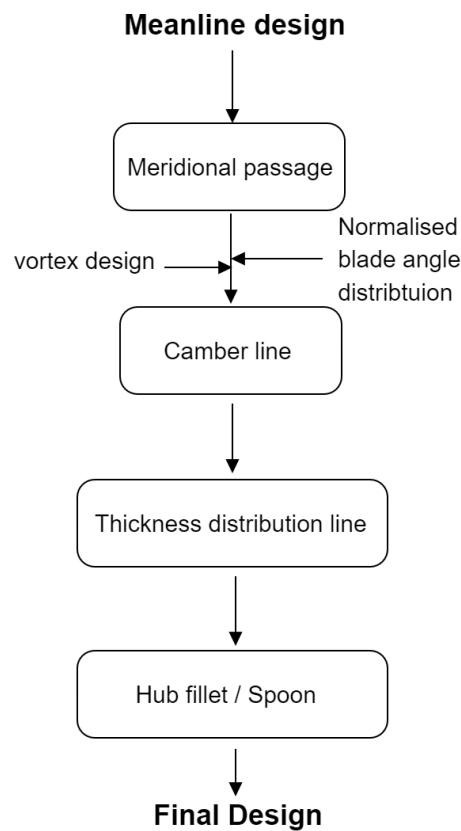


Fig. 2.5 design methodology flow chart

Meridional Geometry

During the preliminary design stage the inlet and exit passage flow area was set by meanline calculation. In addition to this, the inlet cone angle and radius ratios have been specified for the respective architectures. The inlet and exit span is then calculated from the inlet and exit area using the equation for a frustum. Note that, the mean radius is located at the centre of area

(centroid of area) which is equivalent to the centre of mass flow for constant meridional velocity across the span. This is then used amongst other parameters to form the meridional passage and will be discussed for the different architectural types.

Axial

For axial architectures, the aspect ratio (span to cord) is specified. From this, the axial length can be calculated from the average span. The hub and casing lines are then constructed from Bezier curves. The control points for the Bezier curves are specified in such a way that the inlet and exit hub and casing lines are parallel to the the x-axis. The construction of the meridional geometry is shown in figure 2.6 A.

Radial and Mixed

The axial locations of the the exit casing and hub points are specified by setting a approximate radius of curvature for the casing, plus an additional axial section as shown in figure 2.6 B. Note that the cone angle is defined as the angle between the span wise and axial direction at the rotor inlet, the use in figure 2.6 B is only used for constructions.

By setting a component of the axial length that is driven by radius of curvature (the circle shown), the axial length can be minimised while avoiding a possible casing separation as a result of high curvature. The radius of curvature is specified via a non-dimensional curvature parameter which is typically used in literature relating to pipe flow. Here it is defined as:

$$\frac{r_{cur}}{h_{exit}} = \frac{\text{radius of curvature}}{\text{exit span}}$$

Baines [2] uses a similar parameter for use in a meanline loss model in which the author doubles the passage loss when this parameter is below a specific value. The author attributed this sharp rise in loss to casing flow separation. Note this parameters become identical to one used here for circular arc casing lines. The value used by Baines for the limit is 0.2, For design preposes it will be set to 0.35. One important thing to point out is that this value will not be able to be maintained for radial designs with high inlet area and can be explained as follows. High inlet area designs with will consequently have large exit area as well, at some point the distance between casing inlet and exit will be smaller than the specified radius of curvature and hence no matter how long the axial distance is set the radius of curvature will be fixed. This is illustrated in figure. 2.7.

The purpose of the additional axial length is to allow designs with high inlet area to have a long enough axial distant in which to turn the flow in the tangential direction. Since most of circumferential turning occurs after the casing inlet's axial location, designs with high inlet area have a short distance in which to achieves this, see figure 2.7. By adding additional axial length that scales with the inlet area this issue can be over come. An alternative approach not used

here, is to design the radial turbines with a rake angle varying along the inlet span such that the curvature is spread to the inlet section.

Now that the inlet exit points are specified the hub and casing lines are constructed from Bezier curves. Point B_3 is set from the intersection of lines passing through points B_1, B_5 and perpendicular to the inlet and exit span. Points B_2 and B_4 run up and down these lines are set in such a way as to reduce maximum curvature. This was done using an inbuilt minimisation function from Matlab. This finalises the meridional geometry. see figure 2.8.

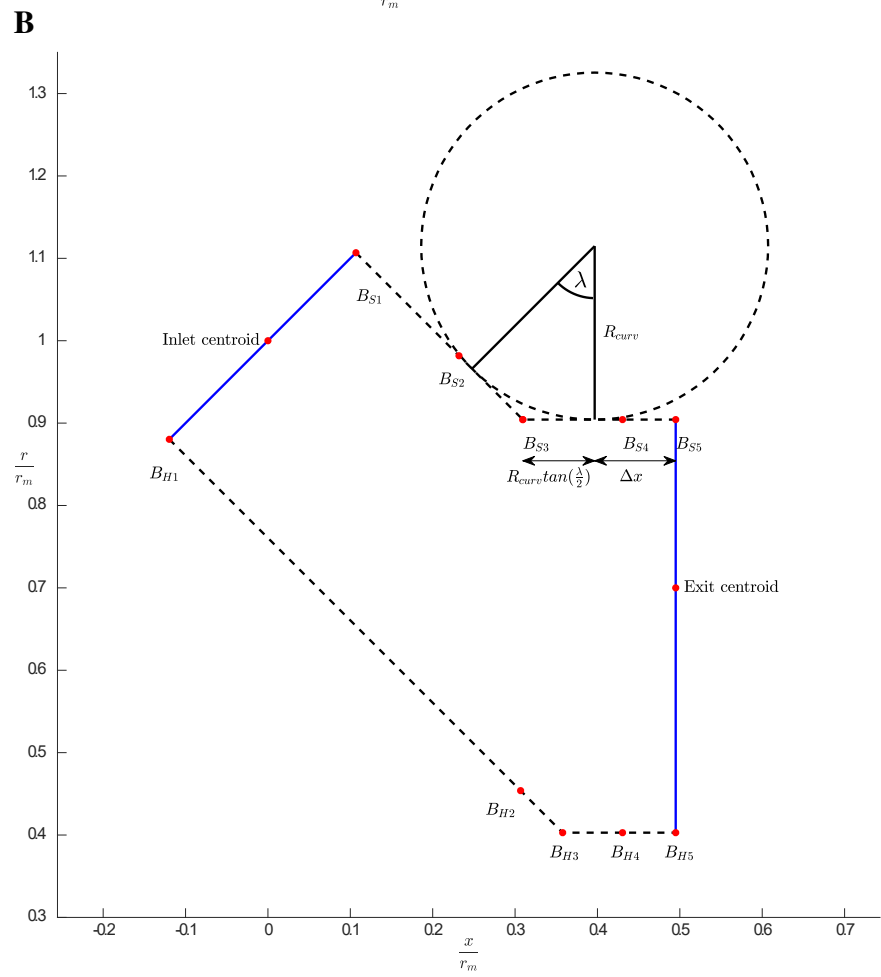
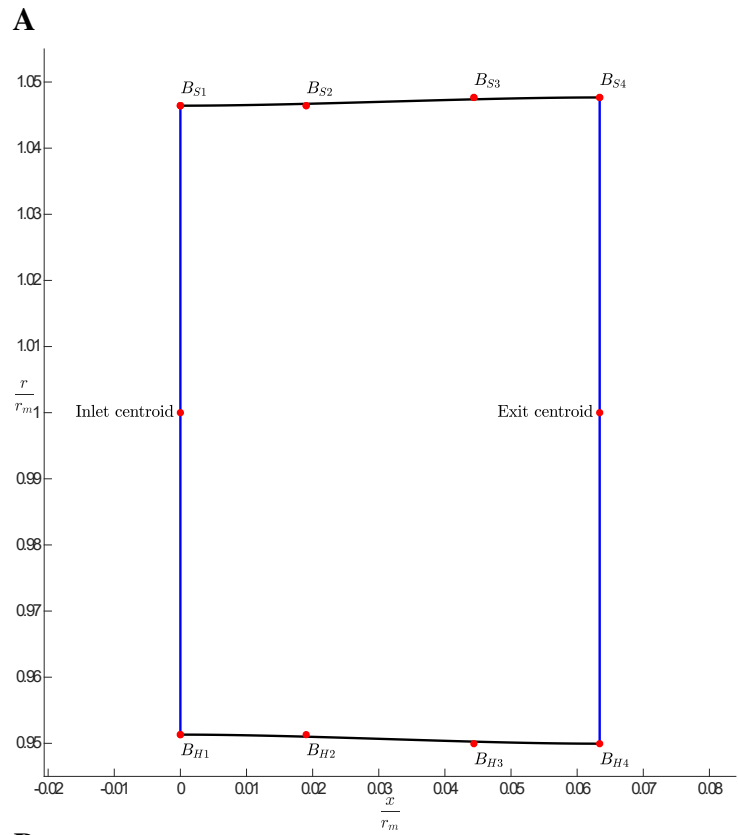


Fig. 2.6 A: Diagram of axial the meridional geometry. B: Diagram of radial/mixed the meridional geometry

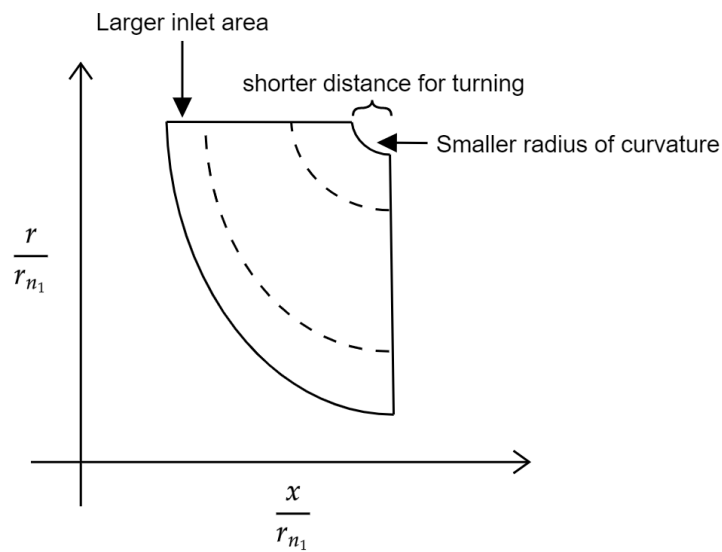


Fig. 2.7 Illustration of the effects of increasing inlet area has on casing radius of curvature

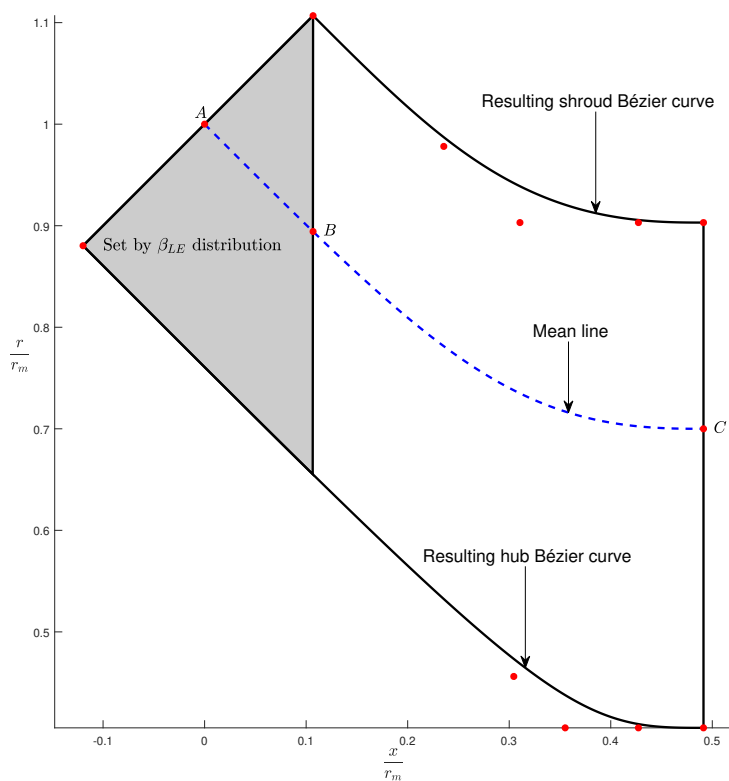


Fig. 2.8 Diagram of the meridional geometry including blade section defined by leading end blade angle distribution

Meridional Design Limitations

The design methodology employed in this thesis is relatively simplistic. As a result it will produce artefacts which will inevitably affect the shape of design spaces being produced. For the radial and mixed flow architectures a number of significant limitations were introduced relating to the meridional geometry.

The hub and casing lines are set to be perpendicular to the inlet and exit span. This partially constrains the casing and hub radius of curvature for the radial to axial bend. Relaxing this constraint can increase the radius of curvature at the inlet (figure 2.9 A), however a consequence of having meridional curvature at the inlet is that this will cause a variation in incidence and thus requires more detailed design.

The hub and casing lines were designed in such a way as to avoid any inflection points. A result of this constraint is that mixed flow turbines with a fixed radius ratio can have long passage lengths when the cone angle is low and the radius ratio is fixed (figure 2.9 B).

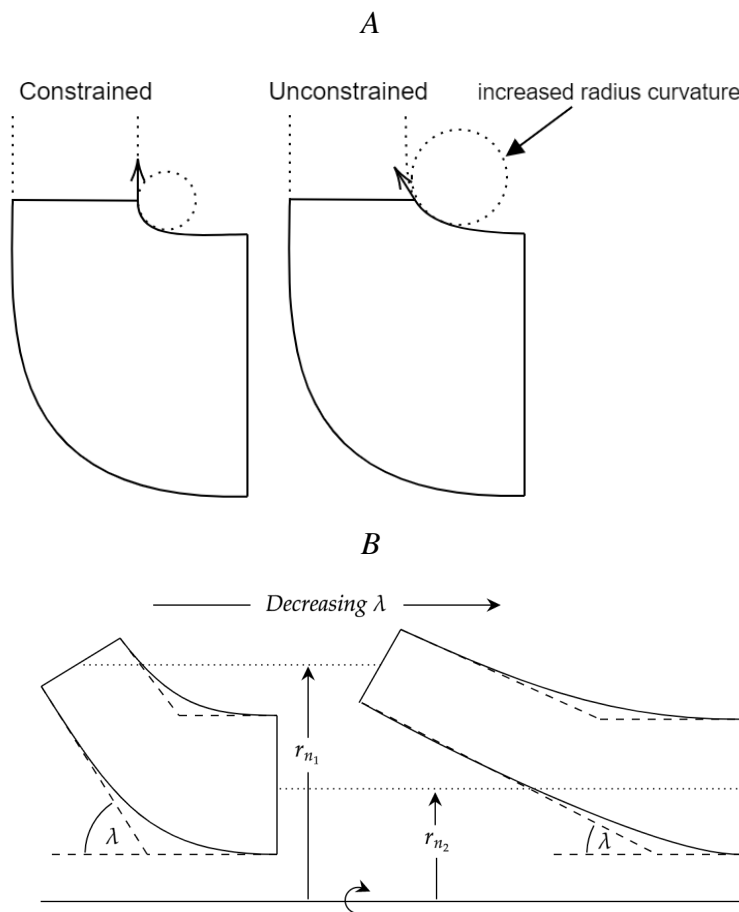


Fig. 2.9 Diagrams illustrating Design limitations

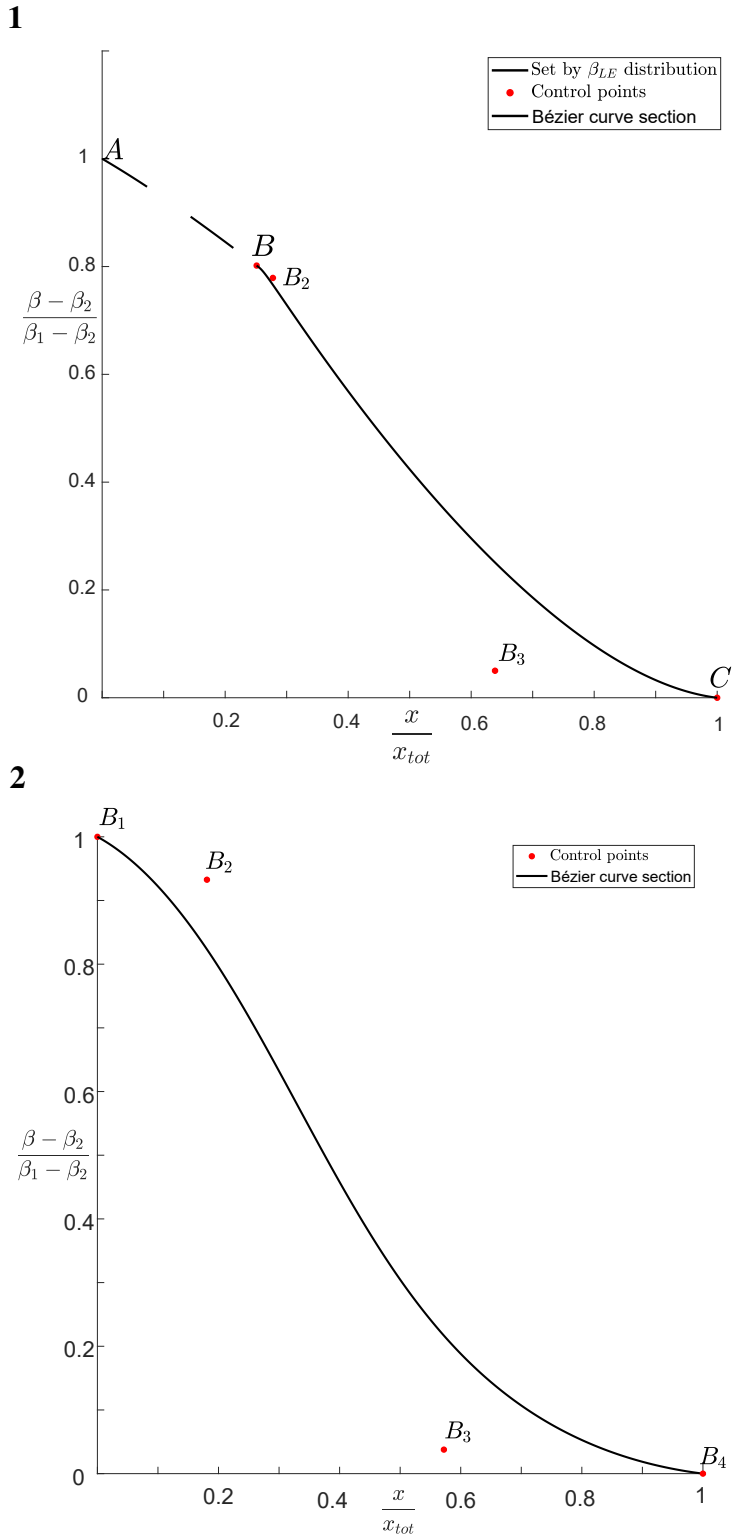


Fig. 2.10 A: Diagram of radial/mixed blade angle distribution. B: Diagram of axial blade angle distribution

Blade angle distribution

Radial and Mixed

Due to the radial blade fibre design a section of the mean line blade angle distribution is fixed, which is set by the projection of the span wise variation of the blade angle at the inlet. The fixed

region is shown in grey in figure 2.8 and the corresponding section of the normalised meanline blade angle distribution is shown by the dashed lines in figure 2.10 1. Since the leading edge section A to B is fixed, control of the blade angle distribution can only be taken after point B . This was done using a fourth order Bezier curve. Control point B_2 is set so that the join is continuous(first order in blade angle) which insures the resulting geometry will be continuous in the second order derivatives. Placing B_2 near B help insure the design methodology is robust to large changes in the inlet section.

The resulting blade angle distribution is then projected to a camber/rake angle distribution using equation 1.17 where the cone angles is taken from an approximation of the mean line cone angle distribution, shown in figure 2.8. Using equation 1.18 this is then integrated forming the camber line. This fully defines the camber surface.

A number of non radially blade fibred mixed flow turbines were produced for comparison. These designs used the same method for generating the meridional passages. The blade angle distributions were generated in the same manner as the axial turbines.

Axial

The normalised blade angle distribution used for the axial architectures is shown in figure 2.10 2. This was also constructed using a Bezier curve. The control points were manually selected and showed to give acceptable performance across the design space. Again this was integrated to form the blade camber lines. These were then stacked at 50% cord yo form the camber surface.

Thickness distribution

For simplicity a symmetrical thickness distribution was used for all architectures. The distributions were set using a shape/class function approach from Kulfan [38]. The thickness to camber line length ratio is set as follows:

$$\frac{t}{s_{tot}} = SH(s^*)CL(s^*) + \frac{\Delta t}{s_{tot}}s^* \quad (2.9)$$

Where Δt is the trailing edge thickness, s^* is the normalised camber line and $SH(s^*)$ is the shape function. Also included is the class function is defined as:

$$CL(s^*) \equiv s^{*n_1}(1 - s^*)^{n_2} \quad (2.10)$$

The value of n_1 sets the shape of the leading edge, a rounded leading edge was used ($n_1 = 0.5$). n_2 sets the shape of the trailing edge, a point one was used ($n_2 = 1.0$).

The shape function sets the remaining characteristics of the thickness distribution such as the leading edge radius:

$$SH(0) = \sqrt{2 \frac{r_{le}}{s_{tot}}}$$

and the trailing edge boat tail angle:

$$SH(1) = \tan \beta_{bt}$$

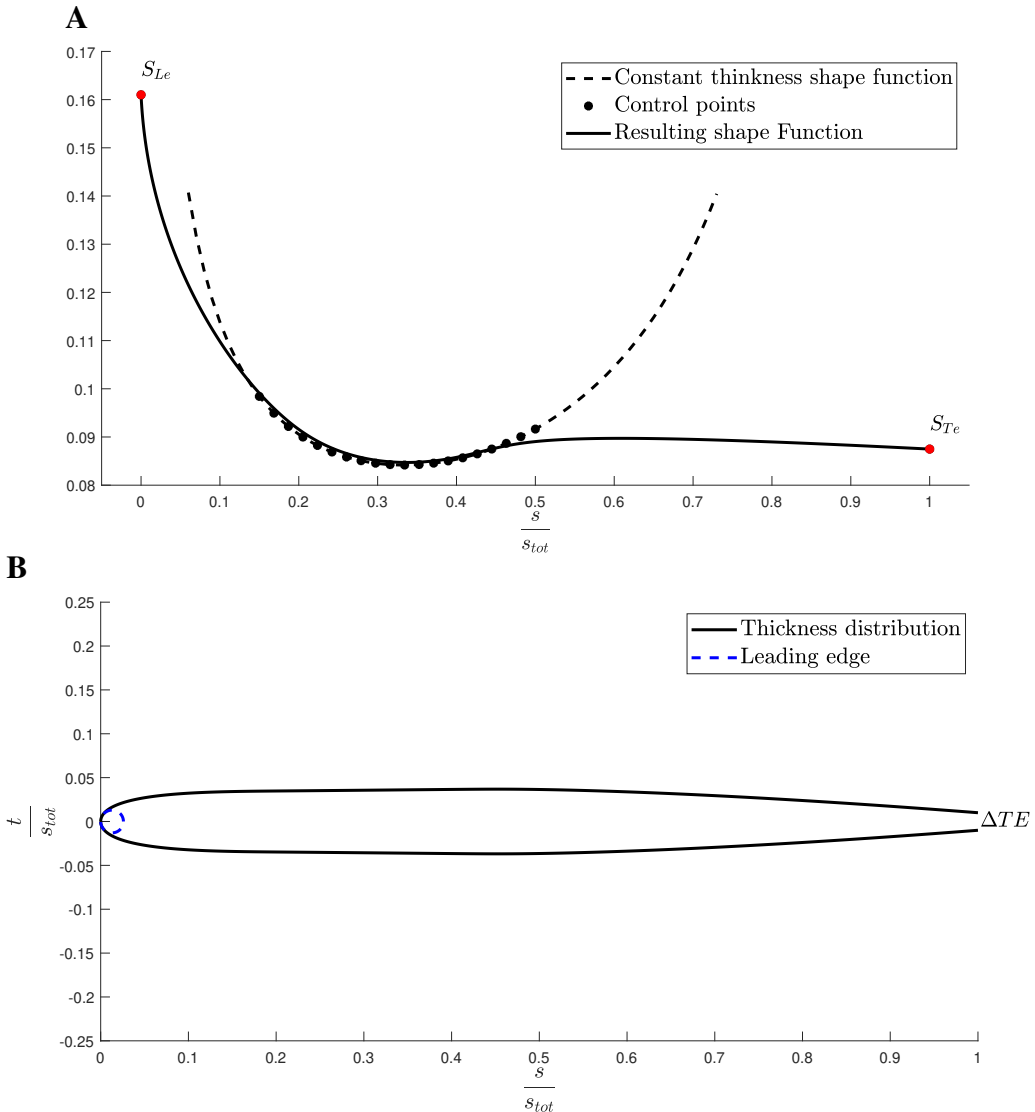


Fig. 2.11 A: Shape Function construction. B: Example Thickness Distribution of Mixed Flow turbine

An example of a shape function and resulting thickness distribution are shown in figure 2.11 A and 2.11 B respectively. After the leading edge and trailing edge shape function value are set, the point/region of maximum thickness are set using Bezier control points placed on

a constant thickness shape function. This can be used to specify the maximum thickness and the flat section of the aerofoil. The radial and mixed flow turbines have a large flat regions and the axial turbine profiles have nearly none at all. The main advantage of using the shape space approach is that, as long as the shape function is continuous in the second order derivative, the final aerofoil will be as well. There is no requirement to "stitch" a leading edge onto a separate thickness distribution. Here the leading and trailing edges are formed by the class function and the thickness distribution is set by the shape function.

Additional features

Hub fillet

In section 6.2 it will be shown that a fillet on the hub suction corner can help extend the range of mixed flow turbines. The fillet was produced by variably rescaling the thickness distribution up the span as well as along the axial direction. The latter scaling was necessary in order to leave the trailing edge thickness unchanged. The new/filletted thickness can be expressed as the old thickness multiplied by a fillet factor f_f which is a function of s^* the normalised camber line and h^* the normalised span.

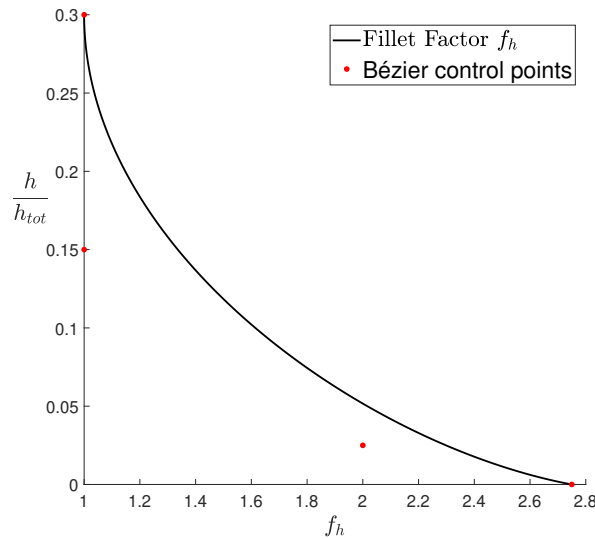
$$\frac{t}{s_{tot \text{ new}}}(s^*) = \frac{t}{s_{tot \text{ old}}}(s^*) f_f(s^*, h^*) \quad (2.11)$$

f_f is calculated from a combination of scaling factors as follows.

$$f_f = f_x(x^*)(f_h(h^*) - 1) + 1 \quad (2.12)$$

One for the variation up the span f_h which creates the fillet effect and the other for the variation in the axial direction which "turns is off" the fillet towards the trailing edge. Both f_h and f_x of these variation were constructed from Bezier curves see figure 2.12. The dashed lines in figure 2.12 shows the resulting rescaled thickness distribution at the hub.

Span Variation



Axial Variation

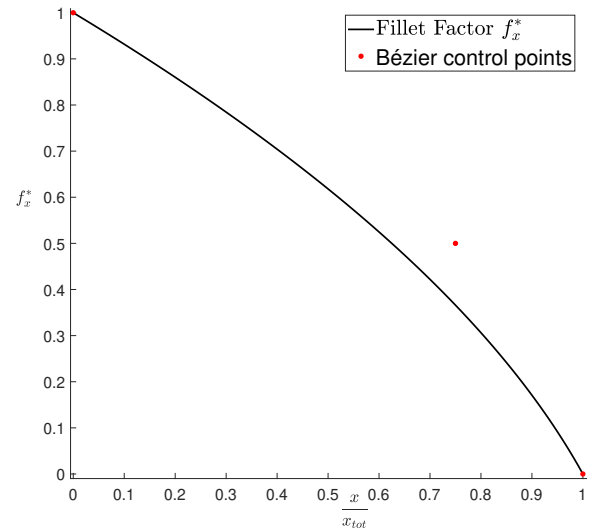


Fig. 2.12 Fillet construction factors

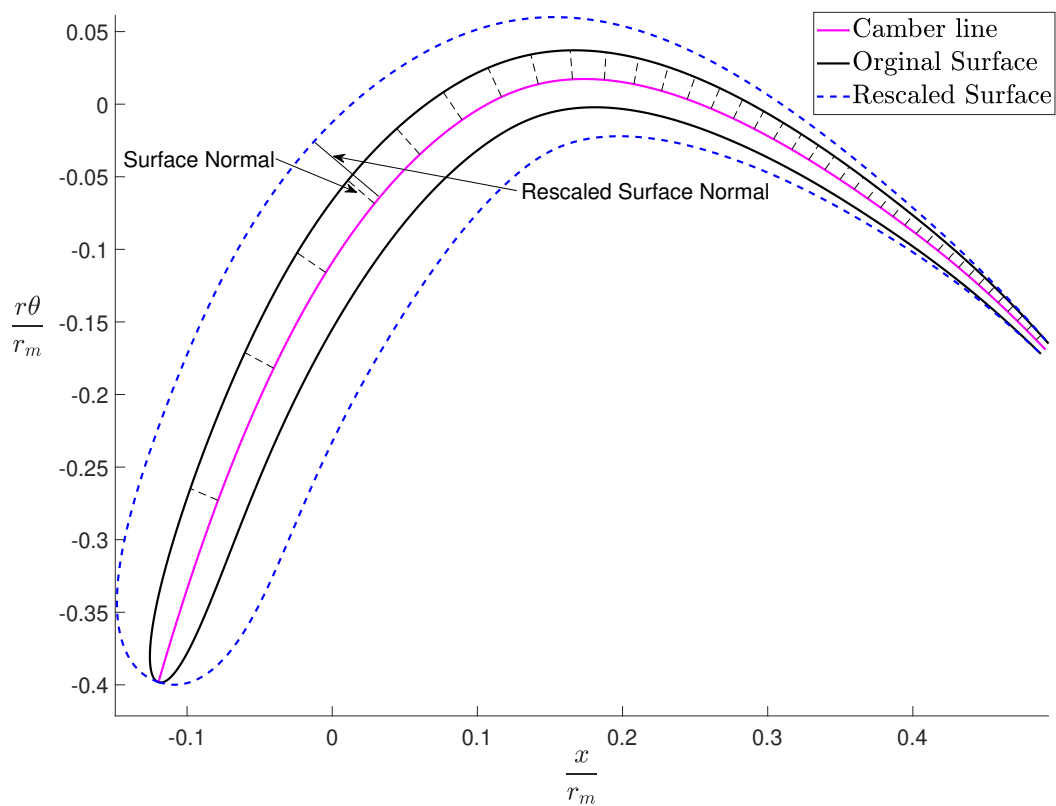


Fig. 2.13 Spoon fill construction

Hub Pressure Surface Fill

Due to the simplistic nature of the thickness distributions used, the axial architectures at higher loadings were prone to high end wall loss. Brear et al [6] showed that pressure surface separation at the hub interacts with secondary flow affecting its development and the loss that it creates. The blades used in this thesis shared some similarities with some profiles used by Brear, in that they are symmetrical and have a modest thickness. Brear suggested that the low momentum flow associated with any pressure surface separation will migrate strongly across the passage, increasing the strength of the secondary flow. Brear goes on to show that by increasing the momentum of the flow in end wall region can decrease the strength of the secondary flow and the loss produced. Brear achieved this by thickening the blade pressure surface around the hub and therefore the same was done for turbines in this thesis, albeit with a different geometric approach. Figure 2.14 shows a modified end wall profile which has a significantly shorter pressure surface flow distance.

Additional advantages of filling in pressure surface can be explained from a "classical" secondary flow theory which is later used in section 3.1.2 of this thesis, for modelling. Building on previous work, Coull [18] showed that the secondary flow loss correlated well with a vorticity amplification factor which itself, is a function of the difference in transit time of flow over the pressure and suction surface. Large difference in transit time result in high vorticity amplification factor which intern lead to high secondary flow. Making the modifications shown in figure 2.14 will increase the pressure surface velocity and decrease the flow distance, both of which decrease the difference in the transit time and therefore reduce secondary flow loss.

Filling in the pressure surface was done using a Bezier curve. The construction is outlined as follows:

- The first control point is set by finding the location of the lowest circumstantial value, i.e the lowest point of the leading edge.
- The circumferential location of the second control is the same as the first point as to maintain a smooth first derivative.
- The axial location of the second control point is set by specifying a short axial distance, keeping it close to the leading edge was necessary.
- The axial location of the third control point is set by specifying a short axial distance, again keeping it close to the leading edge was necessary.
- The circumferential location of the third control point is set in such a way as to maintain a smooth second derivative, see [1].
- The circumferential location of the forth, fifth and sixth point are set as fraction of the distance between highest and lowest points on the pressure surface. The axial locations

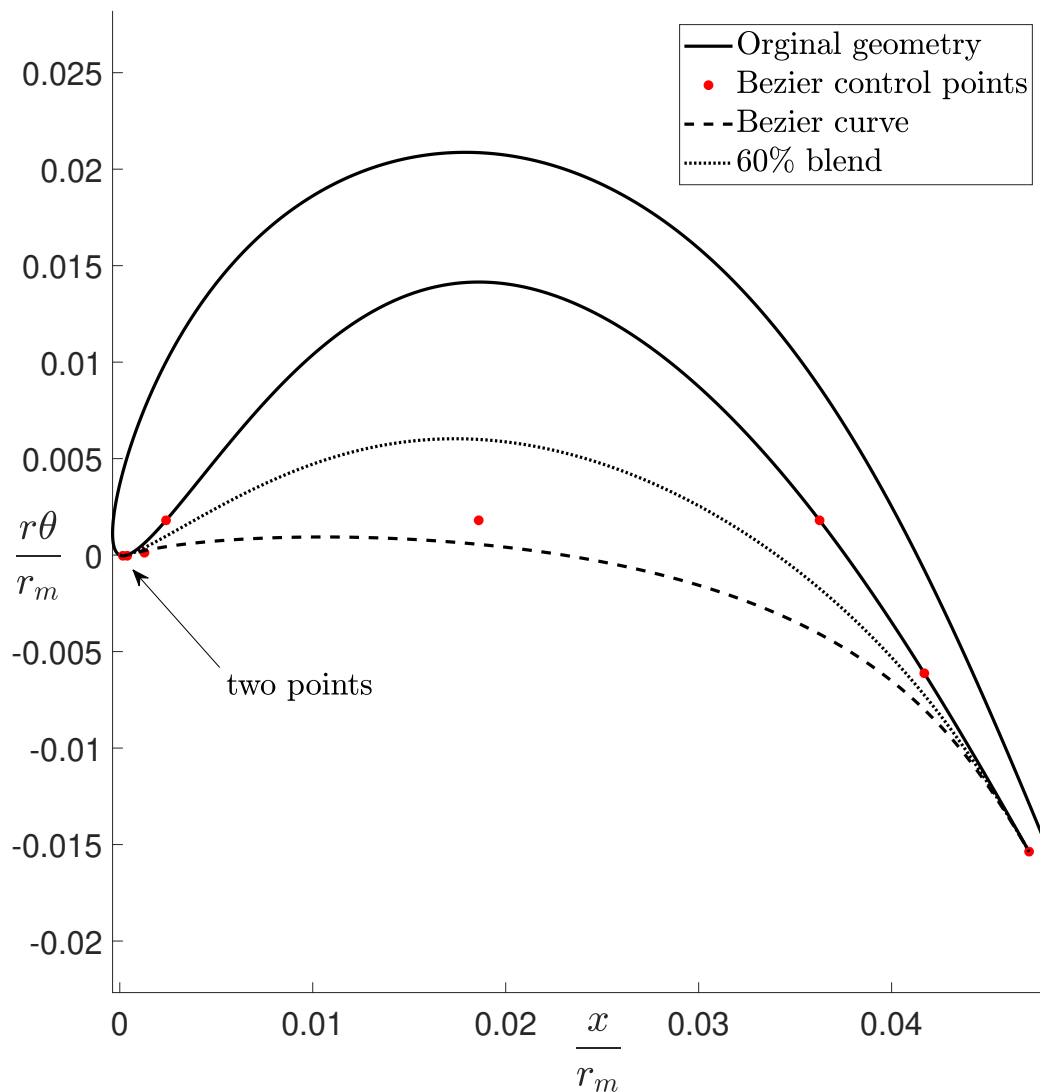


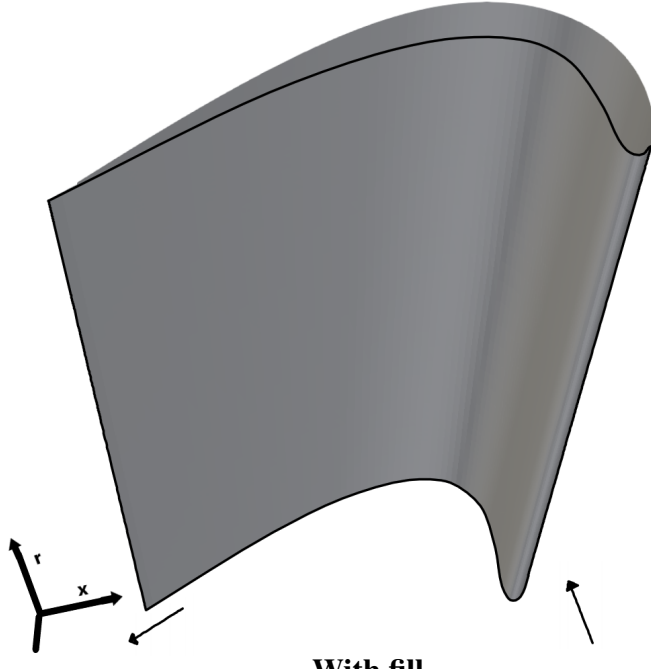
Fig. 2.14 Spoon fill construction

for the forth and 6th points are found by intercepts with the pressure surface and the fifth point sits between them.

- The final point is located at the trailing edge.

The profile created is then used in conjunction with a blending function which varies up the span in a similar manner used by Brear et al [6]. The effect on the blade geometry is shown in figure 2.15.

Without fill



With fill

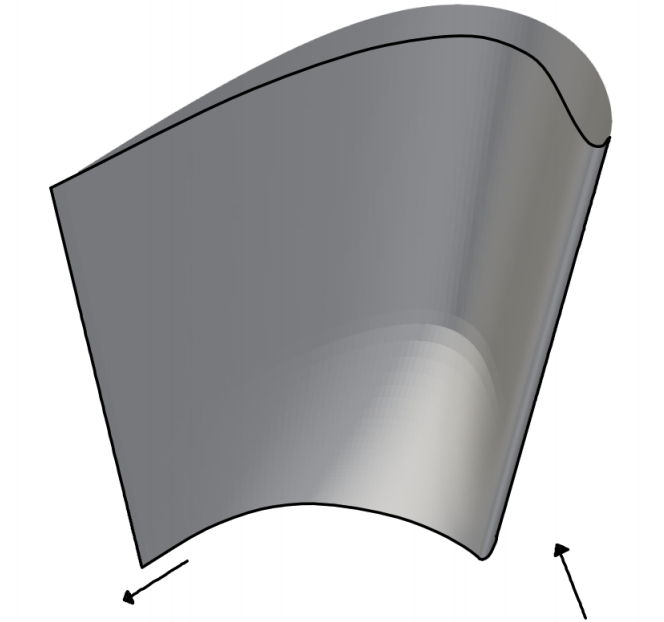


Fig. 2.15 Hub pressure surface fill

Chapter 3

Low Order Model And Numerical Method

3.1 Low Order Model

Low order models are critical tools during the preliminary design stages. Shortcomings in these models can push designers into sub-optimal regions of the design space. Currently, the models used for axial and radial turbines have diverged but this was not always the case. In the past, some well known radial turbine modelling used correlations developed from axial turbine cascades, e.g. the work of Rohlik [46], but due to the low performance of these models specialist correlations were developed specifically for radial turbines. These models grouped secondary and profile loss into a combined passage loss. This was typically calculated using classical hydraulic theory in which the turbine's geometry was characterised by a hydraulic length and diameter. The current state of the art is shown in Equation 1.14 [2].

Because mixed flow turbines are typically used as turbochargers, most designers have used models developed for radial turbines. There are currently no dedicated loss models for mixed flow turbines, nor are there models designed to bridge architectures. This section of the thesis will introduce a set of modified models developed in an attempt to bring this under one roof. The modelled loss will be split up as follows:

- **Profile loss**, which will be broken down into trailing edge, surface and mixing loss. These sources of loss will be modelled using an approach developed by Denton [26]. In this thesis, the surface loss will be expanded upon using thin aerofoil theory.
- **End wall loss**, which will be broken down into end surface dissipation due to the end wall boundary layer and secondary flow loss. The surface dissipation will be modelled in the same way as done by Denton, and the secondary flow loss will use the approach developed by Coull [18] with an additional term which partially models the effects of casing curvature.
- **Leakage loss**, which will be modelled using Denton's equation for over tip leakage but with a modification to the discharge coefficient to take the scraping effect into account.

3.1.1 Profile Loss

A good starting point for a profile loss model is Equation 1.12, here written in terms of a boundary layer entropy thickness at the trailing edge and assorted shape factors.

$$\zeta = \frac{C_{pb} t}{p \cos \beta_2} + \frac{2\delta_s H_s^{-1}}{p \cos \beta_2} + \left(\frac{t + \delta_s \frac{H_*}{H_s}}{p \cos \beta_2} \right)^2 \quad (3.1)$$

The entropy thickness at the trailing edge represents a measurement of all the entropy produced upstream of this point and is defined as

$$\delta_s = \frac{T_\delta}{\rho_\delta V_\delta^3} \int_0^\delta \rho V(s - s_\delta) dy. \quad (3.2)$$

This definition is identical to the energy shape factor at low speeds. H_* is the typically used shape factor, which is defined as

$$H_* = \frac{\delta^*}{\theta}, \quad (3.3)$$

and H_s is entropy based shape factor, which is defined as

$$H_s = \frac{\delta_s}{\theta}. \quad (3.4)$$

The entropy produced at the surface is calculated by leveraging the fact that the surface dissipation coefficient C_d is largely insensitive to the boundary layer state, as shown by Denton[26]. By assuming a constant dissipation coefficient, Equation 1.7 can then be used in conjunction with a velocity distribution model to calculate the entropy being produced up until the trailing edge. This then can be calculated over the entire blade surface from hub to casing for both pressure and suction side. Denton decomposes the surface velocity into a mean passage velocity, \bar{W} , and a change in velocity, ΔW , which is added or subtracted from the mean to produce the suction and pressure surfaces respectively.

$$W_{surf} = \bar{W} \pm \frac{1}{2} \Delta W \quad (3.5)$$

Denton's velocity distribution model is a deliberately idealised rectangular distribution, which is intended to predict the systematic trends across the design space. Because the velocity distribution is rectangular, the values \bar{W} and ΔW are kept constant.

The modification relaxes these assumptions and attempts to model these as distributions which vary along the cord and up the span. Another point of note is that Denton does not

calculate \bar{W} and ΔW but instead calculates the optimal ratio of the two, which in a sense only represents a specific set of profile loss optimised designs.

In the model presented in this thesis, \bar{W} is imagined to be the pitch wise, mass averaged relative velocity, i.e. a single streamline which characterises the change in momentum at a specific span wise location. ΔW is then calculated from Equation 3.6, which was derived using the momentum equation and thin aerofoil theory, and is derived in Appendix G. p is the pitch and s is a parametrised surface distance. The terms in the brackets on the right hand side represent the change in momentum of the flow though the passage, the first of which is the centrifugal loading and the second is the tangential loading.

$$\Delta W(s) = \frac{p}{r} \left(\omega \frac{d(r^2)}{ds} + \frac{d(rW_\theta)}{ds} \right) \quad (3.6)$$

To test whether the thin aerofoil theory gave reasonable approximations for the velocity profile, an initial test was done whereby the mass averaged values for the terms in Equation 3.6 were taking directly from the numerical solution. The velocity profiles from thin aerofoil theory were then compared to the velocity profiles taken directly from the CFD, the results of which can be seen in Figure 3.1. While not perfect, the simple approach captures the trends of the different velocity profiles remarkably well. There are a couple of shortcomings. The modelled profiles for the mixed and radial turbines are shifted higher, where as the axial is shifted lower. This likely stems from the assumption made in equation 3.5 where by the difference in velocity is split equally.

The modelled velocity distributions shown above are constructed retrospectively from the numerical solution. As it stands this cannot be used as a predictive tool unless the designer has an idea of the mass averaged streamline they intend to use. Instead, it might be more useful to construct the velocity distribution from the blade geometry.

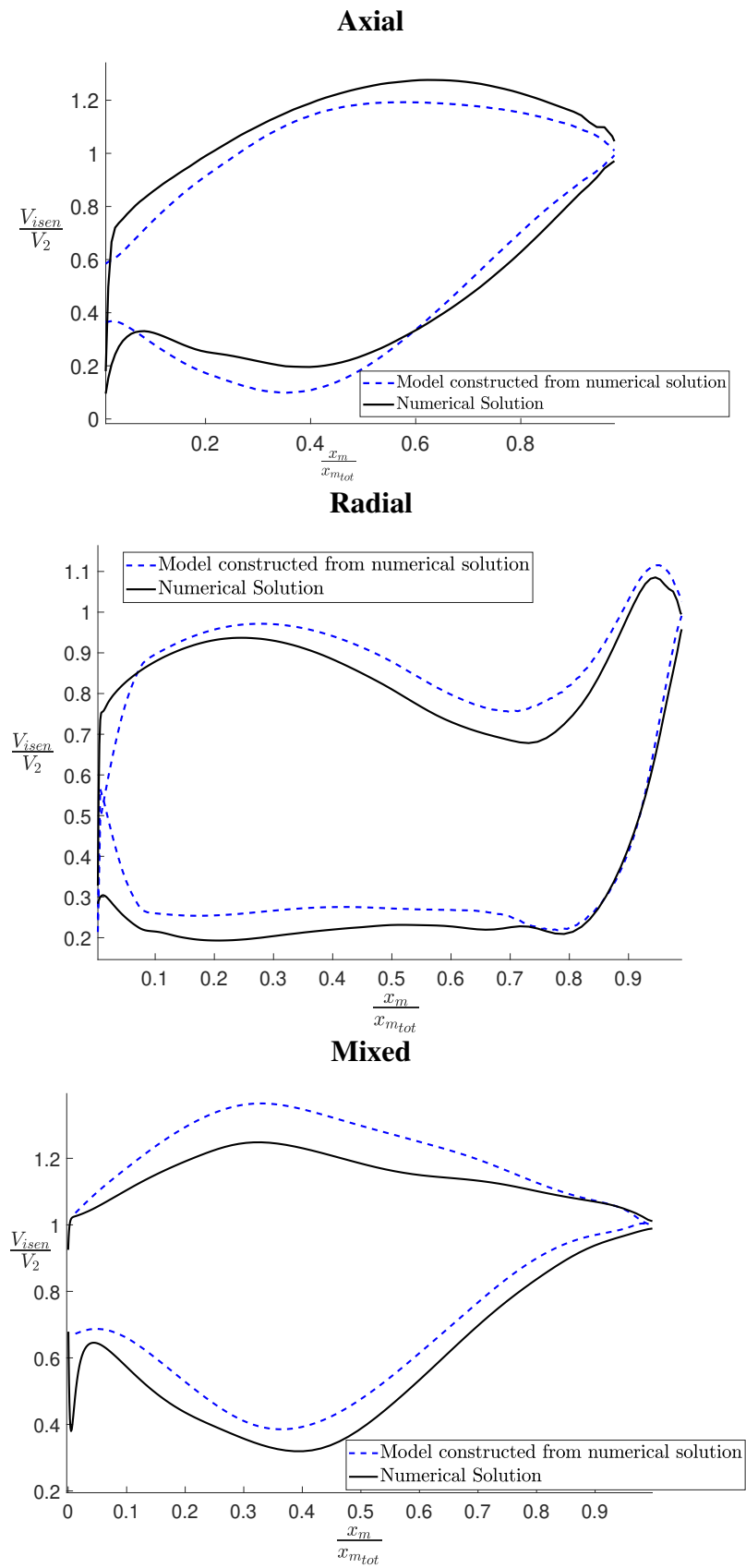


Fig. 3.1 Velocity distribution modelled from numerical solution mass averaged quantities.

Average Passage Velocity

The average streamline is the backbone of this approach. From this, all terms in Equation 3.6 can then be derived. The average velocity can be calculated from the meridional velocity and the flow angle distribution. The meridional velocity can be calculated from continuity and the flow angle distribution can be approximated from the normalised metal angle distribution, which is then rescaled back into a flow angle distribution.

$$\bar{W} = \frac{V_m}{\cos(\beta)} \quad (3.7)$$

For incompressible flow,

$$V_m = V_{m_{ref}} \frac{A_{ref}}{A}. \quad (3.8)$$

The way in which the mean area distribution through the passage is calculated as follows. The meanline is used to construct lines perpendicular to itself. These meanline normals are then used in conjunction with the blade tangential thickness to calculate the area distribution. Figure 3.2 illustrates this. Taking the tangential thickness into account was important for the axial architecture and less so for radial and mixed which are relatively thinner.

The meridional velocity is then calculated by Equation 3.8. This value essentially represents an area average and hence the average velocity calculated from this will also represent an area average which can differ significantly from the mass average value. This occurs particularly where the difference between the suction and pressure surface velocities is high, i.e where ΔW is high. This can be seen half way down the passage in Figure 3.3, where the average and meridional velocity are too low. This also causes the average velocity to be "wobbly". To overcome the difference between the mass and area averaged value of the meridional velocity, a correction was derived by assuming a linear variation in velocity between the suction and pressure surface,

$$V_m = \Delta V_m \left(\frac{p}{p_{total}} \right) + \bar{V}_M^a - \frac{1}{2} \Delta V_m, \quad (3.9)$$

where superscript *a* denotes area averaged values. The ratio between area and mass averages can then be calculated,

$$\frac{\bar{V}_M^m}{\bar{V}_M^a} = \frac{\frac{1}{\dot{m}} \int \rho V_m^2 dp}{\frac{1}{A} \int V_m dp}. \quad (3.10)$$

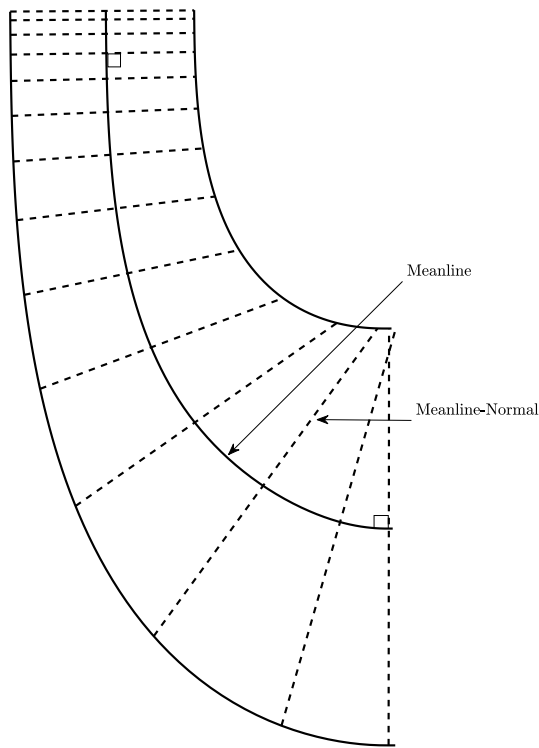


Fig. 3.2 Illustration of how the area distribution is approximated from geometry.

Substituting Equation 3.9 into Equation 3.10 leads to

$$\frac{\bar{V}_M^m}{\bar{V}_M^a} = \frac{1}{12} \left(\frac{\Delta V_m}{\bar{V}_M^a} \right)^2 + 1. \quad (3.11)$$

Using $\Delta V_m = \Delta W \cos \beta$, the readjusted meridional velocity can be calculated. Note that this requires the calculation of ΔW and thus this is done iteratively. Two to three iterations were generally enough. To reduce any remaining turning points (wobbles) in the average velocity, a spline was loosely fitted (10 control points) and then re-interpolated. The results can be seen in Figure 3.3. This gave reasonable results over the design space but there is potential room for improving the way in which the average streamline is modelled.

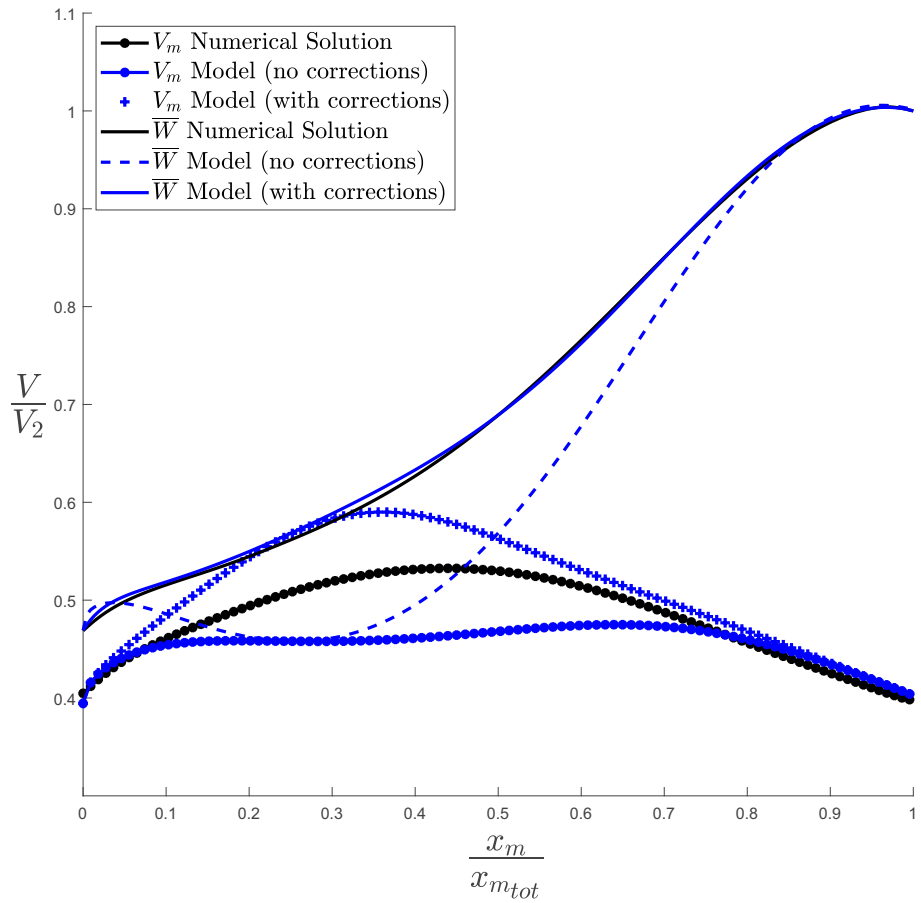


Fig. 3.3 Various passage velocities for an axial: numerical solution, uncorrected model, model with mass average and smoothing corrections.

Velocity difference

Equation 3.6 is then used to calculate the velocity difference between the suction and the pressure surface. The first term in the brackets on the right hand side can be simply calculated from the meridional geometry of the rotor. The tangential velocity required for the second term is calculated from the average velocity and the blade angle (camber line) distribution. The distribution is rescaled for the correct inlet and exit flow angles because the metal angles differ from the flow angles. For the purposes of modelling, the second term in the bracket is split into terms using the chain rule,

$$\Delta W(s) = \frac{p}{r} \left(\omega \frac{d(r^2)}{ds} + W_\theta \frac{dr}{ds} + r \cdot \frac{dW_\theta}{ds} \right) \quad (3.12)$$

A comparison with the numerical solution of the variation of these terms is presented in Figure 3.4, which is for a mixed flow turbine.

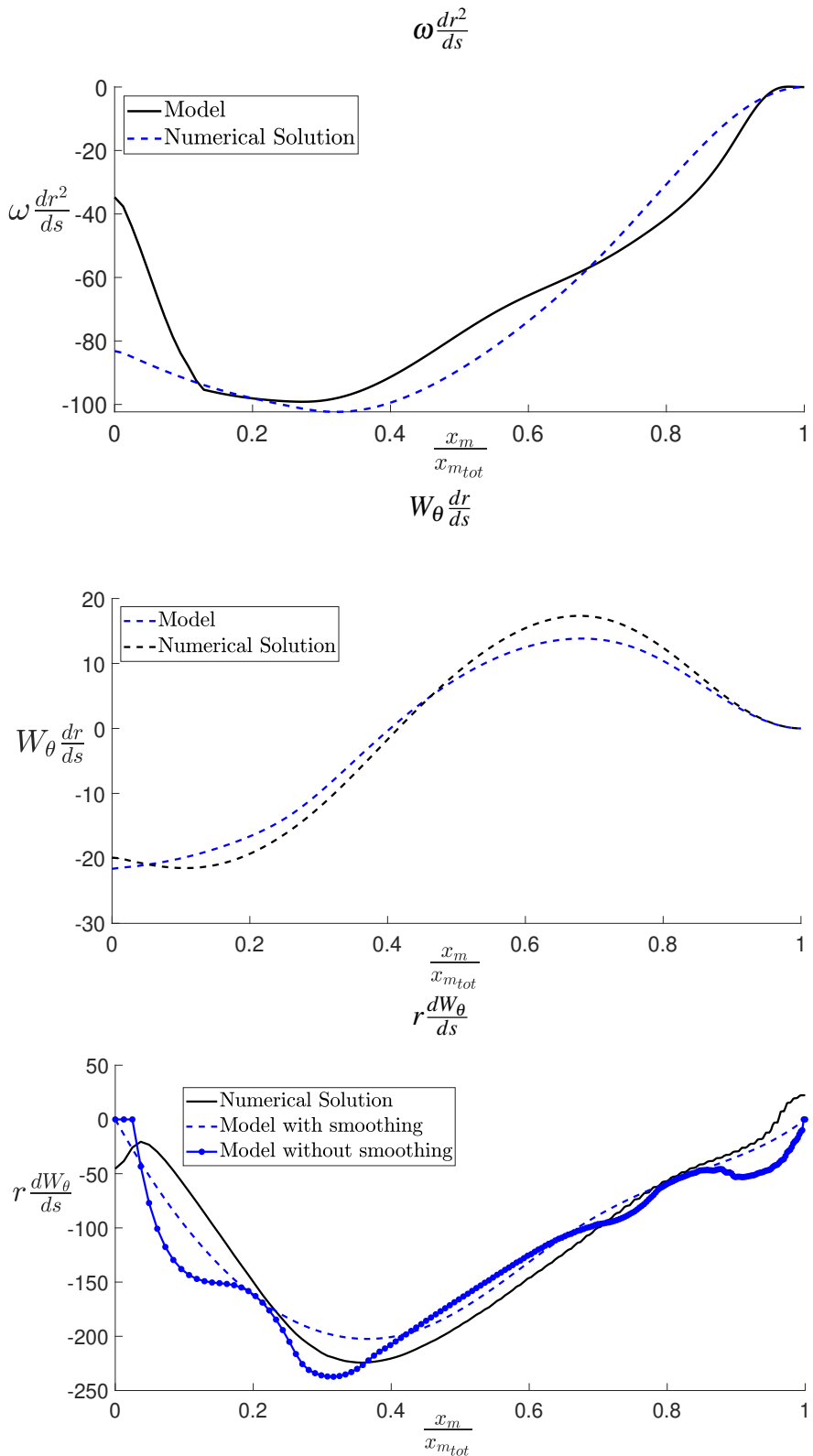


Fig. 3.4 Comparison of different loading terms to the numerical solution for a mixed flow turbine.

The behaviour of the first term, i.e. the centrifugal term, is captured quite well by the model. The second term in Equation 3.12, which is one of the components of the tangential term, is also modelled reasonably well, however the contribution from this term is small. The reason these two terms are being modelled well is that the derivatives are dependent only on the rotor geometry, whereas the derivative in the final term is dependent on the tangential velocity (calculated from the average velocity), which contains modelling artefacts as previously shown. To remove these artefacts, a spline is again loosely fitted through the initial result and re-interpolated. This is shown in Figure 3.4 by the dashed line. It must be noted that other filter methods could potentially show better results and should be tested. Using equation 3.6 in conjunction with a modelled average velocity can result in velocity with higher or lower circulation than intended and should be corrected. Equation 3.6 can be decomposed into the change in velocity due to the different loading terms.

$$\Delta W_{cen} = \frac{p}{r} \omega \frac{d(r^2)}{ds}$$

$$\Delta W_{tan} = \frac{p}{r} \frac{d(rW_\theta)}{ds}$$

These terms can then be rescaled individually such that the final distribution has the correct amount of circulation. This is achieved as follows. The total amount of circulation for a thin aerofoil can be calculated by integrating the local velocity difference over the length,

$$\Gamma = \int \Delta W ds$$

From this, the circulation of the model can be calculated and then rescaled,

$$\Delta W = \Delta W_{cent} \frac{\Gamma_{cen}}{\Gamma_{cen,mod}} + \Delta W_{tan} \frac{\Gamma_{tan}}{\Gamma_{tan,mod}}$$

where the individual components of circulation then can be calculated from the circulation coefficients of those terms (refer to Equation 2.8 and Appendix F for more details).

$$\Gamma_{tan} = C_{o_{tan}} W_2 S_{tot}$$

$$\Gamma_{cen} = C_{o_{cen}} W_2 S_{tot}$$

The results of the velocity distribution model are presented in Figure 3.5. The distributions still contain a number of modelling artefacts. The location of maximum velocity is shifted forward for the Axial case and is likely due to the left skew in the meridional velocity correction, which can be seen in Figure 3.3. For the mixed flow architecture, the loading has also been shifted forward. This was similarly due to a skew in the meridional velocity. The radial architecture slightly overpredicts pressure surface and the loading at the leading edge. Despite these artefacts, the model velocity profiles constructed from geometry captures the behaviour

reasonably well. There is still room for improvement in these profiles. Unfortunately, as ΔW is proportional to the derivative of the average streamline velocity, any artefacts in this cause further errors in the final velocity profile. Therefore, improvements in calculating the average streamline should be the next step in further development of this model.

Surface Dissipation

To calculate the full 3D surface loss, the rotor is discretized up the span to form stream tubes. The process for calculating the velocity profiles is done for each of these sections and thus the surface velocity for the entire rotor surface has been modelled. Equation 1.7 is then used to calculate entropy produced. The value for the dissipation coefficient suggested by Denton [26] is $C_d = 0.002$.

In reality, the dissipation coefficient varies over the blade, being relatively high at the leading edge and then reducing to roughly a constant value when moving down stream (for fully turbulent boundary layers). To capture this behaviour, the dissipation coefficient should be inside the integral in equation 1.7. Instead, averaged values can be used to compare with the CFD. For axial architectures, the dissipation coefficient varied in the range $0.0021 < C_d < 0.0027$ and as high as $C_d = 0.0032$ for some radial architectures. As will be discussed in Section 3.2, the numerical method used here assumed steady flow, a fully turbulent boundary layer and used a simple mixing length model. Whether these values are reflected in reality requires further experimental work and is outside the scope of this thesis. For the sake of comparison with the numerical solutions, a constant value of $C_d = 0.002$ was used in the model.

Real world turbine boundary layers are subject to more complex features and flow conditions such as transition, laminar separation bubbles and an inherently unsteady environment, and therefore this approach is likely to fall short. A potential improvement would be to model the dissipation coefficient as a distribution, which itself can be calculated by either boundary layer solvers or acquired experimentally (if the profiles prove to be largely similar). Pre-calculated DNS solutions over small sections could potentially be another route to this.

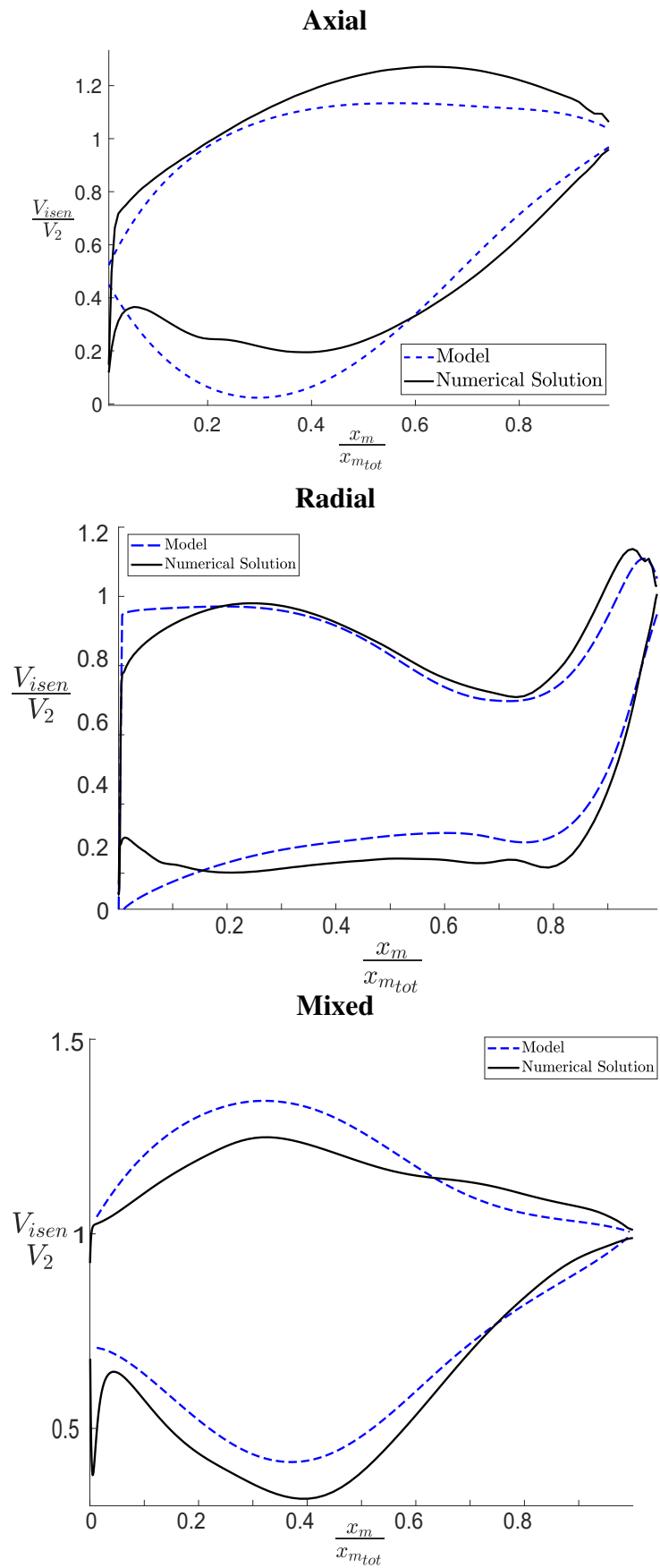


Fig. 3.5 Comparison of velocity distribution models with numerical solution.

Trailing Edge Base Pressure Loss

The trailing edge loss was calculated by using the trailing edge terms from Equation 1.12. The base pressure coefficient C_{pb} was assumed to take a value of -0.2.

$$\zeta = \frac{-C_{pb}t}{p \cos \beta_2} \quad (3.13)$$

Mixed Out Loss

The loss calculated from dissipation above is a measure of the entropy generated up to the trailing edge and does not include the loss that must occur as a result of mixing out of the boundary layer. In other words, a loss coefficient based of this entropy would only represent a portion of the second term on the RHS of equation 3.1 and none of the third term which is due the blockage at the trailing edge. Miller [29] pointed out that for thin blade (zero thickness TE), the ratio of the down stream mixed out loss to the amount at the trailing edge can be determined from

$$\frac{\text{down stream entropy}}{\text{entropy at the trailing edge}} = \frac{2\theta_{te}}{\delta_s} = \frac{2\delta_s H_s^{-1}}{\delta_s} = \frac{2}{H_s},$$

which can be seen by the presence of the H_s in the second term of equation 3.1. For low speed flow, the entropy thickness is identical to the energy thickness, hence H_s can be replaced with $\frac{\theta}{\delta_e}$. For a turbulent boundary layer with a typical shape factor of about $H = 1.6$, the energy based shape factor is $\frac{\theta}{\delta_e} \approx 1.7$ (Schlichting [49]).

To approximately account for the additional mixing losses of the second term, the loss present at the trailing edge is simply multiplied by 1.18. The final term in Equation 3.1 is calculated in a similar fashion by assuming fixed shape factors.

The use of a fixed shape factor presents a significant limitation to this simplified approach to mixing loss. According to Miller, the energy based shape factor tends to unity when the boundary layer is close to separation, which mean large amounts of additional loss is generated. This could be a potential point of improvement in future.

3.1.2 Secondary/End wall loss

While the end wall loss is a complex mechanism with many intricate factors, it can be loosely broken down into two parts, the viscous dissipation in the end wall boundary layers and the mixing loss of the secondary flow.

End wall surface dissipation

As suggested by Denton [26], the end wall surface dissipation is calculated by assuming a linear variation in velocity with pitch between the suction and pressure surface values at the end walls. This distribution is then integrated using Equation 1.7 for surface dissipation to calculate the entropy produced at the end walls.

$$V_{end} = (V_s - V_p) \left(\frac{p}{p_{total}} \right) + V_s \quad (3.14)$$

Secondary flow loss and amplification factors

The flowing subsection draws from Coull and Clark [15]. The loss arise from the dissipation of secondary Kinetic Energy (SKE) associated with the secondary flow, which itself is produced by streamwise or "secondary" vorticity.

The secondary vorticity arises due to the turning and stretching of vortex filaments, present at the inlet, into the streamwise direction. The vorticity induces rotating flow normal to the bulk flow direction. The severity of the loss is therefore largely determined by the amount and distribution of streamwise "secondary" vorticity at the exit.

Came and Marsh [8] analysed this process mathematically by applying Kelvin's circulation theorem. The approach taken in this these is a modified version of this approach done by Coull [18] which itself is based upon on the work done by Came and Marsh [8]. Like Hawthorne [33], Marsh derived three terms for the streamwise circulation these being the passage vortex, counter vortex, and trailing edge shed vortex. The dominant of these is the passage vortex.

Marsh's approach to the passage vortex (distributed secondary vorticity) is to predict the circulation contained at an exit plane, which is normal to the primary flow direction. The author does this by applying Kelvin's Circulation theorem and tracking the plane back in time and upstream to the vorticity source, which in this case is the inlet boundary layer. Coull[18] presents this in the form of a vorticity amplification factor, shown in equation 3.15, and showed that it correlated very well with secondary loss.

$$AF_{pv} = 2M^* \left(\frac{V_1}{V_2} \right)^2 \left[\frac{\Delta T^* C_x}{p \cos \alpha_2} \frac{|(\frac{V_2}{V_1}) \sin \alpha_1 - \sin \alpha_2|}{\cos \alpha_2} \right], \quad (3.15)$$

where M^* is a compressibility factor and ΔT is the difference in transit time between flow passing over the pressure and suction surfaces and is non-dimensionalised.

$$M^* = \left(1 + \frac{\gamma - 1}{2} M_1^2 \right) \quad (3.16)$$

$$\Delta T^* = T_{ps}^* - T_{ss}^* = \int_{ps} \left(\frac{V_2}{V_{fs}} \right) d\left(\frac{S}{C_x} \right) - \int_{ss} \left(\frac{V_2}{V_{fs}} \right) d\left(\frac{S}{C_x} \right), \quad (3.17)$$

where V_{fs} is the free stream velocity at the edge of the boundary layer. A version of Equation 3.15 used here has been extended to include radius ratio and meridional velocity ratio.

$$AF_{pv} = M^* R_r R_{vm} \left(\frac{W_1}{W_2} \right)^2 \left[\frac{\Delta T^* C_x}{p \cos \alpha_2} \frac{|R_r^{-1}(\frac{W_2}{W_1}) \sin \alpha_1 - \sin \alpha_2|}{\cos \alpha_2} \right] \quad (3.18)$$

In order to calculate the amplification factor, a velocity profile is required. Here a simplified rectangular velocity distribution will be used instead of those produced in Section 3.1.1. The rectangular velocity distribution proved to be more robust across the designs space. In some cases (mostly radial) the distributions produced by the thin aerofoil approach would stagnate the flow which would create infinite difference in transit time, breaking the model.

$$W = \bar{W} \pm \Delta W \quad (3.19)$$

The average velocity is calculated from the averages of the inlet and exit velocity $\bar{W} = \frac{1}{2}(W_1 + W_2)$ and ΔW is also constant and is calculated from circulation.

Effects Of Casing Curvature

One of the key difference between axial and radial architectures is the radial to axial bend as discussed in section 1.2, which drew on the work done by Zangeneh [58]. Due to the meridional curvature in the bend, there is an acceleration due to this curvature. Associated with this is a pressure field with a gradient in the direction of the blade boundary layer vorticity. This results in secondary flow.

Modelling the exact physics including the interaction with the blade to blade flow is particularly complex. Instead, this effect might be modelled by a curved rectangular duct. The full derivation can be found in Appendix D.

The approach used here is similar to that used by Came and Marsh [8]. In short, a material plane is tracked upstream in order to calculate the amount of circulation at the exit. Again, this is done using kelvins circulation theorem (Figure 3.6). The change in orientation is solely determined by the difference in the transit time between the duct "hub" and "casing" lines. The difference is calculated by assuming that the velocity field in the duct bend takes the form of a free vortex. Once the orientation of the material plane at the inlet is known, the circulation

can be calculated using the dot product of vorticity vector and the plane normal vector. Zero streamwise vorticity assumed here.

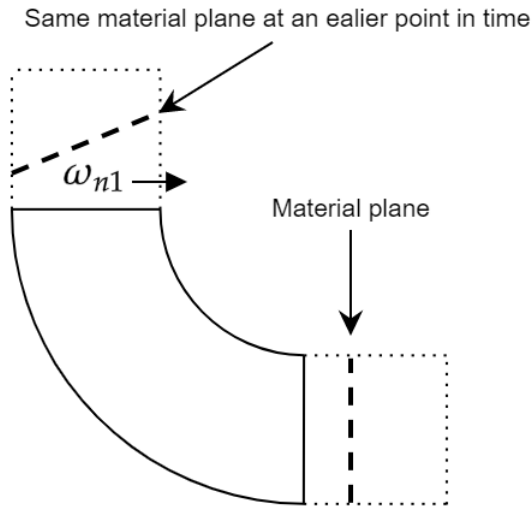


Fig. 3.6 Variation of total to total efficiency with shroud radius of curvature.

The resulting equation is

$$AF_c = \lambda \ln \left(1 + \frac{h}{r_c} \right) \left(2 \frac{r_c}{h} + 1 \right), \quad (3.20)$$

where h is the duct height (span), r_c is the radius of curvature of the smaller radius (casing) and λ is the cone angle.

In reality, for a turbine, the component of vorticity in the span wise direction up stream of the leading edge is in fact likely to be zero. However, this vorticity is produced in the blade boundary layer through out the passage with a large amount produced at the leading edge, particularly if there is a significant levels of incidence (which is typically the case for radial turbines).

To test whether or not this simple model correlates with changes in efficiency for a radial turbine, a test case was set up with varying radii of curvature at the casing. Two groups were created, one where the axial length of the turbine was kept constant and another where the axial length would reduce with the radius of curvature. Other than these changes, all other parameters where kept constant.

The results are presented in Figures 3.7. As expected, reductions in the radius of curvature reduce performance for both groups. The group with the shortening axial length drops of faster which is likely a result of a shorter distance in which to turn the flow in the tangential direction.

There is also a sharp drop in performance at low non dimensional radius of curvature, which is due to casing separation. Changes in the curvature amplification factor mirror the behaviour

well. From figure 3.7 *B*, changes in the difference of efficiency are linearly related to the amplification factor up until the point of separation.

How exactly the amplification factor relates to loss is still unclear and require further research. For now it will serve to multiply the factor calculated by Equation 3.18,

$$AF_{tot} = AF_{pv}(1 + f_{cur} AF_{cur}), \quad (3.21)$$

where $f_{cur} = 1$. This should be considered a first attempt at the relationship between the end wall loss and casing amplification factor.

Secondary flow loss model

To formulate a secondary flow loss model, a relationship with aspect ratio is required. Coull and Clark [15] point out that there is significant evidence that the end wall loss scales with span. Most authors tend to define aspect ratio as the ratio of span to axial cord. Coull and Clark instead show that the most appropriate measure is actually the ratio of span to exit passage width, $\frac{h}{p_m \cos \beta_2}$, which will be used here. The secondary flow loss is then calculated by

$$\zeta_{sec} = 0.0032 AF_{tot} \frac{p_m \cos \beta_2}{h}. \quad (3.22)$$

Note that the coefficient in front of Equation 3.22 differs from that found in Coull [18]. This is because of the addition of the aspect ratio term which is not present the correlation produced by Coull at the time. Coull and Clark have since developed a far more rigorous secondary loss modelling technique, however due to some of the assumptions made the approach could not be directly applied to the non axial architectures in its current form.

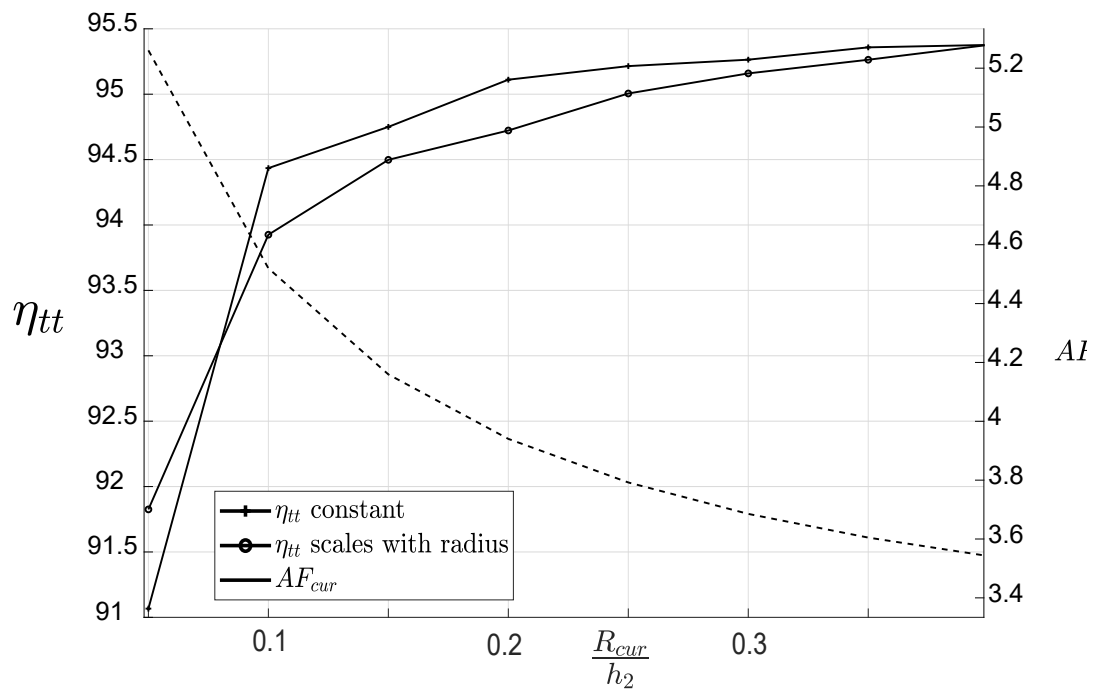
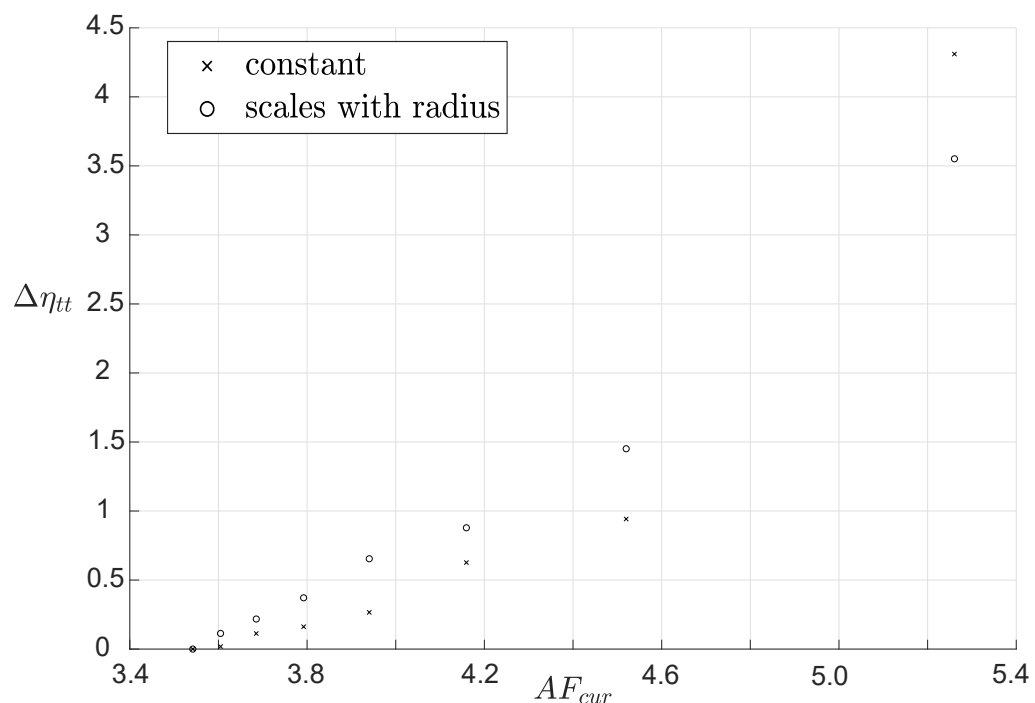
A**B**

Fig. 3.7 A: Variation of total to total efficiency with casing radius of curvature. B: Variation of total to total efficiency with shroud radius of curvature.

3.1.3 Tip leakage

Denton [26] pointed out that the leakage loss can be approximated by applying the global conservation equations. The author derived a method for approximating the leakage loss (equations 3.23, 3.24, 3.25) with the following assumptions:

- The chord wise component of flow at the pressure surface is unaffected as it moves across the tip gap.
- The tip flow mixes out immediately with the local chord wise velocity on the suction surface.
- The local leakage flow rate is determined by a static pressure difference across the passage and a discharge coefficient.

The model does not explicitly take into account the effects of relative casing motion (RCM), which is particularly important for radial turbines. However, Denton suggested that either the discharge coefficient or the pressure difference across the gap could be reduced, with Denton preferring the latter.

$$T\Delta S = \int V_s^2 \left(1 - \frac{V_p}{V_s}\right) dm \quad (3.23)$$

$$dm = C_{dis} t \sqrt{2\Delta p} ds \quad (3.24)$$

$$\Delta p = \frac{1}{2} \rho (V_s^2 - V_p^2) \quad (3.25)$$

Dambach [23] made detailed measurements of the clearance flows in a radial turbine. The results indicated a large variation in leakage mass flow per unit length from inlet to exit. This was attributed to the effect of a scraping flow in the relative frame. The significance of the effect of the scraping was characterised by the ratio of over tip driving pressure and the component of RCM dynamic head.

$$R_{scr} = \frac{\Delta p_{tip}}{\frac{1}{2} \rho (\omega r)^2 \cos^2 \beta} \quad (3.26)$$

Dambach and Hodson [23] reported that for $R_{scr} < 1$ ($t/h = 0.6\%$), the scraping fluid is dragged through the gap, whereas for $R_{scr} > 1$ the scrapping layer inside the gap could not

be resolved. From Figure 3.8, it can be seen that for the case with smallest tip clearance (A0) the leakage flow stagnates and the scraping flow dominates the gap, whereas for the B0 the tip leakage flow takes up half the gap.

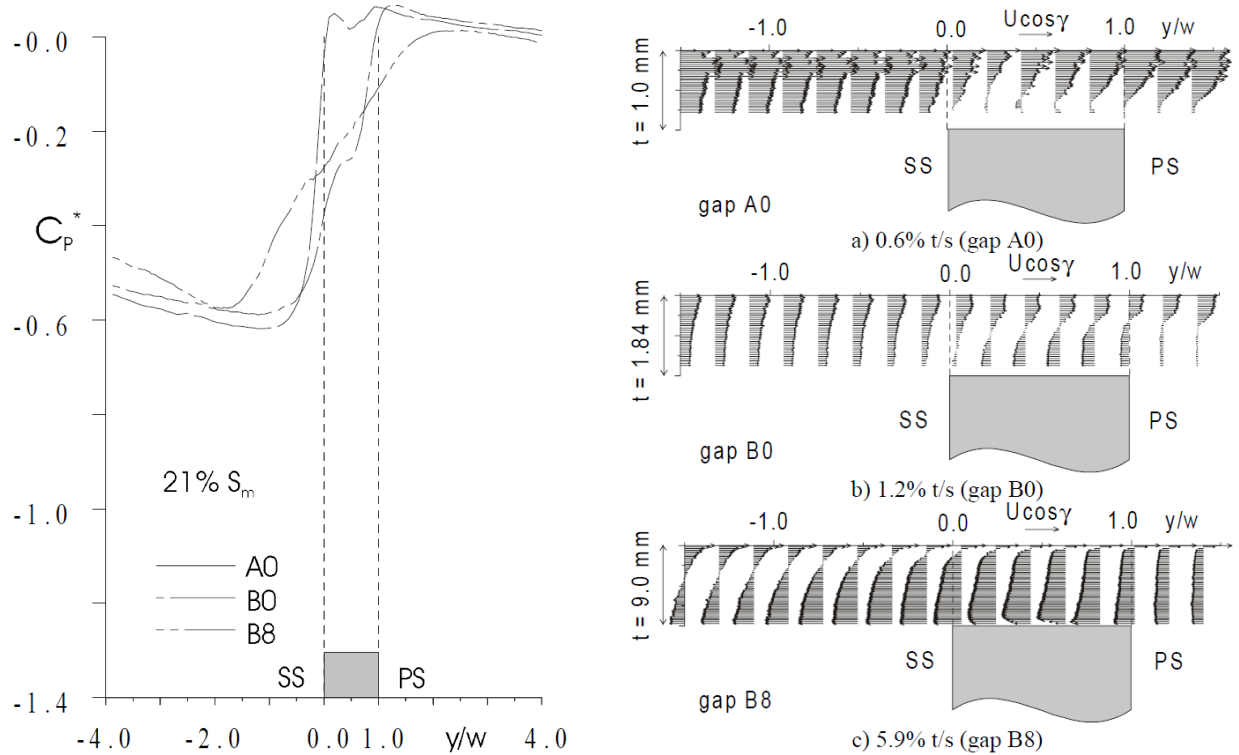


Fig. 3.8 Tip flow and driving pressure, Dambach [23]

Coull and Atkins [19] undertook a computational study that studied the effects of upstream inlet conditions and relative casing motion on leakage flow. For the case where RCM was introduced on its own, the driving pressure changed quite significantly and that this difference was remarkably close to the local RCM dynamic head as shown.

In order to shed some light on the potential reasons for the variation in the discharge coefficient, a comparison was made of Dambach's [23] original data by calculating an effective discharge coefficient based solely on the reduction in driving pressure as a result of the RCM dynamic head. The effective discharge coefficient was modelled by assuming a "competition" between the relative casing stream tube and a portion of the leakage flow. This is illustrated in Figure 3.10. The mass flow in the stream tubes are determined using Equation 3.24. The competing stream tubes are assumed to have the height of the relative casing boundary layer's displacement thickness and have a lower driving pressure, which is reduced by the amount of relative casing dynamic head. The remaining space is occupied by an unobstructed stream and its driving pressure is unchanged. Applying continuity, the effective discharge coefficient is derived as

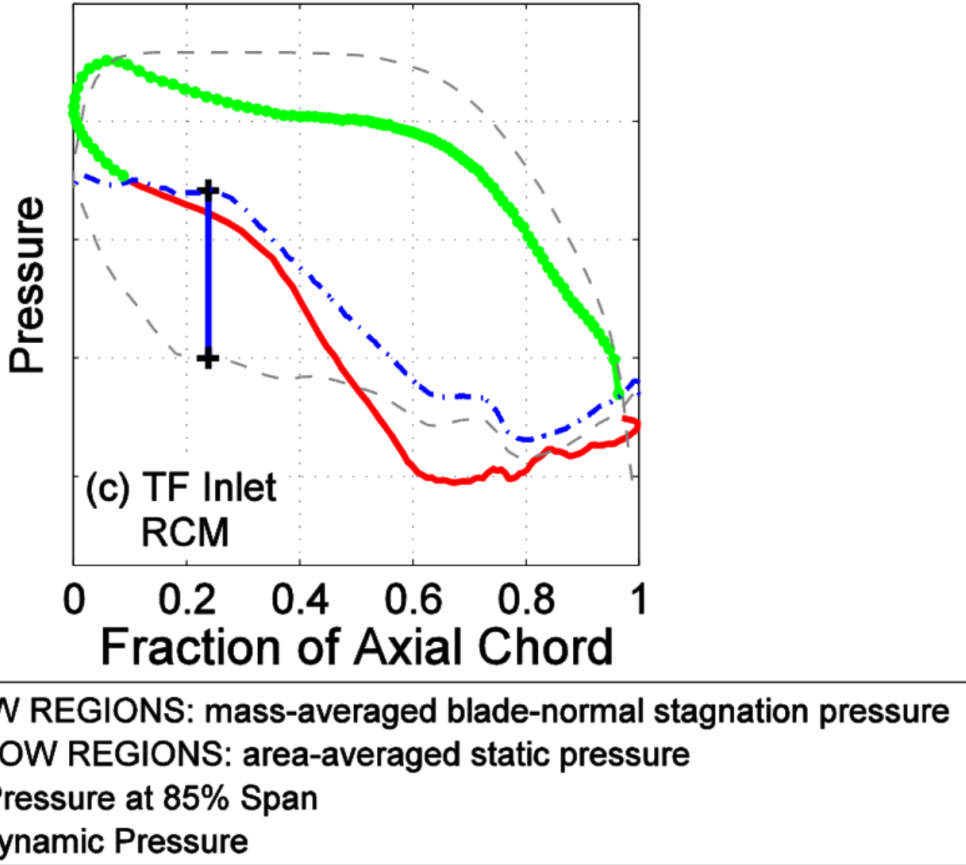


Fig. 3.9 Over tip driving pressure from Coull and Atkins[19]

$$C_{dis_{eff}} = C_{dis_{con}} \left(\frac{\delta^*}{t} \sqrt{1 - R_{scr}^{-1}} + 1 - \frac{\delta^*}{t} \right). \quad (3.27)$$

This equation needs to be constrained. When $1 - R_{scr}^{-1} < 0$, this term is set to zero. In other words, the RCM flow cannot form "negative leakage" flow. When $\frac{\delta^*}{t} > 1$, this term is set to one as the upper stream tube can only be as big as the tip gap.

Figure 3.11 shows a comparison of the discharge coefficient measure by Dambach [23] compared with the effective discharge coefficient derived here. The effective discharge coefficient captures the general behaviour reasonably well. This suggest that changes in the leakage flow due to relative casing motion can largely be explained by a change in the driving pressure due to RCM dynamic head. On top of this, Equation 3.27 is used in this thesis to roughly model these effects.

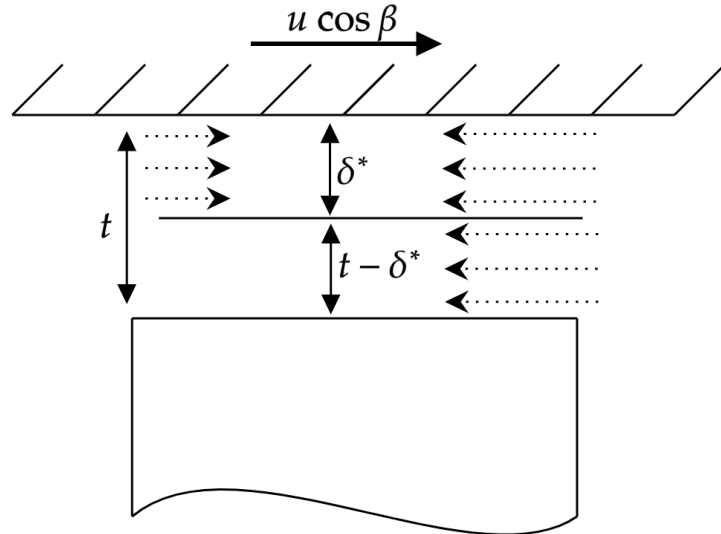


Fig. 3.10 Illustration of competing stream tube model.

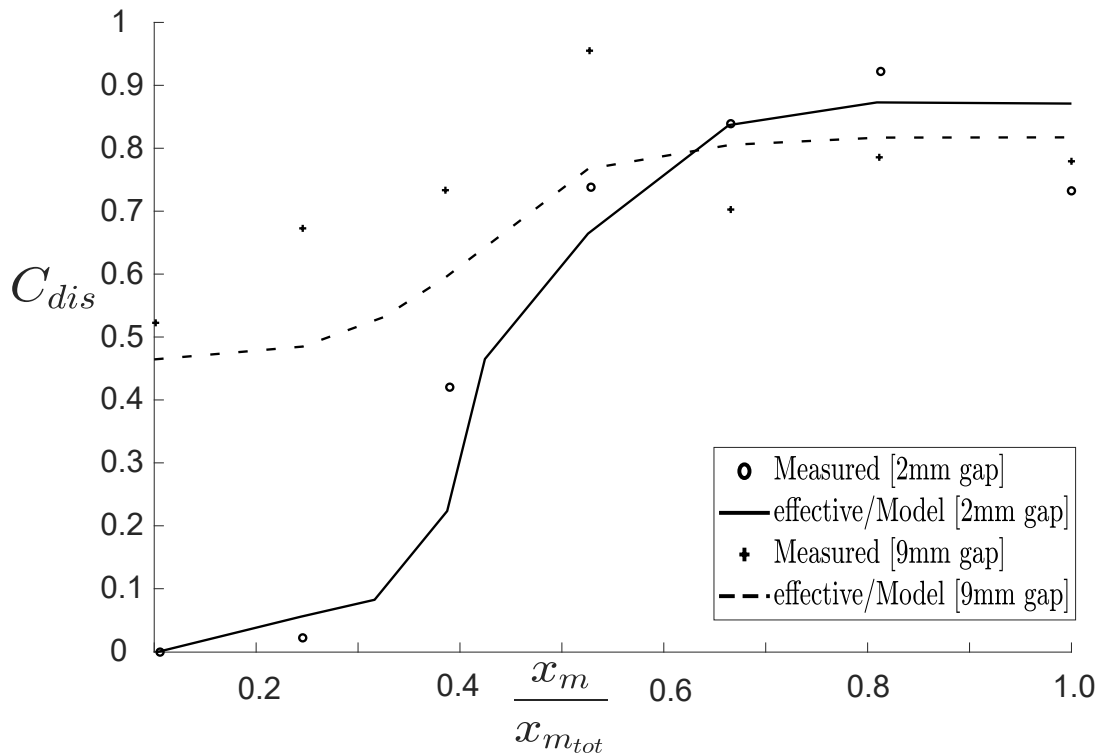


Fig. 3.11 Comparison of effective discharge coefficient with measured values from Dambach [23]

3.2 Numerical Method

The next section described the numerical technique used in this thesis. Included are details on the solver, meshing technique, boundary conditions and loss mechanism decoupling.

3.2.1 Choice of tool

As shown in section 1.5, design spaces were previously mapped out predominantly using loss correlations. This has inherent drawbacks as these loss correlations tend to only function reliably in regions of the design space and architectures for which they were designed. Hence the use of these models to extrapolate to the outer regions of the design space, or be used across architecture, is questionable. Introducing more physics into these correlations, say by building the model around a largely invariant empirical constant (e.g dissipation coefficient), can improve robustness. However, even then these models require limiting assumptions. The next logical step is to use a tool that is less dependent, or ideally independent of, the architecture or region of the design space in which it operates. Using numerical methods such as RANS, LES and DNS (which are built around fundamental conservation laws) captures more of the physics that is driving the shape of the design space and are not, by design, limited to specific regions of the design space. However, there will be greater uncertainty in the results for designs sitting at the extreme edges of the space (e.g very high turning). Between these tools there is a balance to be struck on fidelity versus computational cost. RANS methods typically under perform for (in part from Yacke and Tucker [53]):

- Transition and relaminarisation (does not resolve instabilities).
- Large scale separations in which strong mixing/shear occurs away from surfaces (e.g separation bubbles and free shear flows).

For example, RANS simulations will struggle to maintain accuracy for large multistage compressor calculations or turbines operating far off design. Eddy resolved methods such as DNS and well implemented LES, can address some of these issues, but with a significantly greater cost. That being said, flows where the Reynolds number is higher and where the boundary layer remains attached, RANS methods work well. This thesis focusses on turbine rotor calculations operating at, or close to, design. Therefore, to map out a design space by simulating a large number of turbines, a RANS method seems to be the most cost effective choice. In addition to this, LES is far more sensitive to the inlet boundary conditions which is highly specific to the applications and since design spaces are typically built to be used for multitude of application, LES would likely introduce further uncertainty.

In order for a RANS tool to function well it will need to qualitatively and quantitatively capture key flow features present in a turbine passage. One challenging source of loss to capture is the end wall loss. Figure 3.12 A from Denton et al.[25] compares the stagnation pressure loss pattern at different intervals along an axial turbine cascades. The calculation shown in this figure was achieved using a RANS solver known as TBLOCK which will be used for the work in this thesis.

The figure illustrates a good agreement between the numerical solution and experiment in the vicinity of the end wall. This shows the ability of TBLOCK to capture the behaviour of the

end wall flow. Furthermore, this agreement was maintained throughout the passage (including the core flow) which is reflected by the good agreement of the growth of stagnation pressure loss in figure 3.12 *B*. At the exit of the cascade, the numerical solution is within 2% of the measured values.

The authors went on to leverage the good agreement to successfully study the end wall loss generating mechanisms. There are many more experimentally validated uses of TBLOCK in the literature including, [40],[43],[47]. This illustrates the strength of this tool when applied to axial turbines.

While TBLOCK has mostly been applied to axial architectures, the solver has successfully been used to study the nature of loss mechanism in radial architectures as well. One strong example of this can be found in the work done by Cao et al. [9]. Here, the numerical method was again validated by experiment, the results of which can be seen in figure 3.13 *A*. A radial turbine characteristic was produced and shows the capability of TBLOCK to predict the radial turbine efficiency. At design the predicted normalised efficiency is within 1% of the measured values. It should be noted that there is a deviation when moving further off design (4.7%). This however will not be a significant issue for most of the turbines in this thesis as these will be operating at, or close to design, where the characteristic is mostly flat. It must also be noted that the radial turbine used in this study featured over tip leakage which will also be present in this thesis.

As mixed flow architectures are a less studied architecture, the author of this thesis was unable to find a validated test case using TBLOCK specifically. However, there are validated test cases using RANS, one of which is shown in figure 3.13 *B* and was taken from Padzillah [41]. The RANS calculation match the measurements reasonably well, but under predicts the efficiency for most of the characteristic. Padzillah attributed most of the uncertainty to the way in which the efficiency was calculated from the experiment.

As pointed out by Denton [27], the use of CFD comes with inherent limitations. It is therefore important to work within these limitations. The framework that this thesis is built around is instructed by two key conclusions taken from Denton's paper on the use of CFD for turbomachinery.

Firstly, "Perhaps the most important result of CFD is an improved ability for the user to understand the flow physics", in that the numerical results in this work will be used to tease out driving mechanisms for the shape of the design spaces.

Secondly, "it [CFD] must be used on a comparative basis rather than as an absolute predictor of performance". That is, in this thesis, importance will be placed on the changes in performance throughout the design spaces as opposed to being focused on the exact levels of machine performance.

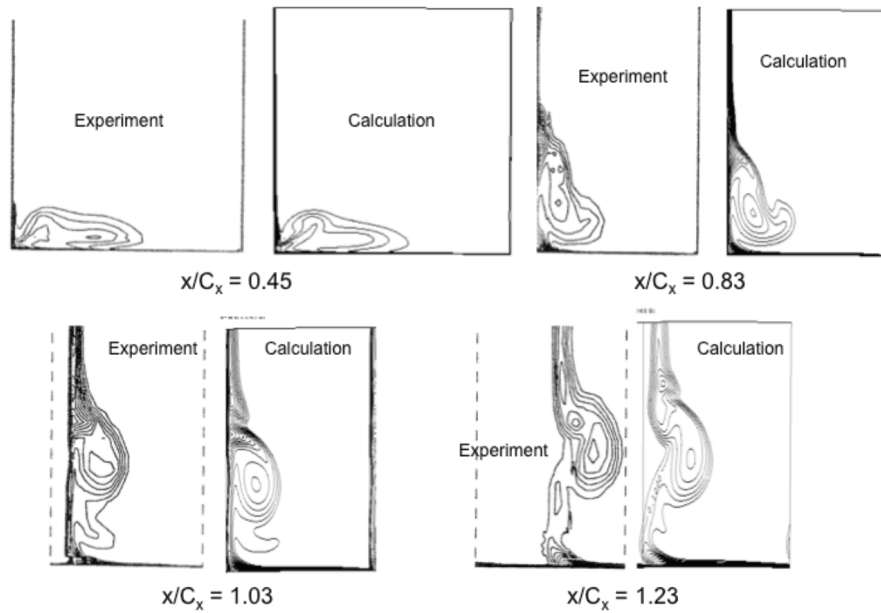
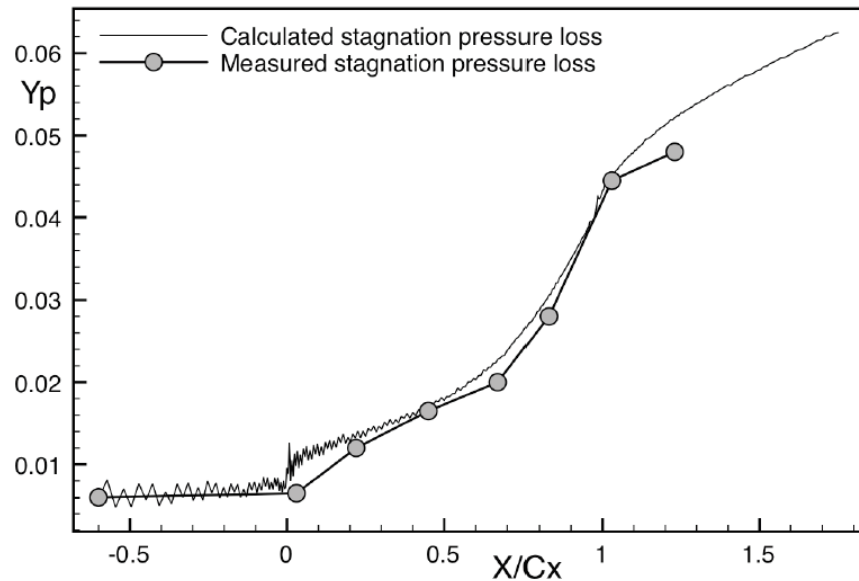
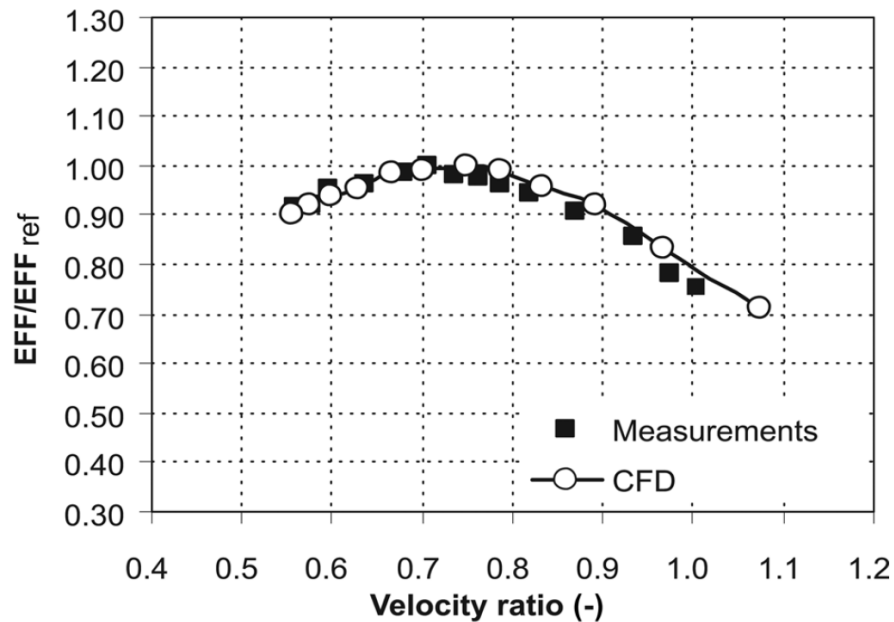
A**B**

Fig. 3.12 A: Comparison of contours of stagnation pressure loss coefficient, Contour interval 0.05 [25]. B: Growth of the stagnation pressure loss coefficient through the cascade [25]

Solver

TBLOCK is a multi block, finite volume flow solver developed by John Denton. The time stepping is an explicit Scree scheme [5]. The approach used allows for low levels of artificial

A



B

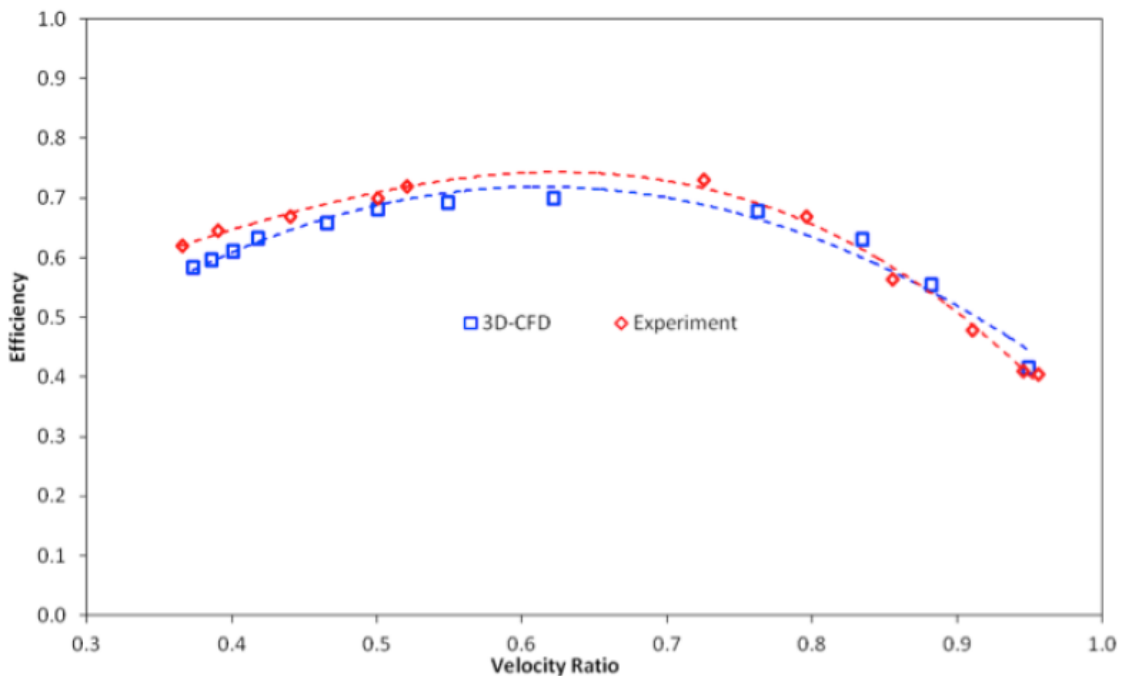


Fig. 3.13 A: Radial turbine steady state turbine efficiency vs velocity ratio [9]. B: Mixed flow turbine steady state turbine performance vs velocity ratio [41]

viscosity, the latter of which needed to suppress odd even decoupling. The mains reasons for using this solver are listed as follows:

- Designed primarily for turbo machinery (can be used for other components)

- Well established tool with numerous validated test cases
- Access to the source code. Source terms can be added such as body forces.
- Developed in-house and as such there is a base of experienced users.
- runs on CPUs (as opposed to GPUs), which was the available computational resource.

The turbulence model used was a simple mixing length model which was also used by Cao [9] and is shown to give good results. In this model a turbulent viscosity is calculated from a mixing length and the local velocity gradient (Equation 3.28). The mixing length L is calculated as the distance to the nearest wall. The near wall region is modelled using a logarithmic wall function. All settings relating to the turbulence model and log wall-function are kept consistent across the architectures and were set to the suggested values of the developer which have been used to validated test cases. The y_{plus} values were kept in the range of (30 to 70). There are some instances where the values exceeded this, some high loading mixed flow design at low duty flow were outside of the aforementioned range. The author does not consider this problematic as no designer would design in these regions of the design spaces.

$$\mu_{turb} = \rho (kL)^2 \frac{dv}{dn} \quad (3.28)$$

Mesh

The grid topology used was a H-mesh. The reasons for this choice are as follows:

- Examples of validated use, Denton et al.[25].
- Simple and robust construction.
- A H mesh tool is built into TBLOCK (manual control was taken over point distribution along blade surface)
- Good performance. While cell around the leading edge can become highly non-orthogonal, good solutions can be obtained with a fine enough mesh as shown by Denton and Dawes [28].
- Single passage block simplifies post processing.

The distribution of points in the j and k directions (Figure 3.14 A) was set by the in-build meshing tool. An expansion ratio of 1.1 was used for j and k directions. The total number of points used in the j and k directions was 90 for both.

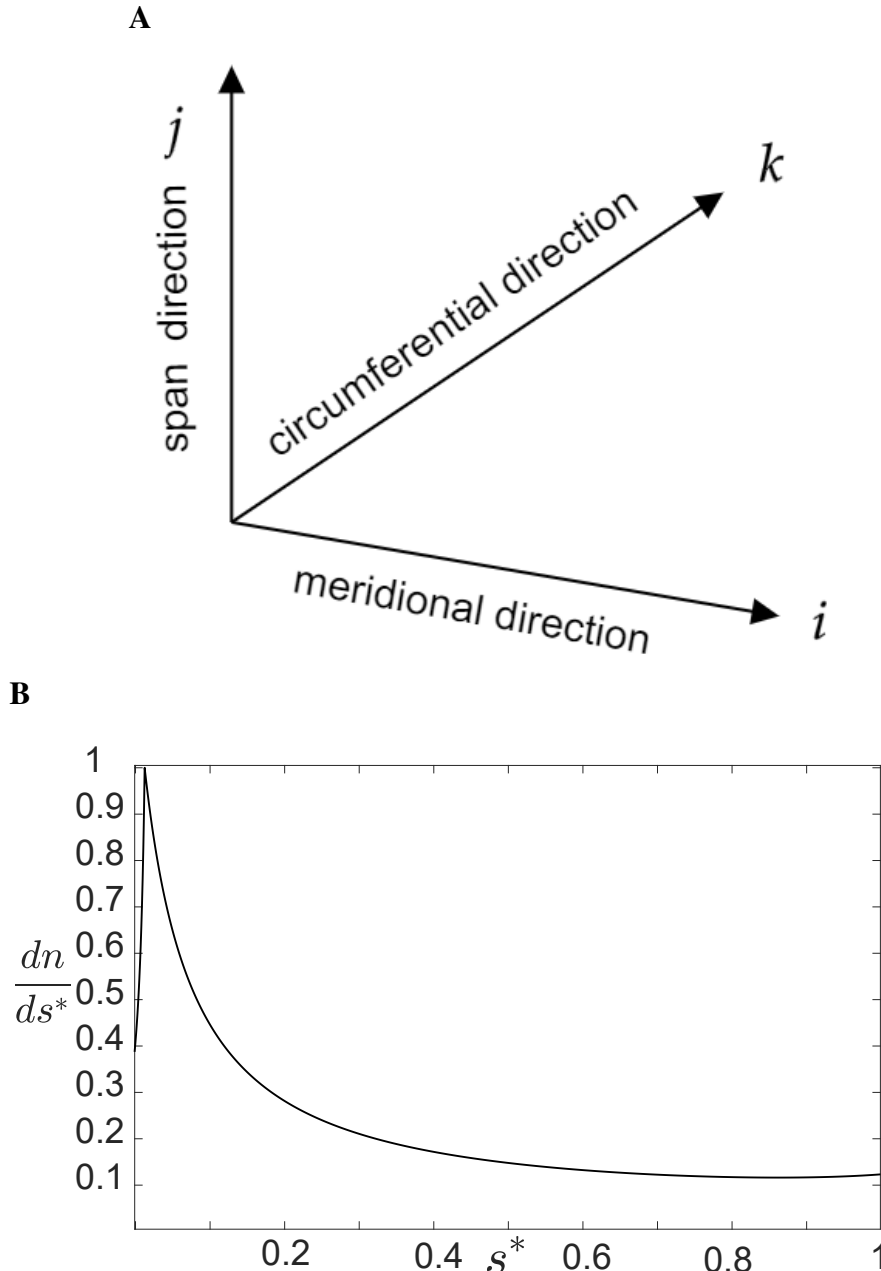


Fig. 3.14 A:Index directions. B: Variation of point density with surface coordinate

Direct control was taken over distribution and total number of points in the *i* direction. This was done to ensure a more robust grid across the architectures. To keep the leading edge well resolved (particularly for mixed and radial) the number of points on the blade surface were partially scaled with the surface length to leading edge ratio. This is represented by NI_{le} term in Equation 3.29. However, scaling purely by this ratio sometimes led to under resolving some axial geometries and so a constant term was added. NI_{le} and NI_{const} were selected such that the leading edges were well resolved. A preliminary mesh sensitivity study was used to inform the required mesh resolutions. The mesh resolutions from this study were increased significantly to

insure a robust set of meshes throughout the design spaces. The typical number of points on the blades surface for an axial radial and mixed are 130, 170 and 190 respectively. In some extreme cases, the number of points for mixed flow architectures could reach as high as 250 points; this occurred for designs with high turning and low radius ratio (long meridional passage lengths and unlikely to be used by designers). These designs have high endwall surface area and low efficiencies.

$$NI_b = fNI_{le} + (f - 1)NI_{const} \quad (3.29)$$

The point i distribution was set using a point density function (Equation 3.30) and an example is shown in Figure 3.14 *B*.

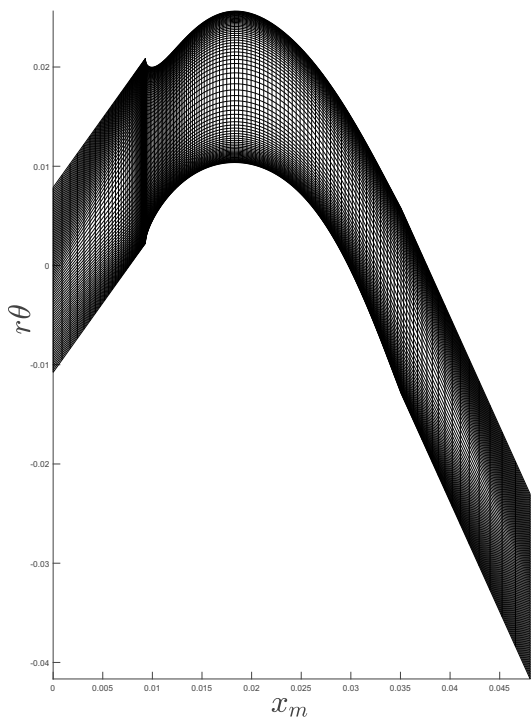
$$\frac{dn}{ds^*} = f_{le} \frac{dn}{ds^*} \Big|_{le} + f_{con} \frac{dn}{ds^*} \Big|_{const} + f_{te} \frac{dn}{ds^*} \Big|_{te} \quad (3.30)$$

$$\frac{dn}{ds^*} = \frac{-e^{-a} - 1}{a((-e^{-a} - 1)s^* + 1)} \quad (3.31)$$

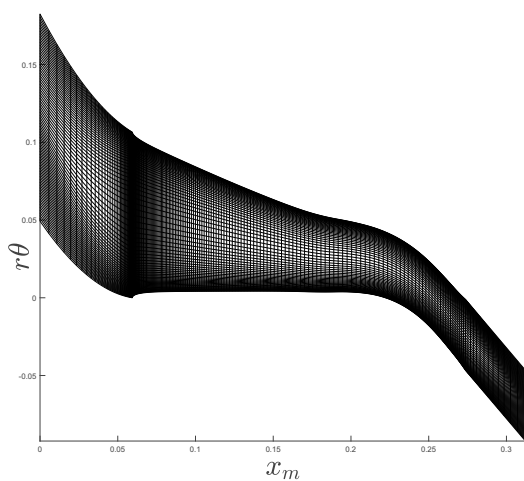
This function is a combination of leading edge and trailing edge expansion ratio function 3.31 and a constant term. Without the constant term, this approach would be very similar to that used by the Tblock. The constant point density term was introduced to improve the mesh for radial and mixed flow architectures which would sometimes be under resolved in the mid/late passage.

To calculate the point distribution, the point density function is integrated and sampled at regular values of n . As recommended by Denton [28], a unloaded cusp is applied at the trailing edge. This ensures that the flow leaves the blade smoothly and provides blockage. Three example girds are shown in Figure 3.15. Denton [27] used inviscid solutions to estimate spurious entropy production due to numerical error. The same was done for a wide selection of meshes used in this study. The result of which are tabulated in the following chapters but was found to be low. The effect on total to total efficiency was calculated to be $\Delta\eta = 0.08\%$ for axial, $\Delta\eta = 0.12\%$ for radial and $\Delta\eta = 0.13\%$ for mixed on average.

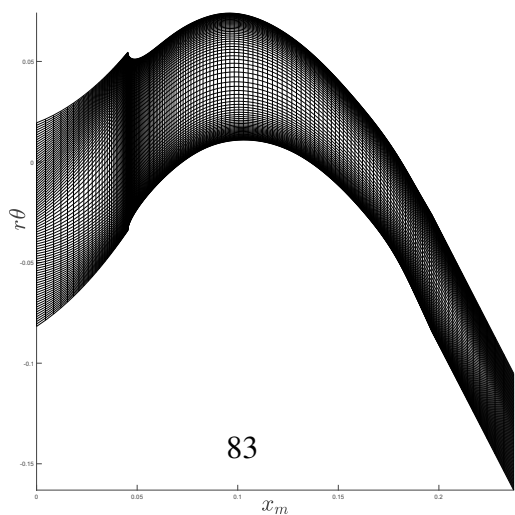
Axial



Radial



Mixed



83

Fig. 3.15 H mesh grids for various architectures.

Turbine duty and boundary conditions

The designs produced in this thesis are produced off of desired non-dimensional flow parameters, however a duty($\dot{m}, \Delta h_0, T_{01}, p_{01}$) also needs to be specified in order to completely specify the design. The duty for the turbines was initially set by referencing a test bench turbine in the Whittle lab, the Peregrine Low-Speed Turbine [31]. However, due to the low rotational Mach number of this turbine, the density-based flow solver took too long to converge. The power was then increased, raising the rotational Mach number which improved the speed of convergence. Note that by fixing the mass flow and power, the different values for of duty flow and loading coefficient are achieved by varying the radius and blade speed.

The author of this thesis found it more realistic to fix viscosity and the thermodynamic constants, therefore the rotational Reynolds and Mach numbers vary through the space with the changes in rotational speed and diameter. Alternatively, the rotational Mach and Reynolds number could be fixed however the cord based Mach number would still vary and vice versa. While the rotational and cord based Mach and Reynolds numbers vary throughout the design spaces, both are kept within ranges where the sensitivity to these parameters are reasonably low. All the relevant values are shown in table 3.1.

Rotors are the primary focus of study in this thesis, as these components are the key distinguishing component. It is in the rotor that differing mechanism of work extraction occurs(e.g centrifugal relative or absolute acceleration). Stators were not modelled in this thesis for three primary reasons: firstly to reduce the size of the problem, as this choice reduces the computational resource or time required. Secondly removing the stator reduces complexity and effort during the design process. Finally, to improve consistency, the different architectures use different up stream topologies to generate the angular momentum that will be extracted by the rotor. Radial turbines use volutes with or without stators and where axial architectures tend only to use stators. Therefore removing the upstream component facilitates the comparison of the rotors.

As for the inlet boundary condition, a simple flat plate turbulent boundary layer profile was used, where the displacement thickness scaled with the span. This was done as a stagnation pressure profile. In addition to this, the inlet turbulent intensity was set to zero.

Loss decoupling

In order to form maps of the loss variations across the design space, the mechanisms need to be decoupled. The profile/secondary loss decoupling for axial turbine cascades is typically done by using design with high aspect ratio ($AR \Rightarrow 3$), with little to no variation in blade metal angle up the span. Unfortunately, this does not work for radial and mixed flow turbines or highly 3D axial (low hub to tip) turbines due to the inherently three dimensional nature of the flow. Instead,

Table 3.1 turbines duty and boundary conditions

Parameter	Value
\dot{m}	6 kg/s
$power$	70 kw
T_{01}	288 k
p_{01}	101325
RE_{rot}	$10^6 - 10^7$
M_{rot}	0.15 – 0.33
$\frac{\delta^*}{h}$	2×0.02
$\frac{t}{h}$	0.01

the author opted to switch inviscid endwalls on and off as well as remove the inlet stagnation pressure profile.

To calculate the efficiency loss due to tip clearance the tip gap was opened (1%) and partially closed (0.1%). The partial closure was to help avoid corner separation while not producing significant amounts of loss due to leakage. Using values smaller than 0.1% t/h sometimes resulted in negative tip leakage losses.

All lost efficiencies due to loss mechanisms are calculated using mixed out flow (constant area) a short distance (20 % cord) down stream.

The overall loss decoupling calculation procedure is as follows:

- A case is run with inviscid end walls and the tip gap is completely closed. From this the lost efficiency due to the profile is then calculated.
- Then a second case is run with viscous end wall and partially closed tip gap (0.1%). The small tip gap was used in an attempt to suppress potential corner separation. The difference between this case and the first then represents the secondary loss.
- Then a case is run where the tip gap is opened (1%) and with viscous end walls. This is then used for the overall efficiency. The difference between this case and the second case represents the leakage loss.

In reality, loss mechanism are not simply additive and are likely to interact. Therefore this approach will have limitation in the ability to decouple these losses. Later it will be shown that in some cases the tip leakage might be beneficially interacting with endwall loss.

Uncertainty across the design parameter space

The author of this thesis wishes to first make it clear that distributions of loss throughout the design space are not presented in this thesis as perfectly reflecting reality. Instead, like

Rohlik [46] and Balje [4], the results are presented as coming from the tool being used. Due to the vast nature of design parameter spaces, previous work contains little information on the uncertainties of the charts produced. Balje, being the only author to directly discuss uncertainty, focusses primarily on the peak values of efficiency, stating that at peak efficiency there is a 8 % variability in performance due to the spread in the underlying experimental data used to form the correlations (much of which came from cascade data).

While it has been shown that RANS methods can achieve good agreement with experimental measurements (particularly for cascades), it is generally accepted that these methods struggle to accurately capture the correct levels of entropy production for the individual loss mechanism.

It is important to understand the limitations of the tool used to properly contextualise the proceeding results chapters. This will aid the reader in understanding the likely uncertainty variations throughout the design parameter space as fully quantifying this uncertainty is currently unfeasible.

Profile loss

The 2D loss in axial turbines is generally taken as the loss measured away from the influence of the endwalls. This is typically calculated by measuring the loss at mid span of high aspect and hub to tip ratio axial turbines. Due to the three dimensionality of radial, mixed flow turbines and low hub to tip ratio axial turbines, the 2D loss cannot be used. Instead a profile loss is calculated by closing the tip gap and setting the end walls to be inviscid. This is then used to calculate the (mixed out) loss generated on the blade surfaces and downstream of the blade. The profile loss consists of dissipation due to the profile boundary layer, the trailing edge loss and mixing out of the wake.

As previously discussed, the state of the boundary layer significantly determines the level of dissipation that occurs in it. Denton and Miller [29] state that for low Reynolds number ($Re_c < 10^5$) the boundary layer is unlikely to be turbulent and for higher Reynolds numbers ($Re_c > 10^6$) that the boundary layer is unlikely to be laminar. In many applications the boundary layer can be transitional and therefore problematic to model using RANS (even when coupled with transition models), particularly as the boundary layer may become sensitive to unsteady effects, see Coull [21].

All turbines in the proceeding charts are above $Re_c = 10^6$ and are therefore, likely to be turbulent. That being said this is a rough rule of thumb and the state of the boundary layer even at high Reynolds numbers depend on a multitude of factors, such as the surface roughness, upstream turbulence levels, unsteadiness and so on. If say the over acceleration on the suction surface is particularly high, transition can be significantly delayed even at these high Reynolds numbers or if already turbulent, the flow could possibly even relaminarise. Later it will be shown that the diffusion factors vary across the charts. This will introduce further uncertainty where these factors are high. In addition to this, flow concavity/convexity can have a significant

effect on turbulence production in a boundary layer. A highly convex suction surface (due to large amounts of turning) can suppress turbulent production. This behaviour is not captured by simple turbulence models and constitutes a uncertainty that would grow with blade turning. The subsequent diffusion of the over accelerated flow will introduce further uncertainty. CFD is notoriously weak at predicting the location of flow separation or worse so, whether this separation remains open or closed(reattaches). This significantly influences the amount of profile loss and constitutes a large uncertainty at higher diffusion factors which can be found at higher local flow coefficients where $\frac{W_1}{W_2}$ is high, particularly for axial architectures in this thesis.

In addition, designers /readers concerned with lower Reynolds number should be wary of designs with lower duty flow coefficients. When considering designs with fixed mass flow, decreasing duty flow will typically result in lower blade Reynolds number, particularly for axial turbines. If these Reynolds numbers dip into the aforementioned regimes uncertainty will increase.

Later it will be shown that the profile loss variations across the charts are largely driven by changes in area and velocity. The RANS calculation should predict these variations reasonably well and therefore any uncertainty associated with changes in area or surface velocity would be low. However these changes will serve to scale uncertainty in surface dissipation loss due slight errors in the local dissipation coefficient. In other words, the shape /pattern of the changes across the design parameters spaces should be well captured but the levels are likely to diverge for blades with high surface area and high surface velocity. Essentially, as the surface dissipation loss increase so too does the uncertainty in the levels of that loss. Later, it will be shown that turbines with low local flow coefficient and high loading coefficient have characteristically high flow turning and low pitch, the latter due to the constant circulation coefficient. Therefore, blades in this region of the design parameter space will have characteristically high profile surface area. It will also be shown that high surface velocity is characteristic of high flow coefficient and low loading and that both area and velocity increase with both loading and flow coefficient. Therefore designers/readers should be wary of increasing uncertainty when considering designs in these regions of the charts.

Mixing length models typically work well for self-similar shear flows with well known mixing lengths, if the boundary layer has separated the assumptions used in the model will break down (incorrect mixing lengths, anisotropic turbulence). Therefore any loss generated in the separated regions will be inaccurate. While most turbine in this thesis have fully attached profile boundary layers some radial architectures with high incidence or meridional curvature experience flow separation and hence the uncertainty in these regions of the design space will be poor. Therefore designers/readers should be wary of radial blades with high loading coefficients which due to the radial blade fibred constraint incur high incidence and radial blades with high duty flow coefficients which results in low casing radius of curvature.

The unsteady vortex shedding at the trailing edge sets up a low base pressure which ultimately leads to additional entropy production. Steady simulations cannot capture this phenomena and using a fine grid around this region can even lead to negative loading due to the flow not separating from the trailing edge early enough. The latter was remedied by use of a cusp. Unfortunately, it is unlikely that a cusp will give the correct base pressure and therefore the correct trailing edge loss. Denton [26] estimates this contributes about 0.0075 to the loss coefficient for a typical axial turbine. The effect of this was partially mitigated by having relatively thin trailing edges. A designer could use Denton's [26] model shown in equation 1.13 to correct for larger trailing edges using a known base pressure coefficient. Additionally, equation 1.13, shows that the trailing edge loss is scaled by the relative trailing edge blockage $\frac{t}{p \cos \beta_2}$. Therefore any uncertainty in trailing edge loss relating to the base pressure coefficient will scale up where the blade angle is high and the pitch is low. This typically occurs at low flow and high loading coefficients.

End wall loss

As previously discussed, the endwall loss stems roughly from two sources, a loss associated with the endwall boundary layer and a loss associated with the mixing out of secondary kinetic energy. However, these are heavily interlinked.

The boundary layers on the endwalls can be complex in nature, making it challenging to model correctly using RANS and turbulence models. The skewness caused by the change to the relative frame (in a rotor) can cause some anisotropy in turbulence, which a turbulent viscosity model cannot capture. In the rotor, there exists a lift off line associated with the pressure surface leg of the horse shoe vortex, after which a new laminar boundary layer is formed and the preceding inlet boundary layer is swept up into the secondary flow structure and is transported to the exit plane. The RANS calculations used here are fully turbulent and will not resolve the newly formed laminar boundary layer. However, due to the high Reynolds number of this study, it is likely that this boundary layer will quickly transition.

If one were to now imagine that all this complexity results in incorrect values of the local dissipation coefficient (which is a gross simplification), the uncertainty in the endwall surface dissipation will (like profile), scale with surface area and velocity. Low duty flow radial design in this thesis exhibit large amounts of end wall surface area and all architectures show increasing end wall surface velocity at high local flow coefficient, it is in these regions that a designer /reader should be wary of the results.

There also exists an additional loss associated with the mixing out of the inlet boundary layer that has now been swept up into the secondary flow structure. As this mixing is occurring away from the surfaces, it is unlikely to be correctly captured by a mixing length turbulence model. That being said, Denton and Pullan [25] point out only the inlet boundary layer loss and

mixing loss are significantly affected by boundary layer thickness as it has been swept up. Note that this was for a collateral boundary layer.

The secondary flow loss associated with secondary kinetic energy is set by the amount of stream wise vorticity at the exit of the turbine, which in turn arises from the turning and stretching of vortex filaments present at the inlet. This process is largely inviscid and hence will be captured well by RANS calculations. However, how much of this secondary kinetic energy should be treated as a loss is still unclear. The work in this thesis errs on the conservative side and mixes out all none uniformities at the exit. The inlet conditions have a significant effect on secondary flow loss and is most likely the largest source of modelling uncertainty of endwall loss. The amount of secondary kinetic energy present at the exit of the turbine is strongly influenced by the magnitude and distribution of inlet vorticity which is a function of the boundary layer velocity profile, skewness and thickness. Denton [26] pointed out that skewness present in axial turbine inlet boundary layers largely increased secondary flow loss. Coull and Clark's [16] work involving turbine cascades, concluded that larger inlet boundary layers result in more dispersed secondary flow with larger amounts of secondary kinetic energy. On top of this, the authors showed that the sensitivity to boundary layer thickness was dependent on the blade geometry, stating that higher vortex amplification factor designs exhibited higher sensitivity. The implications of this is that blades with higher flow turning and larger difference in transit time which are characteristically towards the boundaries of the design parameter space (particularly at higher loading) will exhibit greater uncertainty in the secondary flow loss relating to inlet conditions.

The inlet conditions of a real machine are difficult to predict or even measure, and are influenced by a multitude of factors such as upstream components, manufacturing tolerances, operating conditions and so on. Considering the variety in architecture and design parameters, including these effects is unfeasible. Instead, the author chose to simplify the inlet conditions. While this will not remove the uncertainty it will help with consistency.

Later, it will be shown the radial and mixed flow architecture at low duty flow coefficients have characteristically low meridional aspect ratios. In these regions of the Balje chart the secondary flow combines and encompass the entire passage, somewhat analogous to fully developed pipe flow but with the loss shifted towards the suction surface. The high interaction of the endwall and profile flow make the decoupling and use of a mixing length model questionable at best. That being said, this region of the design space is dominated by endwall surface dissipation (velocity cubed rule) the behaviour of which should be capture reasonably well by the CFD. None the less, the author is still less confident of the results in this region of the design space.

Tip leakage loss

Denton [27] regarded RANS tip leakage modelling as very imprecise, arguing that because of the lower Reynolds numbers of the tip gap region and the acceleration of flow into the gap, that the flow is likely transitional and therefore the application of turbulence models in this region is questionable. Of all the methods of modelling the tip gap, Denton deemed the gridded tip (as opposed to a pinch or periodic tip) to be the most realistic and is therefore used in this thesis.

The lost efficiency due to over tip leakage is a result of the large entropy rise in the leakage flowing through the tip gap and also from this leakage fluid mixing with the fluid from the next passage. Denton [26] himself, regarded his model of tip leakage loss as simple, however this model is useful in helping understand potential drivers of uncertainty across the design space (see equations 3.23 and 3.24).

It is generally accepted that the loss is proportional to the mass flow of the leakage which is governed by the area of the contracted (vena contracta) leakage flow and driving pressure. Changes to the leakage mass flow driven by variations in driving pressure and total gap area ($t \times ds$) should be captured well by CFD. However reproducing the correct contracted jet size (of which C_{dis} is a function) is challenging as it is likely dependent on resolving the correct mixing scales in this region. Assuming for now that most of the uncertainty therefore lies in the discharge coefficient, Denton's model shows that the uncertainty in the levels of loss likely scales with area, driving pressure and suction surface velocity. Later, it will be shown that turbines at higher loading coefficients and lower local flow coefficients have increased blade surface lengths and counts and thus high surface area. It will also be shown that the suction surface velocity and driving pressure increase at high local flow coefficient.

Dambach [23] showed experimentally that the relative casing motion has a significant effect on leakage flow in radial turbines and is therefore important to capture. In their work on the effects of boundary conditions on leakage flow in axial turbines, Coull and Atkins [19] showed that RANS calculations can capture the effects that relative casing motion has on leakage flow. This was also observed in this thesis. The authors conclude that, on their own, realistic inlet boundary conditions or relative casing motion has only a small effect on leakage flows, but when applied together, the leakage flow will change significantly. This further highlights the uncertainty pertaining to inlet flow conditions.

It is widely accepted that there is significant interaction between the tip leakage flow and the secondary flow at the casing. In some cases, a small amount of tip leakage flow can be beneficial to performance. This interaction will add significant uncertainty in decoupling tip leakage loss. This is likely to occur where both the secondary flow and leakage are high. This typically corresponds to high turning blades which is characteristic of designs with high loading and low local flow coefficients.

To summarise, RANS based solvers have a number of significant limitation affecting the resulting solutions. These limitations stem from the imperfect modelling of the loss driving

mechanism. This results in varying uncertainty across the design space. As the uncertainty is mostly tied to the variations in the loss mechanisms, regions of the design space with high loss due to a specific mechanism will also have high uncertainty as a result. In some sense this can be seen as a positive, as designers would naturally steer clear of these regions.

Chapter 4

Axial Turbine Design Space

4.1 Chapter Objectives

The following chapter explores both Smith and Balje axial design spaces (rotor only), mapped out using RANS. The key objectives of this chapter are as follows:

- To show that the general shapes of the design spaces can largely be explained in terms of surface dissipation, and to then break this down into the individual contribution of area and surface velocity cubed.
- To explore the effects design parameters have on performance and to show how these parameters shift the work split between the components of loading shown in Equation 2.3 (Section 2.1).
- To understand how (according to RANS) the individual loss mechanism shape the design space and, where possible, understand what drives the shape of the loss distributions.
- To compare the individual loss mechanisms with simplified models from Chapter 3 that were derived with physical interpretation of the flow.

Together this will build a deeper understanding of the design space in which engineers operate, allowing for more informed decisions during the preliminary stages of design. As a reminder to the reader, the outcome and discussion of the results in the following chapter should be taken in the context of the framework used to build these design spaces. The loss correlations used by Balje [4] and Rohlik [46] came with inherent limitations and so does the RANS methods used in this thesis, (see section 3.2.1).

4.2 Axial Total-Total Smith Chart

In order to form a Balje diagram based off a duty flow coefficient, it is important to pick the correct local flow coefficient for a given loading and duty flow coefficient. Therefore, before moving onto Balje diagrams, it is crucial to first build an understanding of a Smith chart where local flow and loading coefficient are varied.

Smith charts are constructed by varying both ψ and ϕ_L while keeping other parameters constant or optimised. Smith [51] produced a chart for 50% reaction axial turbines and kept the hub to tip ratio constant, which is equivalent to keeping $\frac{A}{r_m^2}$ constant. This results in a similar meridional geometry across the space when paired with a constant aspect ratio. The work presented below is a computationally constructed rotor only Smith chart. The following non-dimensional parameters were kept constant:

Table 4.1 Axial Smith chart parameters

Parameter	Value
$\frac{A}{r_m^2}$	0.59
AR	2
R_{ym}	1
$\frac{TE}{C_x}$	0.025
$\alpha_2(\text{mean})$	$0 \pm 3\text{deg}$
$C_o(\text{mean})$	$0.7 \pm 4\%$
$\Delta\eta_{ne}$	$0.08\% \pm 0.025\%$

The chart presented here will differ from that produced by Smith as here the reaction is not fixed. Instead, the design exit swirl is fixed to zero. This allows the data to be used for both total to total and total static designs.

The solid black contours in Figure 4.1 A, is the total to total isentropic efficiency calculated from the mass averaged stagnation pressure ratio. The dashed blue contours are of an equivalent total to total isentropic efficiency calculated using surface dissipation as found in Denton [26] and discussed in 1.3. It must be noted that $C_d = 0.002$ is assumed to be constant throughout the design space and that the same value is used for all surfaces, i.e the C_d value for the profile is the same value used for the end walls. Isentropic surface velocities were used as the velocity at the edge of the boundary layer.

Figure 4.1 A, illustrates that surface dissipation, by and large, describes the shape of the design space. Both sets of contours have a similar topology that exhibits an oval like pattern with an optima laying close to each other. Both sets of contours have sharper drops in efficiency when moving from the optima to lower flow coefficients than when moving from the optima to higher flow coefficients, where the changes are more gradual.

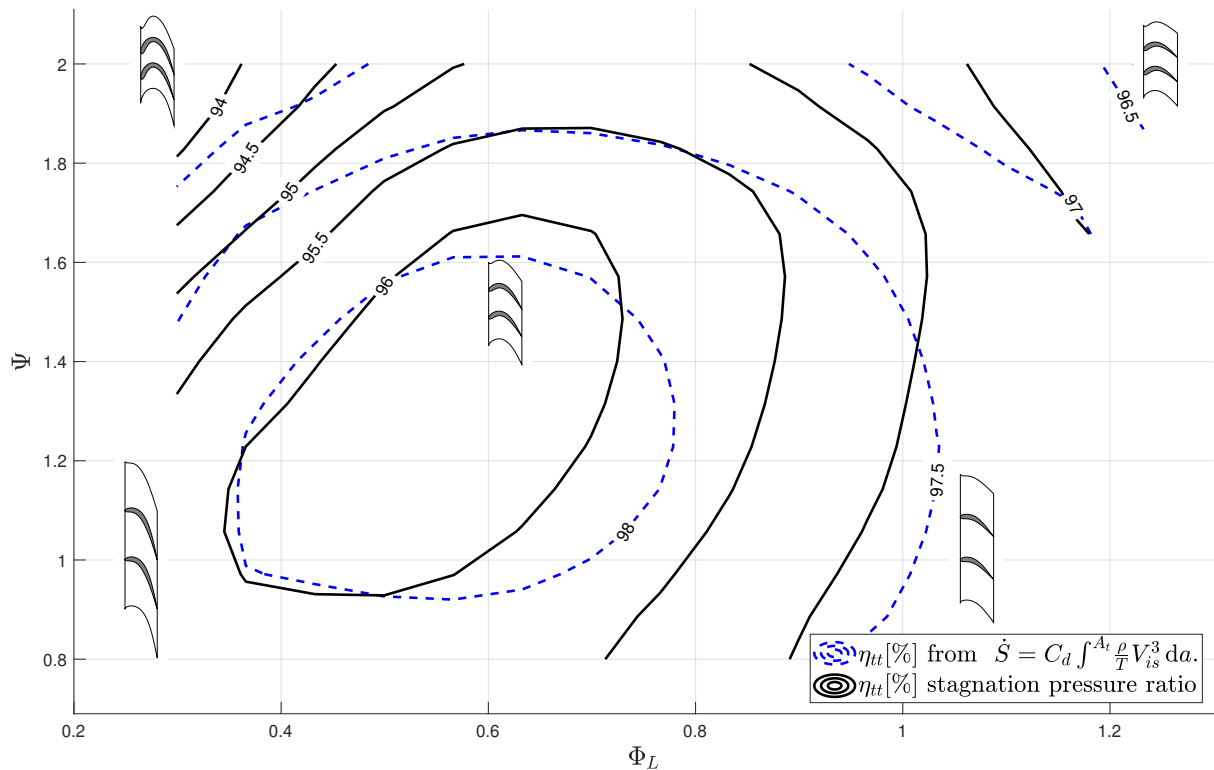
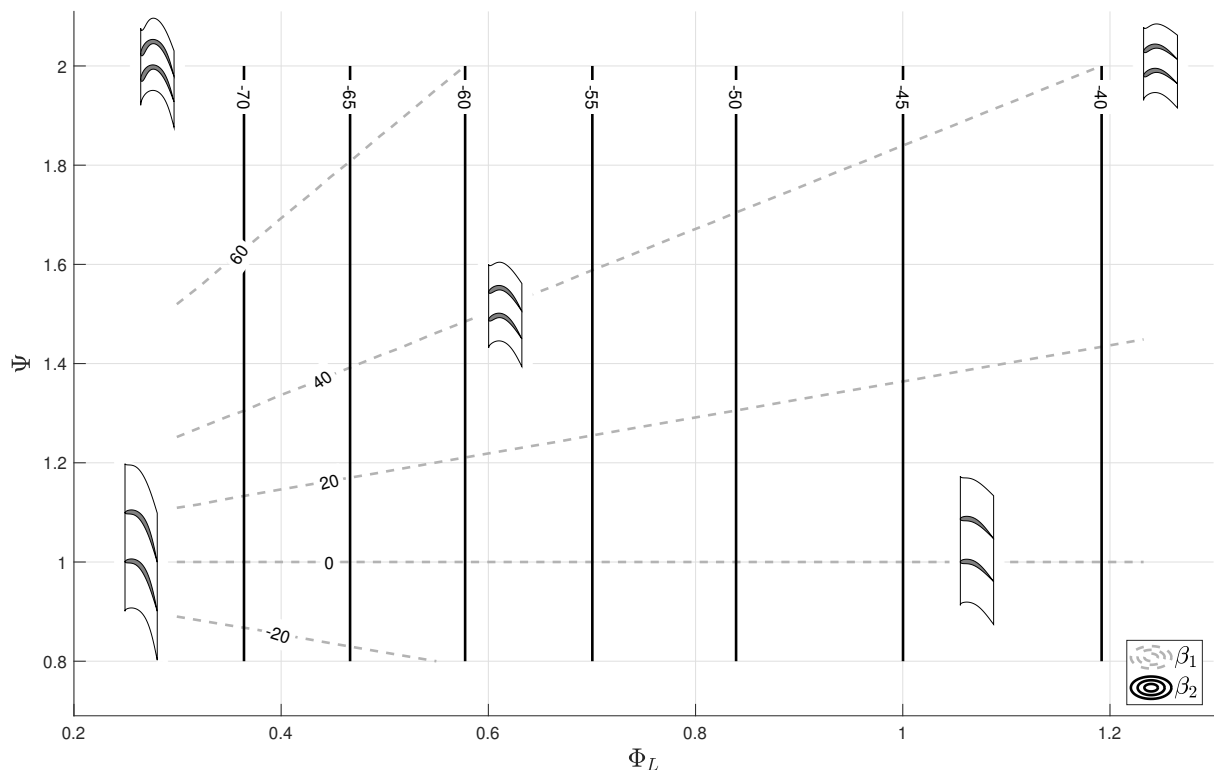
A**B**

Fig. 4.1 A: Total-total Smith chart with fixed $\frac{A}{r_m^2}$. B: Inlet and exit meanline relative flow angles.

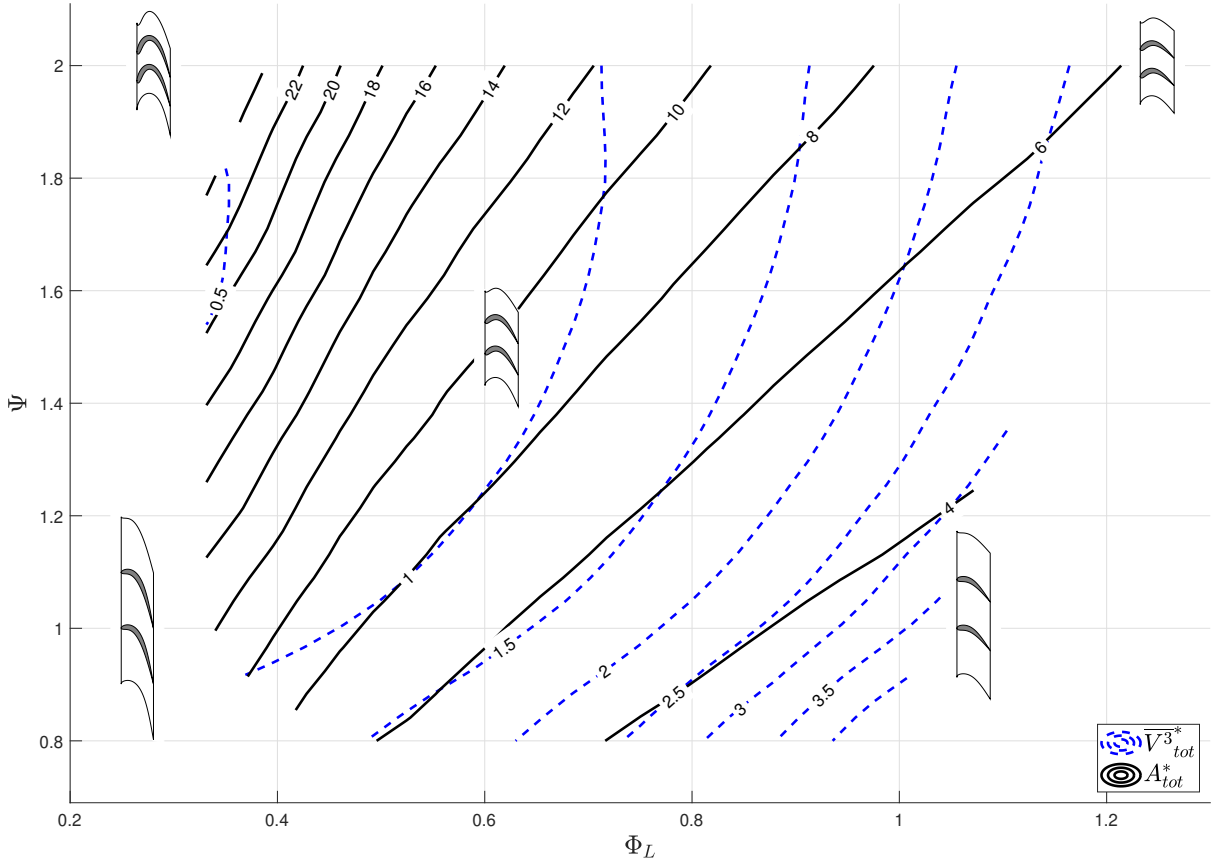


Fig. 4.2 Contours of blade profile surface area and surface-area averaged cubic velocity.

However, there are understandably some key differences in the shape and values of these contours. Firstly, there is a difference in the peak efficiency of 2%. Secondly, the changes in performance when moving away from the optima are lower for surface dissipation calculation. Finally, the surface dissipation is less sensitive to increasing flow coefficient.

The surface dissipation calculation obviously does not include the effects of tip leakage and secondary flow, which will contribute to the difference in the contours. It will later be shown that the secondary flow plays a large roll at higher loadings and lower local flow coefficients. Furthermore, it will be shown that leakage flow effects designs at lower loading and higher local flow coefficients.

The boundary layers in this thesis are modelled as fully turbulent and as previously discussed, at lower Reynolds numbers or in some cases even at higher Reynolds numbers, the flow can be transitional. Under these conditions the C_d value might vary considerably through the design space. That being said, Figure 4.1 shows that a surface dissipation (velocity cubed rule) is a powerful tool for preliminary design as it can get designers into the correct ball park when picking flow parameters. It was this observation that inspired the further development of the low order model in Section 3.1.1.

Since surface dissipation scales with $\overline{W^3}A_{tot}$, the analysis can be taken one step further and be used to show how the shape of the design space is driven by the surface area averaged velocity cubed $\overline{W^3}$ and total surface area A_{tot} . These two terms are non-dimensionalised with volume flow rate and change in specific enthalpy (Section 1.3).

The variations across the design space are shown in Figure 4.2. Surface dissipation in the top right corner is driven largely by high surface area. This is due to a combination of the high individual blade surface area and high blade count. Both are a result of increased flow turning, which is illustrated in Figure 4.1 B.

The variation in dissipation when moving to the bottom right of this design space is driven by increasing surface velocity. The shape of the contours can be explained using Equation 4.1 (derived from velocity triangles and Euler equations), which shows the changes in the average of the inlet and exit velocities squared as a function of loading and local flow coefficients, amongst other parameters.

$$\frac{W_1^2 + W_2^2}{2U^2} = \frac{1}{2}((\psi - 1)^2 + \phi_L^2(1 + R_{vm})) \quad (4.1)$$

From Equation 4.1, it is clear that the average velocity through the passage increases with local flow and loading coefficient. This only illustrates the variation in average velocity across the Smith chart. The difference in velocity between the suction and pressure surfaces have yet to be described. This can be illustrated using an idealised thin blade with rectangular velocity distribution.

It can easily be shown that $\overline{\Delta W} = C_o W_2$, where $\overline{\Delta W}$ is the velocity difference between the suction and pressure surface. Since the design circulation coefficient is remaining constant, ΔW increases with W_2 , which increases with the local flow coefficient, further increasing surface velocity.

Figure 4.3 shows velocity distribution in four corners of the design space. The high loading low flow coefficient design illustrates a limitation in the design methodology used. The velocity distribution exhibits two suction surface maxima in velocity. This is due to the symmetric and thin thickness distribution. From Figure 4.1 B, blades in the upper left corner have large amounts of turning. This results in highly concave pressure surfaces. Due to the low pitch to cord ratio of these designs, the pressure surface pressure field depresses the suction surface pressure field. When shifting to lower overall turning, by either decreasing loading or increasing flow coefficient, the depression is removed. This could be remedied in future by filling in the pressure surface.

A consequence of using a fixed circulation coefficient throughout the design space is that turbines with high flow coefficient have higher diffusion factors. This can be explained using Equation 4.2, which was derived from a model rectangular velocity distribution.

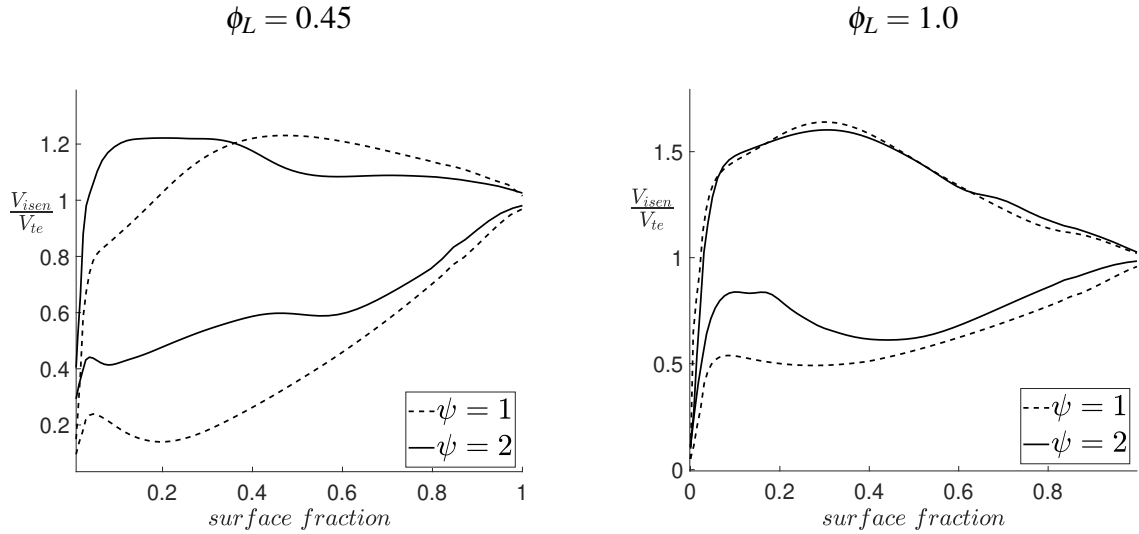


Fig. 4.3 Sample of smith chart velocity profiles.

$$DF_i = \frac{1}{2}C_o + \frac{1}{2}\left(\frac{\cos\beta_2}{\cos\beta_1} + 1\right) - 1 = \frac{1}{2}C_o + \frac{1}{2}\left(\frac{W_1}{W_2}\right) - \frac{1}{2} \quad (4.2)$$

Equation 4.2 shows that the level of diffusion is set by two terms: the circulation coefficient (which is kept roughly constant) and the inlet and exit flow angles /velocity ratio. The effects of the latter term can be explained as follows.

Increases in the local flow coefficient result in a reduction in the exit blade angle and inlet angle varies less with local flow coefficient, particularly at lower loading coefficients. This increases the second term on the right hand side of Equation 4.2 and with it the diffusion factor. In other words, the inlet velocity is increasing relative to the exit velocity. This is reflected in the velocity profiles, where the left hand side is lifted up for designs with higher flow coefficients. This raises the peak velocity and therefore the required diffusion. The increasing diffusion will ultimately lead to flow separation on the suction surface. RANS calculations will likely struggle to accurately predict the location and nature (open /closed) of the separation. This additional uncertainty could be removed in future, by designing axial architectures with constant diffusion factors across the design space.

As previously discussed, design parameters can shift the work split amongst the various terms. The direction in which the local flow coefficient shifts work(for zero exit swirl) depends on the value meridional velocity ratio. Equation 4.3 shows that for $R_{vm} > 1$, increasing the local flow coefficient shifts loading from the absolute kinetic energy term to the relative acceleration term and vice-versa. Incidentally, changes in local flow coefficient does not shift loading between terms if the meridional, (axial) velocity ratio is set to one.

Changes in the loading coefficient of a turbine not only increases the work, but also shifts loading between the various components of work. Equation 4.3 shows that increasing the loading coefficient shifts loading from the relative acceleration term to the change in absolute kinetic energy term.

$$\psi_{rac} + \psi_{ke} = \frac{1}{2} [1 + \phi_L^2 (R_{vm}^2 - 1) - (\psi - 1)^2] + \frac{1}{2} [\phi_L^2 (1 - R_{vm}^2) + \psi^2] \quad (4.3)$$

Note the above equation is only valid for zero exit swirl and radius ratio set to unity.

4.2.1 Profile loss

Until this point, there has been no mention of loss mechanisms in detail. The following subsections explore each mechanism and their contribution to the shape of the design space. Figure 4.4 shows the variation of profile loss from the numerical solution (black) and the model (blue) developed in Section 3.1.1. The shape of these contours can largely be explained by the variations in surface area and surface velocity. While Figure 4.2 represents all surfaces, the shape is largely driven by the profile and hence can be used to explain the nature of the profile loss. In the top right corner of the Smith chart, the profile loss is driven up by increasing profile surface area and in the bottom left is driven up by increasing profile surface velocity both of which were explained in the previous section.

The model shows a lower sensitivity to increasing local flow coefficient but capture this general behaviour quite well. This highlights the strength of the velocity cubed approach when comparing to these numerical solutions. As previously discussed the RANS calculations exhibit many limitation relating to the state of the boundary layer. Therefore the models results will not translate well to the real turbines under all conditions. The profile loss model presented here, is developed with a goal of developing consistent model that can be used across multiple architectures and as such is simplistic in nature. In the literature there exist more detailed empirical/semi-empirical profile loss models targeted for more specific applications and Reynolds number. These models will show higher accuracy when used in scenarios for which they were designed. One strong example of this for axial low pressure turbines is that of Coull [17].

At such small variations in loss, effects of numerical errors could influence the results. To test for this, a sample set was taken and run without the viscous terms. Efficiencies were calculated from the inlet up until the beginning of the cusp and downstream of the cusp. The results showed that the largest change in the numerical error up until the cusp was less than 0.005%. This shows that the numerical error produced at the leading edge and over the blade surface did not significantly influence the results. However, the loss in efficiency produced by the cusp increased about by 0.15% (Appendix B.1). This would partially explain the difference.

The trailing edge loss model uses a constant base pressure coefficient; in reality, this is likely to vary across the design space.

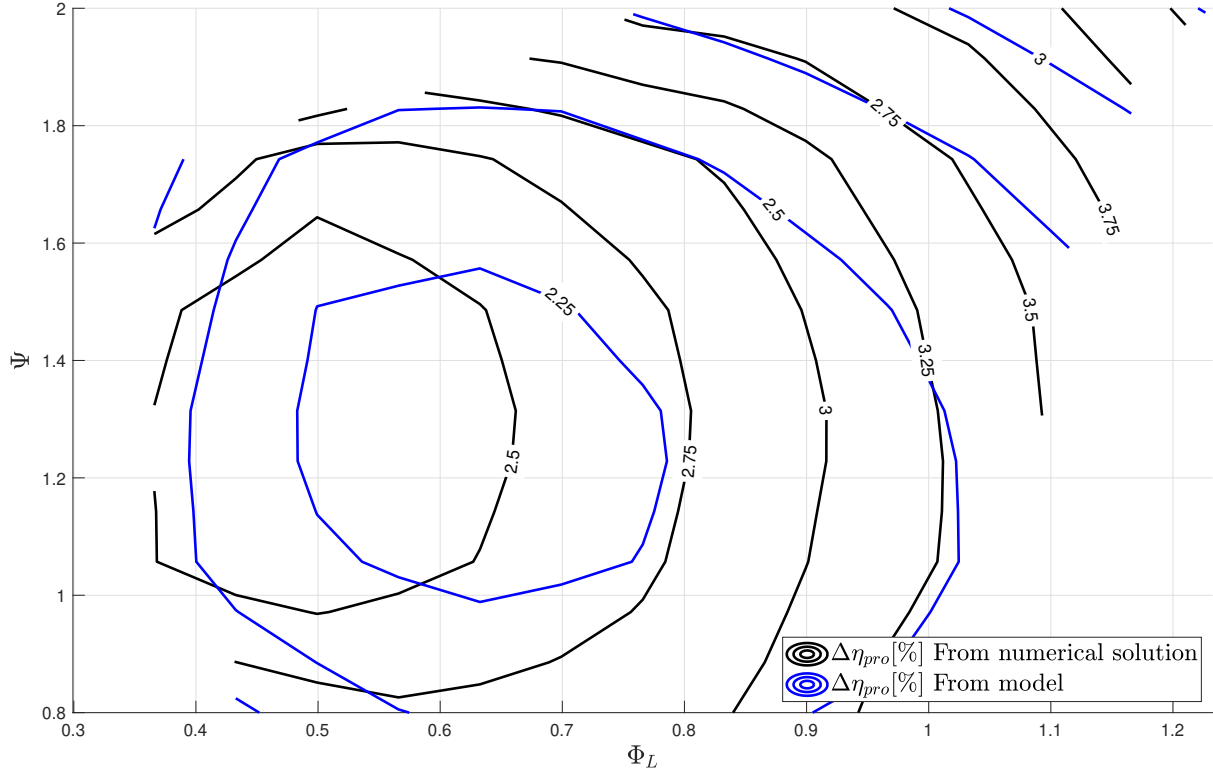


Fig. 4.4 Lost efficiency due to profile loss.

4.2.2 Endwall/Secondary loss

Figure 4.5 A is a contour plot of lost total to total efficiency as a result of end wall flow. This includes secondary flow loss and end wall surface dissipation from the end wall boundary layer. Again, the black contours are of the numerical solution and the blue contours are of the low order model presented in Section 3.1.2.

Figure 4.5 B is a contour plot of the decoupled end wall loss from the numerical solution. Like Coull [18], this was done by estimating the end wall surface dissipation loss using Equation 1.7. Using the surface dissipation, the secondary flow loss can be estimated as the difference between the total loss and the surface loss such that

$$\Delta\eta_{end} = \Delta\eta_{sec} + \Delta\eta_{surf}. \quad (4.4)$$

Note that this is a very rough estimation. In reality the dissipation coefficient varies significantly on this surface, (see Denton[25]).

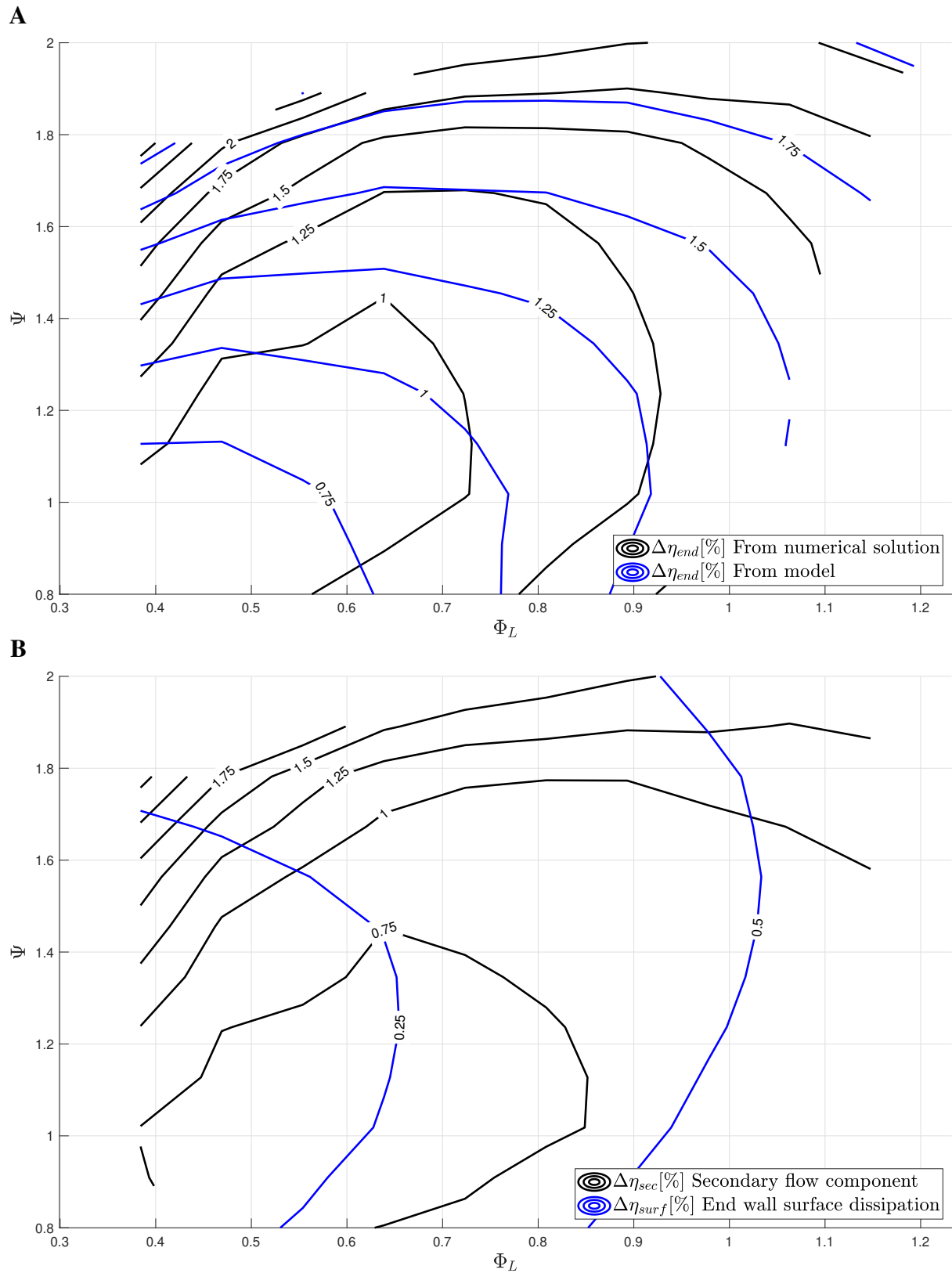


Fig. 4.5 A:Lost efficiency due to secondary/endwall loss. B decoupled endwall losses.

For the designs presented here, the secondary flow dominates and drives most of the variation of end wall loss throughout the space (Figure 4.5). This is particularly the case in the top left of the design space. The secondary flow is high in this region due to the high flow turning (Figure 4.1 *B*) which increases the vorticity application factor.

The bottom right is far less sensitive to end wall loss and is driven by both secondary flow and end wall dissipation. The surface dissipation increases with the increasing surface velocities found in the region, (Figure 4.2).

The model captures the overall trend well, but has a slightly lower sensitivity with flow coefficient. Coull [18] has a further developed model which includes the effects of end wall boundary layer thickness on secondary flow. Designers concentrating on axial architectures only should instead use this further developed model as it is considerably more rigorous.

4.2.3 Tip leakage loss

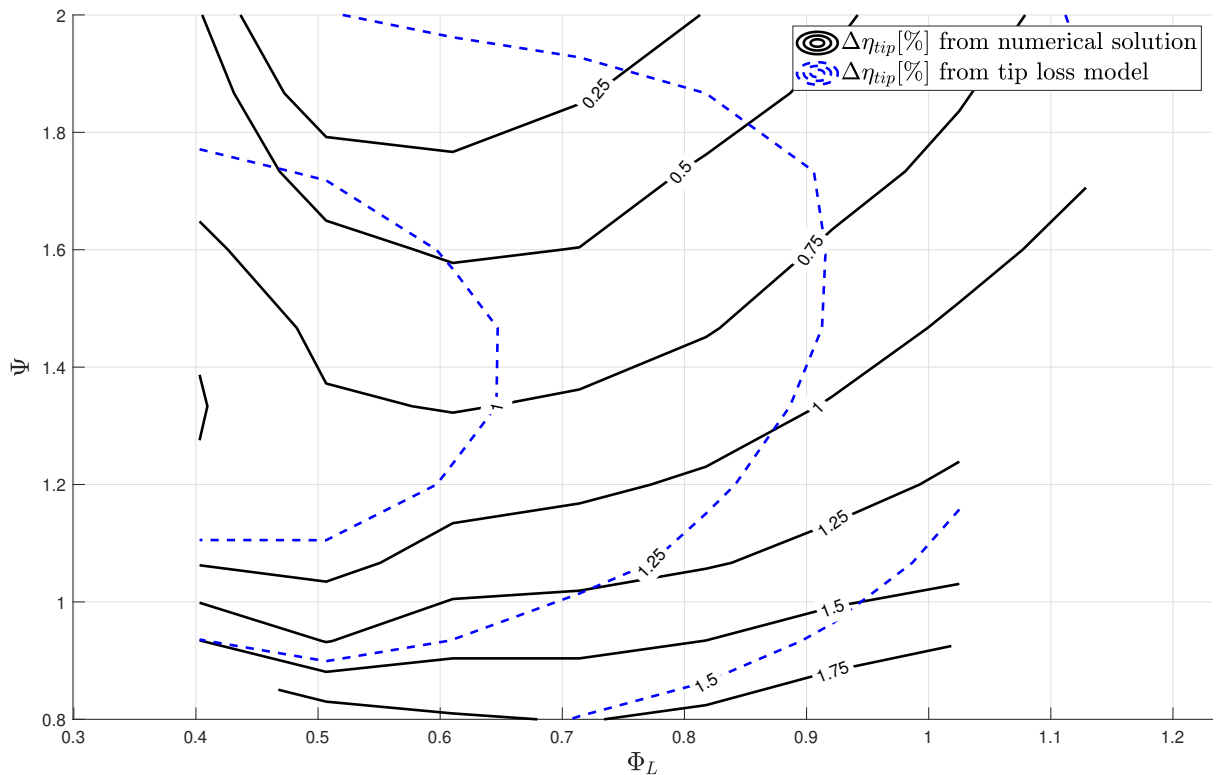


Fig. 4.6 Lost efficiency due to tip leakage loss.

Figure 4.6 is a contour plot of lost total to total efficiency as a result of over tip leakage. Similarly, the black contours are of the numerical solution and the blue contours are of the low order model presented in Section 3.1.3.

Tip leakage modelling in CFD is generally regarded as very imprecise and therefore the author of this thesis suggest the reader be somewhat wary of these results in the context of real

machines. Variations in efficiency driven by changes in driving pressure, leakage gap area and mixing velocities will likely translate to real machines well. However the contracted leakage area, (vena-contracta) is sensitive to the detailed flow conditions in the tip gap which is unlikely capture by the current methodology.

The result of the numerical solution's loss decoupling suggest that the lost performance rises with increasing flow coefficient and decreasing loading coefficient. The model has a similar behaviour in this region of the design space but predicts increasing loss at higher loadings, illustrating a significant discrepancy between the model and decoupled CFD loss.

Since the tip leakage model of Denton [26] agrees in the bottom right hand corner, it might explain the loss generated in this region. In the model, entropy generation is proportional to $W_s^2(1 - \frac{W_p}{W_s})$. Previously, it has been shown that the flow velocities in this region of the design space are high. While Figure 4.2 represents an integral of surface velocities over all surfaces, it still is indicative of the trend in velocity at the casing suction surface. Given this, the loss in performance in the bottom right can be explained by the high free stream velocity with which the leakage flow is being mixed. Additionally, the over tip driving pressure in this region is high (since ΔW is high), as discussed in Section 4.2.

Unfortunately, an absolute conclusion can not be drawn yet as the decoupling approach itself can be called into question. The shape of the loss contours at higher loadings could be a result of the interaction between the leakage and secondary flow. This would make sense, since the secondary flow is high in the upper left corner of the design space.

To further explore this, a comparison of the lost work for a high loading design with an open and partially closed tip gap can be seen in Figure 4.7. The additional loss core from leakage is evident (top left) for the 1% tip gap, which would come with the expected leakage loss. Therefore, one might expect a lower overall performance as a result. However, it would seem that the secondary flow loss core from the casing is bigger for the 0.1% tip gap. This change in size might explain the behaviour seen in Figure 4.6. The generality of this is unclear and further work, which is outside of the scope of this thesis, is required. However, one potential explanation could be that the vorticity from the tip leakage vortex is partially cancelling out the induced velocity from the secondary flow vortex, since the vorticity in the two loss cores are rotating in the opposite direction. In other word it might be possible that the tip leakage vorticity obstructs the formation of some secondary kinetic energy.

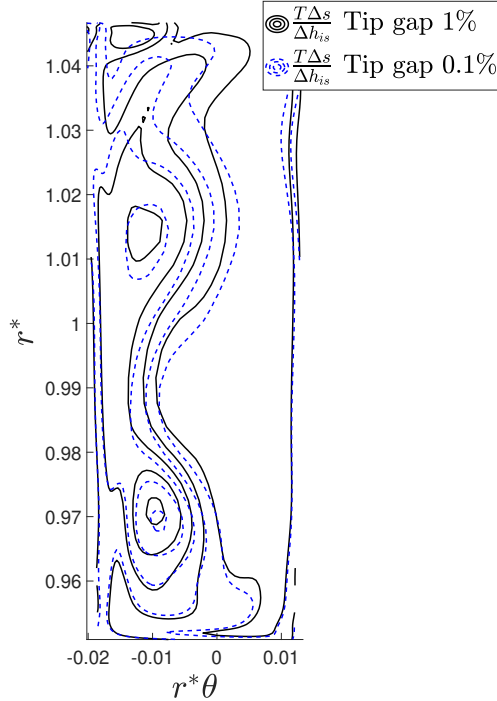


Fig. 4.7 Contour plot of lost work for 1% and 0.1% tip clearance [$\psi = 2$, $\phi_L = 0.6$].

4.3 Axial Total-Static Smith Chart

Figure 4.8 is a total-static Smith chart using the same turbines as Figure 4.1 with some additional data in the top left corner. Again, the solid black contours are total to static isentropic efficiency calculated from the mass averaged stagnation-static pressure ratio from the CFD directly. The dashed blue contours are of an equivalent total to static isentropic efficiency calculated using a surface dissipation coefficient as found in Denton [26] and discussed in Section 1.3.

It must be noted that some of the additional data/designs used to complete the previous data set are introduced here for illustrative purposes. The designs in question lie outside the tolerances shown in Table 4.1.

In comparison to Figure 4.1, the optimum performance is shifted to lower local flow coefficients and slightly higher loading coefficients. This is due to the addition of exit loss and the effect can be described using Equation 4.5.

$$\Delta\eta_{eke} = \frac{(R_{vm} \phi_L)^2}{2\psi \cos^2(\alpha_3)}. \quad (4.5)$$

For these designs, the interstage swirl is close to zero and hence $\cos(\alpha_3) = 1$. The shift to the left is a result of a ϕ_L^2 proportionality of the exit loss. This is because the lost kinetic energy is proportional to the square of the meridional velocity. The shift to higher loadings is a result of

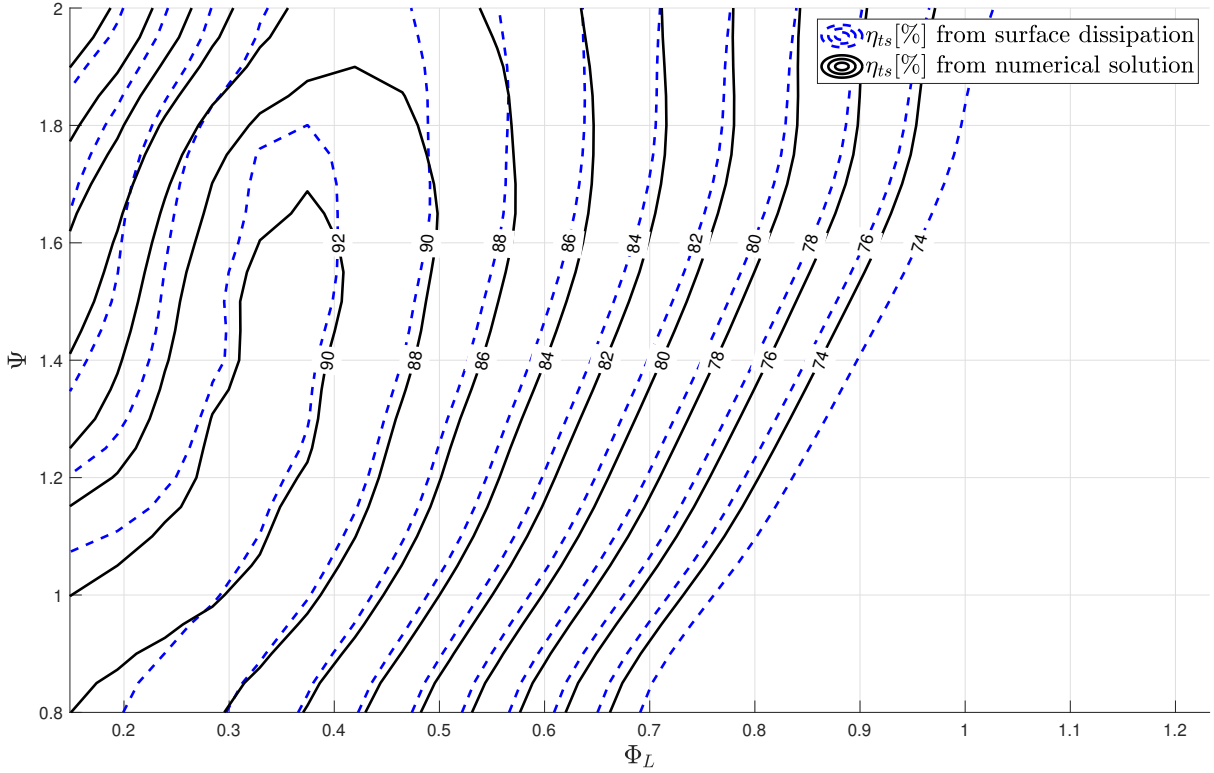


Fig. 4.8 Total-static Smith chart with fixed $\frac{A}{r_m^2}$.

the $\frac{1}{\Psi}$ proportionality. As previously mentioned, increasing the loading coefficient shifts loading to the change in absolute kinetic energy term. Since more absolute kinetic energy is extracted, less is lost at the exit.

The two sets of efficiency contours match more closely in terms of shape than that of the total-total efficiency contours in Figure 4.1. This is a result of the inclusion of exit loss which is very predictable. This then masks deficiencies in the surface dissipation calculation. This is particularly the case on the right hand side of the chart where the exit loss dominates. However, the difference between the surface dissipation model and the numerical calculation gets larger with increasing loading, which stems from the increasing secondary flow loss.

The difference in levels (roughly 2%) is again, due to surface dissipation not capturing the additional sources of loss due to leakage and end wall flows.

4.4 Meridional Velocity Ratio

For most axial turbines the meridional velocity ratio is typically set close to unity. However, exploring variations in this parameter is useful for the design of single stage application or the final stage of larger systems.

The partial derivatives of efficiency with respect to the meridional velocity ratio can be used to gauge both the sensitivity of the parameter and the direction to push the parameter for

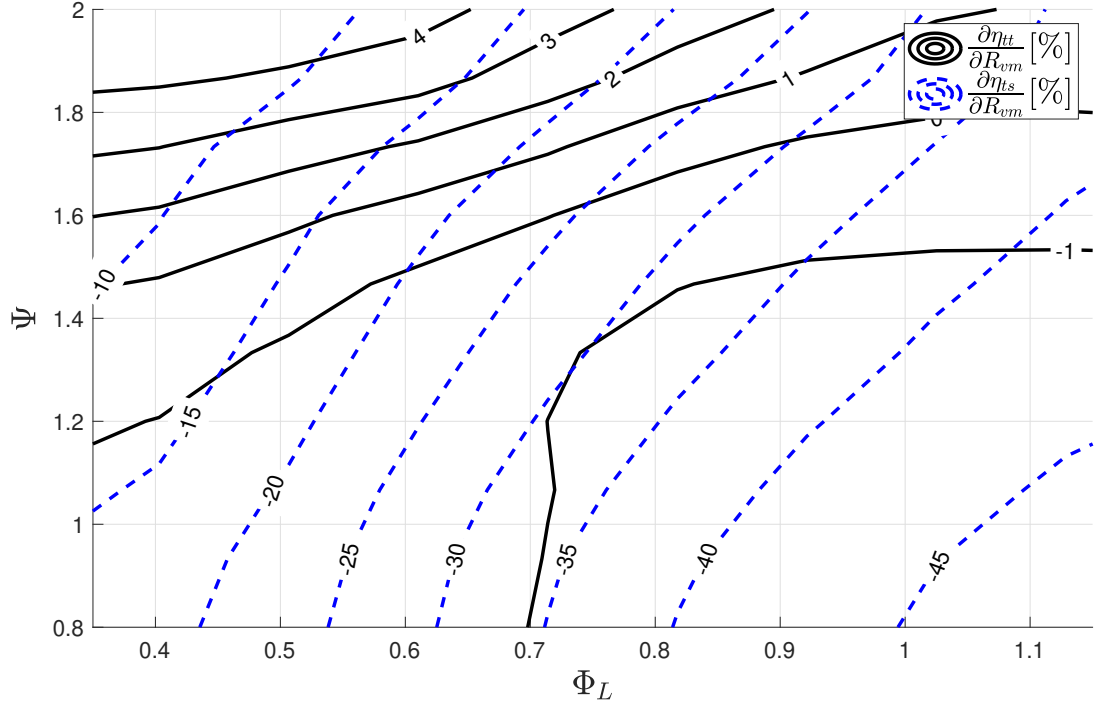


Fig. 4.9 Partial derivatives of total to total and static efficiencies with respect to meridional velocity ratio.

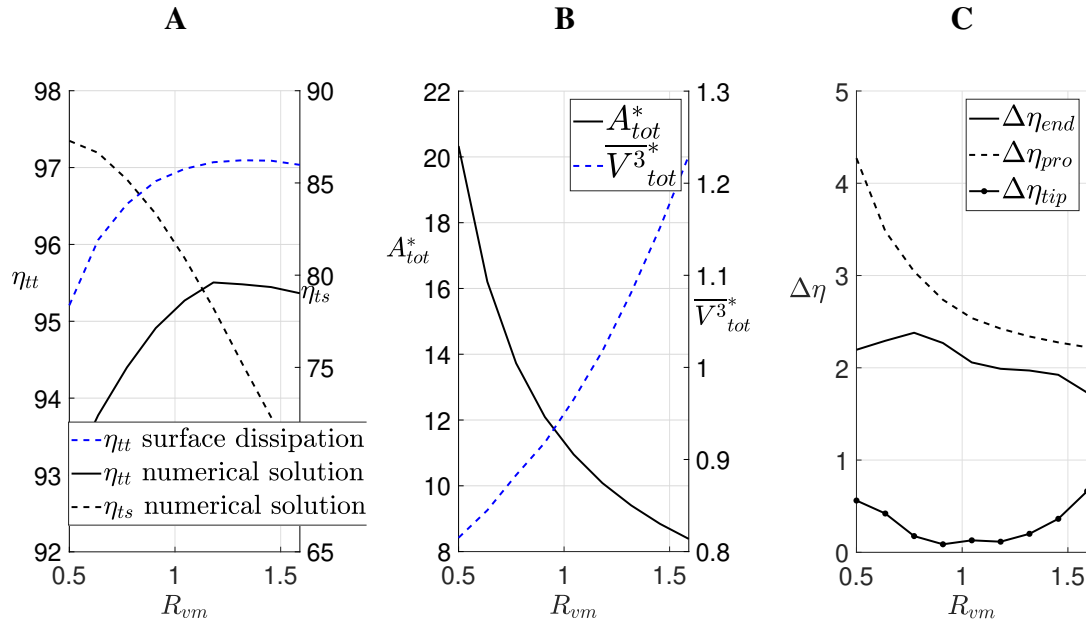


Fig. 4.10 Variation of efficiencies (A), Variation surface area and velocity (B) and loss components (C) with changes in R_{vm} at $\phi_L = 0.7$, $\psi = 1.9$.

beneficial changes in performance. Figure 4.9 shows the numerically approximated partial derivative of total to total and total to static efficiency with respect to meridional velocity ratio. The figure illustrates that the total to total designs at higher loadings and low local flow

coefficients benefit from increased meridional velocity ratios, whereas designs at lower loadings and high local flow coefficients suffer a small loss in performance.

Figure 4.10 A shows the changes in performance with varying meridional velocity ratio for a design point located at $\phi_L = 0.7$, $\psi = 1.9$. Figure 4.10 B depicts the effects of the variation of R_{vm} on surface area and velocity cubed, and Figure 4.10 C depicts the corresponding changes in the different loss mechanism.

Starting with total to total efficiency, Figure 4.10 (A) shows that the surface dissipation qualitatively tracks the change in performance of the numerical solution. Considering this, the behaviour can largely be explained by changes in area and average surface velocities. From (B) the performance increases for the turbines in this region of the design space are a result of reducing surface area. Considering that this region of the design space is dominated by high surface area turbines, this is further reinforced (Figure 4.2). The reductions in loss are mostly driven by a reduction in profile loss which comes from a reduction in the profile area (C).

As with the loading coefficient, changes in meridional velocity ratio serves to shift the work split. In this case, the parameter shifts loading between the relative acceleration term and the change in absolute kinetic energy term (Equation 4.3).

Increasing meridional velocity increases relative acceleration which results in higher passage velocities. Since the circulation is fixed, fewer blades are required. On top of this, increasing the meridional velocity ratio also reduces the relative exit flow angle (Equation 4.6, valid for zero exit swirl). Lower blade angles reduces the blade surface length. In addition, the decrease in blade exit angle could also explain the lower secondary flow loss.

$$\tan \beta = -\frac{R_{rr}}{\phi_L R_{vm}}. \quad (4.6)$$

When designing for high total to static efficiency, reducing meridional velocity ratio is a particularly powerful means of improving performance. This can simply be explained using Equation 4.4, where $\Delta\eta_{eke} \propto (R_{vm} \phi_L)^2$. Thus reducing R_{vm} reduces exit kinetic energy loss. Since the meridional velocity ratio is scaled by the flow coefficient, changes in meridional velocity will have an even stronger effect at higher local flow coefficients. This is reflected in Figure 4.9. Therefore, variations in meridional velocity ratio can be used to shift the optimum design flow coefficient for total to static machines to higher values. This is particularly useful for developing highly loaded single stage turbines. By shifting the optima to higher local flow coefficients, the inlet blade angle will be reduced, easing design and improving performance.

The improvement in total to static performance can also be explained in terms of a shift in the work split. By reducing the meridional velocity ratio, loading is being transferred from the relative acceleration term to the change in absolute kinetic energy term. Thus, more absolute kinetic energy is being extracted from the flow which means less is lost at the exit.

4.5 Interstage swirl & Circulation coefficient

Figure 4.11 A are contours showing the partial derivative of total to total (in black) and total to static (in blue dashed) isentropic efficiency with respect to α_2 . The derivative was numerically approximated with $\Delta\alpha = -10^\circ$.

Firstly, considering total to total efficiency, the orientation of contours indicate that negative interstage swirl is beneficial for higher loadings. Surface dissipation has been shown to largely explain the behaviour of changes in parameters across the design space so far. The change in area, (ΔA) is shown in Appendix B.2 and suggest that a significant portion of the change in performance is likely driven by a reduction in area.

The high loading designs with negative interstage swirl have lower surface area, reducing surface dissipation. As for total to static application, swirl is mostly detrimental, since $\Delta\eta_{eke} \propto \cos^2 \alpha_2$ (Equation 4.5). In other words, exit swirl results in additional kinetic energy lost.

Figure 4.11 B are contours of the partial derivative of total to total isentropic efficiency with respect to circulation coefficient. The derivative was numerically approximated with $\Delta C_o = -0.07$. Designs with optimal circulation coefficient of 0.7 are present in the design space, which would imply 0.7 is indeed a reasonable choice. That being said, it seems that the current design system might benefit from fewer blades at higher loadings and flow coefficients. The overall sensitivity to this parameter seems somewhat low for the given design system. For example, for a 10% change in circulation coefficient, the largest change for a single turbine present in the data set was $\Delta\eta = 0.5\%$ and the largest difference between two turbines was $\Delta\eta = 0.68\%$.

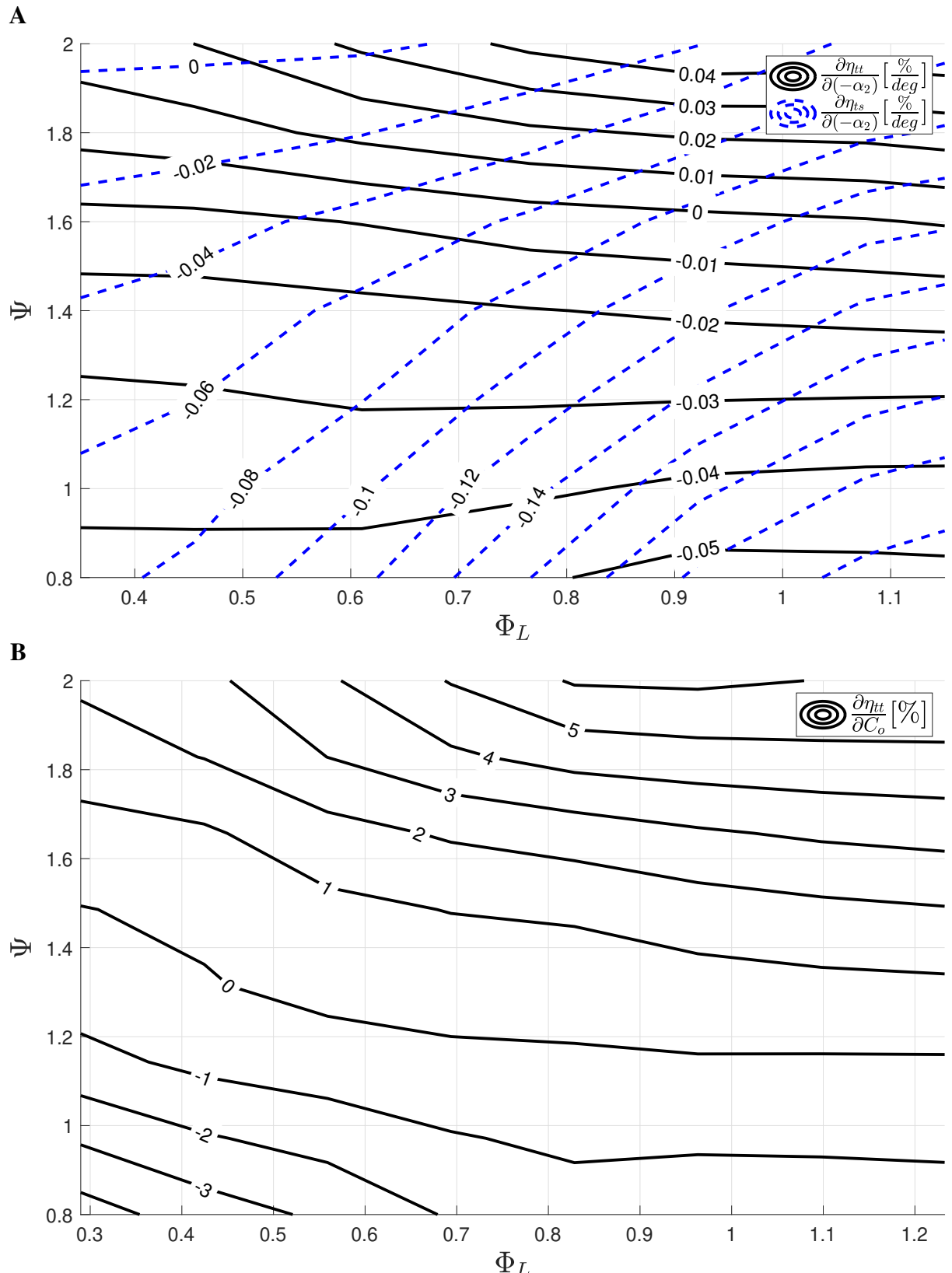


Fig. 4.11 A:Partial derivatives of total to total and static efficiencies with respect to interstage swirl. B Partial derivatives of total to total efficiency with respect to circulation coefficient.

4.6 Loading and Duty Flow Coefficient Based Balje Diagram

A Balje chart can be described as a efficiency variation as a function of duty parameters. Typically, these would be non-dimensional/specific speed and diameter. Section 1.5.3 introduced the use of alternative similarity parameters Φ_D and Ψ . It is the opinion of the author that these parameters are easier to interpret from an aerodynamics perspective and therefore will be used to form a new style Balje chart. Bearing this in mind, one possible combination of flow parameters that fully describes the meanline flow characteristics can be written in a functional form,

$$\eta(\Psi, \Phi_D, \Phi_L, \alpha_0, \alpha_2, R_{vm}, R_r), \quad (4.7)$$

which needs to be reduced to

$$\eta(\Psi, \Phi_D). \quad (4.8)$$

Ideally, all of these parameters, as well as the blade geometry, should be optimised for each point in the design. This would form an idealised Balje chart. To do this using RANS would be unrealistic at present. Instead, α_2, R_{vm}, R_r will be fixed. Since Φ_L is related to Φ_D (Equation 4.9), an optimal value for Φ_L will therefore be selected. This was done using a large data set, whereby a range of designs were produced with different local flow coefficients for each location in the design space. The procedure used for extracting the optimum local flow coefficient is as follows:

- For a given value of duty flow coefficient and loading, designs were produced with different local flow coefficients to produce a sub sets shown in Figure 4.18.
- The left and right hand bounds are prescribed by setting maximum limits for blade angles and maximum flow coefficients.
- A polynomial is fitted and the optimum value for total to total and total to static efficiency is then extracted.
- This is then repeated over a range of different loading and duty flow coefficients.

In addition to the mean line flow parameters, other parameters that influence performance will also be kept close to constant and are listed below. The aspect ratio term is fixed at $AR = 2$ through out the design space. This choice was made to keep the design space more inline with that of Balje [4]. Alternatively, the chord could be scaled with diameter. However, this would result in low aspect ratio blades at low duty flow coefficients and vice versa.

The percentage tip gap (t/h) is kept constant through out the design space. This was chosen largely for simplicity. Alternatively one could fix the absolute value of tip gap or scale the clearance with the diameter. This might better represent the variations across the design space

of real machines, however this would require more accurate tip modelling and more detailed control of the tip gap mesh. While fixing the percentage tip gap is not mechanically realistic, one still can conjecture on how mechanism relating to tolerance limits would vary across the design space and will be discussed later in this thesis.

Table 4.2 Axial Balje chart parameters

Parameter	Value
R_r	1
AR	2
R_{vm}	1
$\frac{TE}{C_x}$	0.025
$\alpha_2(\text{mean})$	$0 \pm 3\text{deg}$
$C_o(\text{mean})$	$0.7 \pm 4\%$
$\Delta\eta_{ne}$	$0.08\% \pm 0.02\%$

4.7 Axial Total-Tot Balje Chart

Figure (4.12 A) is the resulting Balje chart produced using the design methodology outlined in Chapter 2. Included are the meridional projections of the blade and disk. Turbines to the left of the space have large diameters, short meridional lengths and heights and vice-versa.

The changes in size with duty flow can be explained as follows, since the mass flow and change in specific enthalpy are fixed, increasing the duty flow reduces the machine diameter. This is because the mass flow capacity is increasing and thus a smaller machine can be used. The higher mass flow capacity is driven by high local flow coefficients and higher non-dimensional through flow area (A_{in}/r_n^2). As a result of the latter, these designs have a low hub to tip ratio and hence are more three dimensional, i.e a larger variation in flow angles up and down the span. The blade count also reduces with increases in duty flow.

Designs on the far left of the space have blade counts in the order of a thousand and designs to the far right are in the order of tens. Since the aspect ratio is kept constant, the blade chord lengths scale with the span. This means that designs to the left of the space have short blade chord lengths and therefore more blades are required to turn the flow when compared to designs to the right of the space. In addition to this, designs to the right of the space have lower turning (a result of the higher local flow coefficients). This increases the required pitch to chord ratio for a given circulation coefficient.

As with the Smith chart, the contours of surface dissipation match well with the numerical solution. Again, this suggests that the shape of the design space can largely be explained by

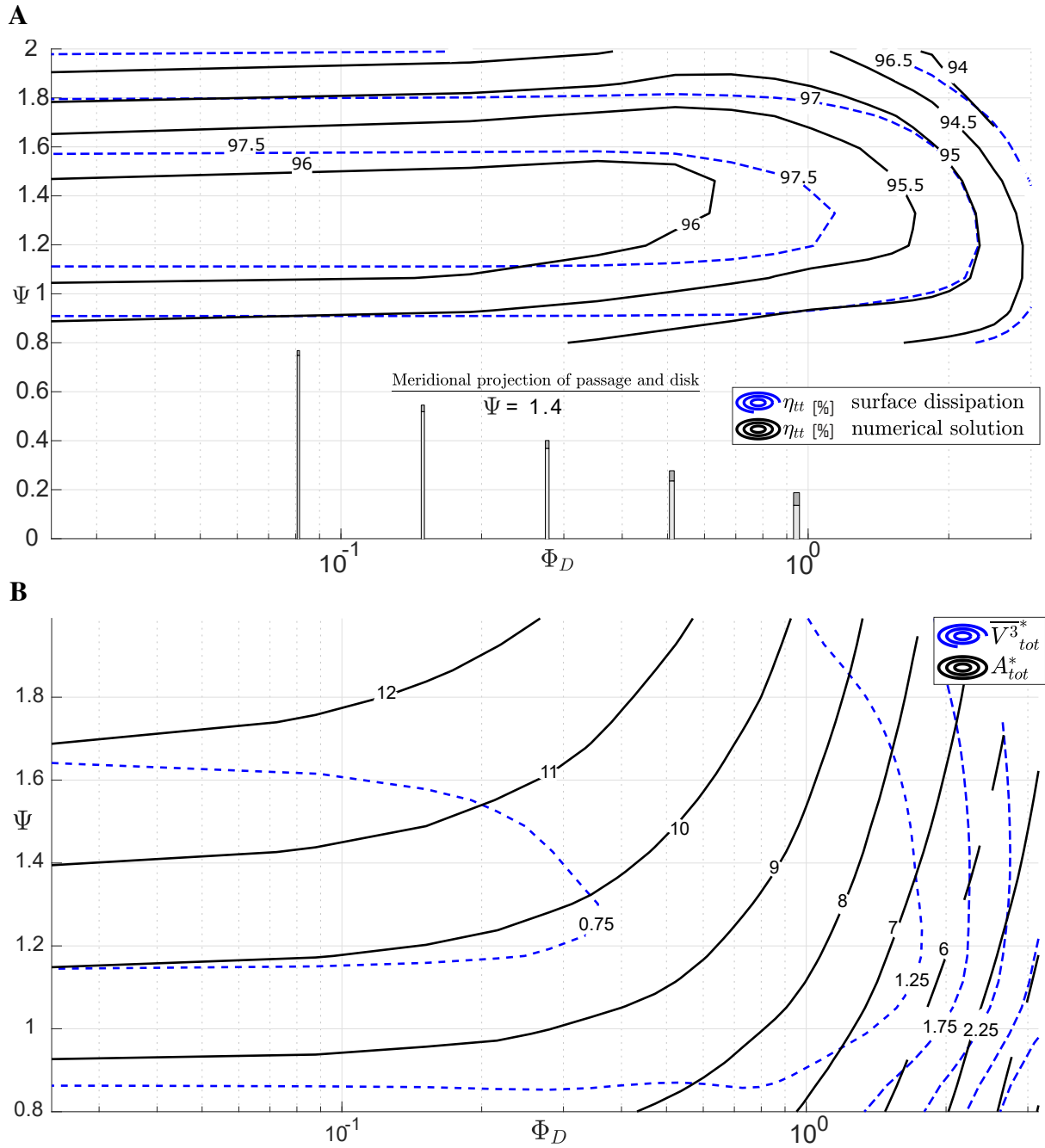


Fig. 4.12 A:Contours of total to total efficiency for axial turbines with varying loading and duty flow coefficients. B Contours of blade profile surface area and surface-area averaged cubic velocity.

surface dissipation. Figure 4.12(B) is a plot of non-dimensional surface area and area averaged cube of the surface velocity as introduced in Section 1.3. The reduction in performance due to surface dissipation at high values of duty flow coefficient can largely be explained by increased surface velocity, figure 4.12(B). Later, it will be shown that loss from all mechanisms contributes to the drop in performance seen here. The Mach numbers in this study are low however it can be

concluded that for increasing rotational Mach numbers, designs to the right of the space will experience the onset of compressibility effects earlier than designs to the left of the space due to higher surface velocities.

The performance drop at higher values of loading coefficient can be explained by increased surface areas. In the top right corner of the design space, both effects are compounded. The high surface velocities to the right of the space are mainly a consequence of the high local flow coefficient of these designs (Figure 4.17), and will be discussed later.

When decreasing duty flow coefficient (moving to the left of the space), the performance remains little changed. This constancy was observed for values as low as $\Phi_D = 10^{-3}$. This is reflected by surface dissipation, where Figure 4.12(B) shows the velocity and area contours flatten off.

Due to the fixed aspect ratio, the normalised meridional geometry is invariant. In addition to this, the velocity triangles are tending to a fixed shape and hence the turbines are essentially converging on a two-dimensional-like design. Since the aspect ratio, trailing edge thickness to chord ratio, and tip gap to span ratio remain constant, the loss mechanisms driven by these geometric ratios also converge. In reality, the trailing edge thickness to chord, tip gap to span as well as blade thickness are set by absolute manufacturing limits and cannot scale with the passage, which is getting smaller, and hence will drive up the associated loss mechanisms. This implies that the performance limits on the left hand side of the space is set by these tolerance limits.

4.7.1 Profile loss

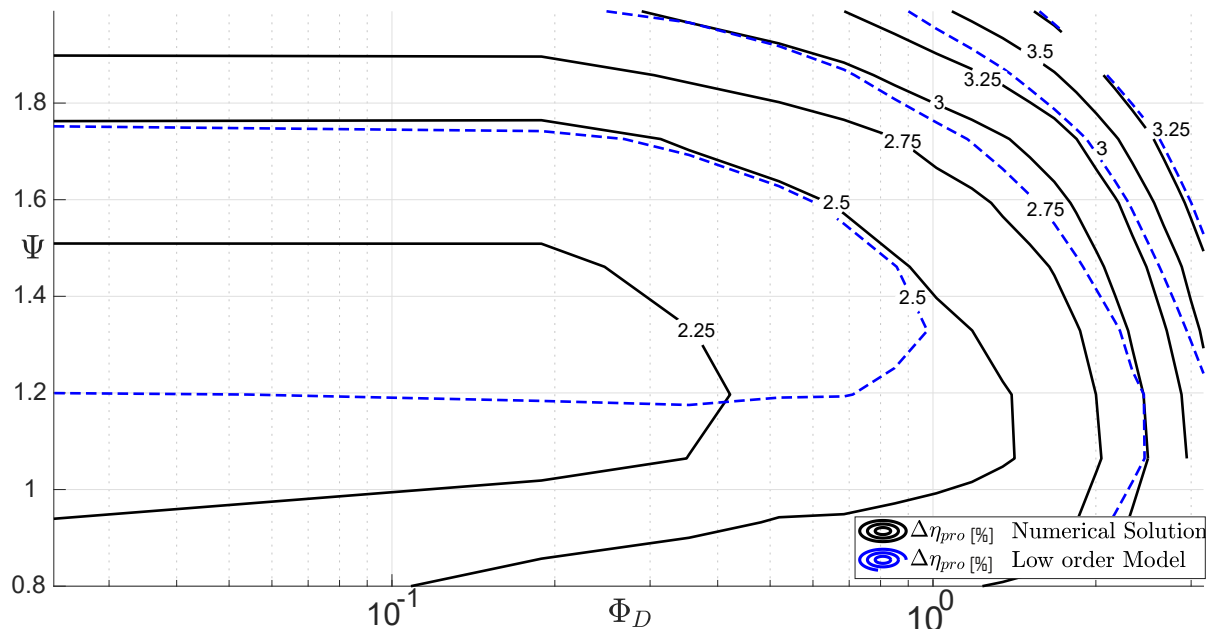


Fig. 4.13 Contours of loss in efficiency of axial turbines due to profile loss.

The profile loss contours in Figure 4.13 takes a similar form to the contours of the Balje chart itself, where profile loss increases with loading and at higher values of duty flow. Again, this behaviour can largely be explained using dissipation arguments. From figure 4.12(B), the increase in profile loss at high duty flow coefficients is driven by high suction surface velocity and the increased loss with loading is due to high surface area.

Later it will be shown that turbines at high duty flow coefficients have characteristically high local flow coefficients and as shown in the Smith chart section 4.2, a consequence of fixing the circulation coefficient is that the diffusion factor increases with local flow coefficient. Therefore the turbines at high duty flow in this Balje diagram have increasing diffusion factors. While no suction surface separation was observed in the results, it is unlikely that CFD is able to predict the onset accurately.

The model captures the shape of the numerical solution's loss reasonably well. This further illustrates the strength of using surface a dissipation model across the design space. It does, however, under predict the rise in loss in the top right corner. More importantly, this model will not be able to capture the effect of suction surface separation and will significantly underestimate loss at sufficiently high diffusion factors.

4.7.2 Endwall loss

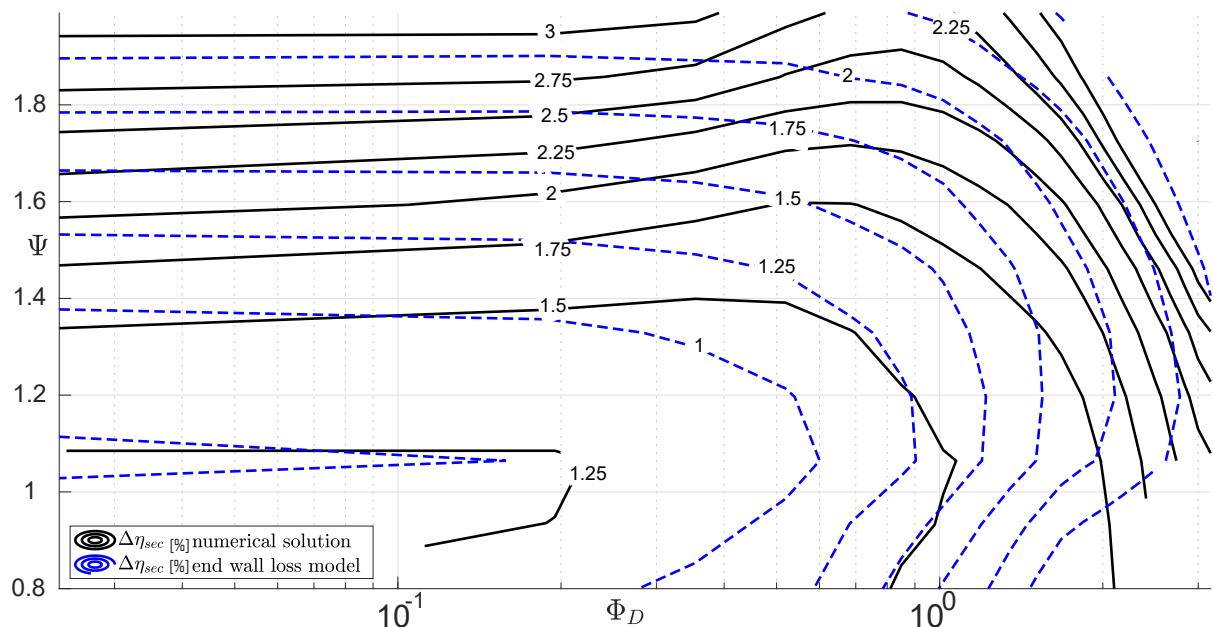


Fig. 4.14 Contours of loss in efficiency of axial turbines due to secondary/endwall loss.

Figure 4.14 shows the variation of the end wall loss across the Balje diagram. Starting from the right of the space, as with the profile loss, the end wall loss is initially constant with duty flow. Then, as the duty flow coefficient increases, there is a slight reduction in loss before sharply

increasing at high duty flow. The vast majority of the changes in loss are a result of secondary flow, since the end wall surface dissipation varies little over the design space (Appendix B.3). This is a result of the constant aspect ratio.

The little rise that there is in end wall surface dissipation occurs at high duty flow and is driven by the rise in surface velocity.

The model roughly captures the trend but has poor agreement at high duty flow and low loading. This could be for a number of reasons. The blades in this region are highly three dimensional (low hub to tip ratio). Since the model is derived for a cascade, it may not capture the behaviour of the secondary flow for highly three dimensional blade surfaces. Another potential cause of the mismatch could be the models linear dependency on the aspect ratio term ($\frac{p_m \cos \beta_2}{h}$). This term increases substantially in the bottom right corner, where the loss is significantly over predicted.

That being said, it is unlikely that a designer would use this region of the design space. Since the model loosely captures the trends, it can be used to roughly describe the behaviour. Using the model, the rises in secondary loss with loading is by and large due to an increase in inlet blade angle and the increases with duty flow is largely due to increased differences in transient times and $\frac{p_m \cos \beta_2}{h}$. The increase in the differences in transient time is a result of larger ΔW at higher duty flow.

4.7.3 Tip Leakage loss

Figure 4.15 is a contour plot of lost total to total efficiency as a result of over tip leakage. The black contours are of the numerical solution and the blue contours are of the low order model presented in Section 3.1.3.

The leakage loss increases with duty flow coefficient and decreases with loading, which is similar in nature to that shown in the Smith chart (Figure 4.6). As mentioned in section 4.2.3, the decoupling approach itself is questionable. The shape of the loss contours at higher loadings could result from a likely interaction between the leakage and secondary flow, since the secondary flow is high in this region.

The leakage loss increases at higher duty flow and lower loading coefficients. As with the leakage loss across the Smith chart, this behaviour can be explained by the high velocity with which the leakage flow is mixing as well as the increased over tip driving pressure. While Figure 4.12(B) represents an integral of surface velocities over all surfaces, it still is indicative of the velocities present at the casing suction surface. As previously discussed, this could explain the loss at high duty flow coefficients and low loading. As a reminder to the reader, the high surface velocity at high duty flow coefficients is again a result of high design local flow coefficients 4.17. Similar to the Smith chart, the model seems to capture the behaviour at lower loading reasonably well, but again predicts a drop in performance at higher loading.

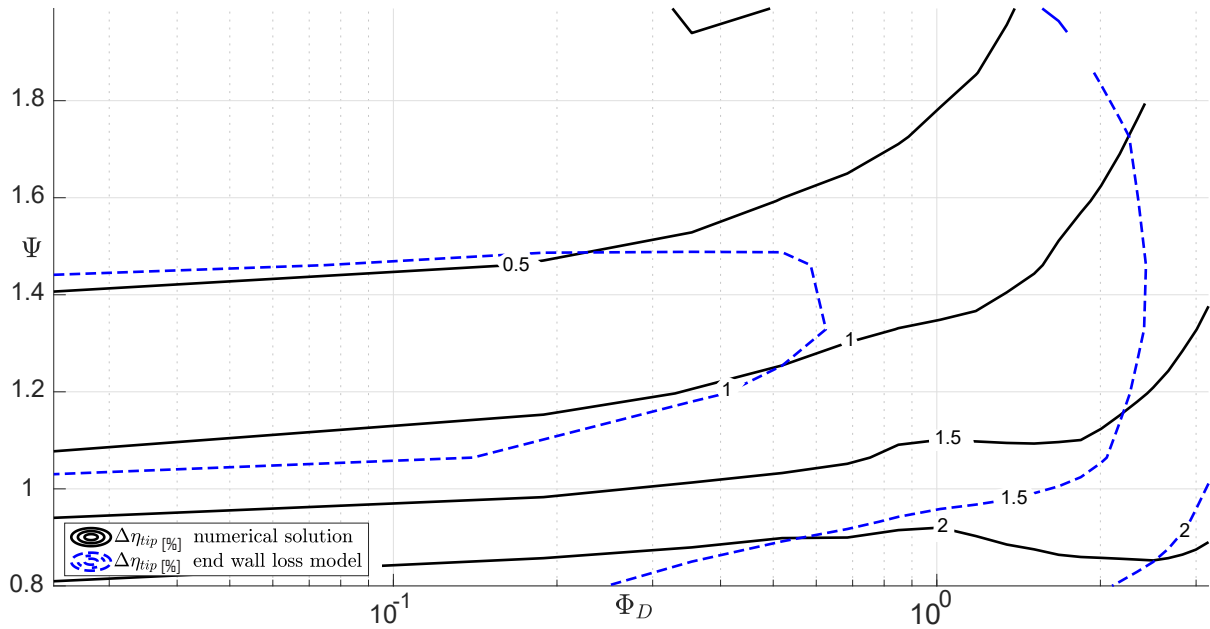


Fig. 4.15 Contours of loss in efficiency of axial turbines due to Tip Leakage loss.

4.8 Axial Total-Static Balje Chart

Figure 4.16(A) is a Balje diagram constructed by selecting a local flow coefficient for optimal total to static performance and Figure 4.16(B) shows the exit loss. The difference between the total to static (Figure 4.16) and total to total (Figure 4.12) Balje charts are as follows:

- There is an 8% difference in peak performance. Roughly 6% of this is exit loss and the remainder is a entropy loss that is a consequence of designing for high total to static performance. The total to static Smith chart (Figure 4.8) indicated that optimal total to static designs sit at lower local flow coefficients and therefore incur increased entropy based loss. The additional entropy loss is being traded for lower exit loss. As shown in Section 4.2, the additional loss is due to high amounts of flow turning and high surface area.
- The performance drops off more dramatically and at earlier duty flow coefficients than that of the total to total diagram. This is a consequence of the exit loss being proportional to the local flow coefficient squared, $\Delta\eta_{eke} \propto \phi_L^2$. Since the design local flow coefficient increases with duty flow coefficient (Figure 4.17), the exit loss rises sharply.

The plot also shows that surface dissipation contours match the shape and drop off of the solution well (with a 2% difference in level). The closer matching shape compared to that in Figure 4.12 is a consequence of including exit loss, as was discussed in Section 4.3.

It must be noted that the data set used to select the optimal local flow coefficient for total to static efficiency was the same as that used for the total to total Blaje diagram and as such the

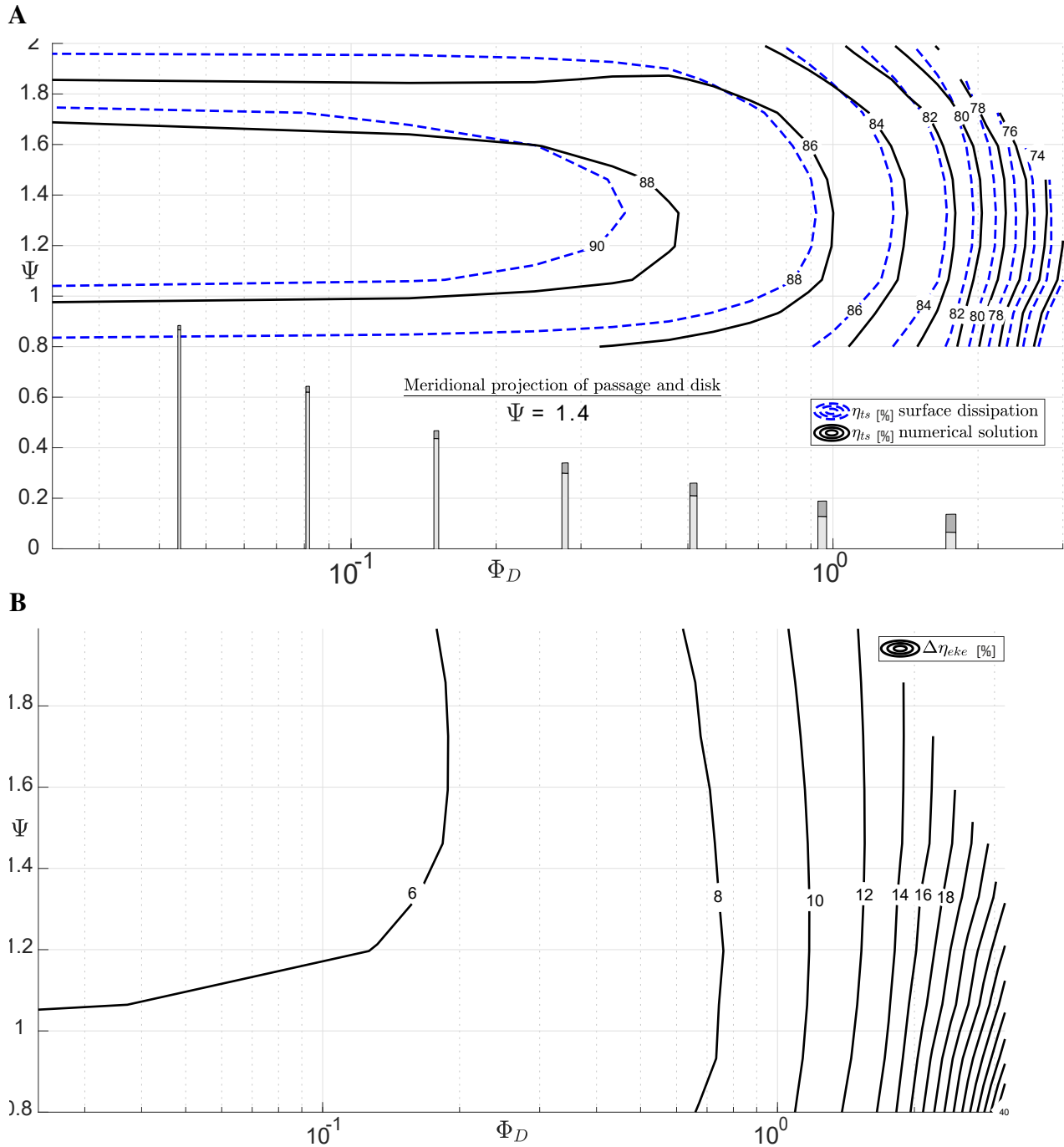


Fig. 4.16 A:Contours of total to static efficiency for axial turbines with varying loading and duty flow coefficients. B Contours of lost efficiency due to exit loss

meridional velocity ratio was set to unity. As previously discussed in Section ??, using lower meridional velocity ratio can dramatically improve total to static performance. Hence in future, the above diagram should be reproduced to include an optimisation for meridional velocity ratio. That being said, it is unlikely that the overall shape, not the levels, will change significantly, as the exit loss will inevitably cause a drop in performance at high duty flow.

4.9 Optimal local flow coefficient

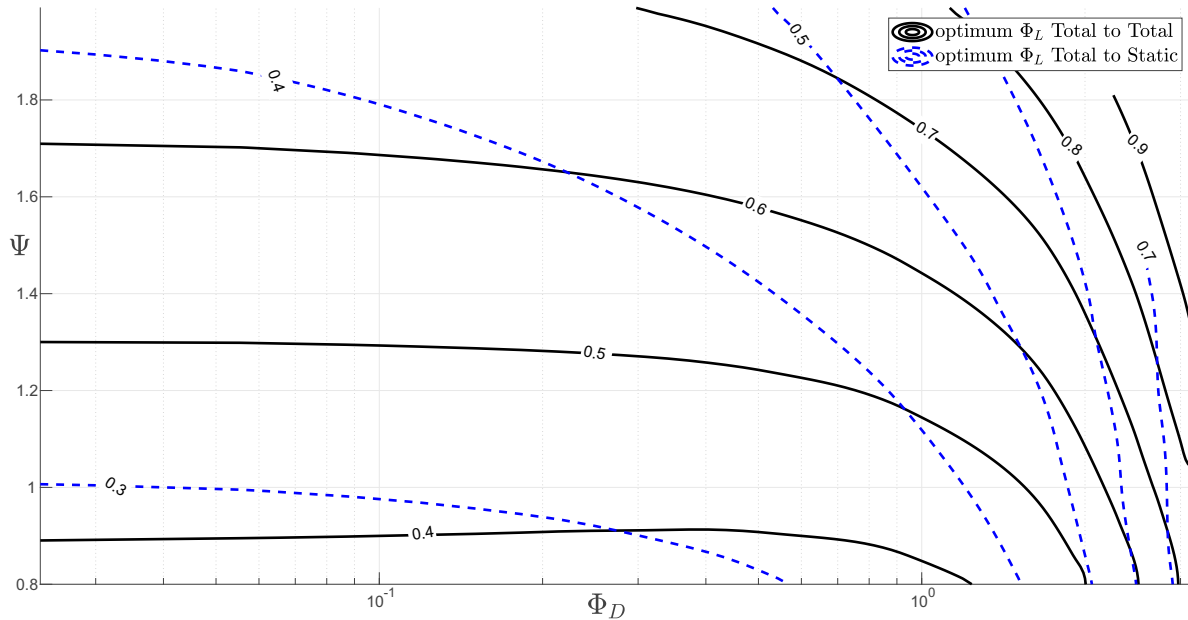


Fig. 4.17 Contours of optimised local flow coefficient for axial turbines with varying loading and duty flow coefficient.

As previously stated, the ideal Balje diagram would require optimisation of all but the duty parameters. Instead, the author chose to select an ideal local flow coefficient due to the direct interrelation between this parameter, the duty flow coefficient and non-dimensional through flow area.

The interrelation between local flow coefficient, the duty flow coefficient and non-dimensional through flow area, in incompressible form, is repeated here for convenience.

$$\Phi_D = \Phi_L \frac{A_{in}}{r_n^2} \quad (4.9)$$

As a reminder, this equation illustrates that, the volume/mass flow is set by either high inlet area or meridional velocity, or both (in non-dimensional form). While both tend to vary, in some regions of the design space, change in the duty flow might stem more from changes in one parameter than the other.

The optimum values of local flow coefficient used to create Figure 4.12 and Figure 4.16 are presented in Figure 4.17. The figure shows that changes in duty flow coefficient at high duty flow are primarily driven by changes in local flow coefficient and conversely change at low duty flow are driven by changes in non-dimensional inlet area, since the local flow coefficient is roughly constant.

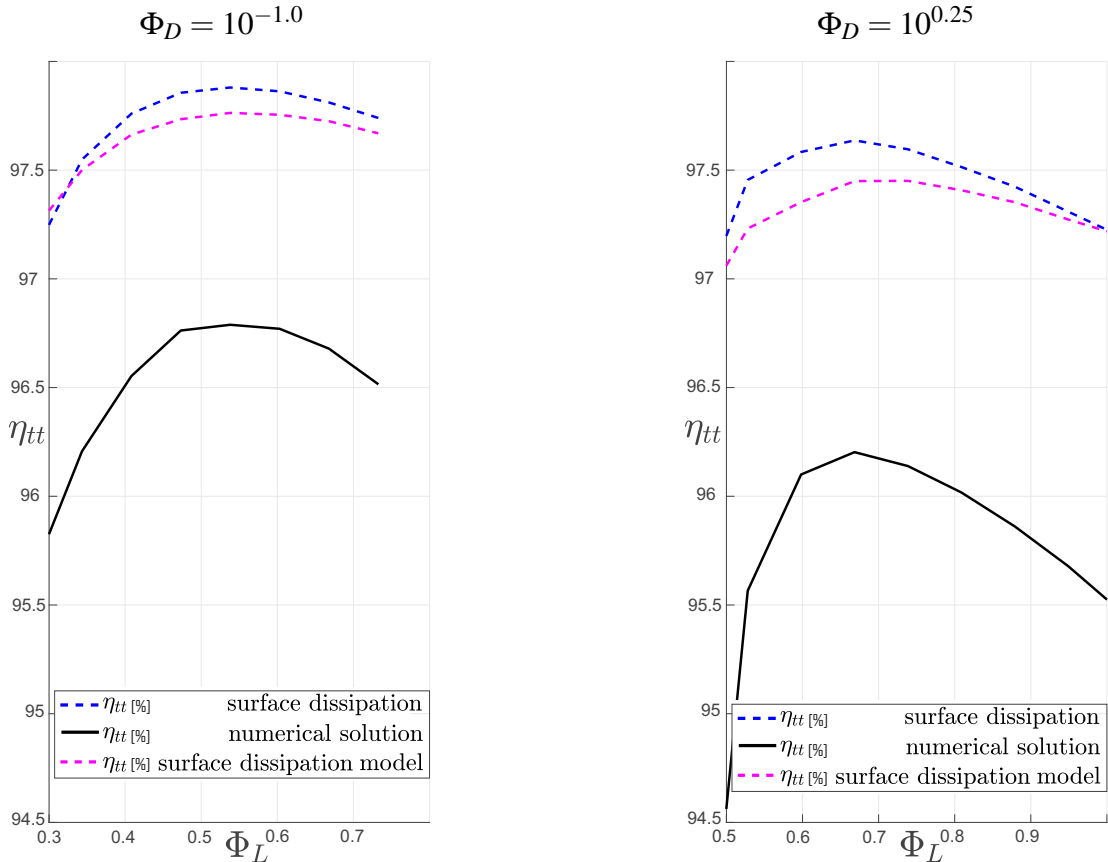


Fig. 4.18 Comparison of optimal design local flow coefficient with a fixed loading coefficient $\Psi = 1.6$ and different duty flow coefficients.

If the local flow coefficient were to be fixed, it would forcibly limit the applicable range of axial turbines as the only possible way to achieve high duty flow would be by high values of through flow area (high A_{in}/r^2). However, this would quickly bump up against a geometric limitation as the hub radius cannot be less than or even very close zero (unphysical).

Figure 4.17 shows that the optimum local flow coefficient for total to total designs increase with loading coefficient. A similar pattern occurs for total to static designs, the range of changes in Φ_L is lower. This increase is typical and can be seen in a Smith chart of axial turbines. At low duty flow coefficient, the contours are nearly horizontal for total to total efficiency and this could be considered the invariant region". Within the current framework, the region seemingly extends indefinitely to lower duty flow coefficients (tested to values as low as $\Phi_D = 10^{-3}$). As a reminder this is unlikely to be the case when considering real world manufacturing limitations.

As the duty flow coefficient increases, the contours slope downwards and the optimum local flow coefficient starts to increase rapidly.

From Figure 4.18, it is clear that the optimum local flow coefficient for total to total efficiency resides close to that predicted by surface dissipation. Hence a simplified explanation of the increase in optimal flow coefficient based on surface area and velocity can also be made. For

simplicity, it will be assumed that the peak total to total efficiency lies close to the minimum value of $\overline{AV^3}$, where

$$\frac{d\overline{V^3}A}{d\phi_L} = A \frac{d\overline{V^3}}{d\phi_L} + \overline{V^3} \frac{dA}{d\phi_L} = 0. \quad (4.10)$$

Hence the location of the optimum is determined, where

$$A \frac{d\overline{V^3}}{d\phi_L} = -\overline{V^3} \frac{dA}{d\phi_L}. \quad (4.11)$$

Equation 4.11 and Figure 4.19 A show that increasing $\overline{V^3}(-\frac{dA}{d\phi_L})$ and decreasing $A \frac{d\overline{V^3}}{d\phi_L}$ shifts the optimum to higher values of local flow coefficient and vice versa. This is because increased changes in area drive designs to the right and increased changes in velocity drive designs to the left. From Figure 4.19, it is clear that the designs with $\Phi_D = 10^{0.25}$ have a slightly steeper derivative of surface area as well as higher velocity. This then explains the shifts to higher local flow coefficients.

The steeper gradient of surface area is a consequence of larger variations in non-dimensional through flow area ($\frac{A_{in}}{r_n^2}$), as seen in Figure 4.19 B . The figure shows that turbines with higher duty flow coefficients have higher values of $\frac{A_{in}}{r_n^2}$ and have stronger variations in these values with local flow coefficient.

The increased velocity can also be explained in terms of increased $\frac{A_{in}}{r_n^2}$. Turbines with higher non dimensional inlet area are more "3D", with larger variation of pitch and flow angles up and down the span. The higher pitch further up the span will have larger velocity differences (ΔW) than the mean line (Equation 3.12). Since the velocity term is cubed, this results in an overall increase in velocity. The arguments presented here are simplified, based solely on velocity and surface area. In reality, the variation in all the loss mechanisms would need to be considered to form a complete picture, especially at high duty flow coefficients where these sources increase rapidly. In addition to this, varying the blade count by change the circulation coefficient can also shift the balance in area and velocity and will therefore have an effect on the optimal flow local coefficient. That being said, it is inevitable that the local flow coefficient will have to rise with increasing duty flow coefficient in order to pass more mass flow through the machine.

The variation of the low order model surface dissipation is also presented in Figure 4.18. The model captures the behaviour surprisingly well. Note this excludes the tip leakage and secondary flow models (includes end wall dissipation). This suggest that the model could be used by designers to get rough estimates for optimal local flow and potentially other parameters (for machines operating with fully turbulent attached boundary layers that is).

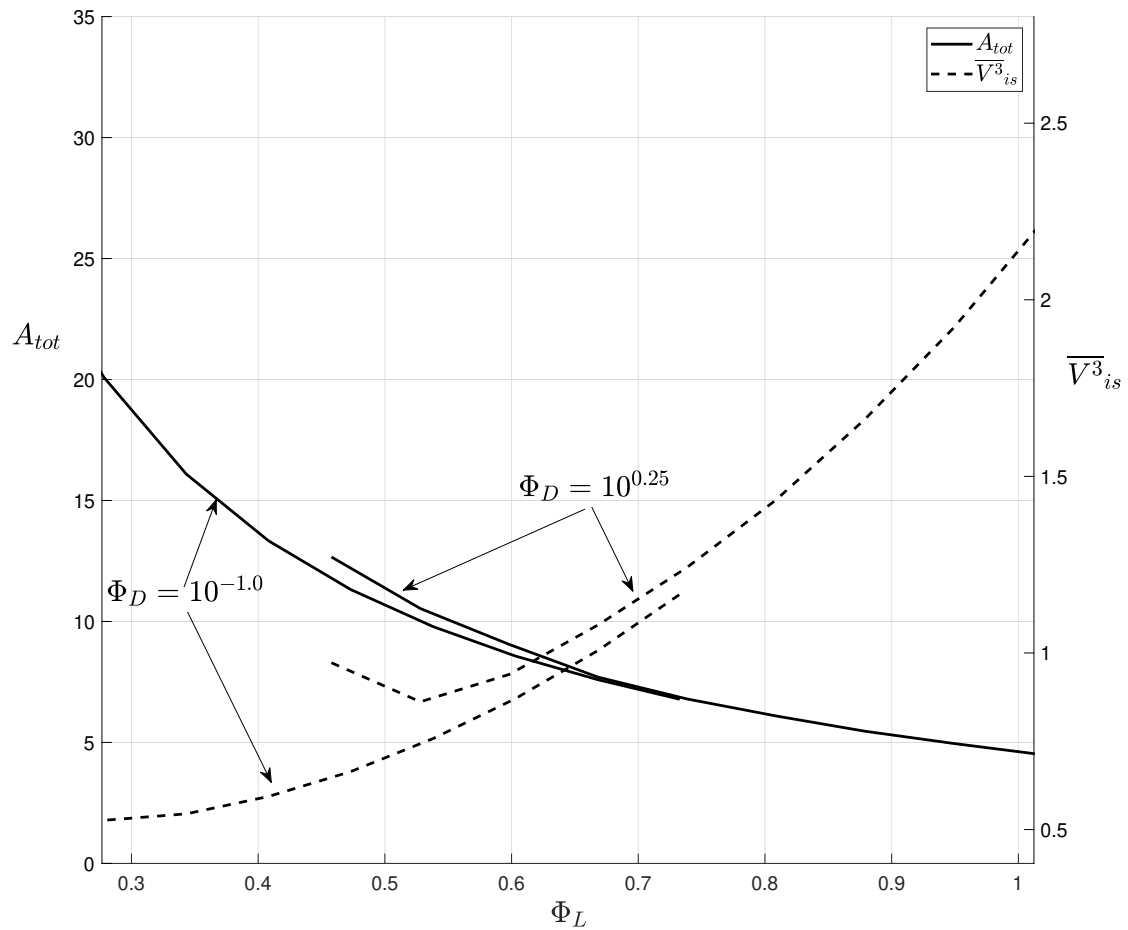
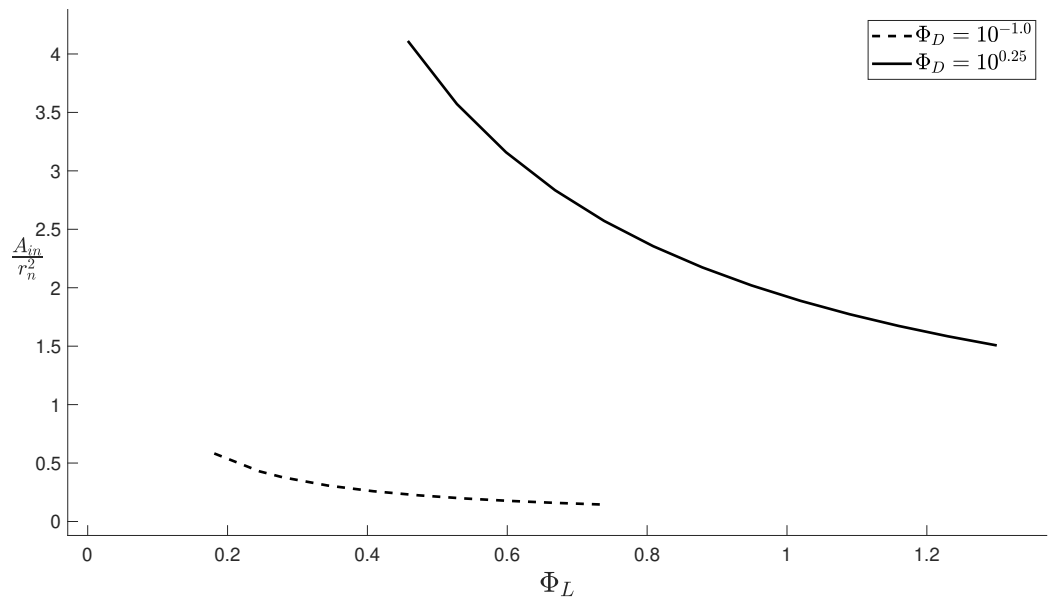
A**B**

Fig. 4.19 A:Area and cubic velocity for turbines with different duty flow coefficient. B: Non-dimensional inlet area for turbines with different duty flow coefficient.

4.10 Chapter Conclusions

Before moving onto the concluding remarks of this chapter, the author would like to remind the reader that these conclusions should be taken in the context and limitations of the RANS and the design methodology. The design parameter spaces produced in this thesis have necessary limitation. Many of the parameters were kept constant, where, in an ideal world they would be optimised. In addition to this, the numerical method itself has significant limitation which were discussed in section 3.2.1.

The overall goal of this chapter was to build an understanding of the shapes of the Smith and Balje chart for axial architectures. The key conclusions pertaining to this are:

- The topology of both Smith and Balje design spaces can largely be explained in terms of surface dissipation(velocity cubed rule), such that

$$\frac{\dot{S}T}{\rho} \propto \int^{A_{tot}} V^3 da = A_{tot} \overline{V^3}. \quad (4.12)$$

This was then used to show that, in regards to the Smith chart, the drop in efficiency at high local flow coefficients and low loading coefficients is driven by high surface velocities and that the drop in efficiency at low local flow coefficients and high loading coefficients is driven by high surface area. As for the Balje diagram, the drop at high duty flow coefficients is similarly a result of high surface velocity.

While the Mach numbers in this study are low, it can be concluded that for increasing rotational Mach numbers, designs with higher duty flow coefficients experience the onset of compressibility effects earlier than designs to the left of the space due to higher surface velocities.

There is no drop in performance when moving to lower duty flow which is also reflected by the area and velocity contours. In the design space study presented here, the trailing edge and tip gap ratios were kept constant. This is not maintainable for real machines with real world tolerance, which implies that the left hand bound of the design space will be set by manufacturing design tolerances. In addition to this, low Reynolds number effects will likely come into play for design in this region of the design space.

- It was analytically shown that the meanline flow parameters can shift the work split, for the case of zero interstage swirl, increases in loading coefficient not only increase loading but also shifts loading from the relative acceleration term to the change in absolute kinetic energy term. Increases in meridional velocity ratio shifts loading in the other direction (kinetic to acceleration). Therefore, decreasing meridional velocity ratio can improve total to static performance by reducing exit kinetic energy.

- The contributions from the individual loss mechanisms to the shape of the Blaje and Smith chart was studied. With regards to the Smith chart, the profile loss contributes significantly to the rise in loss for increasing loading and local flow coefficients. The rise in loss at low local flow coefficients and high loading is attributed to high profile surface area, whereas the rise in loss at high local flow coefficients is attributed to high surface velocities. The end wall loss contributes mostly to the increase in loss with increasing loading and local flow coefficients, which is driven by secondary flow. End wall surface dissipation does, however, contribute to a small increase in loss with increasing flow coefficient. The results for tip leakage flow are not entirely clear since the interaction between tip leakage and secondary flow could not entirely be decoupled. The result suggests that the leakage loss increases with decreasing loading and increasing local flow coefficient, and shows a reduction in loss at higher loading, which is not predicted by Denton's model. This might stem from an interaction with secondary flow.

As for the Balje chart, the profile loss contributes to the rise in loss at high duty flow which is attributed to the high surface velocities in this region of the design space (due to high local flow coefficient). The profile loss is also responsible for an increase in loss with loading. The secondary flow loss is shown to have a similar topology to the profile loss, but with a significantly higher increase in loss with loading. This is attributed to the increase in flow turning with loading. Similar to the Smith chart, the tip leakage loss increases with reducing loading. In addition to this, the leakage loss rises at high values of duty flow. This is attributed to a high over tip driving pressure and high velocity with which the leakage flow is mixing.

- It has been shown that the profile and secondary flow loss models designed for multiple architecture types functions fairly well for the axial design spaces produced in this work. However, the secondary flow model does significantly over estimate the increase in loss at high duty flow coefficients and at low loadings. It must be pointed out that a more rigorous secondary loss model has been developed for axial turbine cascades by Coull and Clark [15], which should instead be used when modelling axial machines. The tip leakage model derived by Denton [26] is in agreement with the CFD at low loading but predicted a rise in loss at higher loading coefficients were the CFD predicts a reduction. This might be due to the aforementioned interaction between the secondary and tip leakage flows.

There are number of potential improvements that should be considered for future work. First and foremost, stators should be introduced into the simulations. While it is unlikely that these will change the topology of the design space, these components will obviously increase lost efficiency and will shift performance boundaries.

another such improvident would be the optimisation of the circulation coefficient(blade count) and velocity profile. As previously shown, the diffusion factor varied with local flow

coefficient. One means of reducing uncertainty and improving performance would be to optimise circulation coefficient while constrained by a maximum diffusion factor.

A choice was made to design for zero interstage swirl, so that the data could be used for both total to total and total to static design spaces. However, when considering only applications where total to total efficiency is important, it would be best to optimise the interstage swirl(or reaction) at given region of the design space. Finally, a simple free vortex distributions was used across the design parameter spaces. At low duty flow, where the hub to tip ratios are close to unity, vortex design will have little effect on performance, however, at high duty flow where hub to tip ratios are low, optimal vortex design could have a strong impact on efficiency potential expanding the usable design space to high duty flow coefficients.

Chapter 5

Radial Turbine Design Space

5.1 Chapter Objectives

The following chapter explores both Smith and Balje/Rohlik radial turbine design spaces (rotor only), mapped out using RANS. The key objectives of this chapter are as follows:

- To show where the general shapes of the design spaces can largely be explained in terms of surface dissipation, decompose this into the individual contribution of area and surface velocity cubed and explore where this comparison breaks down.
- To explore the limitations of radial blade fibred designs.
- To explore the effects of design parameters on performance and the work split, including the effects of changing radius ratio.
- To understand how the individual loss mechanism shape the design space and understand what drives the shape of the loss distributions where possible.
- For the Balje/Rohlik diagrams, compare the individual loss mechanisms with simplified models that are derived with physical interpretation of the flow.

As with the axial design space, this will build a deeper understanding of the radial design space and allow for more informed decisions during the preliminary stages of design.

5.2 Radial Smith Chart

As previously discussed, Smith charts are constructed by varying both ψ and ϕ_L while ideally keeping other parameters constant. For axial architectures, this is usually a hub to tip ratio which is equivalent to fixing the non-dimensional through flow area $\frac{A}{r_m^2}$. The same is done in this

section. This is paired with a fixed radius ratio and axial length, resulting in a similar meridional geometry across the space.

In addition to this, the following non-dimensional parameters were kept constant:

Table 5.1 Radial Smith chart parameters

Parameter	Value
$\frac{A}{r_m^2}$	2
R_r	0.7
R_{vm}	1
$\frac{TE}{C_x}$	0.025
$\alpha_2(\text{mean})$	$0 \pm 4\text{deg}$
$C_o(\text{mean})$	$0.7 \pm 6\%$
$\Delta\eta_{ne}$	$0.09\% \pm 0.035\%$

5.3 Total to Total Isentropic Efficiency

Figure 5.1(A) is a rotor-only Smith chart generated using the design methodology introduced in Chapter 2. The solid black contours show the total to total isentropic efficiency from numerical solution. The blue dashed contours show an equivalent total to total isentropic efficiency calculated using surface dissipation as found in Denton [26] and discussed in Section 1.3. The figure also shows the meridional geometry which is similar for all designs in the space.

The axial turbines in the previous chapter were designed so that the stagnation point lay on or very close to the leading edge and therefore will have low effective incidence. This is not the case for the radial architectures presented here as these have been designed with radial fibres and therefore the inlet blade metal angle is fixed to zero for all points in the space. Since flow angles vary, the incidence also varies as shown by the grey dashed contours in Figure 5.1(B).

However, it must be noted that this is not the effective incidence that the leading edge experiences. The effective incidence is higher as a result of the so-called incidence effect, discussed in Section 1.2. To briefly recap, it is a result of angular momentum being partially conserved in the inducer region, (radial section). The effect that incidence has on the velocity profile can be seen in Figure 5.2. The turbine with a loading coefficient of 0.92 has the stagnation point on the leading edge which results in a velocity profile with gradual acceleration on the suction surface. The other two profiles with increasing effective incidence exhibit an over-acceleration towards the leading edge and a region of stagnated flow on the pressure surface for the highest loading case.

The numerical solution in Figure 5.1 shows a peak in total to total isentropic efficiency around $\psi = 1.00$ and $\phi_L = 0.4$. This differs from the radial Smith chart presented in Chen and Baines [13] where the peak efficiency is below a loading coefficient of 1 (Appendix B.6). The difference likely stems from multiple sources. Firstly, the blade profiles in this work are smooth, including the leading edge i.e. they have no discontinuities in thickness and curvature. This is due to the use of a shape-space based profile. Many of the radial turbines presented in Chen and Baines [13] have blunt leading edges and therefore are more prone to separation as a result of incidence. This would reduce the performance of more highly loaded designs. Secondly, boundary layers in this thesis are fully turbulent with a simple mixing length turbulence model. This might delay the onset of flow separation. In addition to this, mixing length models typically work well for self-similar shear flows with a well known mixing length, after the boundary layer has separated the assumptions used in the model will break down. Therefore any loss generated in the separated regions will be inaccurate.

Finally, the inlet flow conditions in the work presented are a simple boundary layer profile and any loss associated with an increase in secondary flow might be under represented. However, the radial turbine studied by Hunstmann [35] had peak performance with a slight amount of positive effective incidence and the associated velocity profile had a similar distribution at the leading edge to the profile with a loading coefficient of one in Figure 5.2. This would suggest that small amounts of positive effective incidence might be beneficial in some cases. It must be noted that Hunstmann's turbine had a rounded leading edge and would be less prone to separation than a turbine with a blunt leading edge.

Surface dissipation captures the shape of the variations with changing local flow coefficient reasonably well, particularly for loadings coefficients around 1. On the other hand, the absolute values differ significantly when using $C_d = 0.002$, (as much as $\Delta\eta = 4\%$ at high local flow coefficients). As discussed in Section 4.2, a simple surface dissipation model does not capture secondary flow and tip leakage losses. The surface dissipation contours match poorly at higher loadings. This is a result of incidence loss which will be discussed in more detail later.

As with the axial architectures, it is of interest to analyse the design space in terms of area and average surface velocities. Figure 5.3 shows that the drop in performance with reducing local flow coefficients is driven by increasing surface area and that the drop in performance with increasing local flow coefficient is driven by increases in surface velocity; both are a similar seen in the axial turbines. An explanation for these variations has already been given in Section 4.2.

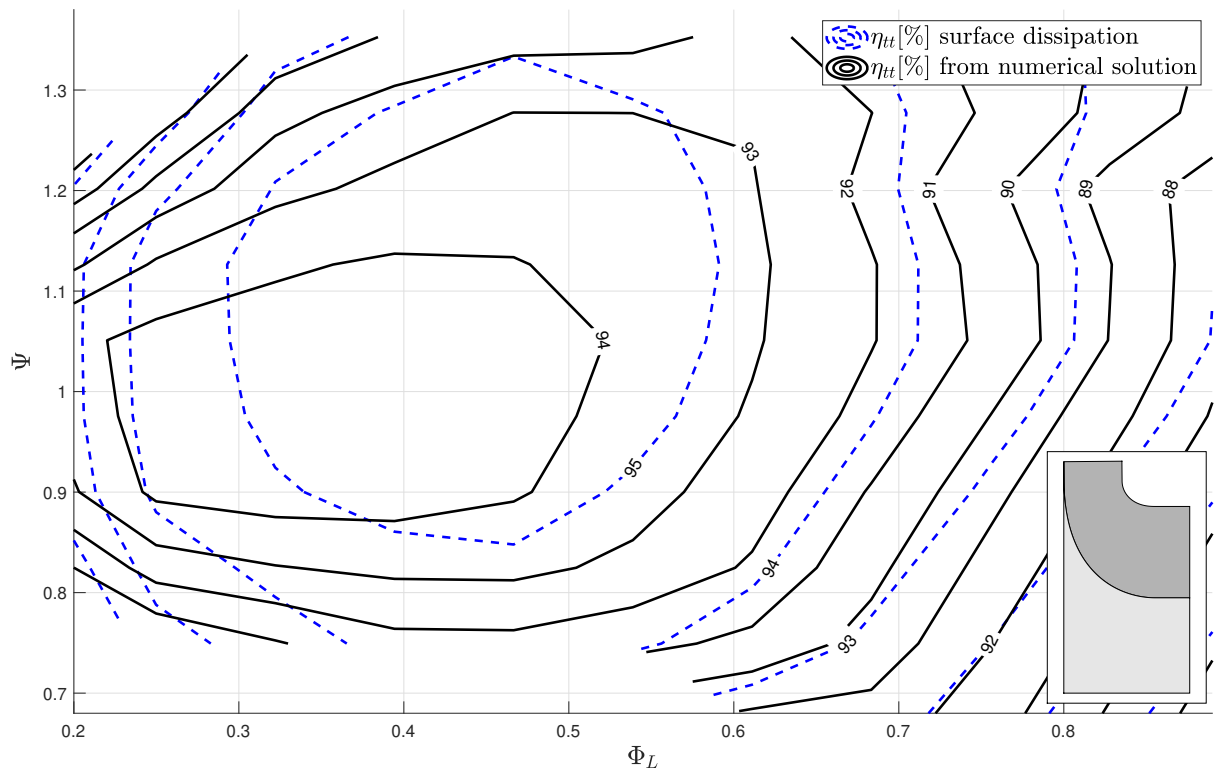
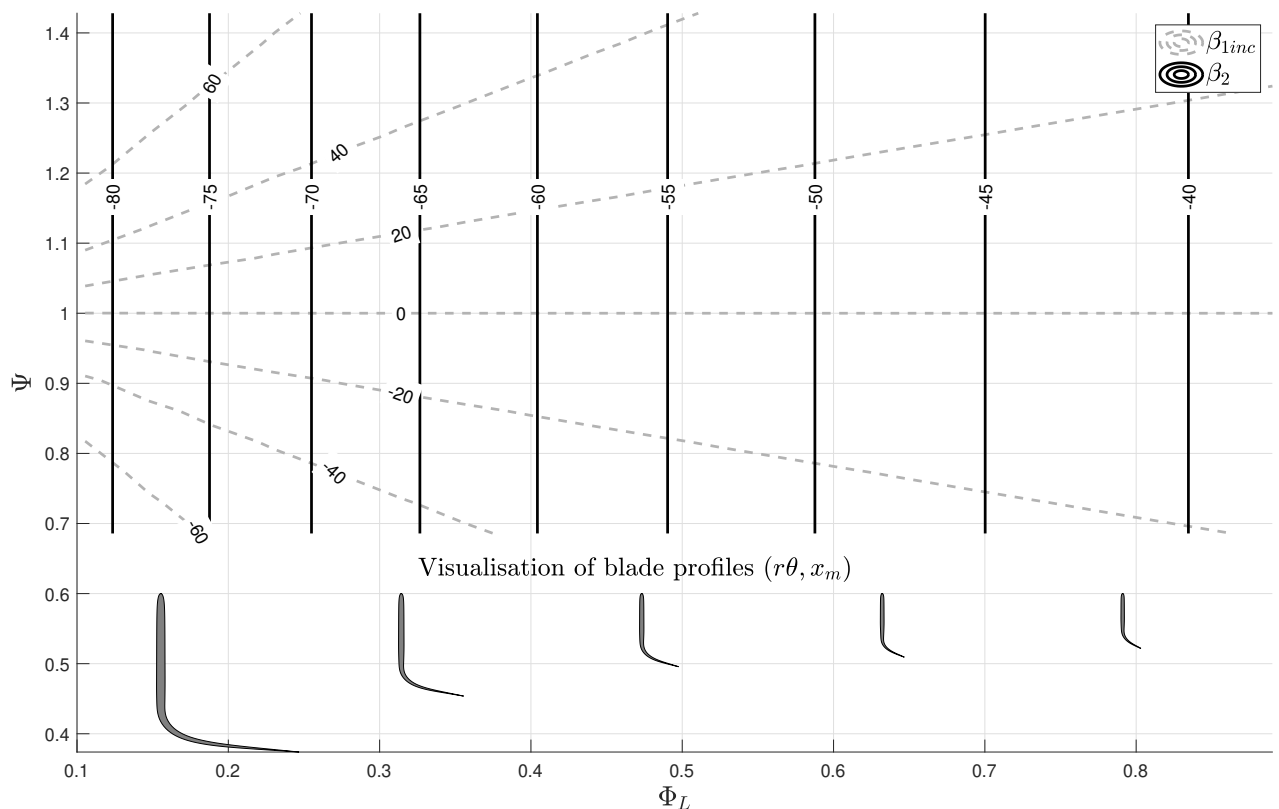
A**B**

Fig. 5.1 A: Total to total Smith chart with fixed $R_r = 0.7$ and $\frac{A}{r_n^2} = 2$. B: Inlet and exit meanline flow angles.

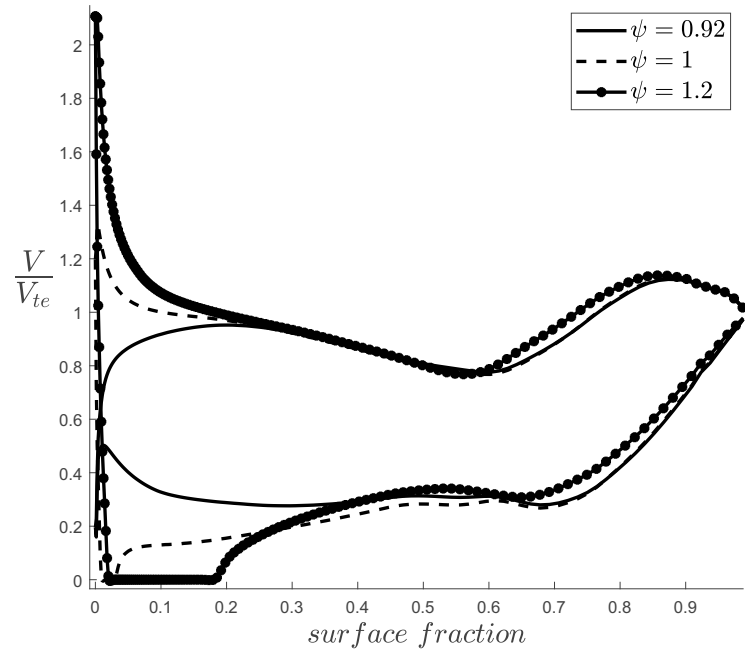
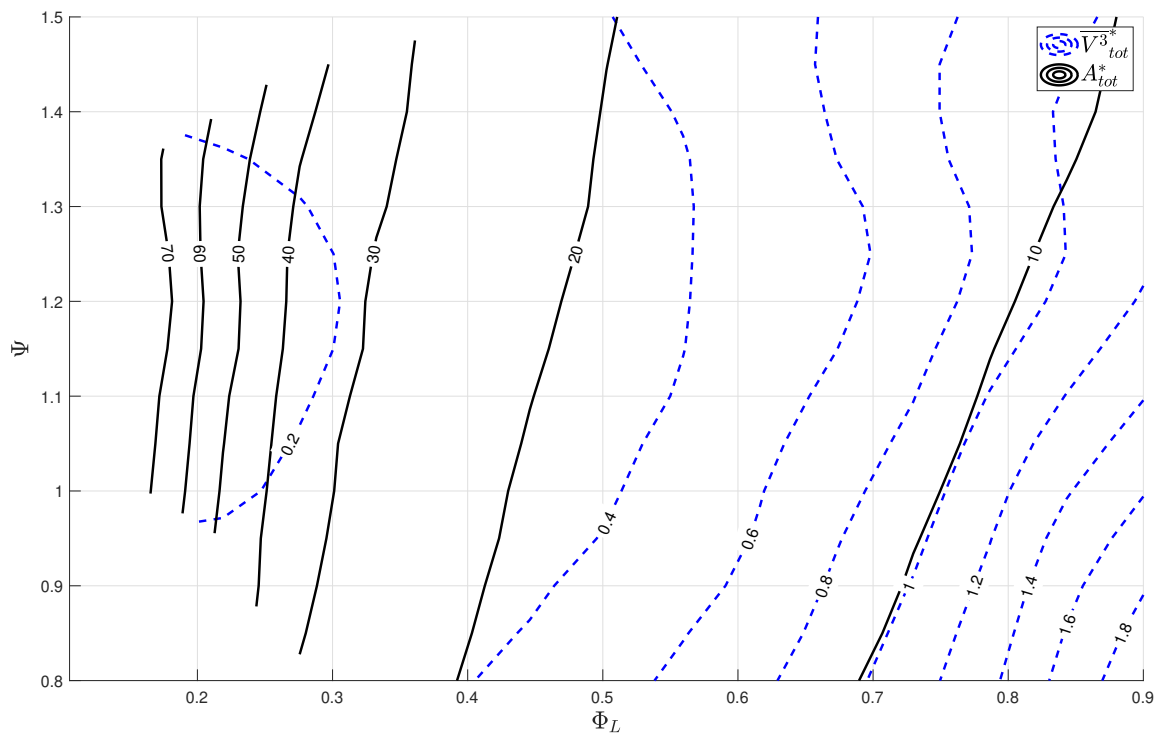


Fig. 5.2 Radial turbine isentropic velocity distributions for different levels of loading, $\phi_L = 0.3$



5.3.1 End Wall & Incidence Loss

Figure 5.4 shows a very rough estimate of the combined secondary and incidence loss. This was calculated by assuming $C_d = 0.0025$ and approximating profile loss with surface dissipation. The combined incidence and endwall loss can then be estimated as the difference between the total lost efficiency and the profile loss. This was done with a tip clearance of 0.1 to ensure minimal contribution from tip leakage.

It is clear from Figure 5.4 that the performance variation with loading (Figure 5.1) is mostly driven by the combined secondary/incidence loss. This is the reason most radial architectures operate at low loading coefficients compared to axial architectures. Mixed flow architectures can reduce this loss by allowing the blade metal angle at the inlet to vary while still maintaining radial blade fibres.

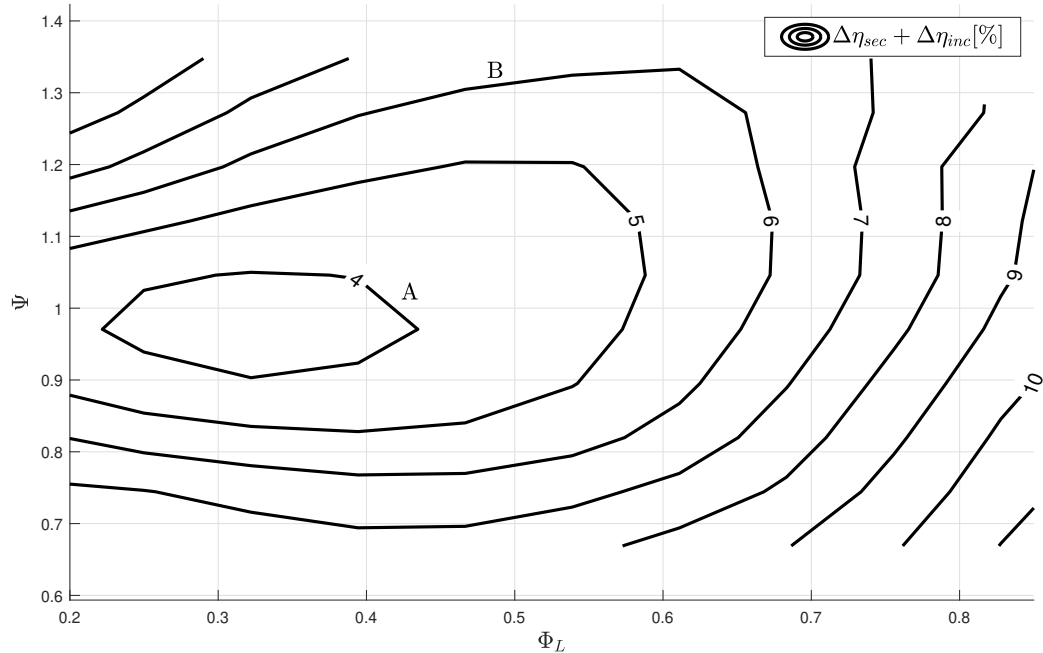


Fig. 5.4 Inlet and exit meanline flow angles

For radial turbines with sufficiently high incidence, the flow separates off the leading edge and rolls up. The separated flow is then driven along the casing due to the pressure field associated with the radial to axial bend which was discussed in section 1.2. The adverse effects of high incidence has on the exit flow field is illustrated in Figure 5.5, where the exit flow field of two turbines with differing levels of incidences is shown. Turbine A has low incidence and no separation. As a result, the passage loss cores are smaller and positioned close to the suction surface casing corner. For turbine B, the loss core is significantly larger and sits between the pressure and suction surface.

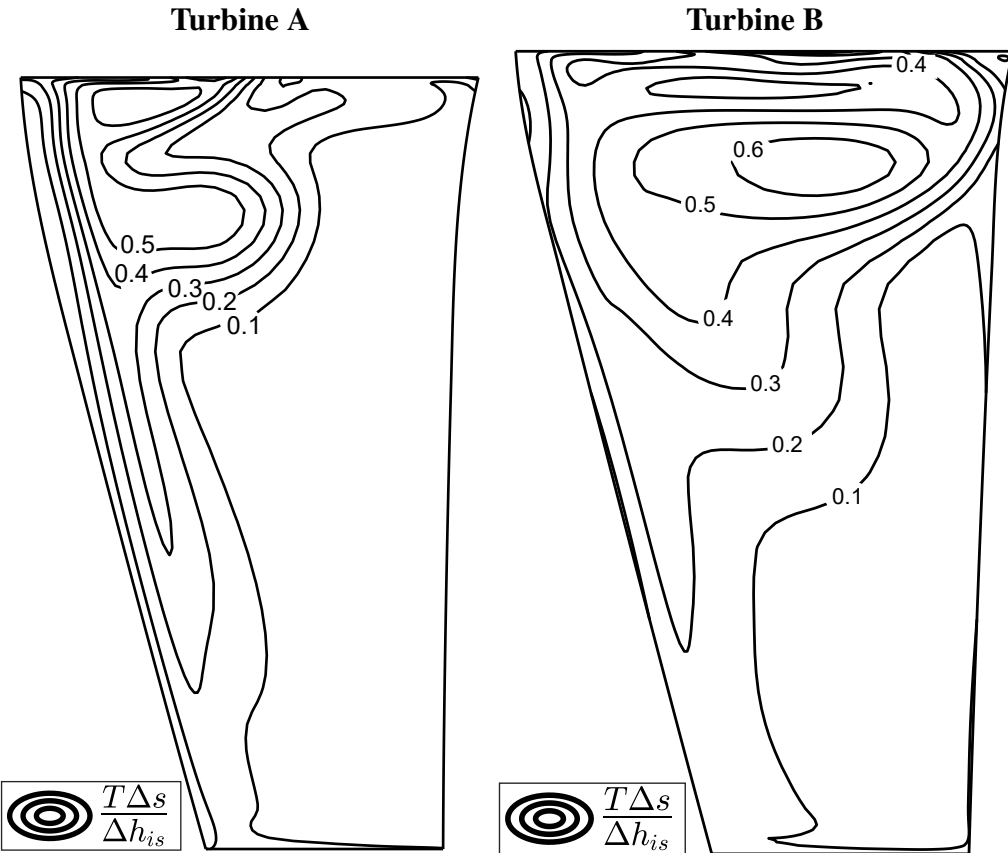


Fig. 5.5 Comparison of exit flow conditions at two different points on a Smith chart.

5.4 Total - Static Isentropic Efficiency

A total to static Smith chart is shown in Figure 5.6. The chart suggested that the optimum local flow coefficient resides between values of 0.2 and 0.3, in agreement with Chen and Baines [13] (Appendix B.6). However, the shape is considerably different and is likely due to the under prediction of incidence loss as previously mentioned. It must be noted that the chart produced by the aforementioned authors were constructed by a curve fit through various turbines taken from literature with varying design parameters. This would make a direct comparison problematic.

Many of the observations made in Section 4.3 for axial total to static Smith charts are applicable here. This is simply because of the behaviour of exit loss. As discussed in Section 4.3, the optimal total to static performance is driven to lower local flow coefficients and to slightly higher loading coefficients due to the inclusion of this loss.

The blue contours in Figure 5.6 are calculated using $C_d = 0.0025$. With this value of dissipation coefficient, the contours of total to static efficiency calculated using a surface dissipation do not match well in terms of shape and locations of optima. The entropy loss predicted by surfaces dissipation is simply too low in this region (high secondary flow) and is washed out by the exit loss. Again, using an artificially high value $C_d = 0.0065$ can achieve a good match in contours (Appendix B.5).

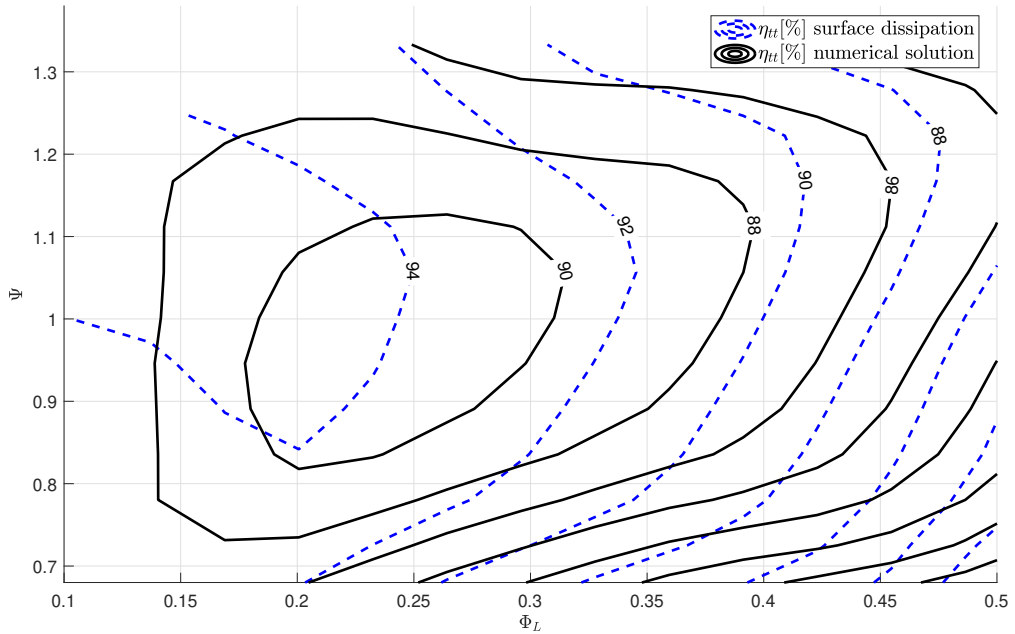


Fig. 5.6 Total-static Smith chart with fixed $R_r = 0.7$ and $\frac{A}{r_n^2} = 2$.

5.5 Radial Turbine Balje/Rohlik Diagrams

The following section explores the computationally constructed Balje/Rohlik diagram of radial turbine rotors. As discussed in Section 4.6, in order to form a Balje diagram, the full set of mean line design parameters needs to be reduced to

$$\eta(\Psi, \Phi_D).$$

Considering that the variation with loading is dominated by incidence this will be further reduced to

$$\eta(\Phi_D) \psi = 0.925,$$

where the effective incidence is close to zero. This also sits close to the optima predicted by [13].

As before, most parameters will be kept constant and an optimal value for Φ_L will be selected. Unlike axial turbines, the mean line radius ratio was varied. This was done in such a way as to maximise centrifugal loading.

This was achieved by fixing the hub radius ratio to a low value, in this case $R_{rhub} = 0.2$, but still allowing space for a drive shaft. Fixing the hub radius ratio allows radial turbines with

lower $\frac{A}{r_n^2}$ to have a larger centrifugal term, since

$$\psi_{cent} = \frac{1}{2}(1 - R_r^2)$$

. This is illustrated in Figure 5.7. The decision to do this is discussed in Section 5.9 but in short, maximising the centrifugal term for radial turbines improved performance by reducing the average flow velocity through the passage. Rohlik [46] did something similar by reducing diameter ratios at lower specific speeds but chose to keep them constant above a specific value. As with Rohlik's work, maximising the centrifugal term across the Balje diagram leads to architectures with low duty flow coefficients having lower radius ratios (larger centrifugal component) and vice versa. This is because designs at low duty flow coefficient have low $\frac{A}{r_n^2}$, allowing these designs more space to reduce the radius ratio as illustrated in Figure 5.7.

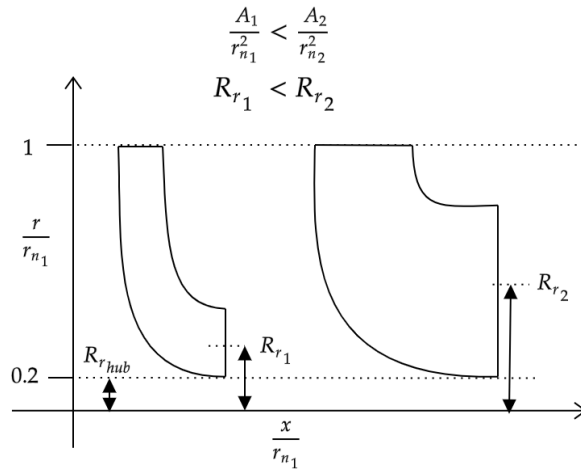


Fig. 5.7 Non-dimensional meridional geometry.

The following parameters were kept constant:

Table 5.2 Radial Balje/Rohlik chart parameters

Parameter	Value
R_{vm}	$1 \pm 4\%$
$\frac{TE}{C_x}$	0.025
$\alpha_2(\text{mean})$	$0 \pm 4\text{deg}$
$C_o(\text{mean})$	$0.7 \pm 6\%$

5.6 Total to Total Balje Diagram

Figure 5.8(A) shows the variation of total to total isentropic efficiency with duty flow coefficient. The total to total efficiency drops off at both high and low duty flow coefficients.

The change in efficiency at lower duty flow differs significantly from the axial architectures presented in Figure 4.12, where the efficiency of the axial architectures remained constant. It will later be shown that the drop is a result of high end wall dissipation, driven largely by the casing surface. The reduction in performance at high duty flow is noticeably steeper than that at lower duty flow coefficients. This will be shown to be a consequence of both a rise in all loss mechanisms and flow separation occurring at the casing.

As before, a comparison with surface dissipation is included. The blue dashed lines represented an equivalent efficiency calculated using $C_d = 0.002$. The figure shows that surface dissipation captures the overall rough trends in performance. In particular, the surface dissipation reflects the more gradual drop at lower duty flow than at high duty flow. However, the optimum for surface dissipation is at higher duty flow coefficients. Additionally, the numerical solution is largely flat close to the optimum. As previously discussed, simple surface dissipation does not include the effects of tip leakage and secondary flow loss. Figures 5.10 and 5.12 show a rise in these loss mechanisms with increasing duty flow coefficient. That being said, decoupling velocity and area still serves a purpose in characterising different designs throughout the space. From Figure 5.8(B), as with the axial design space, turbines at high duty flow coefficients have high surface velocities and those at low duty flow coefficient have high surface area. While similar in nature to axial architectures (Figure 4.12), there is no "2D" region at lower duty flow coefficients. This is a consequence of the reducing radius ratio (increasing ψ_{cent}) and will be discussed in more detail in Section 5.9.

Included in Figure 5.8 is a total to total "like" efficiency calculated by Rohlik [46] (Figure 1.13). To briefly recap Section 1.5.2, Rohlik analytically calculated the optimum efficiency and geometry with the use of loss correlations. The line extracted from Figure 1.13 represents a combination of the lost efficiency for tip leakage and "rotor loss" (without stator and windage loss). Making a direction comparison should be done with caution as the ideal geometries presented by Rohlik differ to those used here. That being said, it seems that the correlation used for rotor loss, which is the dominant term, over predicts the loss at lower duty flow coefficients (lower N_s). The optimum total to total performance is predicted to be at significantly higher duty flow. Potential sources of difference between Rohlik's space and the one presented here are as follows:

- Rohlik only optimised the turbines for best total to static performance.
- The loss model used by Rohlik for the rotor loss was developed for axial turbines and is unlikely to function well for geometries with significantly different shapes.

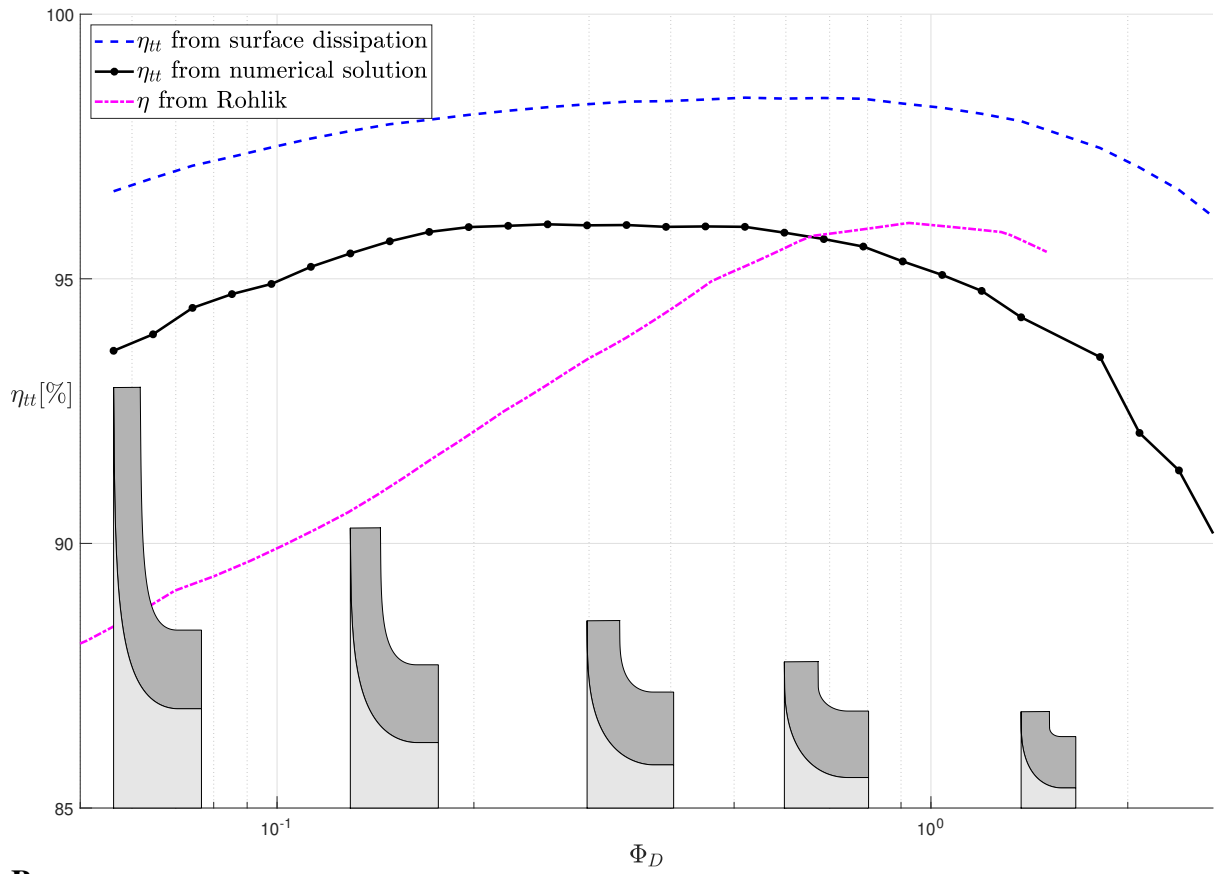
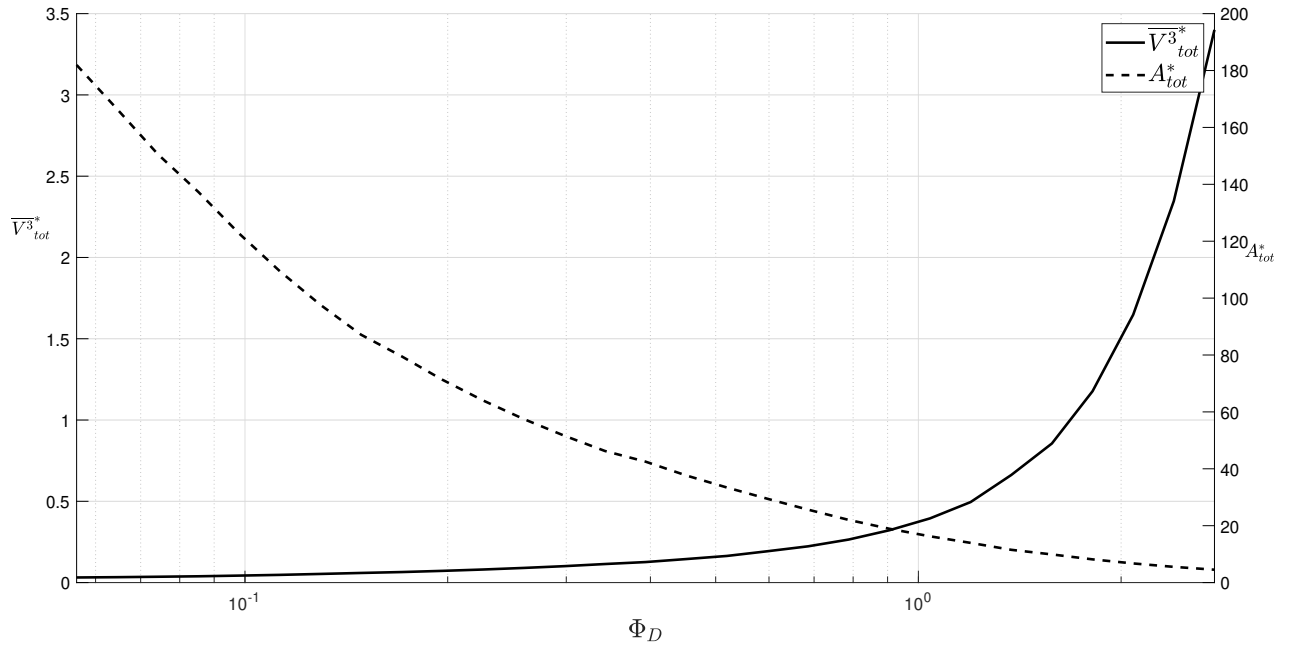
A**B**

Fig. 5.8 A: Total to total Balje diagram with optimised local flow coefficient and hub $R_{rhub} = 0.2$.
B: Blade surface area and surface-area averaged cubic velocity.

- The end wall loss is calculated by linearly scaling profile loss with aspect ratio. It also does not include effects of passage/casing curvature which are important for the high casing curvature designs to the right of the design space.
- The loss is not a direct function of surface velocities which also drives up loss at high duty flow.

5.6.1 Profile loss

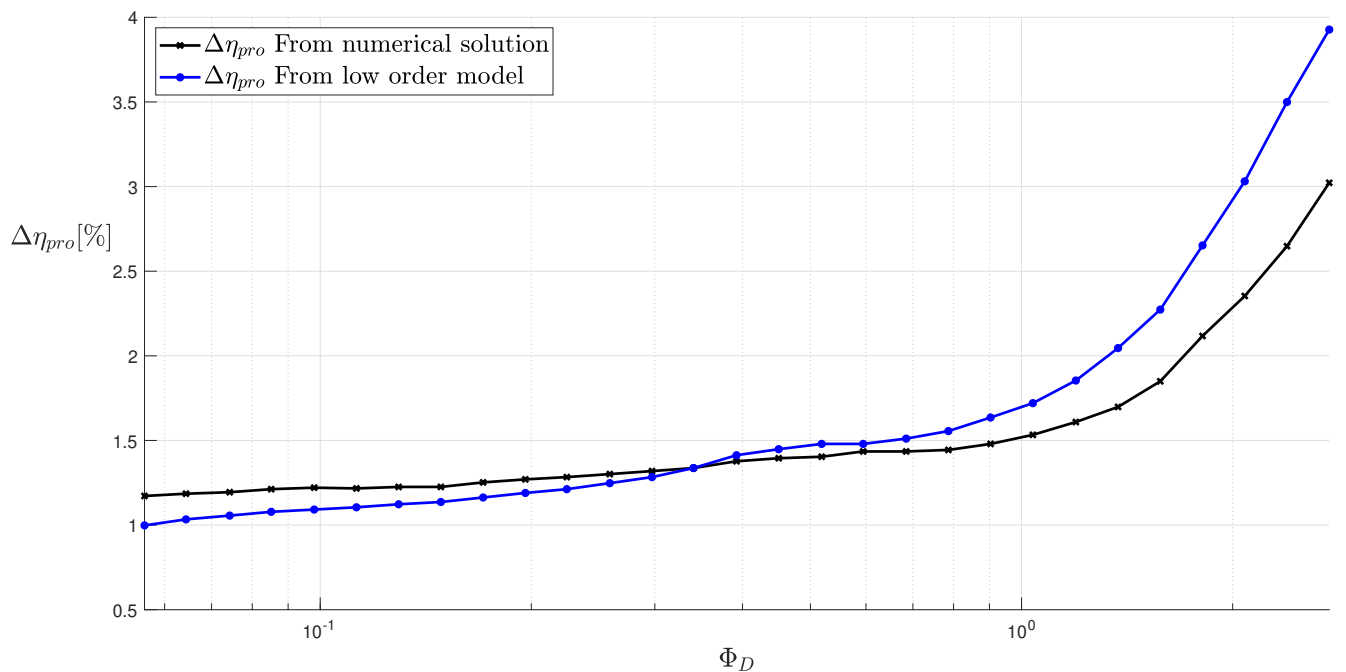


Fig. 5.9 Estimated loss in isentropic efficiency as a result of profile loss.

The profile loss across the design space is presented in Figure 5.9. At low duty flow, the loss is low and largely insensitive, then rises sharply at higher duty flow. This behaviour is directly tied to the surface velocities seen in Figure 5.8 B. As with axial turbines (discussed in Section 4.2), the rise in surface velocity at higher duty flow coefficients is largely a consequence of the higher design local flow coefficients (Figure 5.15). In addition, the drop in radius ratio and therefore centrifugal loading will also result in increased surface velocity for a given loading. This will be discussed in further detail in Section 5.9.

While the profile area does rise at lower duty flow, it does so far less than presented in Figure 5.8 B which is a combination of both end wall and profile surface area. In this case, most of the rise in total surface area is a result of the end wall.

The model developed in Section 3.1.1 captures the behaviour reasonably well, though there is significant over-prediction and under-prediction of flow velocities at high and low duty flow

respectively. On further inspection, the errors stemmed largely from errors in the velocity profile model.

5.6.2 Endwall/Secondary loss

Figure 5.10(1) depicts the variation in end wall loss across the design space. Figure 5.11 shows the exit flow field for the corresponding points labelled on Figure 5.10(1) .

Turbines in the low duty flow coefficient range A are characterised by low aspect ratio meridional passages with large radial sections. The longer passages allow flow to develop significantly. This can be seen for Turbine A in Figure 5.11 where the loss core fills the entire passage, somewhat analogous to fully developed pipe flow but with a slight bias towards the suction surface.

The dominant loss source in this region is the end wall dissipation which is a consequence of the large proportion of surface area from the radial section. The contribution from end wall surface dissipation was estimated to be $\Delta\eta \approx 4.5\%$, of which 3.5% was from the casing surface. The reason for this large contribution from the casing is due to the high absolute velocities in the radial section. This would imply that a significant reduction in end wall loss can be achieved (in this region of the design space) with shrouded or partly shrouded rotors. Due to the relatively simple nature of this loss mechanism, the model captures the behaviour well in this region.

As a result of the increased effective aspect ratio at point B, the loss core takes up a lower portion (roughly half) of the exit flow. In addition to this, the contribution from the casing end wall is significantly lower at $\Delta\eta \approx 1.5\%$. As a result, the overall end wall loss is lower. At point C, the end wall loss remains relatively low and even less of the flow is taken up by the secondary flow loss core.

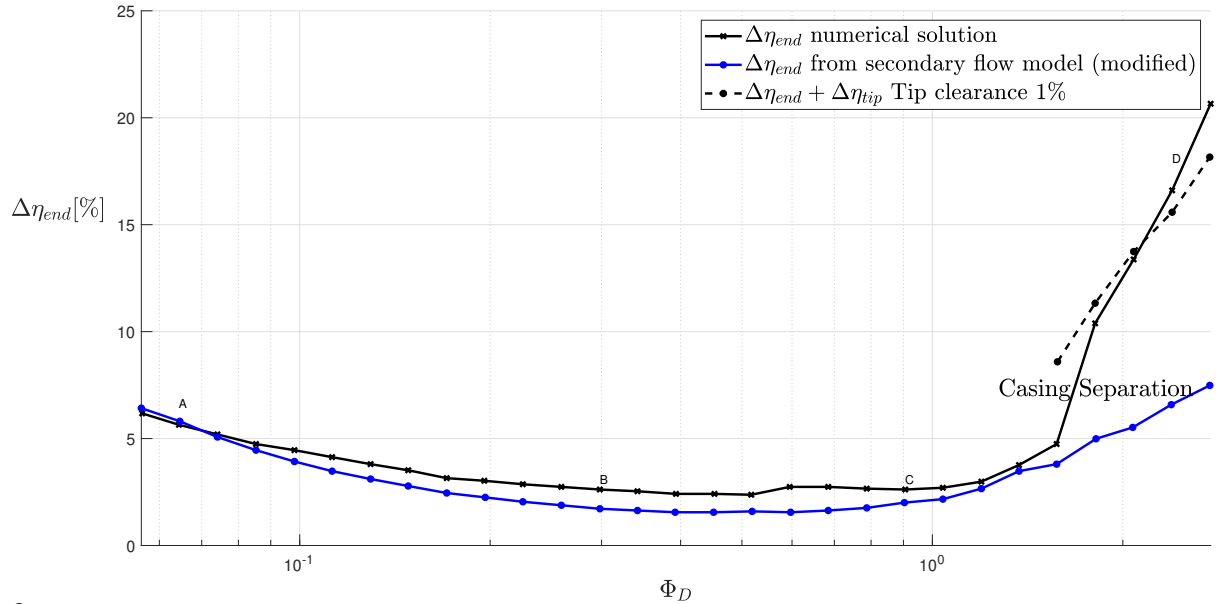
Turbines at high duty flow coefficients are characterised by small radii of curvature at the casing (Figure 5.10 2). This is because the casing radius of curvature is low at high inlet through flow areas ($\frac{A}{r_n^2}$) regardless of the axial length.

As the casing curvature increases, so does the end wall loss. This effect was isolated in Figure 3.7. The inevitable consequence is flow separation at the casing. This is due to the adverse pressure gradient downstream of the apex of the radial to axial bend, see section 1.2. The duty flow coefficient at which this occurs is annotated in Figure 5.10(1). The effects this has on the exit flow field can be seen for Turbine D in Figure 5.11, where a large loss core is present in the top left corner. The separation and sharp rise in this loss can be delayed by reducing the casing curvature. As discussed in section 2.2 and is illustrated in figure 2.9(A), this can be achieved by relaxing the design constraints which enforces the casing lines to be perpendicular to the span at the inlet. This relaxes the curvature but requires more detailed design as this will created a span wise variation in incidence.

The combined end wall loss model captures the behaviour up until the point of separation reasonably well. With further development, this model in conjunction with the profile loss

model could potentially serve as a architecture unifying "rotor loss" model, since they functions reasonably well for both axial and radial architectures.

1



2

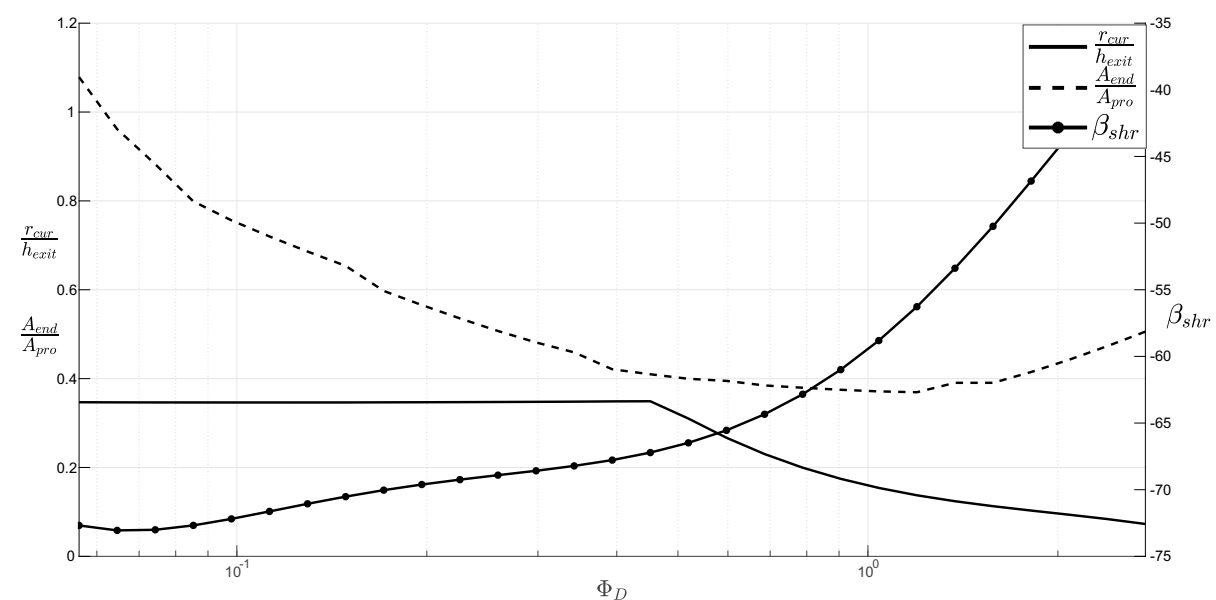


Fig. 5.10 A:Variation of endwall loss with duty flow. B: Variation of shroud meridional curvature, end-wall to profile surface area ratio and exit shroud blade angle with duty flow coefficient.

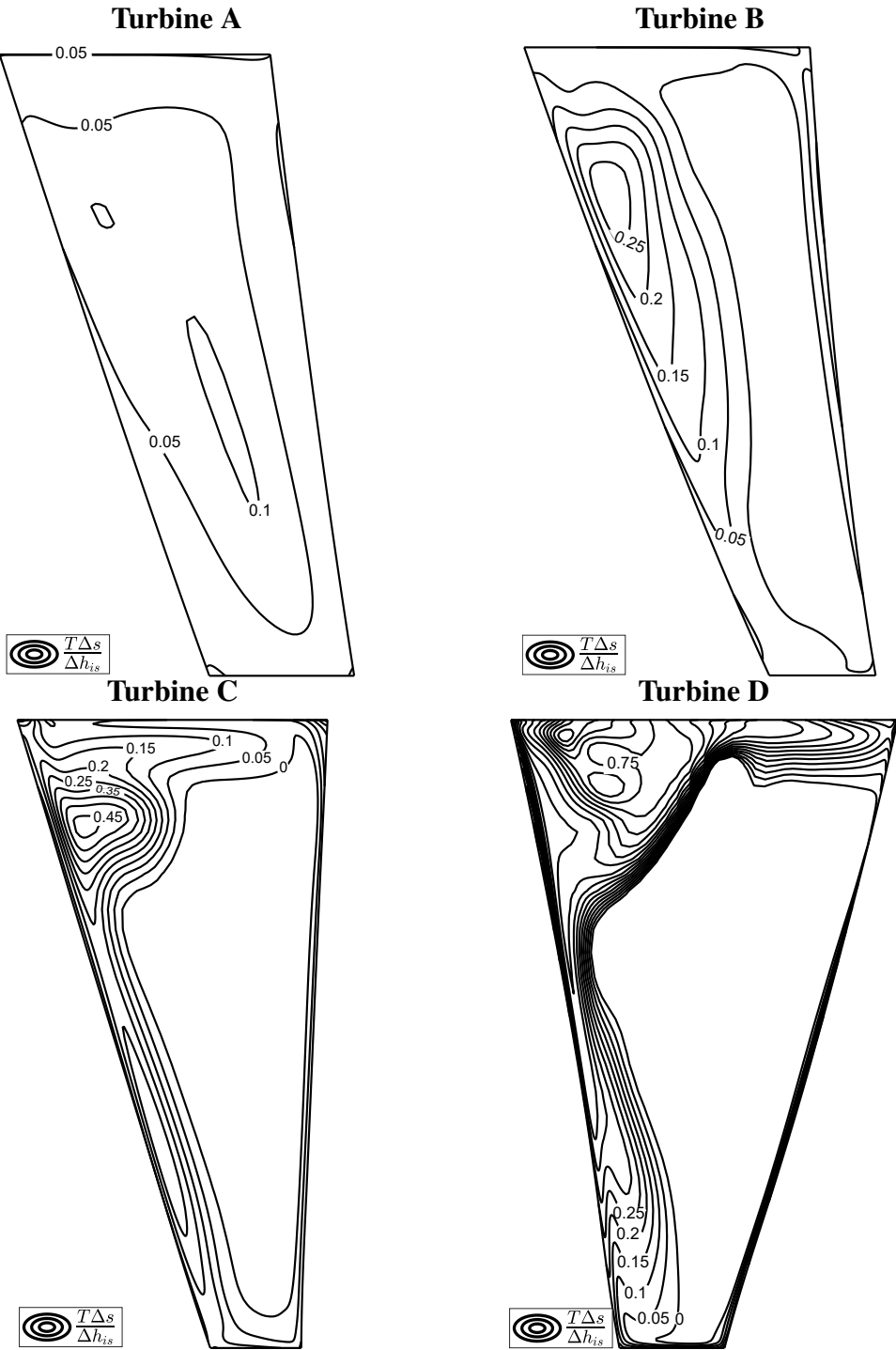


Fig. 5.11 Comparison of exit flow conditions at different points on a Balje chart.

5.6.3 Tip clearance loss

The tip leakage loss across the design space is presented in Figure 5.12. At low duty flow coefficient, the leakage loss is relatively low and insensitive to changes. This is likely a consequence of two effects. The first is that the radial sections are large in this region of the

chart. It is well documented that the inducer, (radial section) exhibits less tip leakage due to the scraping effect, as shown by Dambach and Hodson [23]. Dambach characterised the significance of this effect with a scraping ratio R_{scr} introduced in section 1.3.3. The scraping ratio essentially represents the ratio of leakage flow dynamic head to relative casing boundary layer dynamic head. The authors reported that for $R_{scr} < 1$, the scraping fluid is dragged through the gap obstructing the leakage flow. An area averaged scraping ratio is presented in Figure 5.12 and remains less than 1 for most of the design space. The second likely reason for low leakage loss at low duty flow coefficients, is the low velocities with which the leakage flow is mixing. From Dentons [26] loss model for tip leakage, the loss is proportional to $W_s^2(1 - \frac{W_p}{W_s})$. As seen in Figure 5.8(B), this region of the design space is characterised by low velocities.

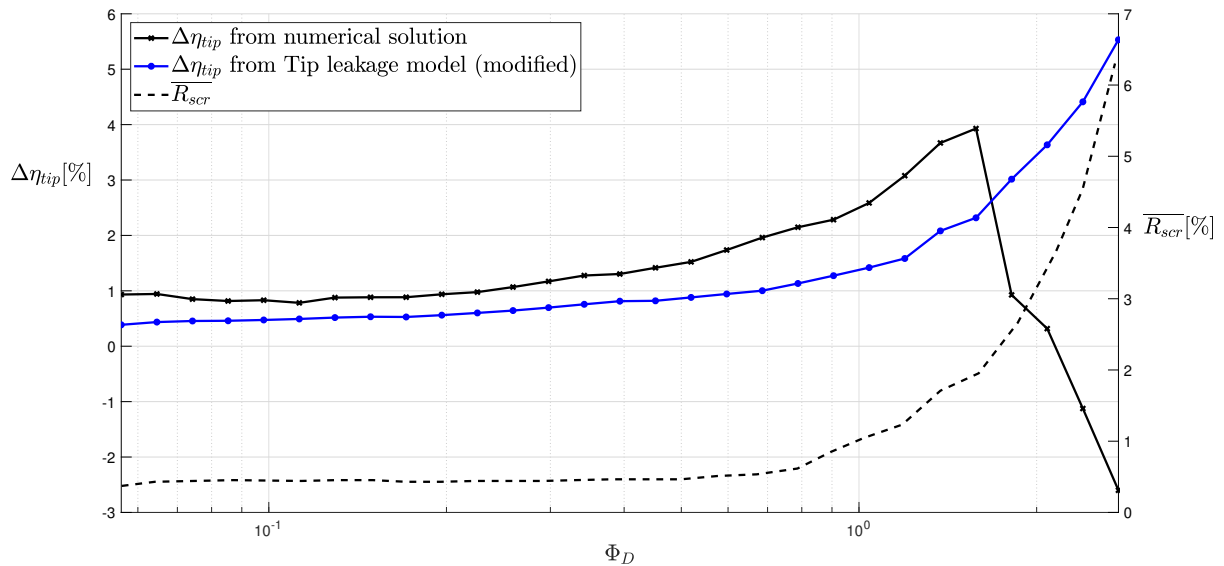


Fig. 5.12 Estimated loss in isentropic efficiency as a result of tip clearance.

The leakage loss rises at high duty flow coefficients. The radial section is decreasing so the scraping effect is reduced. In addition to this, the velocity through the turbine passage is now increasing, which according to Dentons [26] loss model, results in increase leakage loss.

At very high duty flow coefficient the decoupling of loss mechanism seems to break down (negative values) which is likely due to an interaction with the end wall loss. In Figure 5.10(1), the combined end wall-tip leakage loss decreases below the value of just end wall loss at roughly the same point at which the leakage loss in Figure 5.12 shows as negative. This suggests that the leakage flow is beneficial. The exact reason for this is unclear but the leakage flow might help suppress the secondary flow or casing separation. Examples of optimum tip clearances for radial architecture can be found in Kammerer and Natkaniec [37].

5.7 Total to Static Balje Diagram

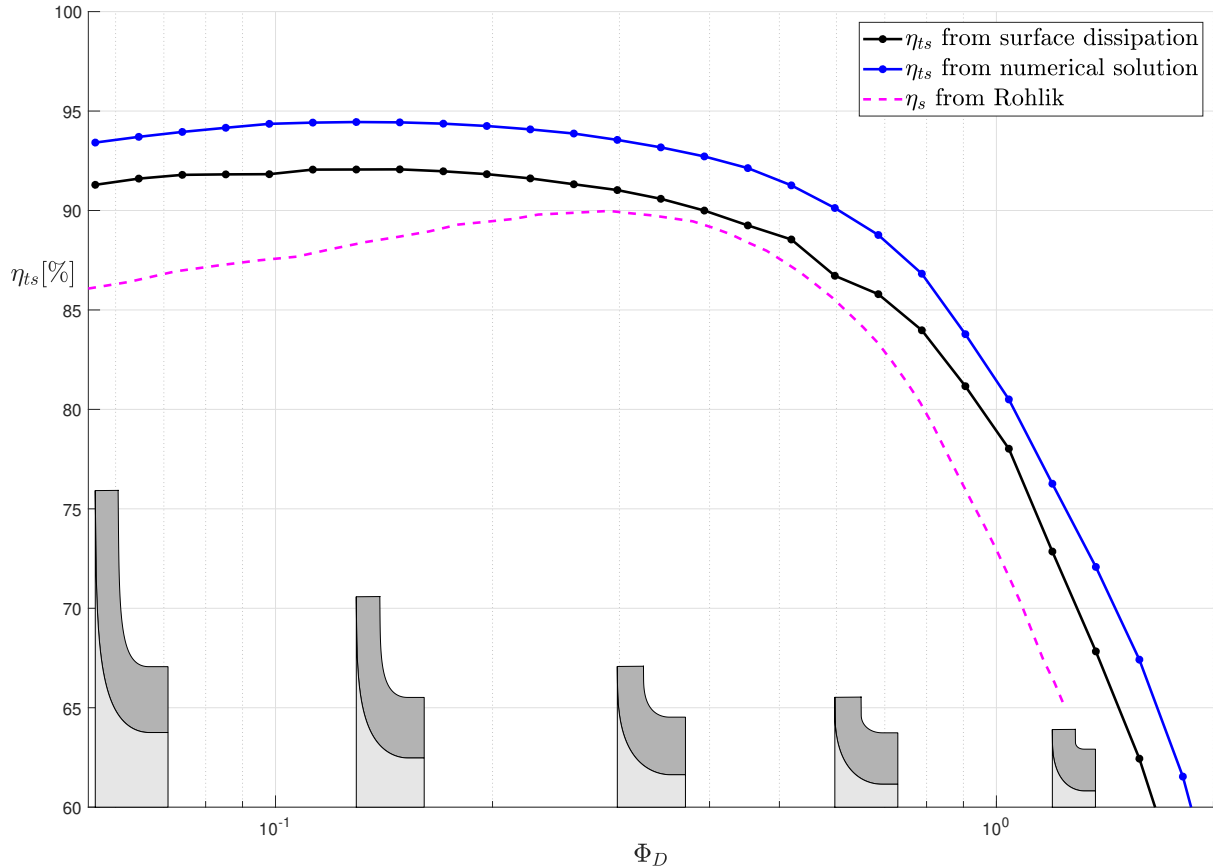


Fig. 5.13 Total to static Balje diagram with optimised local flow coefficient and hub $R_r = 0.2$

The variation in the total to static efficiency across the design space is plotted in Figure 5.13. As with axial turbines, the difference between the diagrams are driven primarily by exit loss, see figure 5.14. The effect that this has on the design space is as follows:

- A reduction of the maximum efficiency by 4%. This difference in performance is significantly lower than that of axial turbines (8%) and is due to the lower design local flow coefficients of the radial architectures. Like the axial architecture, some of this drop in efficiency is from the exit loss itself and entropy based loss being traded for lower exit loss.
- As it does with the axial architectures, the exit loss shifts the drop off in efficiency to lower values of duty flow coefficient. This is a result of the exit loss scaling with local flow coefficient squared. Designs at higher duty flow coefficient have higher local flow coefficients and hence will have increased exit loss.

Comparing the efficiency with that predicted by Rohlik, the lines show a far better match when compared to the total to total case. This is simply because the exit loss can be predicted with little-to-no error and since it is a dominant source of loss, particularly at higher duty flow, it washes out the difference in the other loss mechanism. That being said, the location of

optimum performance predicted by Rohlik is at higher duty flow coefficient. Again, this is a likely consequence of the rotor loss model and tip leakage used by Rohlik. When compared to the numerical solution, these models tend to overpredict loss at low duty flow coefficients.

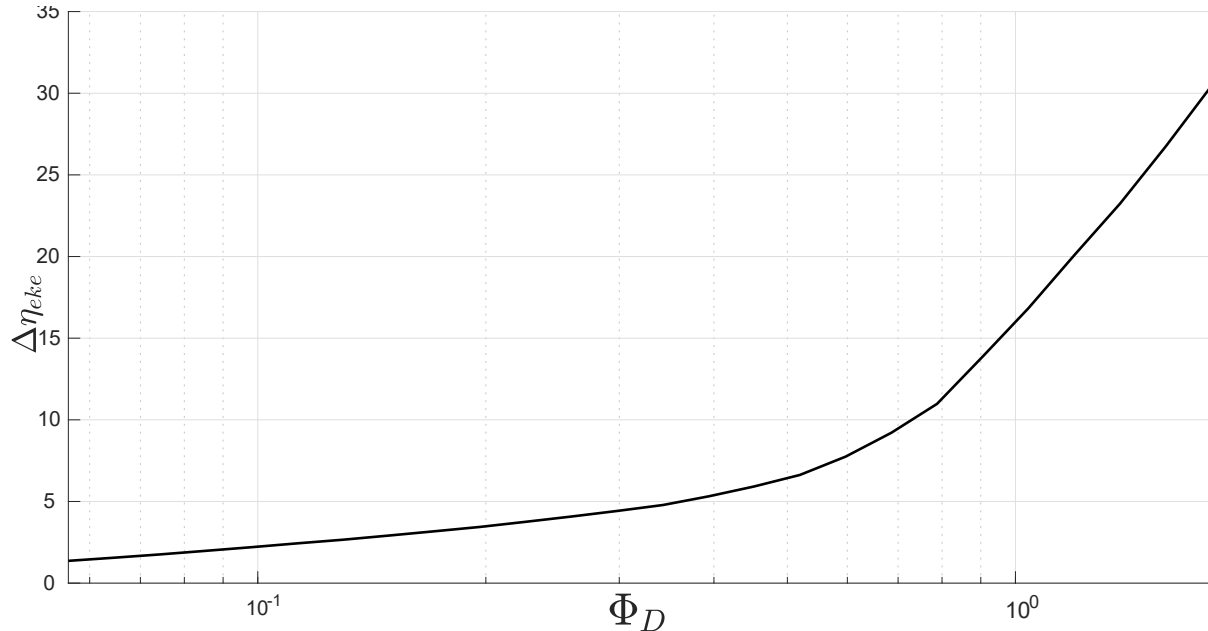


Fig. 5.14 Exit loss variation across design space.

5.8 Optimal Local Flow Coefficient

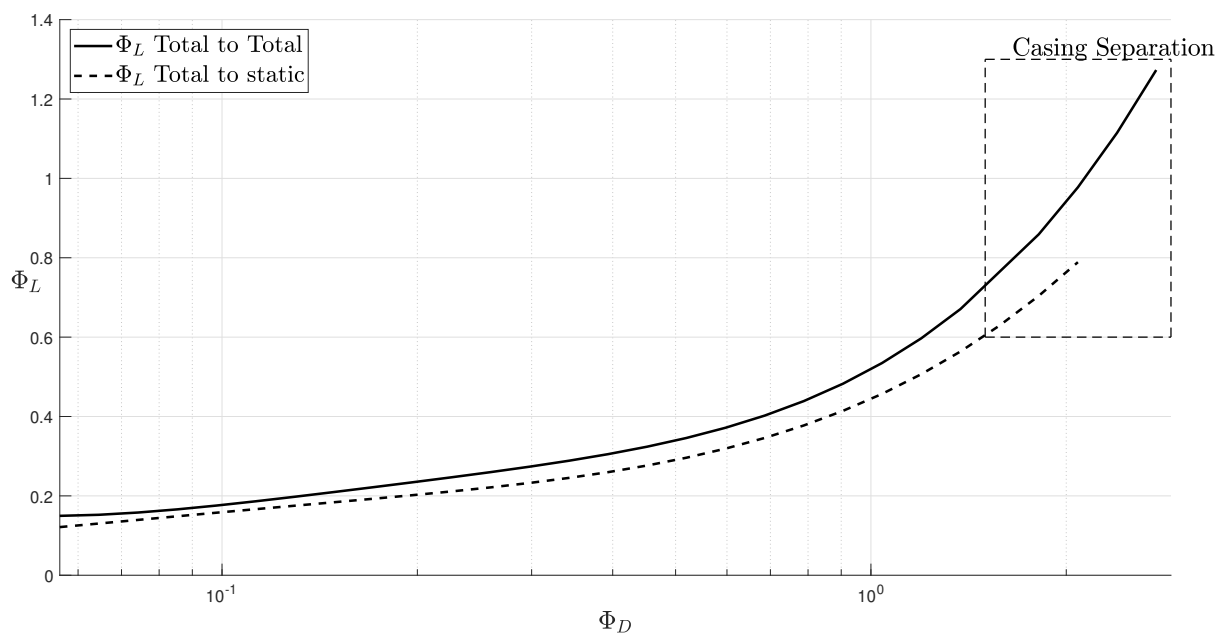


Fig. 5.15 Optimised local flow coefficient corresponding to Figure 5.8.

Figure 5.15 shows the variation of optimised local flow coefficient. Included is a region where casing separation occurred. Some of the architectures in this region used for the optimisation of local flow coefficient did not converge and peak performance could not be resolved. Instead, the highest performing converged solution is used.

There are some key differences when comparing Figure 5.15 to axial architectures in Figure 4.17. Firstly, radial architectures show considerably lower design local flow coefficients, particularly at low duty flow coefficients. The lower design local flow coefficients are characteristic of radial architectures and are a result of using reduced radius ratios. This can be seen in Figure 5.18 and will be discussed in further detail in that section. Another result is that the optimal local flow coefficient for best total to static and total to total efficiency are similar. This means that there is less trade-off between exit loss and other mechanisms, and hence radial architectures show higher total to static performance than a typical axial architectures. It is notable that the performance of axial architectures can be significantly improved by using lower meridional velocity ratios. Finally, unlike the axial architectures the optimal local flow coefficient varies significantly throughout the design space where as axial architectures have a "invariant" region where most of the change in duty flow is driven by changes in non-dimensional inlet area.

As with axial architectures, the optimum local flow coefficient for total to total efficiency resides close to that predicted by surface dissipation, see Figure 5.16. A simplified explanation can then be formulated to roughly explain the trends in Figure 5.15, again using the trade-off between area, velocity and their derivatives (Equation 4.11).

The manner in which these terms are being traded off differs to that of axial architectures. The push to higher local flow coefficients for axial architectures was primarily driven by an increase in $-\bar{V}^3 \frac{dA}{d\phi_L}$ which was driven by both an increase in velocity and steeper derivative of area. For radial architectures, the change is driven primarily by a reduction in $A \frac{d\bar{V}^3}{d\phi_L}$, which itself is largely driven by a reduction in end wall surface area (Figure 5.17).

At low duty flow coefficients the non dimensional through flow area, $\frac{A_{in}}{r_n^2}$ and radius ratios are characteristically low. As previously shown, this leads to low meridional aspect ratio and large amounts of endwall loss. Hence this plays a significant role in determining the optimal local flow coefficient.

Here, the optimal designs "attempt" to keep the local flow coefficient low to reduce velocity in order to minimise the end wall loss on this large surface. However, reducing local flow coefficient also increases the magnitude of the blade exit angle and profile area which in turn increases profile loss. Hence a balance is struck between the two.

At higher duty flow, the radius ratio and characteristic non dimensional inlet flow area is increased and with it comes a reduction in end wall surface area, (δA_{end}^* in figure 5.17). Therefore, the local flow coefficient does not need to be as low in order to compensate for the end wall loss and as such rises, decreasing the blade exit angle and surface area.

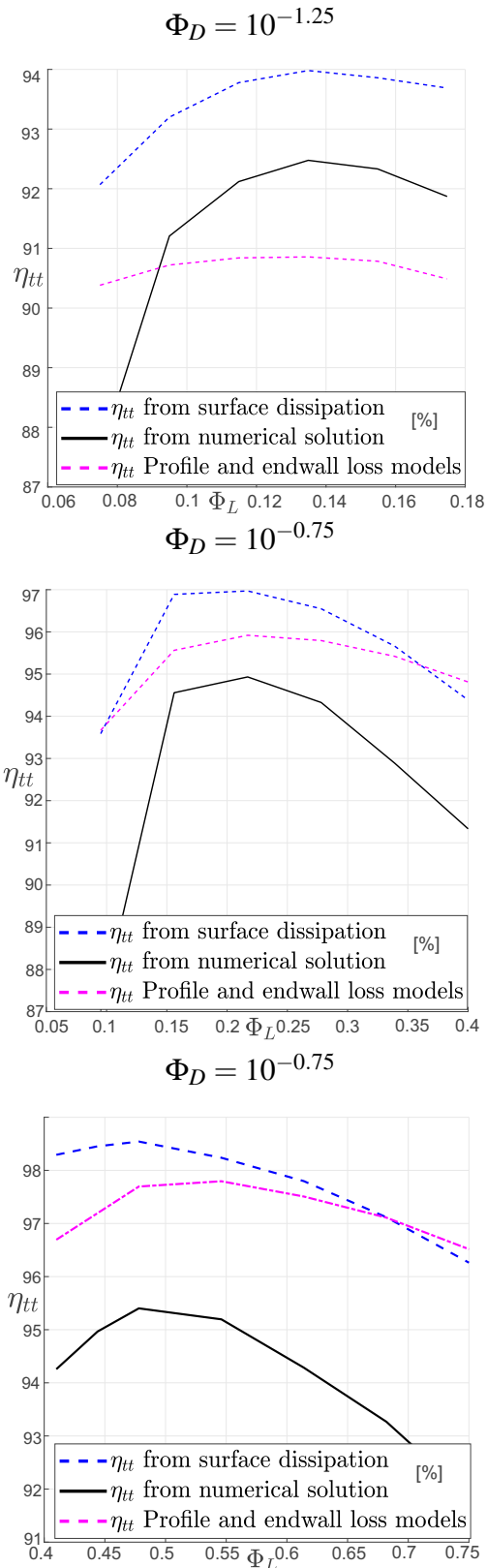


Fig. 5.16 Comparison of exit flow conditions at different points on a Balje chart.

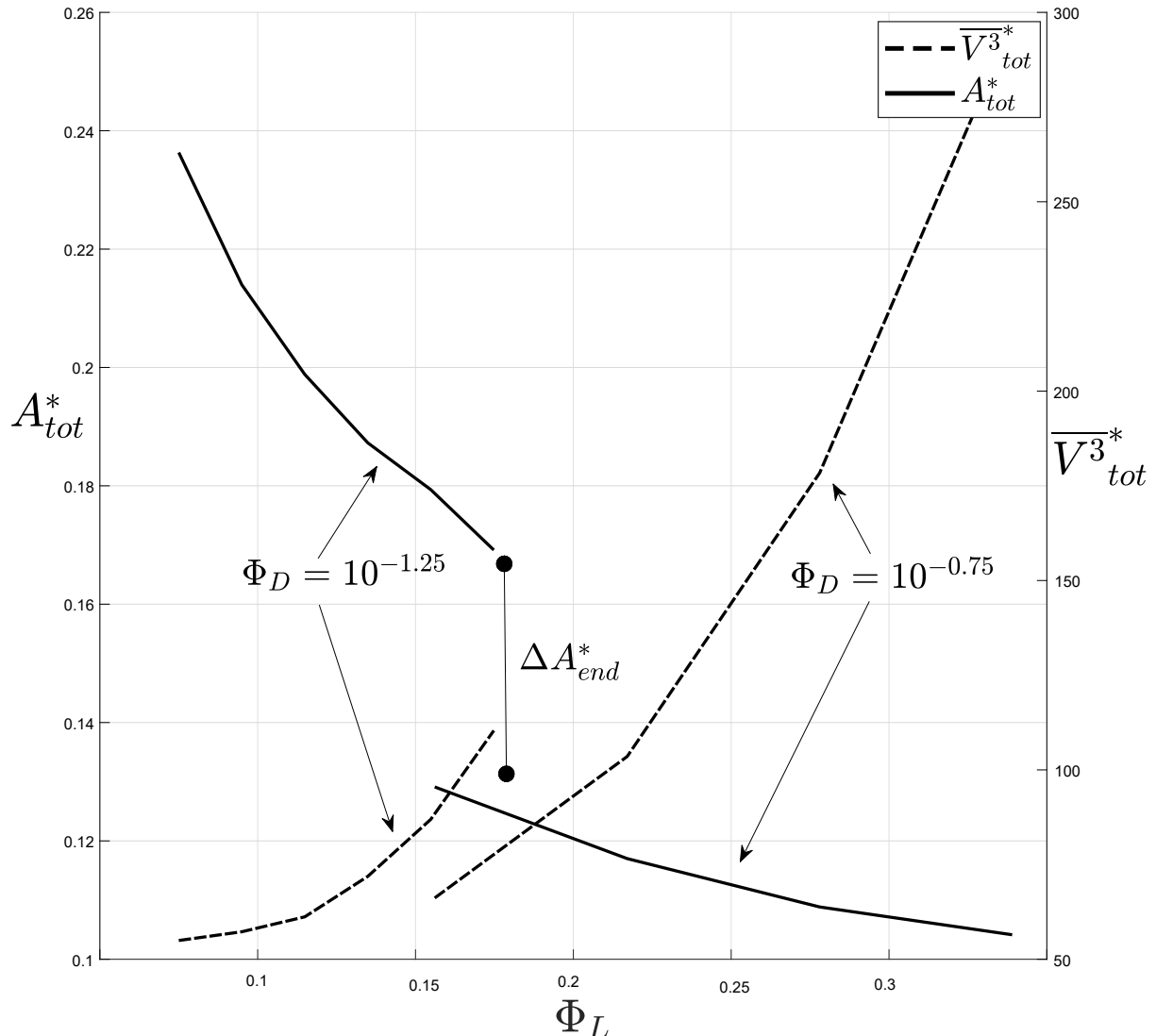


Fig. 5.17 Non dimensional Area and cubic velocity for turbines with different duty flow coefficient.

5.9 Radius ratio

The key geometric parameter that differentiates radial and axial architectures is the radius ratio. As previously discussed, reducing the radius ratio increases the component centrifugal loading done by the turbine. An expression for the components of loading for radial turbines with a loading coefficient of 1 and zero exit swirl is

$$\psi = \underbrace{\frac{1}{2}(1 - R_r^2)}_{\psi_{Centrifugal}} + \underbrace{\frac{1}{2}R_r^2 + \frac{1}{2}\phi_L^2(R_{vm}^2 - 1)}_{\psi_{relative\ acceleration}} + \underbrace{\frac{1}{2} + \frac{1}{2}\phi_L^2(1 - R_{vm}^2)}_{\psi_{absolute\ KE}}. \quad (5.1)$$

From Equation 5.1, it is clear that decreasing radius ratio takes loading from the relative acceleration term and adds it to the centrifugal term.

Figure 5.18 shows the changes in total to total efficiency with radius ratio and local flow coefficient for a fixed duty flow $\Phi_D = 10^{-0.75}$. The same design spaces were generated at higher ($\Phi_D = 10^0$) and lower ($\Phi_D = 10^{-1}$) duty flows, and the same overall pattern was found. The figure shows that by shifting the loading, improvements in efficiency can be achieved. This suggests that radial turbines generally benefit from increasing centrifugal loading. In addition to this the change in efficiency is also indicated by surface dissipation. Therefore, the space can again be explained using similar velocity cubed arguments as before. Figure 5.19 indicates that the rise in efficiency with reducing radius ratio is driven by a reduction in surface velocities through the turbine passage.

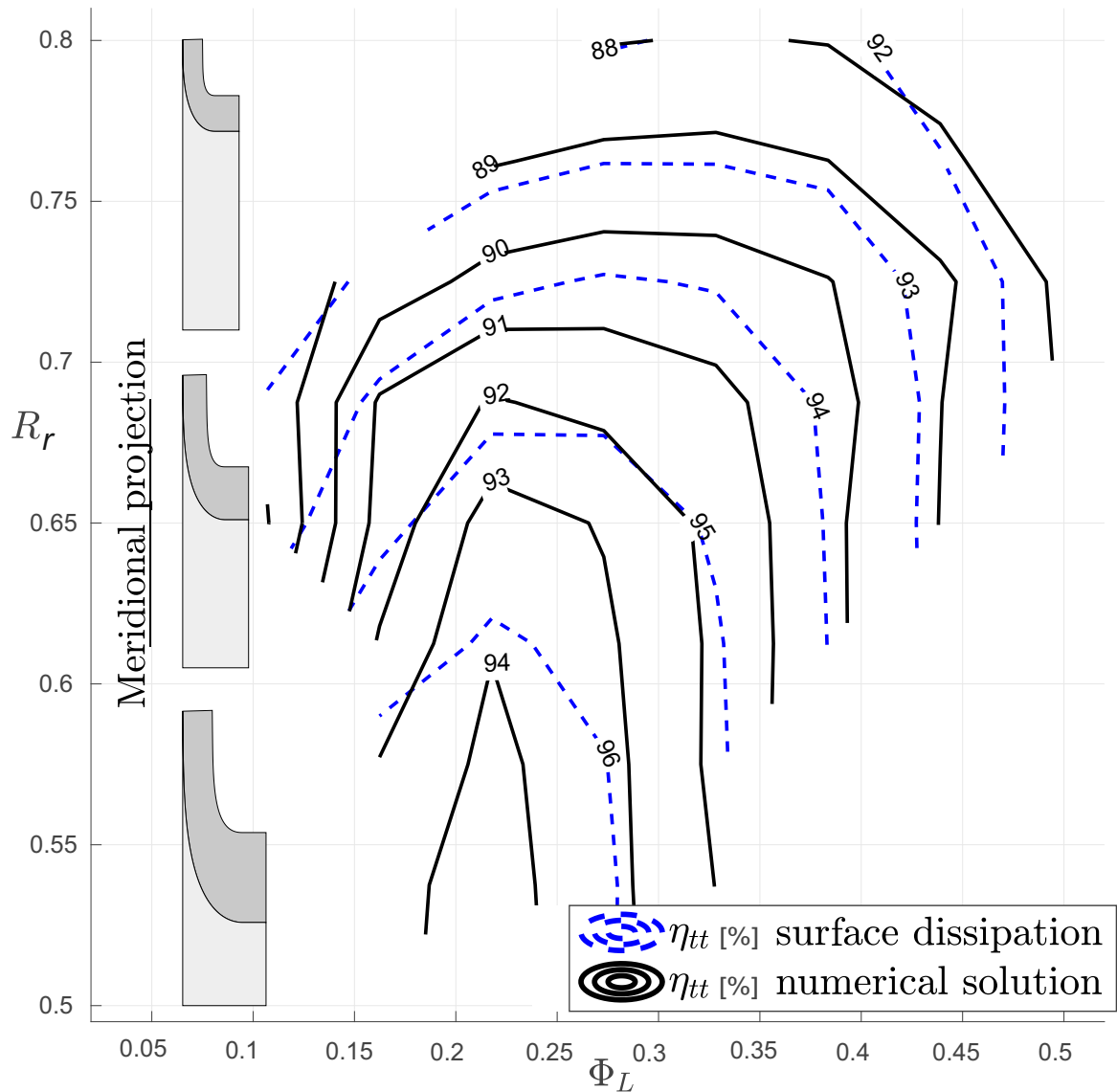


Fig. 5.18 Effect of radius ratio on performance and optimal flow coefficient.

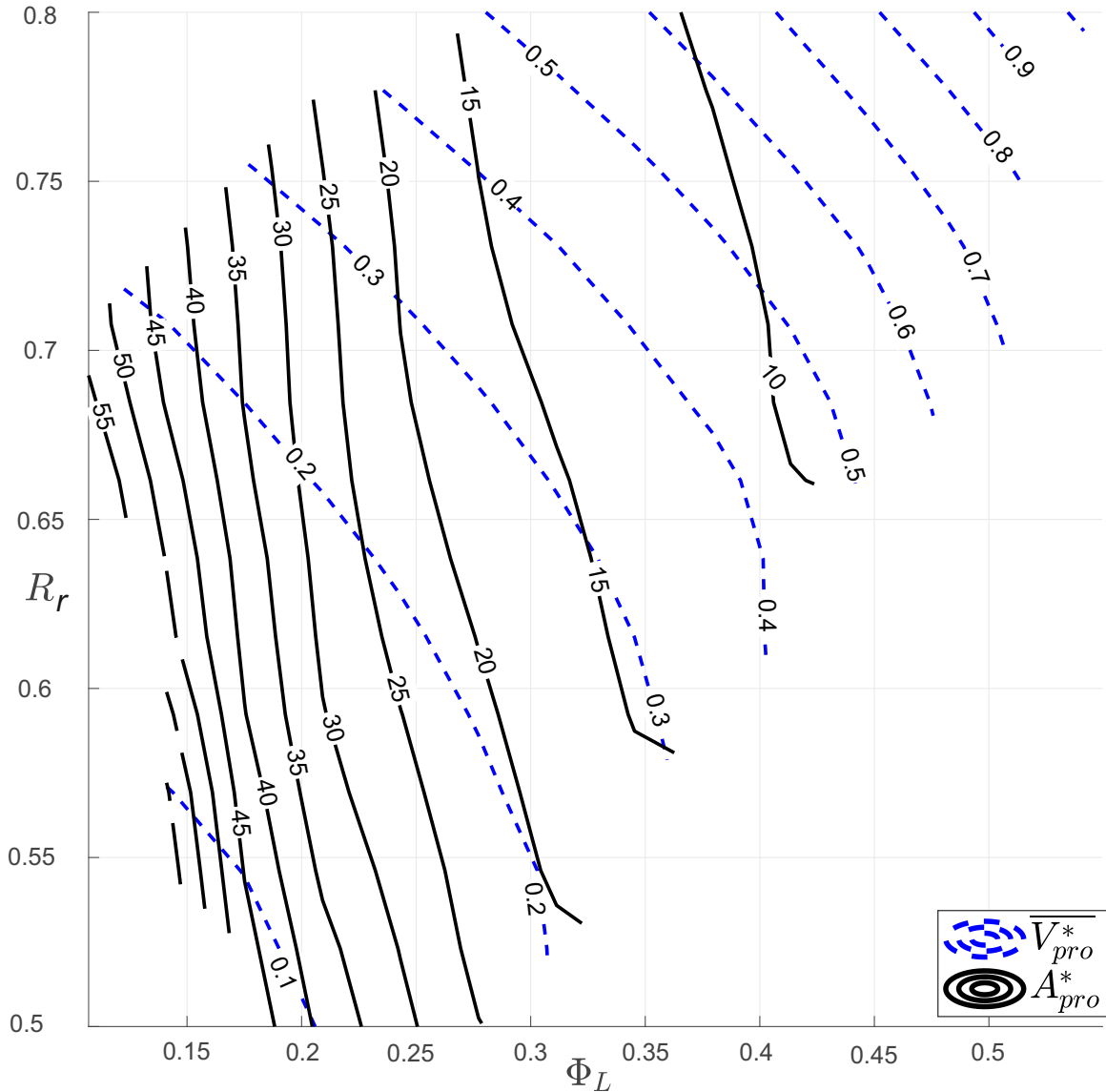


Fig. 5.19 Effect of radius ratio on profile surface area and area averaged cubic velocity.

The shape of the velocity contours can be explained using Equation 5.2, which was derived from the velocity triangles and Euler equations. Equation 5.2 shows that the average of the velocities squared decreases with both radius ratio and local flow coefficient.

$$\frac{W_1^2 + W_2^2}{2U^2} = \frac{1}{2}(1 + R_{vm}^2)\phi_L^2 + R_r^2 \quad (5.2)$$

To summarise, reducing the radius ratio shifts loading from the relative acceleration to centrifugal term. In doing so, the flow through the passage experiences less accelerations. This reduces the surface velocities and, therefore, the loss. In addition to this, reducing radius ratio is beneficial for high Mach number machines. The lower relative velocities will delay the onset of

chocking. On top of this, reducing radius ratio lowers the absolute exit blade angle, which is likely to help reduce secondary flow.

Decreasing the radius ratio also shifts the location of optimal total to total performance to lower local flow coefficients. Similar to the results in Section 5.8, the optima shifts to surface velocities.

This also has a significant effect on the total to static performance. While the changes in the radius ratio do not directly reduce the exit loss, the shift in optimum total to total efficiency to lower flow coefficient reduces the compromise between entropy and exit losses. This, in turn, improves the overall total to static performance of the turbines.

Since the model developed in Section 3.1.1 is based on surface dissipation, it is able to capture the behaviour of changing radius ratio. It, however, does slightly overestimate the optimal local flow coefficient (Figure B.7 in the appendix).

5.10 Meridional velocity ratio

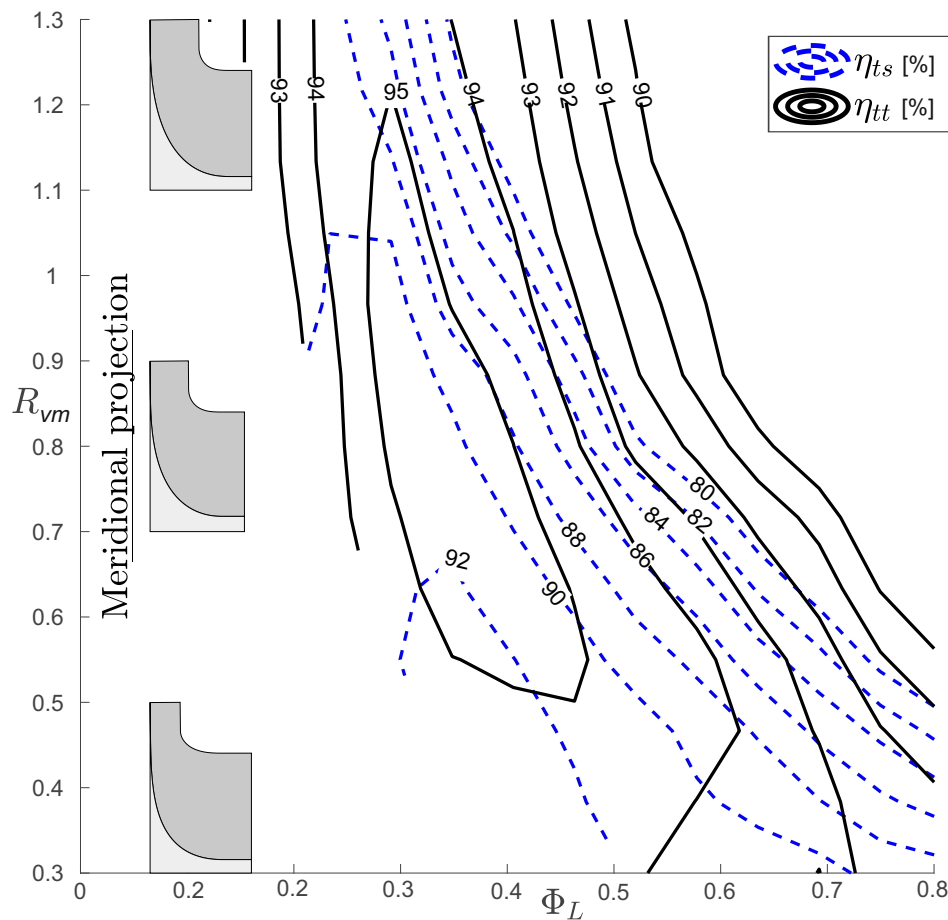


Fig. 5.20 Effect of Meridional velocity ratio on performance and optimal flow coefficient.

Figure 5.20 shows the effects of varying meridional velocity on total to total and total to static efficiency. For these designs, the total to total efficiency is largely insensitive to changes in meridional velocity ratio, particularly around optimum local flow coefficient. Decreases in meridional velocity ratio do however reduce the sensitivity of optimum flow coefficient, which can be explained by Equation 5.2 for the average velocity. In this equation, the velocity ratio scales the local flow coefficient term and hence adjust the averages velocity's sensitivity to local flow coefficient.

Similar to the radius ratio, changes in the meridional velocity ratio shifts the work balance. From Equation 5.1 it can be seen that reducing the meridional velocity ratio shifts loading from the relative acceleration to the absolute change in kinetic energy term. Furthermore, Equation 5.2 indicates that reducing meridional velocity ratio decreases the average velocity through the turbine. This also explains the decreases in sensitivity at high flow coefficients. However, unlike radius ratio, decreasing the meridional velocity increases the magnitude of the blade exit angle, which results in higher profile area and would likely increase secondary flow loss. Note equation 5.3 assumes zero interstage swirl.

$$\tan \beta_2 = -\frac{R_r}{\phi_L R_{vm}} \quad (5.3)$$

As with axial turbines, decreasing meridional velocity ratio is particularly useful when designing for high total to static efficiency. Figure 5.20 shows close to a 2% increase when decreasing meridional velocity ratio from 1 to 0.6. If tracking the optima, this comes at nearly no cost to total to total performance. One thing to note is that if the hub radius is constrained, possibly by drive shaft diameter, there will be an inherent geometric trade-off between the use of radius ratio and meridional velocity ratio. This is because decreases in either of these parameters reduces the hub radius. For a given hub radius design, decreasing meridional velocity ratio will have to have an increasing radius ratio and vice versa. Studying this trade-off over the design space should be done in future to establish the correct balance between the two parameters.

5.11 Chapter Conclusions

The overall goal of this chapter was to build an understanding of the shapes of the Smith and Balje/Rohlik chart for radial architectures. The key conclusions pertaining to this are:

- The topology of both design spaces can to some extent be explained in terms of surface dissipation (velocity cubed rule), but to a lesser extent when compared to the axial design spaces. More specifically, dissipation loosely captures the trends with varying local and duty flow coefficients but significantly underpredicts the drop in performance with changes

in loading coefficient(Smith chart). The latter is a result of the increasing incidence due to the fixed metal angle, itself a consequence of the radial blade fibred design.

As with the axial architectures, the drop in performance at high local flow coefficients (Smith chart) is driven by high surface velocities and that the drop at low local flow coefficients is driven by high surface area. For the Balje diagram, the drop at high duty flow coefficients is similarly a result of high surface velocity. However, unlike the axial architectures, the radial architectures do experience a drop in performance at low duty flow coefficients. This is a result of the high end wall surface area of these designs.

- It was shown that for the case of zero interstage swirl, that reducing radius ratio transfers loading from the relative acceleration term to the centrifugal term. This in turn reduces the flow acceleration through the passage and therefore decreases the surface velocities that are driving dissipation. However, some of the benefit is counteracted by an increase in surface area. That being said, the CFD results imply that designers should maximise the centrifugal component of loading.

The effects of varying the meridional velocity ratio was also studied for radial architectures, which again showed that reducing this parameter significantly improved total to static performance; the total to total performance was largely insensitive. When varying meridional velocity ratio, there then is a trade-off between the use of radius ratio and meridional velocity ratio, since both are limited by the hub radius ratio. This trade-off should be studied in future.

- Contributions from the individual loss mechanisms to the shape of the Balje/Rohlik chart were studied. At low duty flow coefficients, the profile loss contributed little to the overall loss. This was due to the low passage velocities as a result of the low radius ratio and local flow coefficients. At high duty flow coefficients, profile loss contributed significantly to the loss in performance. This was a result of increasing passage surface velocities due to high local flow coefficient and radius ratio, characteristic of this region of the design space. The endwall loss was the primary driver for the reduction in performance at low duty flow. This was caused by the high end wall surface dissipation due to the large amounts of surface area. The endwall loss also increased substantially at high duty flow. The sharp rise is caused by flow separation at the casing due to the decreasing radius of curvature of the radial to axial bend. Note that this rise can be delayed by relaxing design constraints used in this thesis(section 2.2). The leakage loss contributed small amounts of loss at low duty coefficients. This was attributed to the scraping effect and low velocity with which the leakage flow was mixing, both a consequences of the characteristically large radial sections in this region of the Balje chart. The loss rose significantly with increasing duty flow and then abruptly dropped off, including going negative. The latter drop in loss was attributed to a likely interaction with endwall loss. This was reflected by the combined

endwall leakage loss, which dropped below the value of just the endwall loss. The rise in loss before the drop off was attributed to the reducing scraping effect, increasing velocity with which the flow was mixing and increasing over tip driving pressure.

- It was shown that the profile and secondary flow loss models designed for multiple architecture types functioned fairly well for the radial Balje/Rohlik charts. However, the secondary flow model was not designed to capture the flow separation at high duty flow coefficients and therefore significantly unpredicted the rise in loss due to casing separation. This could be introduced in future in a similar manner to that of Baines [2]. The modified tip leakage model first derived by Denton [26] is in agreement with variation predicted by CFD throughout most of the space but underpredicts the levels. However, since the model does not include any interaction terms, it does not capture the reduction in loss at higher duty flow.

This concludes the radial turbine design space study.

Chapter 6

Mixed Turbine Design Space

6.1 Chapter Objectives

Mixed flow turbines are by far the least studied of the turbine architectures. This is likely due to there being less use of these types of turbines across the industry in comparison to radial and axial architectures, as well as the inherently more complex flow physics. As discussed in the introduction, the primary modern use of mixed flow architectures is for turbocharging, but in the past were typically used in hydroelectric dams. Turbocharging turbines need to be compact and relatively cheap. To meet these requirements, they are typically designed with radial blade fibres as this allows for smaller faster spinning rotors. For radial turbines with a cone angle of ninety degrees, the design is constrained such that the inlet metal angle is fixed at zero. Mixed flow turbines have a cone angle less than ninety degrees by definition, which allows for non zero blade inlet angles. As a result, mixed flow turbines can be designed with higher loading coefficients, which is particularly useful for optimum energy extraction at the peak engine pulse. The following chapter explores the nature of the design space of radially fibred mixed flow architectures. Smith and Balje axial design spaces (rotor only) have been mapped out using RANS. The key objectives of this chapter are as follows:

- To bring to attention a loading limiting flow feature of mixed flow turbines that limits its applicability across the design space and then to show a design change which can help improve performance further expanding the design space.
- To test the degree to which the general shapes of the design spaces can be explained in terms of surface dissipation (velocity cubed rule). Then to break this down and explain the individual contribution of area and surface velocity cubed.
- To explore the effects design parameters have on performance, specifically the relationship between radius ratio and cone angle.

- To understand how the individual loss mechanism shape the design space and understand what drives the shape of these loss distributions where possible.
- To compare the individual loss mechanisms with simplified models that have been derived with physical interpretation of the flow.

6.2 Mixed Turbine Hub Flow Separation

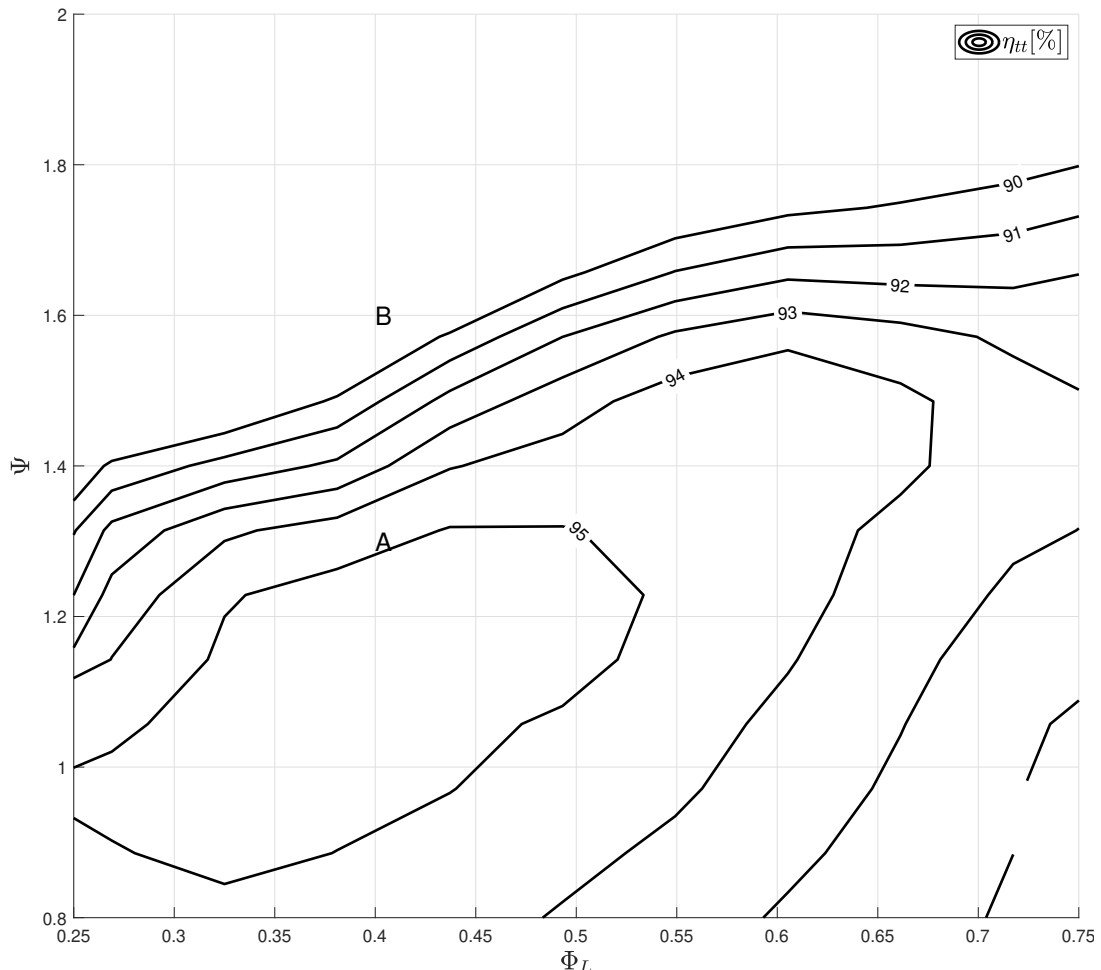


Fig. 6.1 Total-total Mixed flow Smith chart featuring detrimental flow separation

As far as the author is aware, there are no examples of Smith charts for mixed flow architectures in the literature. In addition to this, the few examples of turbines that do exist in the literature tend have a small range of loading coefficients. The highest that was found was $\psi = 1.3$ (radially blade fibred) from Baines [2]. Bearing this in mind, Figure 6.1 shows an early attempt at generating a mixed flow Smith chart by the author of this thesis. The results from this design space show a diagonal boundary line after which the performance drops off rapidly (high gradient in the figure) when attempting to design for high loading.

On closer inspection, the feature which drives this loss in efficiency is a separation that occurs at the hub suction surface. Figure 6.2 in conjunction with Figure 6.1 illustrates this.

Point *A* sits just inside the boundary before the onset of separation, whereas point *B* lies in a region where the hub flow has already lifted off. Figure 6.3 shows that there is a high entropy flow structure that seems to form at the hub and is then driven towards the casing. Baines [2] reported a similar separation at the suction surface near the hub (also from CFD). In addition to this, a similar flow structure can be found in the work done by Yang [56] and [41] which seems to indicate it as universal issue for higher loaded mixed flow turbines.

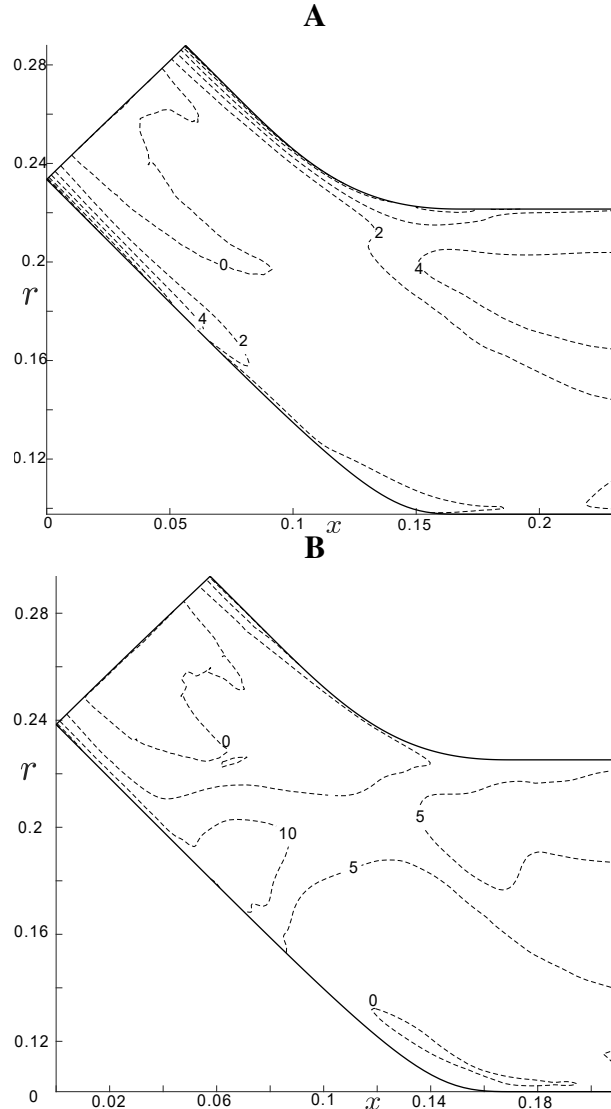


Fig. 6.2 A&B: Meridional projections (near suction surface) of entropy contours

Typically, flow separation is associated with an adverse pressure gradient which depletes the already low momentum of fluid contained within a boundary layer. While the hub flow for turbine *A* has not yet separated, it can be used to illustrate the pressure field leading up to this

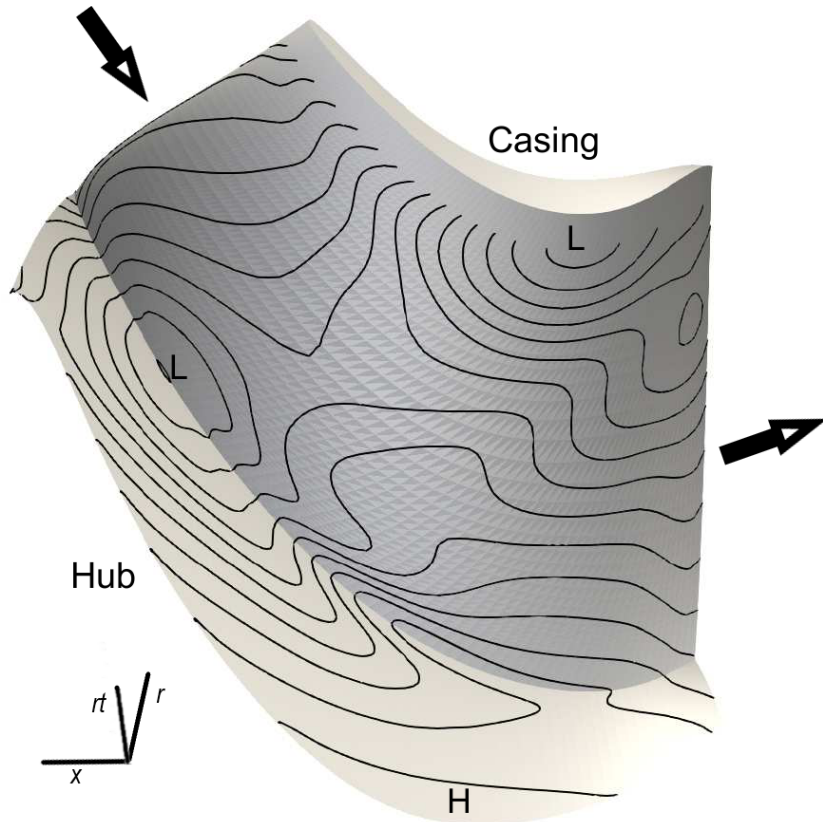


Fig. 6.3 Surface contour plot of reduced static pressure (Turbine A), L and H denotes regions of low and high pressure respectively

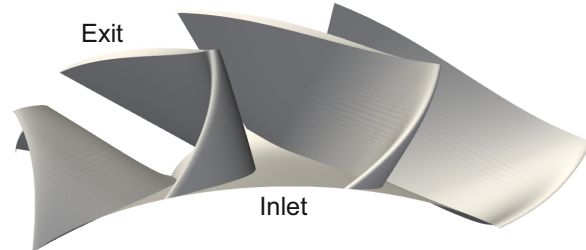
separation because it sits relatively close to the drop in performance. Once the flow lifts off, the potential field completely changes and obstructs the source of the problem.

Figure 6.3 is a contour plot of reduced static pressure on the hub and suction surfaces. *H* and *L* denote regions of high and low pressure respectively.

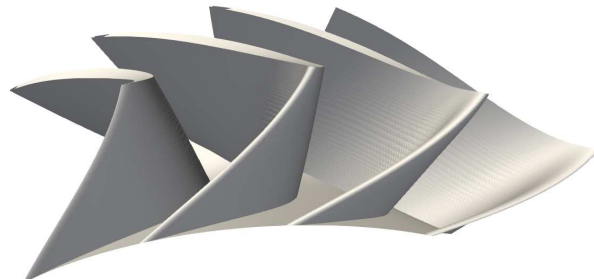
The flow entering the passage close to the hub initially experiences an acceleration as it moves toward the low pressure region on the hub suction surface corner. After this, the flow experiences a sharp adverse pressure gradient when moving down stream of the low pressure region. It is this adverse pressure gradient that is the likely cause of the flow separation. It will later be shown that there are two important factors driving this low pressure region, lean/rake and Coriolis force.

Once lifted off, the separated flow structure rolls up and is driven towards the low pressure region at the casing. This low pressure region is driven by the convex radial to axial bend and high pitch-wise flow turning.

$$\psi = 1$$



$$\psi = 1.3$$



$$\psi = 1.6$$

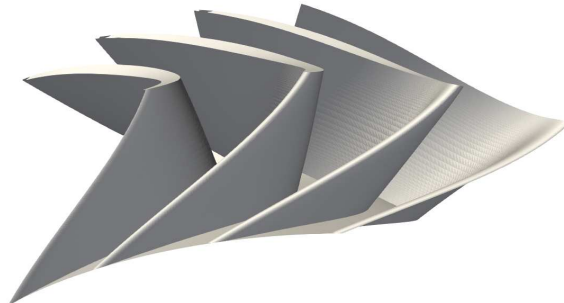


Fig. 6.4 Variation in Mixed flow blade geometry with Loading

Effects of rake/lean

Rake plays a significant role in increasing the drop in pressure formed at the hub. As previously discussed in Section 1.4, increasing the blade angle causes the blade to lean over, bringing the

suction surface closer to the hub. The change in geometry for different loading coefficients is shown in Figure 6.4, illustrating that increasing the loading increases the leaning over of the blade.

By bringing the suction surface closer to the hub, the flow is further accelerated, increasing velocity and significantly reducing the pressure in the region. This can be seen in Figure 6.5, which shows a comparison of the pressure field for a radially blade fibred and non radially blade fibred design (cut taken through hub lower pressure region). The figure shows a significantly lower pressure in the SS-Hub corner of the radial fibre case.

The non radial blade fibred design is stacked along the leading edge which creates an angle larger than 90 degrees between the span-wise and circumferential direction in this region of the blade, as a result has less of a pressure drop at the hub. Section 2.2 discusses how this blade was designed.

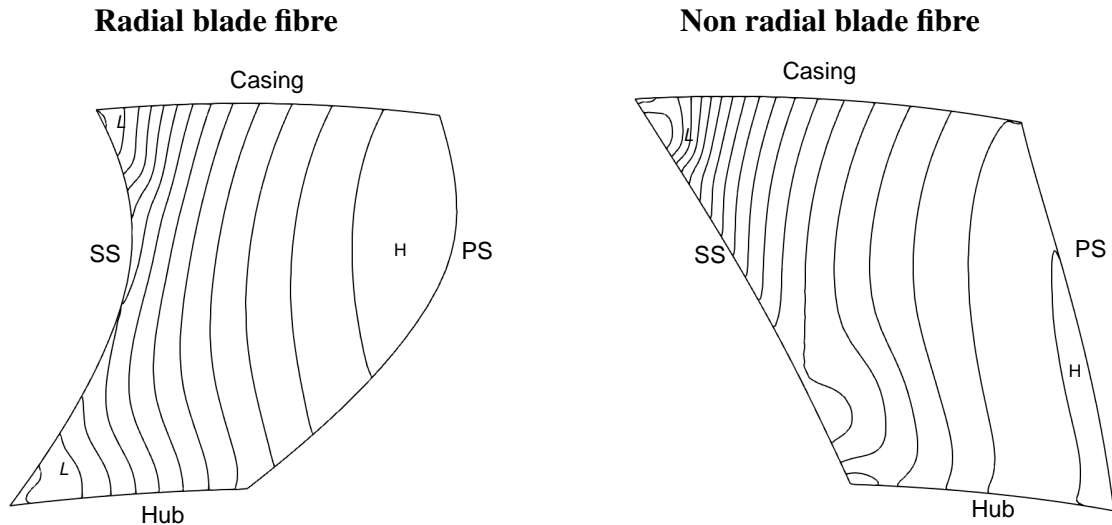


Fig. 6.5 Comparison of static pressure variations for radial and non radial blade fibre designs, contour spacing equal

Effects of Coriolis force

The Coriolis force also plays a significant role in the inlet region of mixed flow turbines. Unlike axial turbines, where the Coriolis force is directed up the span, mixed flow and radial turbines have a component of this force that is perpendicular to the blade surface which then needs to be balanced by the pressure field. While radial turbines (with zero inlet metal angle) only have to contend with the $V_r\omega$ component of the Coriolis force at the inlet, mixed flow architectures have to contend with both the $V_r\omega$ and the $V_\theta\omega$ terms, (see 1.2), bare in mind, that the components of these force normal to the blade surface are proportional to cosine of cone angle.

Figure 6.6 *A* shows a zoomed in section of the inviscid solution for the turbine in Figure 6.3. This was achieved by modifying the slip conditions on all surfaces and setting the solver to solve for inviscid flow.

The results show that the same low pressure region(black contours) is present and that it correlates well with contours of the total Coriolis force(blue contours). To further test the degree to which this plays a role, the source code of TBLOCK was modified by adding addition source terms which cancelled out the apparent Coriolis terms. TBLOCK solves the Navier stokes equations in the following form, (Brandvik [5]).

$$\frac{\partial \vec{U}}{\partial t} = \frac{\Sigma \vec{F}}{V} + \vec{S} \quad (6.1)$$

\vec{U} is a vector of the primary flow variables. \vec{F} is a vector of the fluxes of the primary variables, the summation of flux is over the cell faces and \vec{S} are the source terms. V is the volume of the cell. \vec{S} was modified such that

$$\vec{S}_{new} = \vec{S}_{old} - m(\vec{\omega} \times \vec{w}) \quad (6.2)$$

The case was then rerun without Coriolis forces and the results are shown in Figure 6.6 *B*. Comparison of the figures suggest that Coriolis significantly amplifies the low pressure pressure region. Note that the contours have the same increments and the low pressure region with the Coriolis force is significantly lower in value.

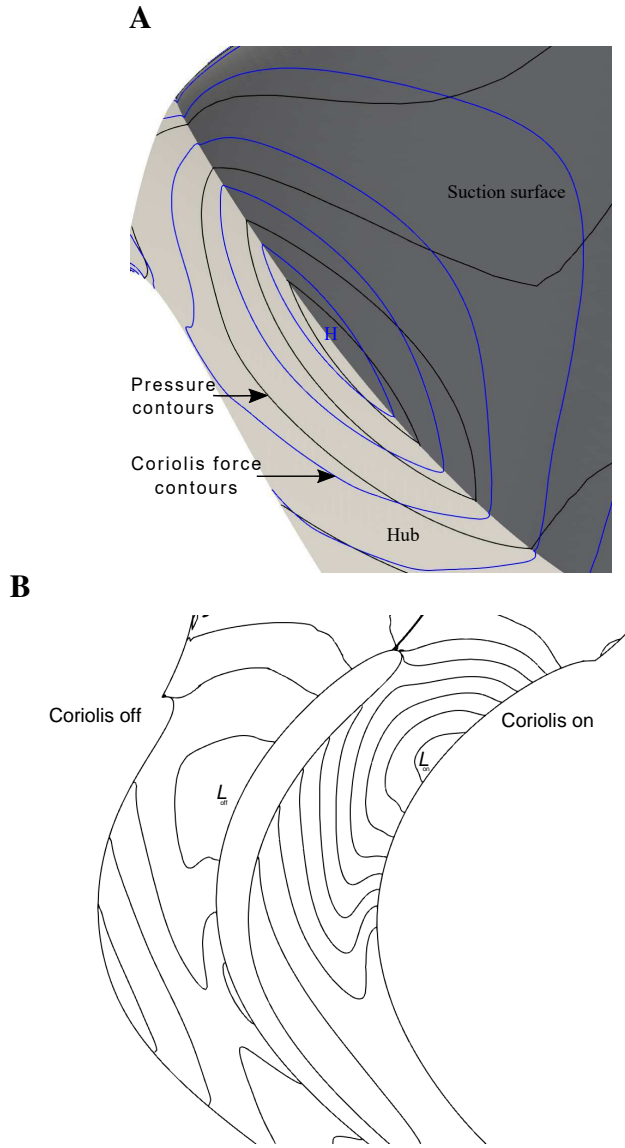


Fig. 6.6 *A*:Zoomed in section of the inviscid solution of the turbine in figure 6.3 Including contours of Coriolis force, where H denotes region of high magnitude. *B*:Difference in the reduced static pressure field with Coriolis terms switch on or off (same contour spacing of $\Delta C_p = 0.05$, $L_{on} < L_{off}$).

6.3 Hub Fillet for Mixed Flow Turbines

As far as the author is aware there are no publicly available design features to address this flow problem. However, from discussion with members of the Whittle, Xu and Cao [55], the separation can be suppressed via detailed hub line manipulation, but that this required detailed and target design. This would therefore not be suitable for use in this thesis as each design would require manual intervention and hence a more robust solution needed to be found.

In an attempt to suppress the hub flow separation, multiple changes in geometry were tried. These included reducing the already low curvature of the blades in this region, simple bumps

in the meridional curvature and changes in incidence, but none of these attempts showed any significant signs of improvement. Inspired by the solutions for corners separation in cascades and the work done by [7], it was then decided to fill in this region with a partial fillet; Section 2.2 describes how this was achieved. The pressure surface was also partially filled in to help reduce the high pressure region due to the concave pressure surface; Section 2.2 describes how this was achieved. It must be noted that this feature was not specifically tuned to any specific design.

The effect this had on the flow and pressure field of turbine *B* is shown in Figure 6.7. Without a fillet, the disruptive nature of the separated structure is clear. The flow in the hub suction surfaces corner separates/lifts off and rolls due to the high vorticity in the preceding boundary layer. The vortical structure is then driven along the suction surface towards the casing by the pressure field, disrupting the suction surface flow. The turbine with the fillet has a significantly different flow field. The fillet has successfully disrupted the formation of the strong cross passage vortex. How this is achieved is likely due to two effects:

- The low pressure region has been shifted slightly further away from the hub surface by the fillet which can be seen in Figure 6.7.
- The fillet has reduced the strength of the corner vortex by reducing the concentration of vorticity in this region.

The robust effectiveness of the fillet like design feature is illustrated in Figure 6.9 which shows the resulting Smith chart using the fillet. This simple design feature has successfully expanded the usable design range of mixed flow architectures to significantly higher loading coefficients and over a range of flow coefficients. It must be reiterated that the filleting did not require targeted design, specific to the flow parameters and has significantly improved performance of all design above the marked boundary(dashed line) shown in the figure. This could serve as an alternative to the previous methods used for controlling this flow feature.

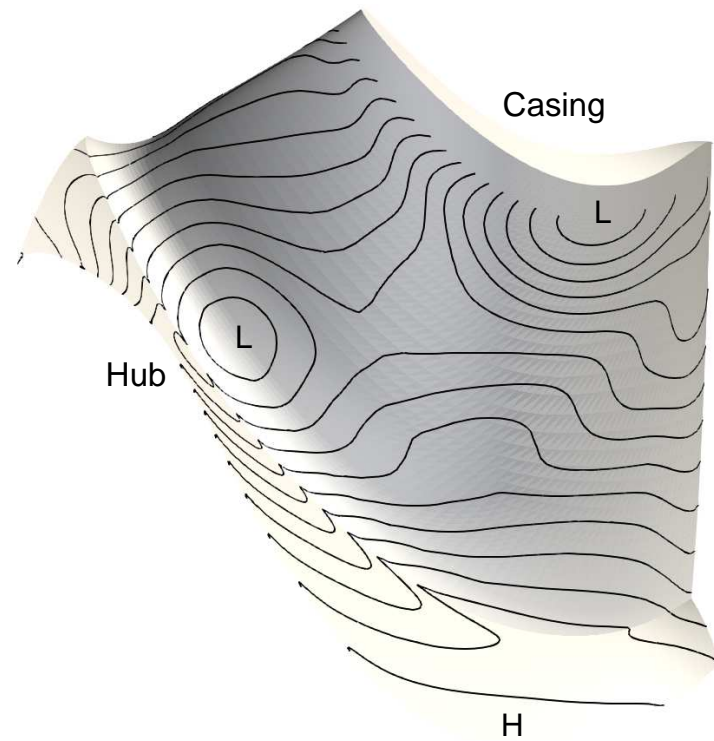
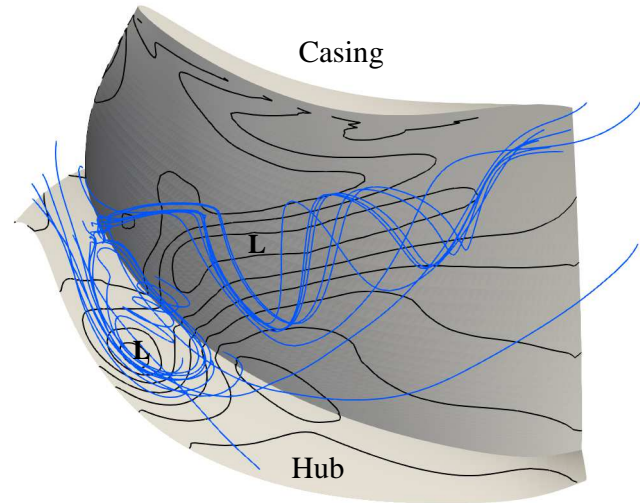
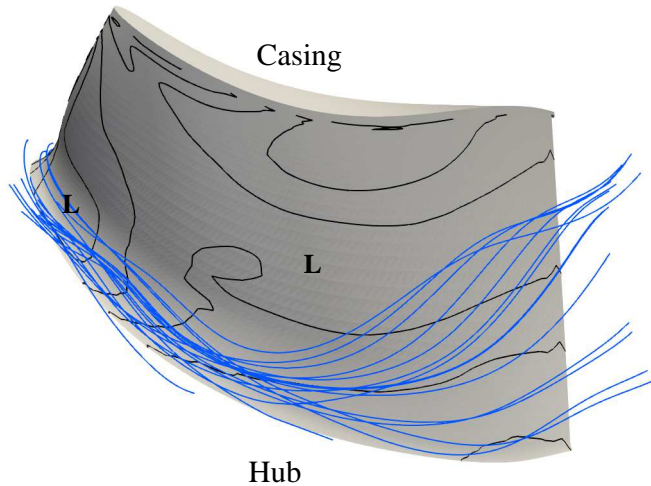


Fig. 6.7 Surface contour plot of reduced static pressure (Turbine A), L and H denotes regions of low and high pressure respectively



Without Fillet



With Fillet

Fig. 6.8 Comparison of a mixed flow turbine with and without a hub fillet and spoon, Contours are of reduced static pressure where L denotes low pressure regions

6.4 Mixed Flow Turbine Smith Chart

As previously mentioned, Smith charts are constructed by varying Both ψ and ϕ_L while keeping other parameters constant or ideally optimising them. For the axial and radial turbines, the non-dimensional inlet flow area A/r_m^2 was kept constant as is done here. Pairing this with a constant radius ratio and cone angle results in a similar meridional geometry across the space. The values of radius ratio and cone angle are of a typical mixed flow architecture such as, Abidat [1]. The following non-dimensional parameters were kept constant:

Table 6.1 Mixed flow Smith chart parameters

Parameter	Value
R_r	0.7
R_{vm}	$1 \pm 5\%$
$\frac{TE}{C_x}$	0.025 (axial section)
$\alpha_2(\text{mean})$	$0 \pm 4\text{deg}$
$C_o(\text{mean})$	$0.7 \pm 6\%$

When comparing to the radial Smith chart (figure 5.1), mixed flow architecture can achieve significantly higher loading where the radial would experience severe incidence loss.

While mixed architectures can achieve better performance at higher loading than radial ones, axial architectures still out perform both. The axial Smith chart 4.1 shows a considerably lower drop in performance with increases in loading. This suggests that, from a purely aerodynamic point of view, mixed flow architecture are best used at intermediate loading coefficient.

As with the other architecture, surface dissipation captures the shape of the design space fairly well. It must be noted that there is a poor match of the contours at lower loading and high flow coefficients. Later, it will be shown that the difference is primary driven by tip leakage (Figure 6.14) and will be discussed later in this chapter.

As with the other design spaces, surface dissipation can be decoupled into area and velocity to help aid in the explanation of the shape (Figure 6.10 A). The increasing loss at higher local flow coefficient is again driven by the increasing surface velocity, and the increase in loss at lower local flow coefficients is a result of increasing area. Compared to the axial turbine (Figure 4.2), the area and velocity of the mixed flow architectures increase more rapidly with increases in loading. This would partially account for the faster drop off in performance of the mixed flow designs. Like the axial architectures, the meanline surface length and blade count of the mixed flow designs will increase with loading. However, for mixed flow architectures there is an additional factor increasing surface area, which is due to increasing rake. As discussed in Section 1.4, high rake angles results in large amounts of surface area due to the blade leaning

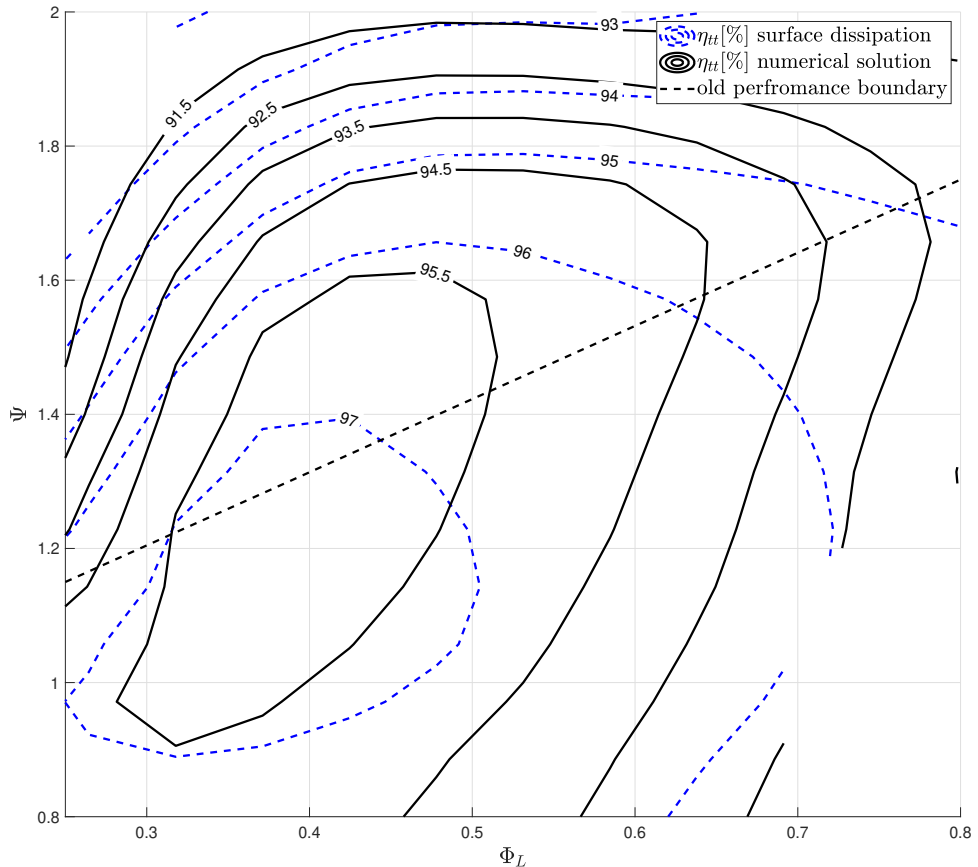


Fig. 6.9 Total-total mixed flow turbine Smith chart with fixed $R_r = 0.7$, $\frac{A}{r_m^2} = 2$ and $\lambda = 45^\circ$

over. This can also be seen in Figure 6.4. The increasing rake angle can be explained using Equation 1.17, which is repeated here for convenience.

$$\tan \beta = \tan \sigma \cos \lambda \quad (6.3)$$

In this case, the cone angle is fixed but the blade inlet metal angle is increasing with loading (Figure 6.10 B) and therefore the rake angle(σ) also increases.

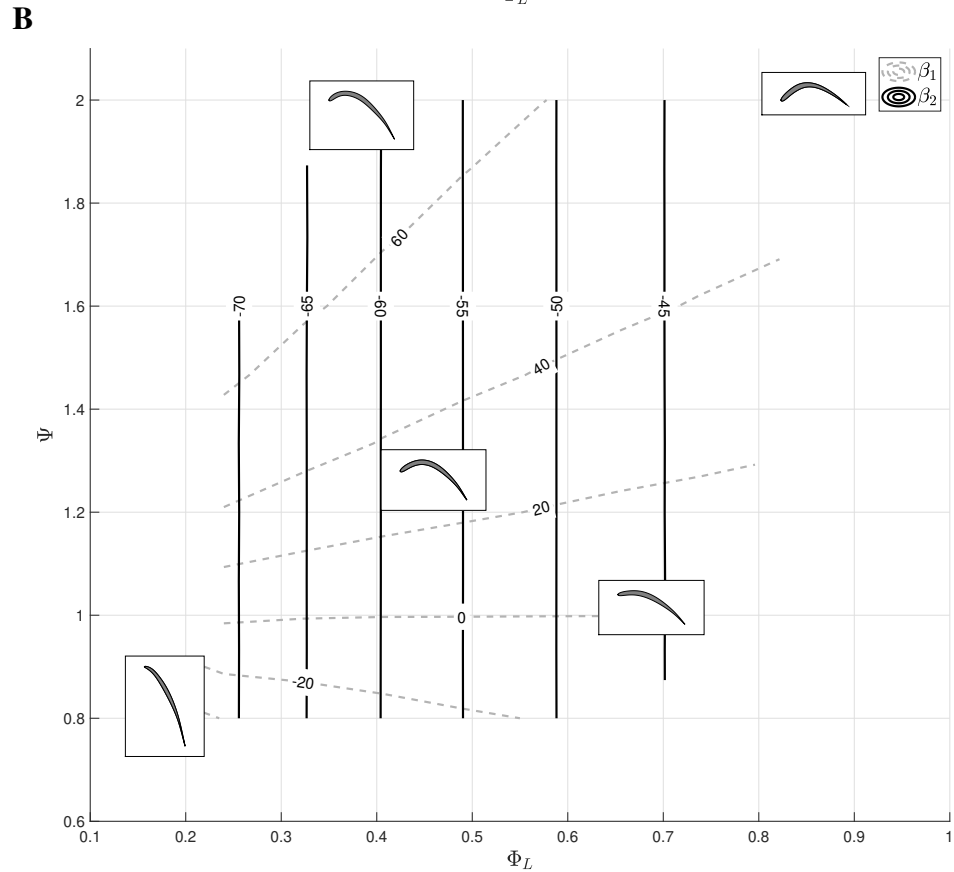
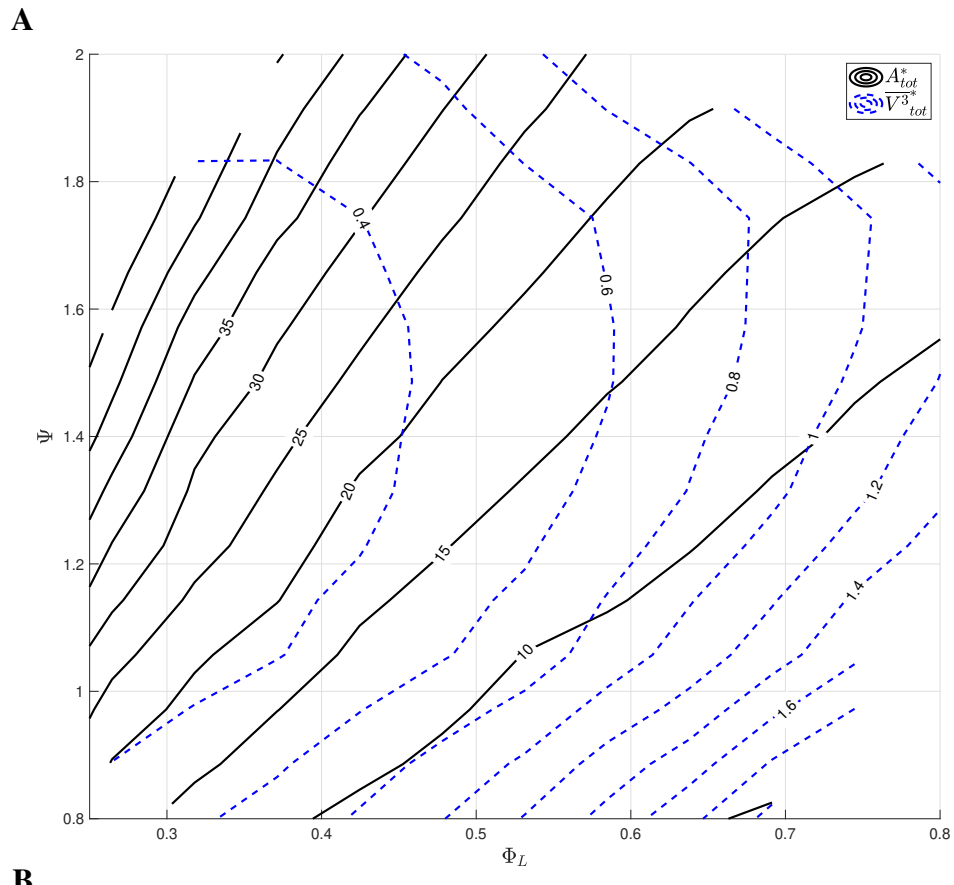


Fig. 6.10 A:Variation of non dimensional surface area and isentropic surface velocity cubed.
B:Inlet and exit meanline flow angles and blade geometry at various points through out the design space.

6.4.1 Profile loss

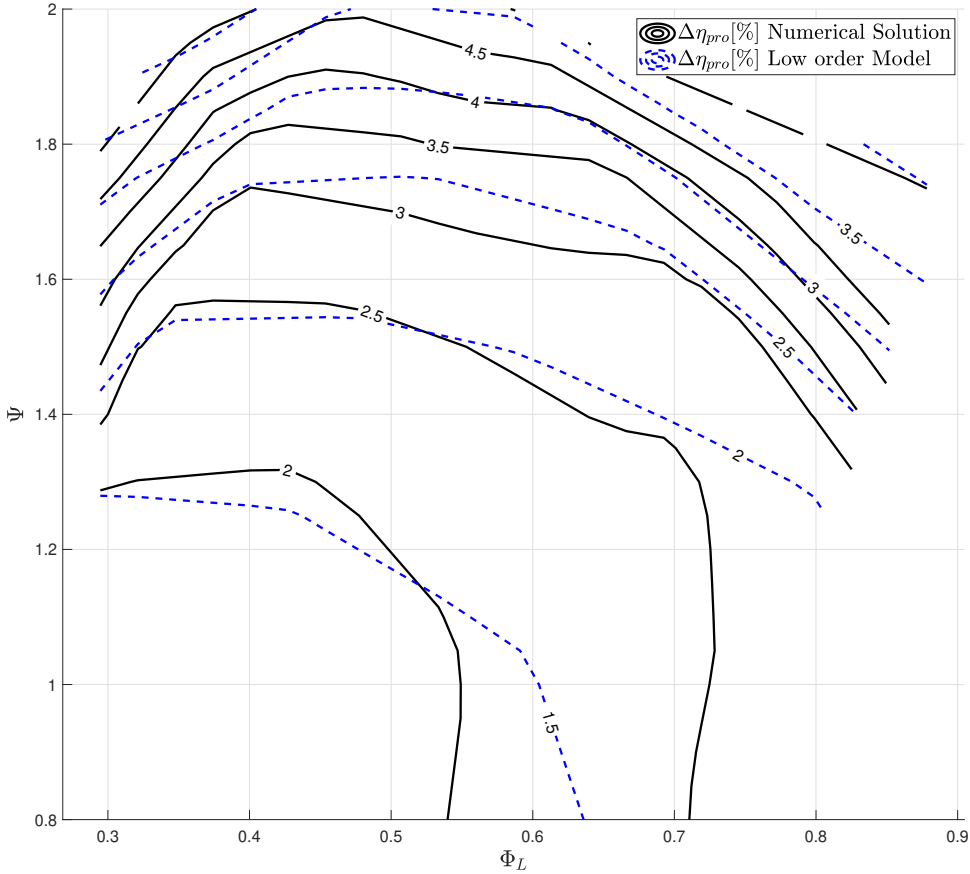


Fig. 6.11 Estimated profile loss

The variation in the profile loss throughout the design space for mixed flow architectures is presented in Figure 6.11 and differs to that of the axial architecture presented in Figure 4.4. There is a lower sensitivity to increases in local flow coefficient and significantly higher sensitivity to loading. These trends are consistent with surface dissipation. Comparing the change in surface velocity with increases in local flow coefficient for both mixed flow and axial architectures, the lower sensitivity of mixed flow turbines is a result of a more gradual increase in velocity. The higher sensitivity of mixed flow turbines to loading, as previously discussed, is a consequence of the more dramatic increase in surface area, as well as the more "bent over" shape of the surface velocity contours. The low order model captures the behaviour well, with the loss only being underpredicted by roughly 0.5%. It must be reminded that the good agreement is, in part, due to the simplistic nature of the CFD used, which cannot capture boundary layer phenomena such as transition nor is it likely to accurately predict the onset of separation on the diffusing section.

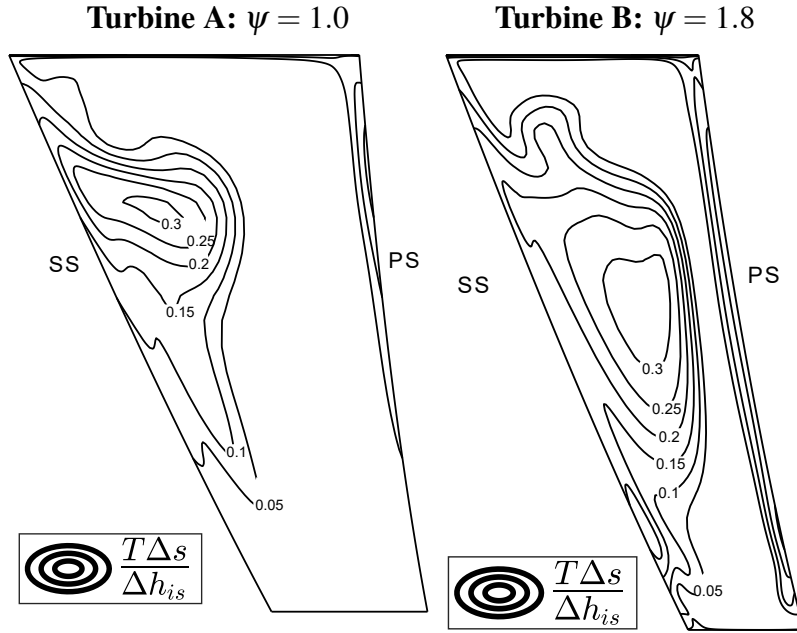


Fig. 6.12 Comparison of exit flow conditions at $\phi_L = 0.4$, A $\psi = 1.0$ and B $\psi = 1.8$

6.4.2 Endwall/Secondary loss

The nature of the secondary flow structures in mixed flow turbines are significantly different to that in axial turbines. One of the biggest differences between axial and mixed flow turbines is the locations of the passage vortices at the exit. For axial turbines the vortices generally remain separated and tend to be close to their corresponding end walls. However, for mixed flow architectures the pressure field associated with the radial to axial bend drives the hub passage vortex up the span towards the casing. As a result, there is only one distinct loss core at the exit (for a no leakage case). This can be seen in Figure 6.12 which is a comparison of the exit flow conditions of two mixed flow turbines with different levels of loading.

Figure 6.13 A show the variation in end wall loss across the Smith chart. While the flow structure of axial and mixed flow turbines is different, the distribution of end wall loss across the space is somewhat similar in the shape of the design space. An estimated decomposition of the end wall loss into secondary flow and end wall dissipation is shown in Figure 6.13 B. As with axial architecture, the end wall loss at higher loading is primarily driven by secondary flow and the loss associated with increasing local flow coefficient is primarily driven by end wall dissipation. Making direct comparison to the levels of lost efficiency between the axial and mixed flow turbines is somewhat dubious as the mixed flow architectures are significantly more complex to design, making a fair comparison difficult. That being said, the end wall dissipation for mixed flow turbines is noticeably higher than that of axial turbines. This is to be expected as the mixed flow turbines have significantly larger end wall surface area. Interestingly, the estimated secondary flow loss of mixed flow turbines is not much higher for mixed flow turbines than one might expect. This might be due to the combination of the end wall flows

into one loss core. Since the vorticity from the different end wall surfaces causes rotation in opposite directions, this could partially cancel each other's effect on inducing secondary kinetic energy. This could explain the similar levels of secondary flow loss, even though the mixed flow architecture has a larger loss core and positioned further from the walls (less self cancellation).

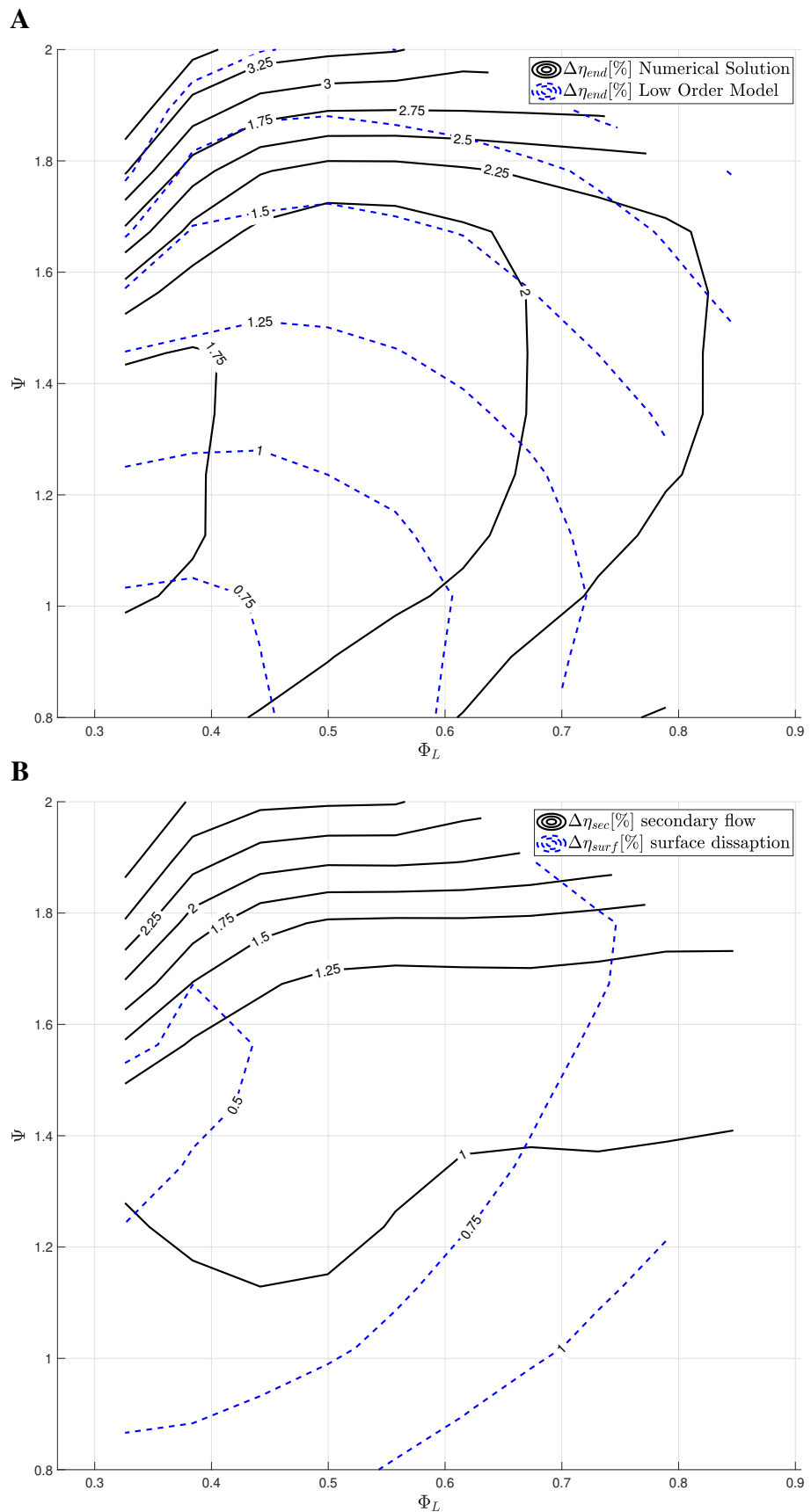


Fig. 6.13 A:Estimated secondary loss. B: Estimated components of end wall loss.

6.4.3 Tip leakage loss

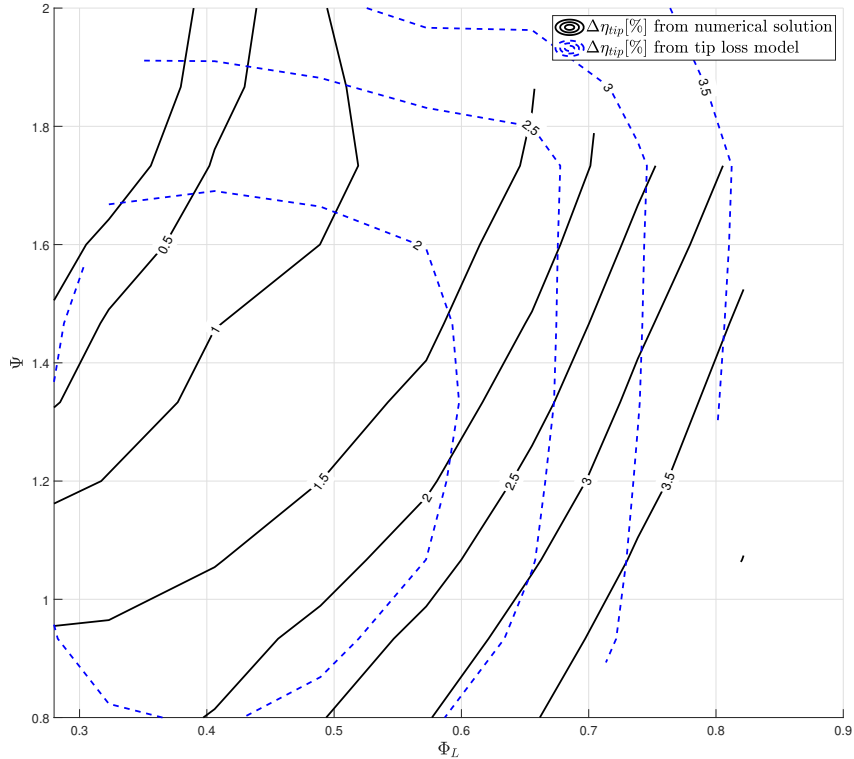


Fig. 6.14 leakage loss

Figure 6.14 shows the variation in the tip leakage loss across the Smith chart for a mixed flow turbine. The distribution again show similarities in shape to that of the axial turbine (see figure 4.6) but has higher levels of loss. As with the axial space, the loss increases at lower loading and higher local flow coefficient and which is likely due to increasing flow velocity (figure 6.10), with which the leakage flow is mixing and increasing over tip driving pressure. However, the mixed flow architectures have nearly double the leakage loss in this region of the design space. When comparing the two architectures, the mixed flow architecture showed to have nearly double the leakage area which would explain the significantly higher leakage loss.

The tip leakage loss decreases when moving from the bottom right to the top left. As previously discussed, the shape of loss contours are likely caused by an interaction between the leakage and secondary flow. However, as previously stated this cannot be confirmed as the decoupling and modelling of the mechanism can be called into question and therefore requires further research.

6.5 Mixed Flow Turbine Balje Chart

The following section explores the CFD constructed Balje diagram of mixed flow turbine rotors. Arguably the mixed flow architecture is the most general form of a turbine, hence encompasses both axial and radial architectures. To produce true mixed flow Balje chart would require the optimisation of many parameters including cone angle (λ) and radius ratio (R_r). This would require vast amounts of computation resources and time. Instead a constrained form of a mixed flow architecture will be analysed.

For the sake of simplicity, instead of varying these parameters, a compromise was struck and radius ratio and cone were kept fixed throughout the design space between radial and axial architectures. A cone angle $\lambda = 45$ degrees (which sits between axial and radial) and a radius ratio $R_r = 0.75$ was used. These values are close to those used by Abidat [1]. Keeping these parameters fixed is by no means an ideal choice and later it will be shown that this leads to poor designs in some regions of the design, later in section 6.7, it will be shown that mixed flow architectures with higher loading coefficients and low duty flow should be shifted towards axial designs. An alternative approach that could be explored in future would be to keep the meridional passage length constant. In this scenario the radius ratio could be varied to maintain the constant length.

Table 6.2 Mixed flow Balje chart parameters

Parameter	Value
λ	45°
R_r	0.75
R_{vm}	1
$\frac{TE}{C_x}$	0.025 (axial section)
$\alpha_2(\text{mean})$	$0 \pm 4\text{deg}$
$C_o(\text{mean})$	$0.7 \pm 6\%$

6.6 Mixed Turbine Total-Total Balje Chart

Figure 6.15(A) is the Balje chart produced for a mixed flow turbine with a fixed radius ratio and cone angle. The figure also includes the projections of the meridional passage geometry. How changes in duty flow affect the geometry are as follows:

- The mean inlet radius increases with reducing duty flow coefficients and vice versa, as with the other architectures.

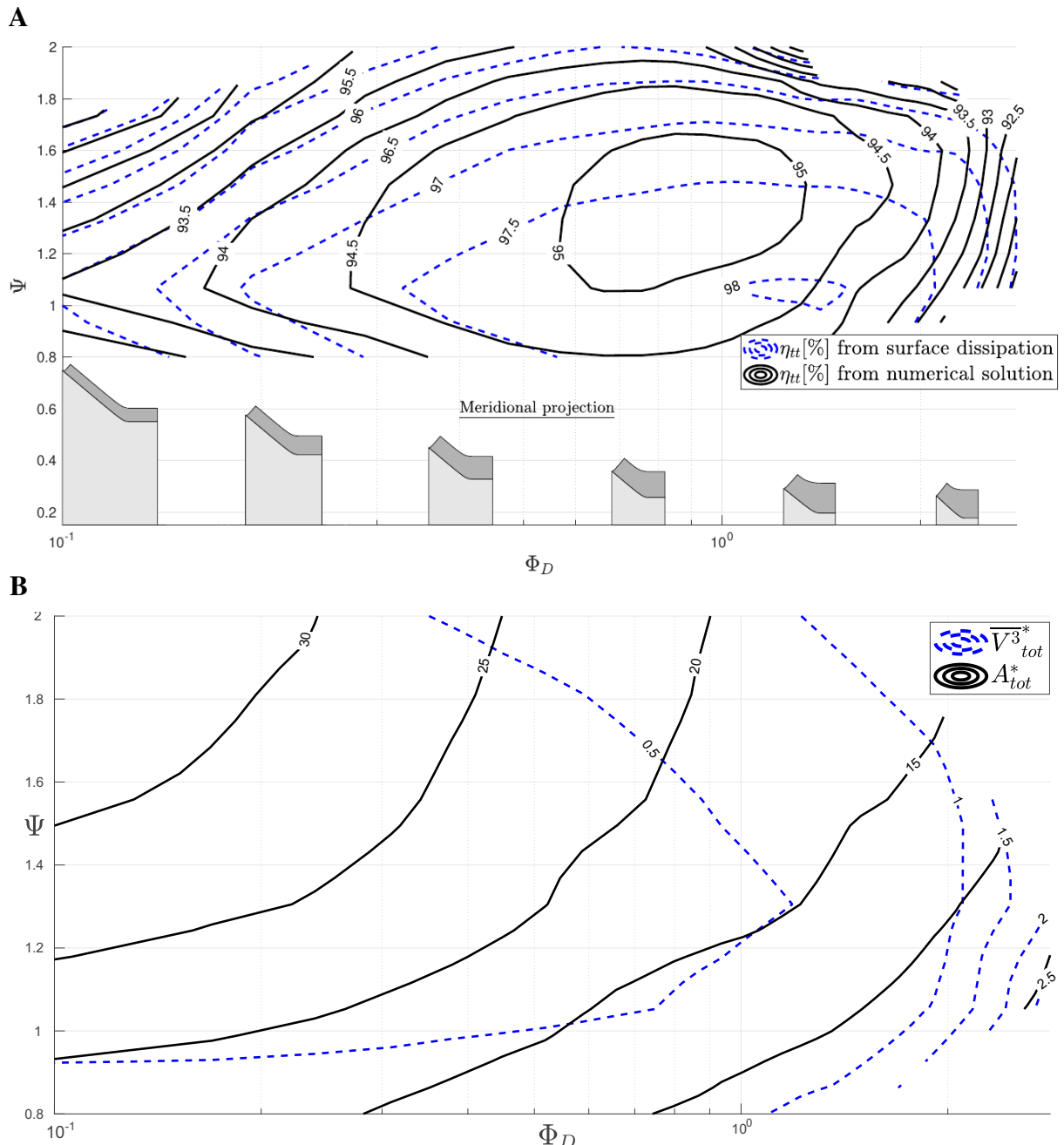


Fig. 6.15 A:Contours of total to total efficiency for mixed flow turbines with varying loading and duty flow coefficients. B: Contours of Surface Area and surface area averaged velocity cubed, varying loading and duty flow coefficients.

- The meridional length of the passages increases with reducing duty flow coefficients and vice versa. This due to fixed radius ratio and cone angle in conjunction with the design constraint discussed in section 2.2 and illustrated in figure 2.9.
 - The passages get thinner with reducing duty flow coefficients and vice versa. This due to changes in $\frac{A_{in}}{r_p^2}$ which sets the hub to tip ratios.

The changes in geometry when reducing duty flow increase the end wall surface area significantly. This drives large amounts of end wall loss which is the primary driver for loss in this region of the design space. Conversely, increasing duty flow coefficient opens the machines up, reducing the amount of end wall surface area and therefore improving efficiency. As previously shown, at high duty flow coefficients, radial architectures suffer high secondary/separation loss due to high casing curvature. For mixed low architectures, these effects are significantly reduced (no separation was found in these designs). This is due to larger radii of curvature as a result of the lower cone angle of these designs.

As with the other architectures, surface dissipation largely captures the shape of efficiency trends. Similar to radial architectures, it can be seen that the mixed flow designs at low duty flow coefficients have characteristically high surface area and designs at high duty flow have high surface velocity (see Figure 6.15 *B*). The latter again being a result of high local flow coefficients of these designs.

As previously discussed, mixed flow architectures can be designed with higher loading coefficients than radial architectures, while maintaining radial blade fibres and little to no effective incidence. Like in the Smith chart of this architecture, the performance drops off sharply at higher loadings where axial architectures can comfortably operate. The drop in efficiency is largely driven by an increase in surface area which is more stark at lower duty flow coefficients. This performance boundary can be extended by relaxing the meridional design constraint that does not allow for inflection points in the casing curvature. Later, it will be shown that these performance boundaries can also be extended by blending mixed flow architectures towards axial designs.

6.6.1 Profile loss

The profile loss across the design space is presented in figure 6.16. The variations in this loss can largely be explained by changes in surface area and surface velocity (Figure 6.15 *B*). The increase in loss at higher loading and low loading coefficients is largely driven by large amounts of surface area. The high amount of area is due to the longer passage length and higher rake angle. As with the axial and radial architectures, the profile loss increases at higher duty flow coefficients. As previously discussed, this is a consequence of the high surface velocity which is due to the high local flow coefficients of these designs. The model captures the behaviour reasonably well. However, it does under predict the loss and is slightly less sensitive to changes in loading.

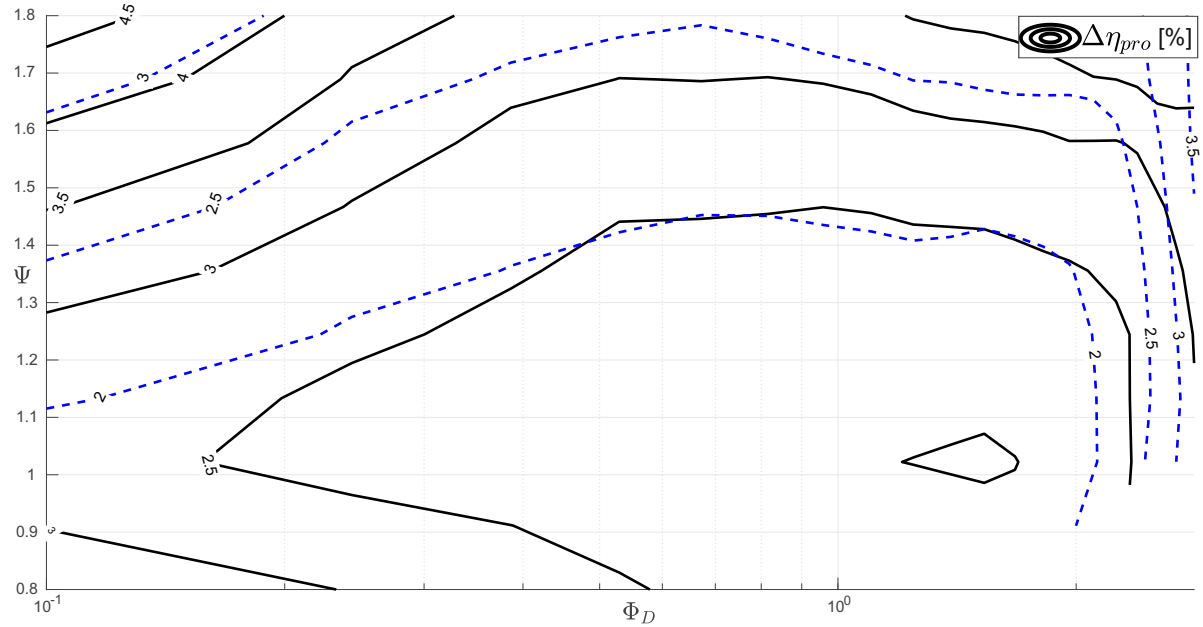


Fig. 6.16 Contours of loss in efficiency of Mixed turbines due to profile loss

6.6.2 Secondary/Endwall loss

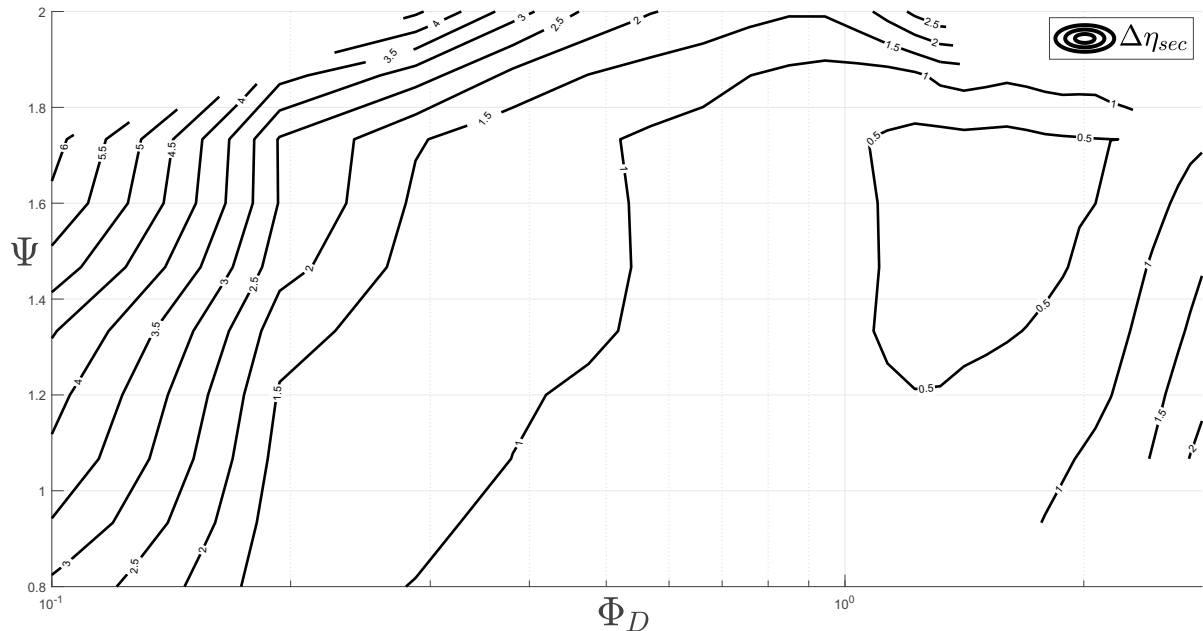


Fig. 6.17 Contours of loss in efficiency of Mixed turbines due to endwall loss

Figure 6.17 shows the variation of the endwall loss across the design space. The loss increases significantly at lower duty flow and higher loading coefficients. As with radial architectures, the increase with reducing duty flow is due to high end wall surface area which is driving large amounts of surface dissipation. The majority of this is from the casing (see Appendix B.9). This is a result of the low meridional aspect ratio, itself a consequence of the low non dimensional

inlet area flow area. The surface dissipation also drives a slight increase in endwall loss at higher duty flow due to high endwall velocities.

The increased loss at higher loading is largely driven by high amounts of secondary flow. This is likely a result of the higher overall turning.

The results of the low order model are not shown here as the secondary flow loss component of the loss model broke down at low duty flow and high loading coefficients. The aspect ratio term $\frac{p_m \cos \beta_2}{h}$ in Equation 3.22 was responsible for this. The top left corner of the design space, where the passages are long, leads to a low blade count and therefore a high pitch which drives down the aspect ratio term. While the secondary loss in this region is indeed high (Appendix B.9), the model overpredicted the loss too dramatically. A non-linear correction could be applied in future to fix this issue.

6.6.3 Tip Leakage loss

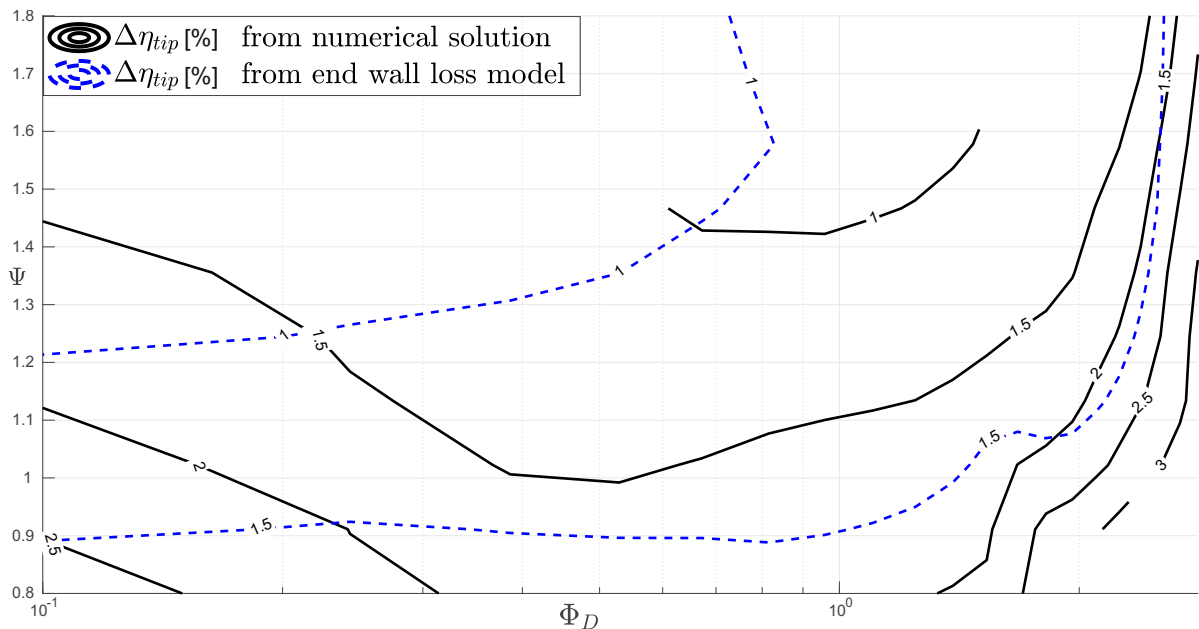


Fig. 6.18 Contours of loss in efficiency of Mixed turbines due to Tip Leakage loss

The variation in the leakage loss across the design space is shown in Figure 6.18. The changes across the space show some similarities with the axial architectures. The loss increases at high duty flow and at low loading coefficients. As with the both radial and axial architectures, the trend can mostly be explained by the higher surface velocities with which the flow is mixing, (Figure 6.15 B). In addition to this, designs at higher duty flow have a larger difference in velocity between the suction and pressure surface at the casing (due to the higher pitch). This will drive up leakage mass flow, further increasing loss.

The low order model loosely captures the trends in loss at higher duty flow but does not predict the rise in loss at lower duty flow. This rise likely stems from the increasing leakage area

due to the longer skinnier passages. This did not increase leakage loss in radial turbines as the blade angle in the radial section remained zero which maximised the scraping effect. For mixed flow turbines, the angle continues changes throughout the passage as there is no radial section and therefore reduces the scraping effect.

6.6.4 Mixed Turbine Total-Static Balje Chart

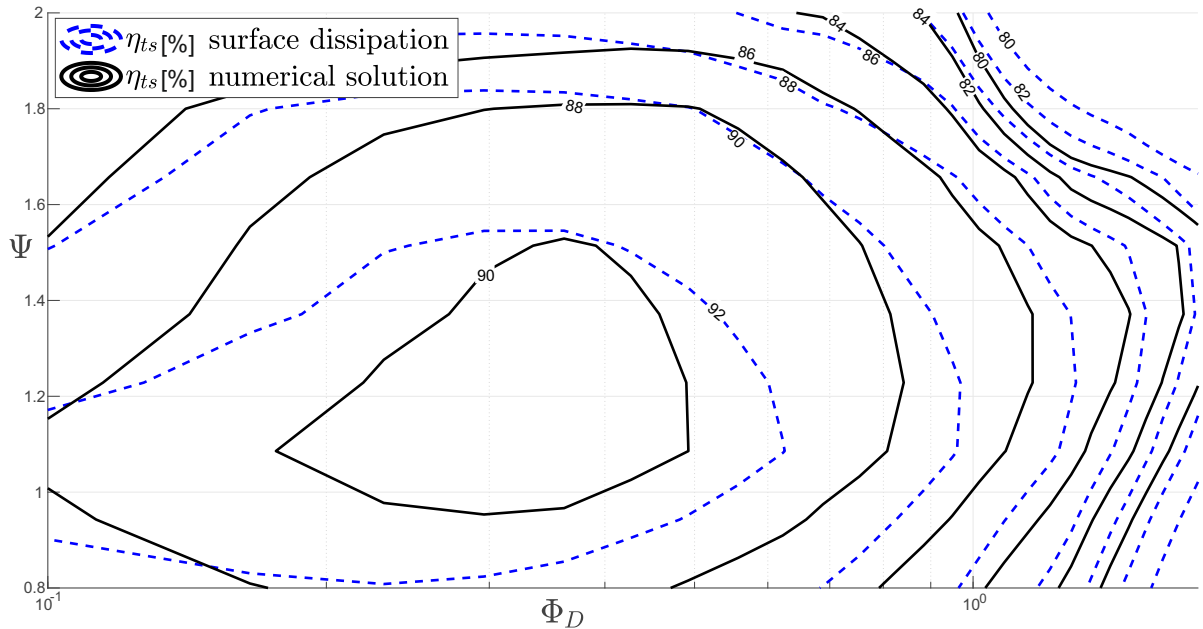


Fig. 6.19 Contours of total to static efficiency for mixed flow turbines with varying loading and duty flow coefficients

The variation in the total to static efficiency across the design space is plotted in Figure 6.19. As with axial and radial turbines, the difference between the total to total design space is driven primarily by exit loss which has already been discussed. The reduction in maximum efficiency of 5% sit between that of axial and radial designs; a more detailed comparison between the architectures can be found in Chapter 7. But in short, the improved performance over the axial architectures is due to the lower local flow coefficients of these designs. The slightly lower performance when compared to radial architectures is driven by higher entropy based loss mechanism. It must noted that the total to static performance of all the architectures could be improved by reducing the meridional velocity ratio. This could bring the performance of many of these architectures in line with one another. As with the other architectures, the exit loss shifts the drop off in efficiency to lower values of duty flow coefficient. This is again a result of the exit loss scaling with local flow coefficient which increases for designs to the right of the chart.

6.7 Radius Ratio vs Cone Angle

The key parameters that distinguish mixed flow architectures from the other architectures is the cone angle when comparing to radial turbines, and both radius ratio and cone angle for axial turbines. Understanding how these parameters can affect performance is key to building a strong design methodology. Therefore the effects of varying radius ratio and cone angle were tested. This was done at a fixed duty flow coefficient and a fixed local flow coefficient for two different levels of loading.

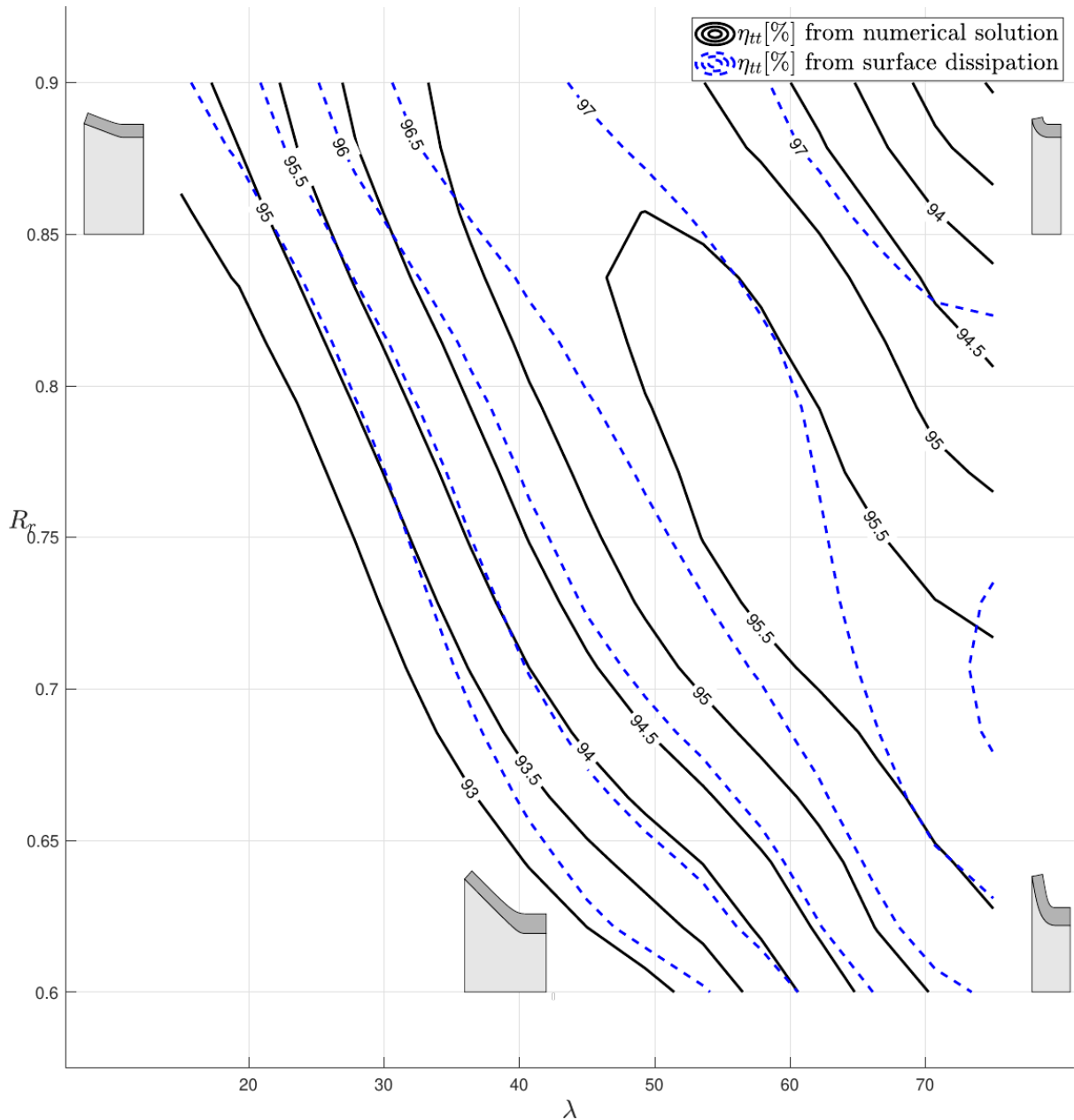


Fig. 6.20 Contours of Total to Total efficiency with varying Radius Ratio and Cone Angle, $\psi = 1.0$ and $\Phi_D = 0.2$

Figure 6.20 shows the variation in performance across a range of radius ratios and cone angles for a loading coefficient of 1. The corresponding meridional geometries are also shown for reference. Turbines in the bottom right of the space are tending towards radial shapes and the turbines in the top left of the design space are tending towards axial turbines (low aspect ratio). A consequence for not allowing any inflection points on the hub and casing lines is that turbines with low cone angles tend to have overly long axial lengths and therefore large amounts of surface area (as discussed in section 2.2). This drives up loss at low cone angles and radius ratio which is mirrored by the surface dissipation.

The turbines in the top right of the design space have low radius of curvature at the casing due to increasing radius ratio and cone angle.

This will likely result in increased secondary flow loss which would explain the difference in the drop off in efficiency between surface dissipation and the results from the numerical solution.

Between the upper right and bottom left low performance regions lies a ridge that runs through the design space, partially bridging the architectures. This suggest that at low loading coefficients either architecture type could be used (for this particular combination of parameters).

As for the higher loading case, shown in Figure 6.21, optimisation would push designs towards the axial regime. The surface dissipation loosely captures this trend. On further inspection, it was observed that the dissipation is nearly entirely driven by changes in surface area. Therefore the variation in surface area can help explain the behaviour this is shown in Figure 6.22. The figure shows that the decrease in surface area is driving the architecture towards the axial regime.

Also plotted is the optimum cone angle for a given radius ratio. Comparisons suggest that in order to find the optimum cone angle for a given radius ratio, a designer should minimise the overall all surface area.

There are two different surface areas which determines where this minimum lies - the end wall surface area and the blade surface area. The end wall surface area increases with decreasing radius ratio and cone angle. This is simply because the meridional passage length increases. The increase in blade surface area at high cone angles is a consequence of radial blade fibred designs. From Equation 1.17 and 1.18 it can be seen that increasing the cone angle increases the camber/rake angle. Higher camber angles results in blades that wrap further around the axis of rotation, resulting in large profile surface area. The explanation for this is given in Section 1.4. The balance of these two sources of area roughly determines the optimum cone angle for a given radius ratio. In the top right corner, the performance drops significantly faster than that predicted by surface dissipation. This is likely due to large amounts of secondary flow, which is similarly driven by the low radius of curvature at the casing.

An additional point of note is that for designs with higher loading coefficients, the centrifugal term represents a lower fraction of the over all loading. For zero interstage swirl, the fraction of centrifugal loading that can be achieved is

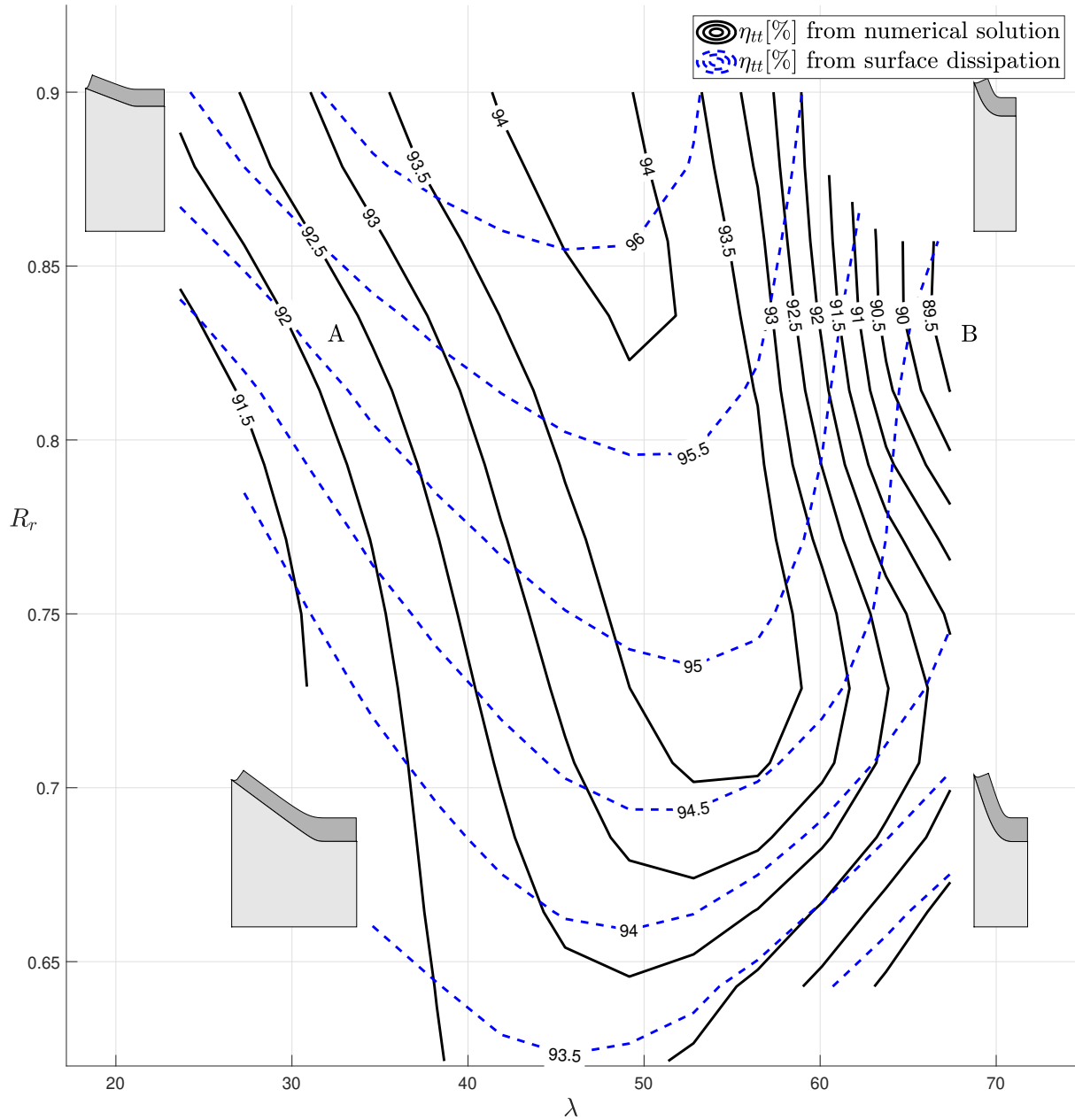


Fig. 6.21 Contours of Total to Total efficiency with varying Radius Ratio and Cone Angle, $\psi = 1.6$ and $\Phi_D = 0.2$

$$\frac{\psi_{ke}}{\psi_{tot}} = \frac{1 - R_r^2}{2\psi_{tot}}$$

where $RR > 0$. Therefore designs with higher loading coefficients will have a lower fraction of centrifugal loading and therefore less of the associated benefits.

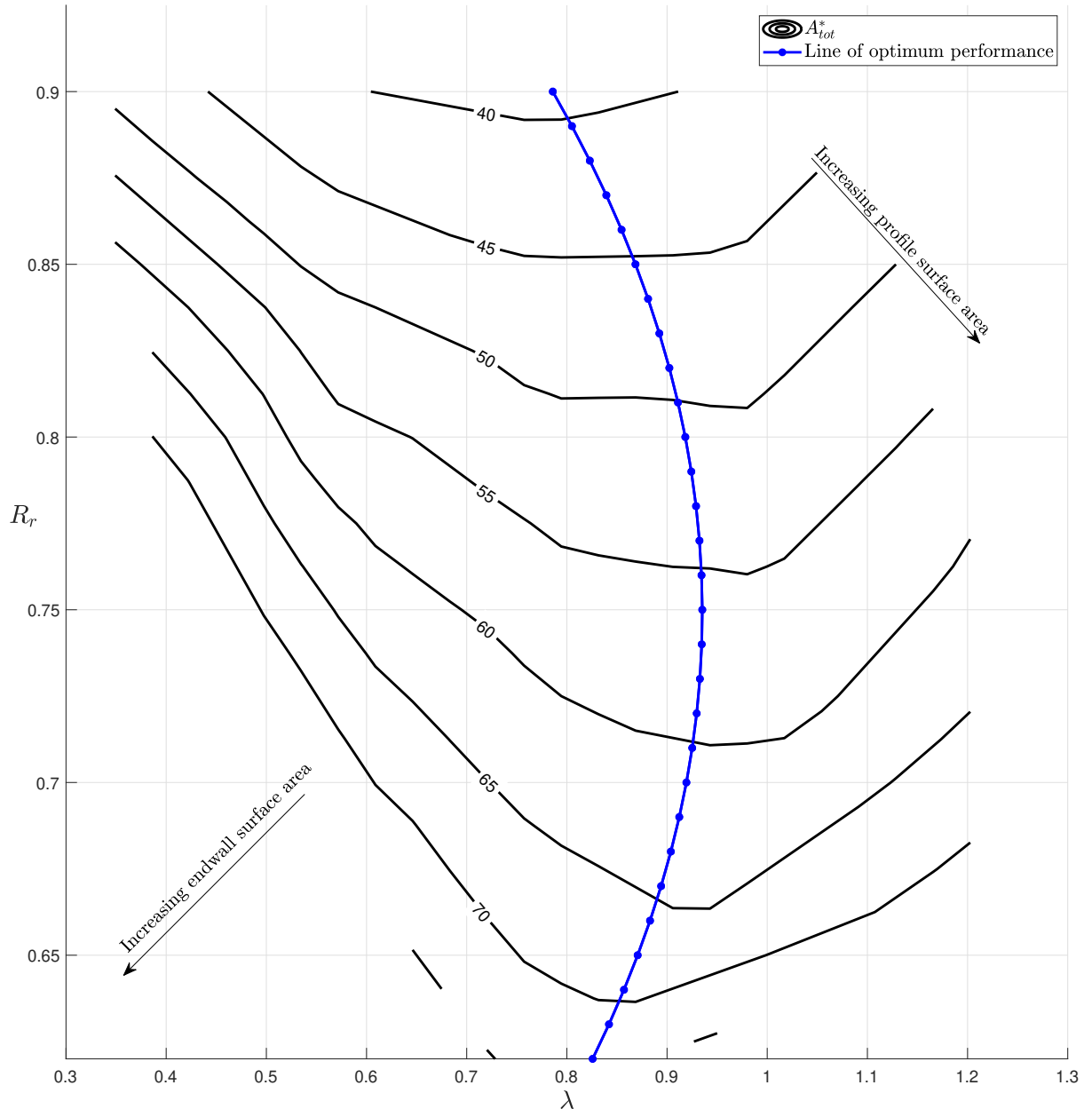


Fig. 6.22 Contours of surface area with varying Radius Ratio and Cone Angle, $\psi = 1.6$ and $\Phi_D = 0.2$

6.8 Chapter Conclusions

Arguably, mixed flow architectures are turbines in their most general form and hence encompass axial and radial architectures, however, these machines have had little attention in the literature when compared to the other two. This is particularly the case for design parameter space analysis. To fully represent the capabilities of mixed flow turbine would require optimising both radius ratio and cone angle, however this is unfeasible given the resources and time available. Instead a constrained design space was mapped to illustrate a truncated form of the mixed flow

space. Not only were the radius ratio and cone angle fixed but designs were limited by a radial blade fibre constraint. These constraints will limit the generality of the design parameter spaces produced. That being said, the mapped out charts can still serve as a starting point to build up an understanding of this complex parameter space. The overall goal of this chapter was to build an understanding of the shapes of the Smith and Balje chart for constrained mixed flow architectures. The key conclusions pertaining to this are now summarised.

- It was shown that the higher loading regions of the design space have a significant performance boundary. Above this boundary, mixed flow turbines can perform poorly due to flow lifting off from the hub suction surface corner. The separated flow is transported across the passage to the casing, disrupting the flow field. Note, cases of this feature have been found in the literature ([2], [56], [41]).

The separation is caused by an adverse pressure gradient downstream of a region of low pressure at the hub suction surface corner. Two important factors that play a role in driving the low pressure are: the increasing rake angle with loading and the Coriolis force. Previous methods used for suppressing this flow feature required carefully target and detailed design changes to the hub and hence could not easily be used across the design space. Instead, it was shown that using a fillet like treatment to the hub-suction surface corner significantly improved the performance by suppressing the separation. The fillet acts to shift the low pressure region away from the hub surface and in addition to this, likely reduces the concentration of vorticity in the hub-suction surface corner. This suppresses the formation of the vortex structure which in turn, robustly opens up the mixed flow design space to significantly higher loadings, all without the requirement of detailed design work.

- As with radial and axial designs, the topology of both Smith and Balje charts can to some extent be explained in terms of surface dissipation (velocity cubed rule). In the mixed flow Smith chart, the contours matched reasonably well for most of the space with the exception of designs at low loading and high flow coefficients. The latter was attributed predominately to the high tip leakage loss in this region. As with the axial and radial architectures, the increase in surface dissipation at high local flow coefficients is driven by high surface velocities, and the high surface dissipation at low local flow coefficients is driven by high surface area. The drop in performance with loading, which is sharper when compared to axial turbines, was in part attributed to the large increase in surface area due to increasing rake. In addition to this, the surface velocity increase faster with loading when compared to the axial design space.

For the Balje diagram, the high surface dissipation at high duty flow coefficients is similarly a result of high surface velocity due to high local flow coefficients. Like radial architectures, the mixed flow designs experience a drop in performance at low duty flow

coefficients. This is a result of the high end wall surface area of turbines in this region of the design space. It must be noted that this boundary can be extended by relaxing the design constraints which enforces no inflection points of the casing line (Section 2.2) or freeing the cone angle and radius ratio.

- A design space was produced in which the radius ratio and cone angle were varied. This was done for a low ($\psi = 1$) and relatively high ($\psi = 1.6$) loading coefficient mixed flow turbines. For both loadings coefficient, designs with low radius ratios and cone angles showed poor performance due to large amounts of surface area, mostly from the endwalls. Designs with high radius ratios and cone angles also showed poor performance, in part due to the small radius of curvature of the casing radial to axial bend. For the low loading case, a ridge in the efficiency contours suggested that, at lower loadings, both regions of the design space (axial vs radial) are valid choices. This is not the case for higher loading coefficient designs. Instead, the efficiency contours suggest that design should be shifted towards axial architectures which would improve performance by reducing surface area. It was also noted that designs with overall higher loading coefficients will have a smaller fraction of centrifugal loading and therefore less of the associated benefits.
- Contributions from the individual loss mechanisms, (according to the CFD) to the shape of the Smith and Balje chart were studied. At low duty flow coefficients, the profile loss contributed a significant amount to the overall lost efficiency, particularly at higher loading. This was due to the high amounts of profile surface area due to long passages and increasing rake angle. At high duty flow coefficients, profile loss also contributed to the increase in lost efficiency. This was a result of increasing passage surface velocities due to high local flow coefficient, characteristic of this region of the design space. The endwall loss is a significant driver for the reduction in performance at low duty flow. This was caused by the high end wall surface dissipation due to the large amounts of surface area. As previously mention, the low performance in this region of the constrained Balje chart can be improved by blending towards axial architectures. The endwall loss also played a role at higher duty flow coefficients, but unlike the radial architectures no flow separation occurred at the casing. This was attributed to the increased radius of curvature at the radial to axial bend. The leakage loss increased with reducing duty flow coefficients. This was attributed to the increasing leakage area and reduced scrapping effect both of which are due to the continuously varying blade angle. In contrast, in radial architectures, the blade angle remains zero for the radial section. Like radial and axial architecture, the leakage loss increased with duty flow. Again, this was attributed to the high flow velocities and over tip driving pressure of these designs.
- The profile loss model functioned well for the mixed design spaces, but the secondary flow model only somewhat captured the trend for the Smith chart and largely failed for

Balje chart. This was due to the linear relationship with the aspect ratio term ($\frac{p_m \cos \beta_2}{h}$). As with axial architectures, the leakage loss model correctly predicted increasing loss with increasing duty and local flow coefficient particularly at low loading. In regards to the Smith chart, the model predicted increased loss at higher loading which was not reflected by the decoupled CFD. As with the axial architecture, this is likely a result of interaction with the secondary flow. The leakage loss model also failed to capture the increased loss at low duty flow (Balje chart).

Chapter 7

Unified Designs And Conclusions

7.1 Chapter Objectives

Balje charts serve three primary purposes, selecting speed and sizing, rough estimations for performance and architecture selection. Thus far, the aerodynamics of these architectures have been analysed one by one. This chapter will bring together all the architectures in one unified Balje diagram. The different architectures will be compared and contrasted across the space in further detail. In addition to further design consideration will be discussed. The key objectives of this chapter are as follows:

- Explain the different shapes of the design space of the architectures studied in this thesis. This will include a relatively detailed discussion on specific points throughout the design space.
- Discuss trends in power density, inertia and cost as designers are not only interested in efficiency. This will further aid designers when making decision on architectural type.
- Discussion on how staging and parallelisation move designs through the space.
- In some applications turbines are used in conjunction with a diffuser. Therefore, a section on combined turbine-diffuser performance is included which will analyse the best choice in design flow coefficient under these circumstances.
- End the thesis with final conclusions.

As previously stated, there are inherent limitations to the methodology used, namely the limitation of CFD and these should be kept in mind. However, when comparing different architectural types there is an additional limitation which is due to the variability in design complexity. For example, mixed flow turbines are inherently more complicated to design due to the additional degrees of freedom and more complex flow paths. Therefore caution must

be taken when directly comparing the architectures, particularly in regions of overlap where turbines have similar performance.

7.2 Total to Total Efficiency

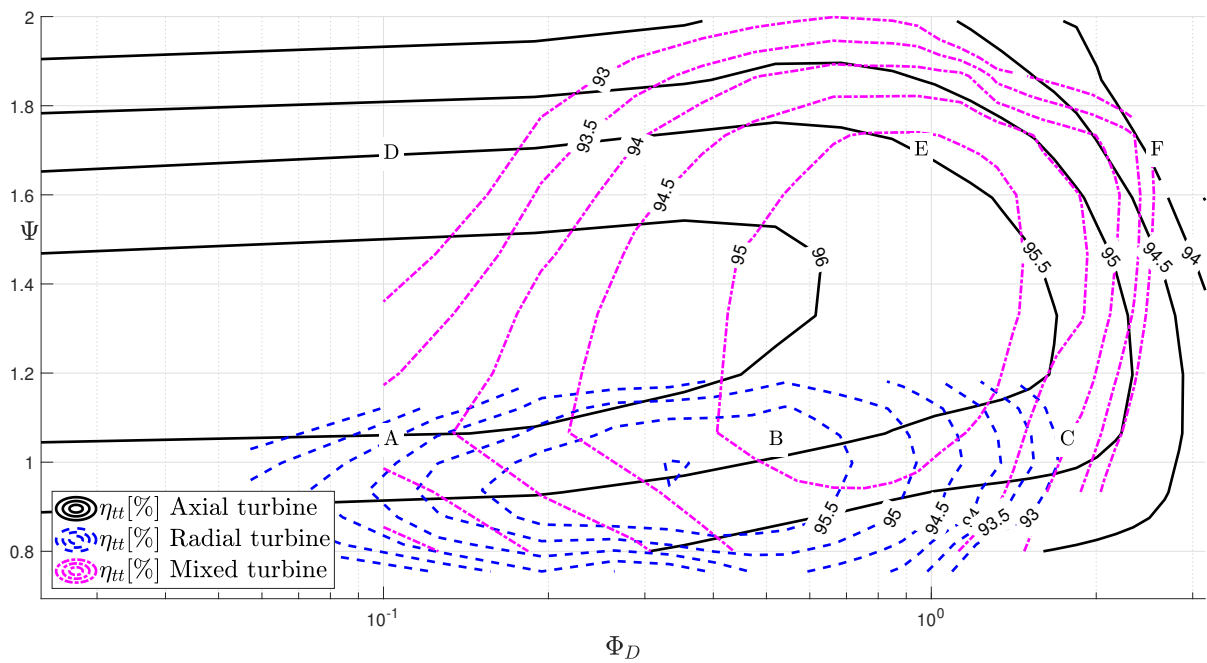


Fig. 7.1 Contours of total to total efficiency for Axial, Mixed and Radial flow turbines with varying loading and duty flow coefficients

Figure 7.1 is a composite Balje diagram for the total to total efficiency of axial, radial and mixed flow architectures.

The axial architectures have the widest range of applicability and can be used at both high and low loading, over a wide range of duty flow. The wide range of usable duty flow coefficients can be attributed to partial invariance of the meridional geometry (fixed aspect ratio). Both mixed flow and radial architectures will suffer a drop in performance at low duty flow due to reducing aspect ratio of the meridional passage which leads to a high endwall surface area. As the axial architecture have a fixed aspect ratio they can be used at lower duty flow without an increase in end wall loss.

Radial turbines have a smaller applicable range of duty flow coefficient than axial architectures. The drop in performance at high duty flow is driven by two factors. The first is the high surface velocities of these turbines, which also occurs with the other architectures. The second and differentiating factor is low radius of curvature at the casing which drives additional secondary loss and ultimately can lead to casing separation. The performance limits shown here can more than likely be extended to higher duty flow by more detailed casing design.

Many turbocharger designers do so by spreading curvature of the casing line upstream in to the volute/inlet region. This is illustrated in figure 2.9 and discussed in section 2.2. One consequence of having meridional curvature at the inlet is that this will cause a variation in incidence at the blade inlet and thus requires more detailed design. Alternatively shifting to mixed flow architectures allows for better performance at higher duty flow.

The performance drop off at lower duty flow coefficients of mixed and radial turbines is a result of the large amount of end wall surface area. This is a consequence of the low radius ratios and non dimensional through flow area $\frac{A_{in}}{r_n^2}$. By reducing the duty flow coefficient, the through flow area reduces. This, coupled with reducing radius ratio, results in long, thin passage geometries and therefore high endwall surface area. The majority of the end wall surface loss for radial turbines at lower duty flow coefficients is from the unshrouded casing due to the high absolute velocities towards the inlet. Radial turbines in this region of the design space will benefit from full or partial shrouding of the inlet section. Like radial turbines, mixed flow turbines suffer the same loss in performance at low duty flow but suffer an even sharper drop in performance at high loading due to the increasing profile surface area.

Radial turbines are constrained to lower loading coefficients. This is a result of radial blade fibres in conjunction with a cone angle of 90 degrees, which constrains the blade inlet metal angles to zero. At higher loading these architectures incur large amounts of loss due to incidence. By virtue of having a cone angle less than 90 degrees, mixed flow architectures with radial fibres can be designed at higher loading coefficients. However, when compared to axial architectures the performance drops quicker due to larger increases in surface area and velocity, which are both consequences of increasing rake. Without the hub fillet introduced in section 6.3, these turbines would be limited to even lower loading coefficients.

It must be pointed out that the axial turbines used here are not purely radially blade fibred (no unique camber line). These designs were radially stacked around the mid cord but this does not necessarily ensure structurally sufficient amounts of blade section overlap, particularly if the blades are thin and have large variations up the span.

Conversely, the radial turbines are purely radially blade fibred and are in reality likely to achieve higher blade speeds before failure. This is particularly the case for small machine applications, Dambach [22](micro turbines) compared a radial turbine to an axial turbine which had a 40% lower blade speed for structural reasons. This meant the axial turbine required a significantly higher loading coefficient (different points in the design space) and as a result had worse performance. The mixed flow turbines are also purely radially blade fibred and as such are likely to achieve similar blade speeds to that of the radial turbines. When considering different architectures, designers should not necessarily only compare designs at the same point in the design space but should take structural limitations into account.

There are additional advantages for radial turbines relating to compressibility, due to the shifting of loading from the relative acceleration term to the centrifugal term, there is less overall

acceleration through the passage and therefore, lower passage velocities. This allows radial turbines to operate at higher pressure ratios before choking (in the rotor).

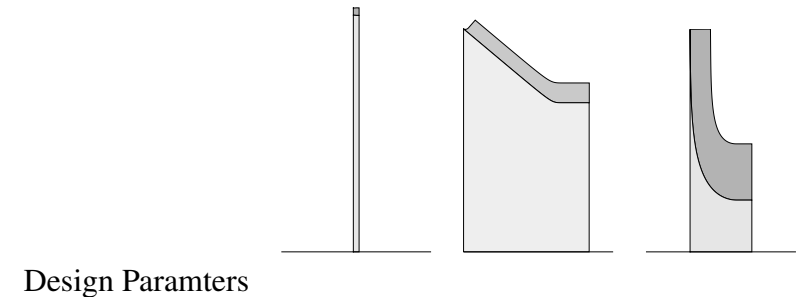
Point A

Table A.5 shows a comparison of radial, mixed and axial turbines in the vicinity of point A in Figure 7.1. Included in this are projections of the meridional geometry, which illustrates the stark difference between the turbines. The mixed and radial turbines have significantly longer meridional flow paths, which is the key factor differentiating performance. The axial turbine at this point in the design space has as superior total to total efficiency and this is largely due to significantly lower end wall loss.

The high end wall loss of the radial and mixed flow architecture is driven by the high end wall surface area, which is more than an order of magnitude larger than in axial turbines. The axial and mixed flow turbines have similar levels of a profile loss. This is likely due to a similar value of $\bar{V^3}_{pro}^* A_{pro}^*$. How this is factored differs significantly between the two turbines. The axial turbine has higher surface velocities, whereas the mixed flow turbine is driven by high surface area. The radial turbine has the lowest profile loss of the three turbines and this is due to the very low surface velocities. The variation between the surface velocities of the three turbines is mirrored by the work split and local flow coefficient. In Section 5.9, it was shown that changes in the radius ratio redistributed loading from the relative acceleration term to the centrifugal term and reduced the average passage velocities. The axial turbine has the largest acceleration loading and local flow coefficient, whereas the radial turbine has significantly lower acceleration loading and flow coefficient. This explains the difference in the surface velocities.

Baring in mind the modelling inaccuracies of leakage loss, the radial and axial turbines have similar values but the loss is driven by very different means. The radial turbine has a significantly higher leakage area but only a slightly higher leakage mass flow. The majority of this area is in the radial section, where the scraping has a strong effect. Another differentiating factor is the velocity with which the leakage flow is mixing. The difference between the axial and radial turbines flow velocity might explain the slightly lower leakage loss of the radial turbine, even though it has higher leakage mass flow.

The mixed flow architecture has significantly higher leakage loss, double that of the radial turbine. It is not entirely clear why this is the case, as the leakage area is more than double that of the axial turbine, but the leakage mass flow is only slightly higher.



Design Paramters

	1.0	1.0	0.925
Ψ_{cen}	0.0	0.22	0.42
Ψ_{rac}	0.5	0.28	0.08
Ψ_{ake}	0.5	0.5	0.425
Φ_D	0.09	0.10	0.1
Φ_L	0.44	0.25	0.17
R_r	1.00	0.75	0.40
Blade number	347	16	29
<hr/>			
Total to Total			
<hr/>			
η_{tt}	96.0	93.0	94.0
A_{tot}^*	9.70	64.10	116.80
$\overline{V^3}_{tot}^*$	0.790	0.252	0.116
<hr/>			
Profile loss			
<hr/>			
$\Delta\eta_{pro}$	2.5	2.7	1.3
A_{pro}^*	7.515	23.97	65.87
$\overline{V^3}_{pro}^*$	0.860	0.328	0.044
<hr/>			
End wall loss			
<hr/>			
$\Delta\eta_{end}$	1.3	5.0	5.0
A_{end}^*	2.19	40.12	50.92
$\overline{V^3}_{end}^*$	0.55	0.20	0.21
$\frac{P_i \cos \Delta \beta_m}{h}$	0.23	0.98	0.12
<hr/>			
Tip leakage loss			
<hr/>			
$\Delta\eta_{tip}$	1.3	2.0	1.0
A_{tip}^*	0.04	0.1	0.26
\dot{M}_{tip}^*	0.014	0.015	0.017
$\overline{V^2}_{cas}^*$	0.854	0.541	0.129

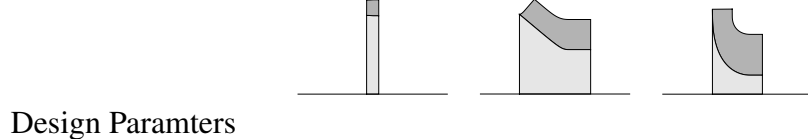
Table 7.1 Turbine comparison for point A

Point B

Similarly, Table 7.2 shows a comparison of radial, mixed and axial turbines in the vicinity of point *B* in Figure 7.1. In this region of the design space, the axial and radial turbines have similar performance, closely followed by the mixed flow turbine which is slightly lower. This lines up reasonably well with surface dissipation, where the axial and radial have similar $\overline{V^3}_{tot}^* A_{tot}^*$ values of 7.4 and 6.1 respectively, and the mixed flow is higher than both with $\overline{V^3}_{tot}^* A_{tot}^*$ of 9.3. The radial turbine likely has increased secondary flow loss which could make up for the difference in surface dissipation. As with the turbines in Table A.5, the radial turbine for point *B* has significantly lower profile loss than the mixed and axial architectures due to the low surface velocity. Note that this velocity is nearly 3 times that of the radial turbine from point *A* and is due to the higher acceleration loading. For this region of the design space, the radius ratio must increase to accommodate the increased exit area which comes with the higher duty flow coefficients. This decreases the centrifugal term and the loading is shifted to the relative acceleration term in addition to this the local flow coefficient also increases to accommodate more mass flow relative to the size.

The radial architecture has the highest end wall loss, closely followed by the mixed flow architecture. Similar to point *A*, high end wall loss of these architectures is driven by the high end wall surface area compared to that of the axial architecture.

The predicted leakage loss for the different turbines are approximately equal. Interestingly, the parameters associated with this loss differ significantly. Comparing the leakage mass flow of the axial and radial architectures, the radial turbine shows significantly higher mass flow than that of the axial. The equal loss might stem from the reduced velocities with which the leakage flow is mixing. The mixed flow architecture has a similar leakage mass flow to the radial architecture and a similar casing velocity to the axial architecture. Therefore, one would expect the mixed flow turbine to have a larger leakage loss. A potential reason for the discrepancy is likely due to an interaction with end wall flow.



Design Paramters

	1.0	1.0	0.925
Ψ_{cen}	0.0	0.22	0.34
Ψ_{rac}	0.5	0.28	0.16
Ψ_{ake}	0.5	0.5	0.425
Φ_D	0.50	0.5	0.5
Φ_L	0.47	0.32	0.34
R_r	1.00	0.75	0.57
<hr/>			
Mechanical properties			
<hr/>			
Blade number	60	15	19
$\log_{10} P_V^*$	-0.80	-1.48	-1.24
$\log_{10} I_V^*$	-0.14	0.49	0.39
<hr/>			
Total to Total			
<hr/>			
η_{tt}	96.0	95.0	96.0
A_{tot}^*	8.98	26.41	34.26
$\frac{V^3}{V^3}_{tot}^*$	0.82	0.354	0.177
<hr/>			
Profile loss			
<hr/>			
$\Delta\eta_{pro}$	2.5	2.2	1.2
A_{pro}^*	6.91	17.64	24.46
$\frac{V^3}{V^3}_{pro}^*$	0.93	0.42	0.12
<hr/>			
End wall loss			
<hr/>			
$\Delta\eta_{end}$	1.5	2.5	3.0
A_{end}^*	2.06	8.77	9.79
$\frac{V^3}{V^3}_{end}^*$	0.528	0.219	0.248
$\frac{P_i \cos \Delta\beta_m}{h}$	0.24	0.33	0.18
<hr/>			
Tip leakage loss			
<hr/>			
$\Delta\eta_{tip}$	1.6	1.7	1.7
A_{tip}^*	0.035	0.074	0.081
\dot{M}_{cas}^*	0.016	0.024	0.028
$\frac{V^2}{V^2}_{cas}^*$	1.070	0.890	0.639

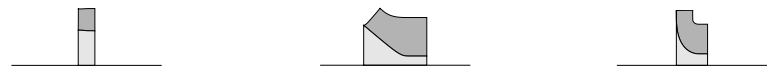
Table 7.2 turbine comparison for point B

Point C

In this region of the design space, the axial and mixed flow turbines have similar performance whereas the radial turbine has significantly lower performance, especially when considering the mixed out efficiency. The low performance of radial turbines in this region is a result of a casing separation due to the small radius of curvature, as discussed in Section 5.6.2. The separation dramatically increases the end wall loss. The mixed flow architecture has not yet separated as it has a larger radius of curvature due to the lower cone angle. This is illustrated by the geometry construction shown in Figure 2.6 shown in Section 2.2.

As with the previous points, the axial and mixed flow architectures have similar profile losses driven predominantly by high surface velocity and area respectively. The mixed flow architecture has higher end wall loss than that of the axial and is due to a combination of both increased secondary and end wall dissipation loss.

The decoupling method broke down for the radial architecture in this region of the design space and is likely a result of the interaction with the now separated casing flow, as mentioned in Section 5.6.3. For the other two turbines, the mixed flow turbine has higher leakage loss. This is predominantly due to the higher leakage mass flow, itself a consequence of having nearly double the leakage area when compared to the axial turbine.



Design Paramters

Ψ	1.0	1.0	0.925
Ψ_{cen}	0.0	0.22	0.28
Ψ_{rac}	0.5	0.28	0.22
Ψ_{ake}	0.5	0.5	0.425
Φ_D	1.62	1.58	1.58
Φ_L	0.65	0.52	0.7
R_r	1.0	0.75	0.66

Mechanical properties

Blade number	24	12	16
$\log_{10} P_V^*$	-0.60	-1.09	-0.72
$\log_{10} I_V^*$	-1.22	-0.31	-0.75

Total to Total

η_{tt}	95.5 (94.0 mixed out)	94.5 (93.0 mixed out)	91.0 (88 mixed out)
A_{tot}^*	6.33	17.04	9.88
$\frac{V^3}{V^3}_{tot}^*$	1.279	0.536	0.839

Profile loss

$\Delta\eta_{pro}$	3.0	2.5	2.0
A_{pro}^*	4.78	13.45	7.02
$\frac{V^3}{V^3}_{pro}^*$	1.445	0.566	0.853

End wall loss

$\Delta\eta_{end}$	1.8	2.8	10.0
A_{end}^*	1.544	3.579	2.859
$\frac{V^3}{V^3}_{end}^*$	0.764	0.422	0.805
$\frac{P_i \cos \Delta \beta_m}{h}$	0.30	0.27	0.30

Tip leakage loss

$\Delta\eta_{tip}$	1.7	2.5	*
A_{tip}^*	0.026	0.054	0.016
\dot{M}_{tip}^*	0.014	0.024	0.014
$\frac{V^2}{V^2}_{cas}^*$	1.66	1.25	3.37

Table 7.3 turbine comparison for point C

Higher loading designs

The tables (similar to A,B and C) for these turbines can be found in Appendix A. There are no examples of radial turbines in the following section. As pointed out, radial turbines with radial blade fibres suffer severe incidence loss at high loading.

For point *D* in figure 7.1, the axial turbine has significantly higher total to total efficiency than the mixed flow architecture. The poor performance of the mixed flow turbine is due to the large amount of end wall and profile loss. This is a consequence of the high surface area of this architecture. Section 6.7 explored the effects of varying radius ratio and cone angle and showed that for the higher loading designs, blending the architecture toward an axial design improved performance by significantly reducing the surface area. Therefore the mixed flow architecture for the point in question can be improved significantly.

For point *E*, both axial and mixed flow turbines have similar performance, with the axial being slightly higher due to lower end wall loss, which again relates to difference in end wall surface area. For point *F* the axial turbine has higher performance and seems to be due to lower leakage loss. However, considering the interactive behaviour between leakage and end wall loss at higher loading, this might not be true. What can be said is that the mixed flow turbine has higher leakage mass flow due to higher leakage flow area.

7.3 Total to static

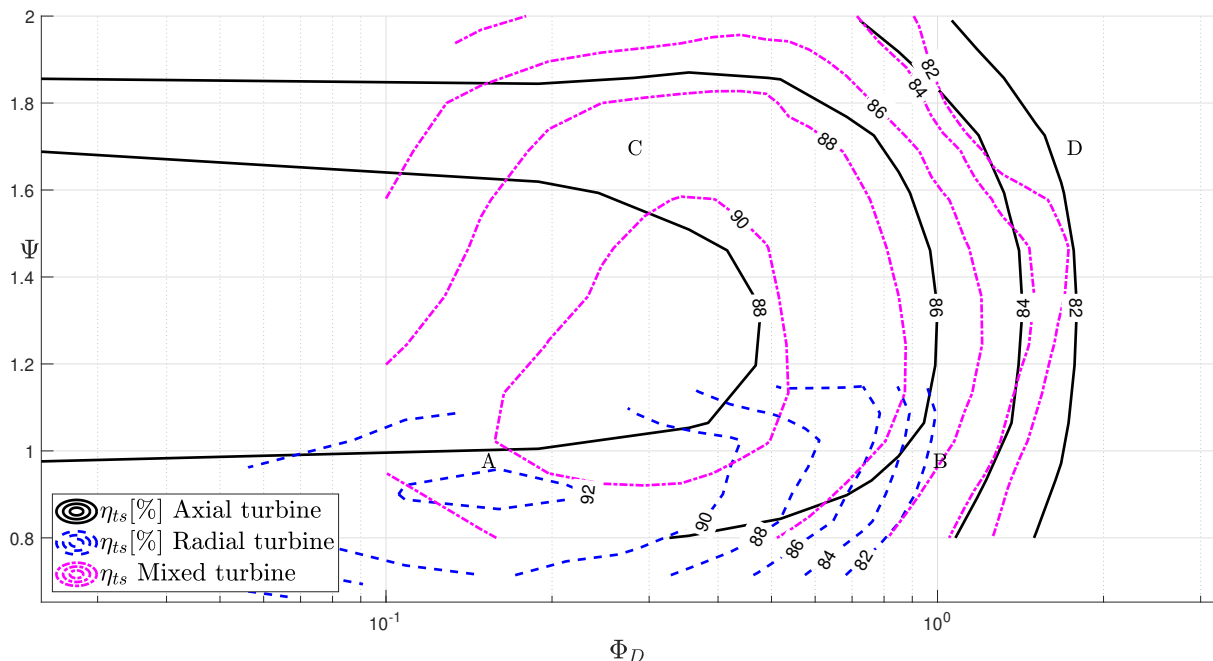
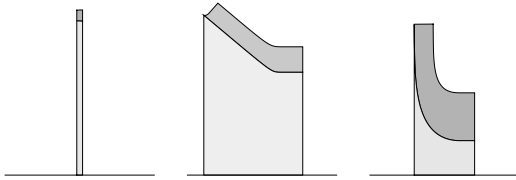


Fig. 7.2 Contours of total to static efficiency for Axial, Mixed and Radial flow turbines with varying loading and duty flow coefficients

Figure 7.2 is a composite Balje diagram for the total to static efficiency of axial, radial and mixed flow architectures. The total to static chart has a similar topology to that of the total to total chart, with a shift to lower duty flow as a result of exit loss. Again, the axial architectures have the widest range of applicability for the same reasons as previously mentioned, but have the lowest peak performance due to higher design local flow coefficients. The mixed flow and radial architectures still show a drop in performance when reducing duty flow, largely due to increasing end wall surface area. However, the sensitivity to the right of the design space is now significantly higher, which is a result of the inclusion of exit loss. As previously discussed, the exit loss scales with local flow coefficient squared, which increases to the right of the space to accommodate the additional mass flow relative to the machine size.

Point A

Table 7.4 shows a comparison of radial, mixed and axial turbines in the vicinity of point A in Figure 7.2. The radial turbine has the highest performance of the three architectures. The high total to static efficiency stems from the high total to total efficiency in conjunction with the low local flow coefficient of the design. Section 5.9 showed that the optimal local flow coefficient for total to total efficiency shifted to lower values when the radius ratio decreased. While the axial turbine matches the total to total efficiency of the radial turbine, its design local flow coefficient is higher and therefore its exit loss is larger. It must be noted that the exit loss of the axial turbine could be reduced by using lower values of the meridional velocity ratio. The mixed flow turbine has the same exit loss as the radial turbine but has a lower total to total efficiency. The mixed flow has a smaller centrifugal term (higher radius ratio) than the radial turbine and as such has higher passage velocities, resulting in more surface dissipation.



Design Parameters			
Ψ	1.0	1.0	0.92
Φ_D	0.15	0.15	0.16
Φ_L	0.37	0.2	0.19
R_r	1.000	0.75	0.43

Mechanical properties			
Blade number	223	15	24
$\log_{10} P_V^*$	-0.75	-1.98	-1.56
$\log_{10} I_V^*$	0.65	1.78	1.28

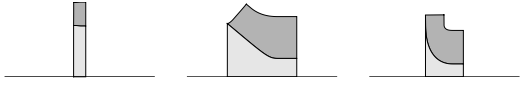
Total to Static			
η_{ts}	88.0	90.0	92.0
η_{tt}	95.0	92.5	94.5
$\Delta\eta_{eke}$	7.0	2.5	2.5

Table 7.4 turbine comparison for point A

Point B

Table 7.5 shows a comparison of radial, mixed and axial turbines in the vicinity of point *B* in Figure 7.2. Here, the mixed flow turbine has the highest total to static performance. Like the radial turbine in point *A*, it is a result of good total to total efficiency combined with the lowest design local flow coefficient. While the total to total performance of the axial and mixed flow turbines are nearly equal, the local flow coefficient of the axial turbine is higher, resulting in larger exit loss. Again, this can be improved with lower values of meridional velocity ratio.

The radial turbine has the lowest performance of the three. This is because of the lower total to total efficiency and a high design local flow coefficient, which is driving up exit loss. Radial architectures in this region of the design space have characteristically high casing curvature. This curvature is tied to the inlet flow area (Figure 2.7), which itself is related to the local flow coefficient via the duty flow. Increasing the local flow coefficient reduces the non-dimensional inlet flow area, which in turn lowers the casing curvature. Hence the radial designs in this region of the design space have been pushed to higher local flow coefficients to reduce the adverse affects of high casing curvature. As previously discussed this curvature can be reduced by other means and therefore, the performance of radial architectures can be improved in this region of the design space.



Design Paramters			
Ψ	1.0	1.0	0.92
Φ_D	0.93	0.93	0.92
Φ_L	0.42	0.35	0.44
RR	1.0	0.75	0.62
Mechanical properties			
Blade number	44	12	17
$\log_{10} P_V^*$	-0.622	-1.266	-1.134
$\log_{10} I_V^*$	-0.77	0.05	0.12
Total to Static			
η_{ts}	85.0	87.5	83.0
η_{tt}	94.0	94.5	93.5
$\Delta\eta_{eke}$	9	7	10.5

Table 7.5 turbine comparison for point B

7.3.1 Power Density, Inertia & Cost trends

Thus far, this thesis has focused primarily on the aerodynamic performance of turbines across the Balje chart. While this is an important factor to be considered when selecting machine architecture and size, it is by no means the only factor affecting these decisions. Machine weight, inertia and cost are important objectives to minimise in the design process. This next section illustrates the variations in these factors across the Balje diagram.

Power Density & Inertia

Figures 7.3(A) and 7.3(B) show variations of the non-dimensional second moment of volume and power density throughout the design space. Here, the second moment of volume represents the inertia of the rotor and disk(solid), since the inertia is directly proportional to the second moment of volume for a constant material density. It is more useful to plot this than the non-dimensional moment of inertia itself; the latter includes the ratio of the rotor metal to fluid density, which is not specified in this work and would limit the applicability to other materials and fluids. The same argument applies to the power density. Both the non dimensional power to weight ratio and moment of inertia can be recovered by simply multiplying by $\frac{\rho_{fluid}}{\rho_{metal}}$ to the correct corresponding power.

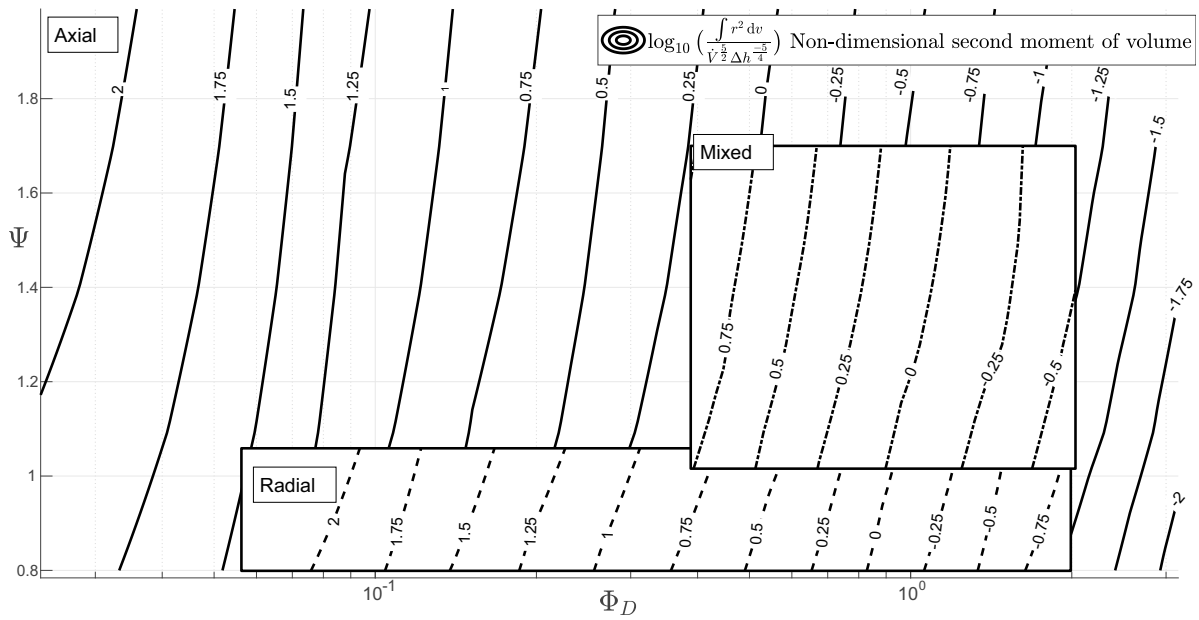
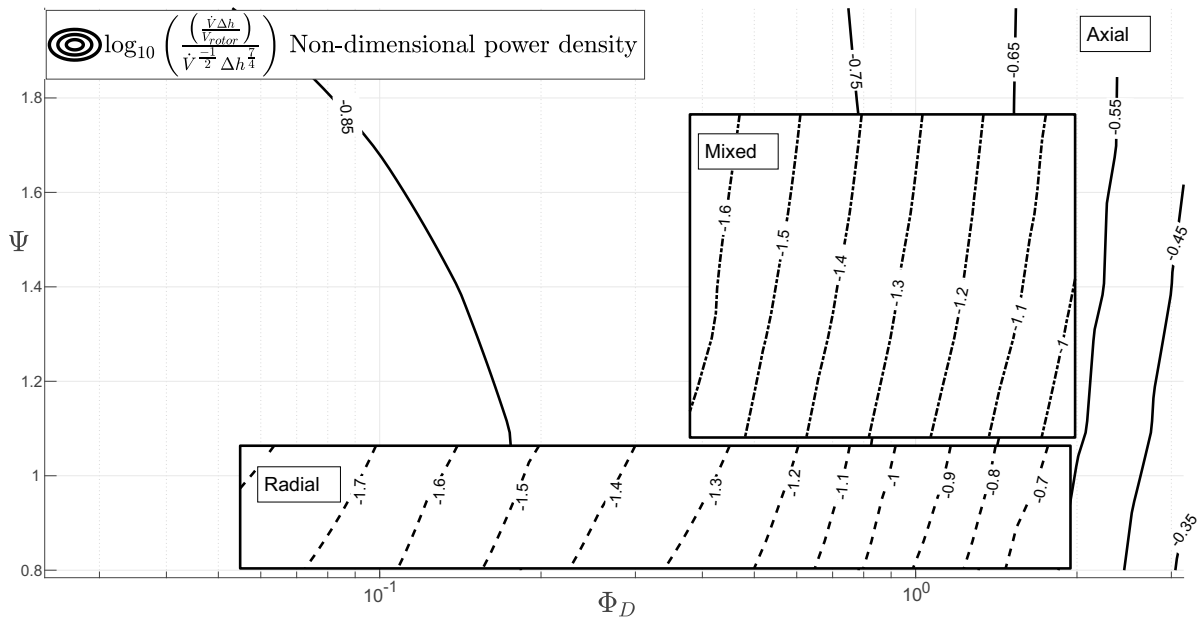
A**B**

Fig. 7.3 A: Contours of non-dimensional second moment of volume for Axial, Mixed and Radial flow turbines with varying loading and duty flow coefficients. B: Contours of non-dimensional Power density for Axial, Mixed and Radial flow turbines with varying loading and duty flow coefficients.

The results show that the power density rises and the inertia reduces with increasing duty flow coefficient (for all architectures). This should come as no surprise considering the rotor radius is reducing when moving to the right of the space. The difference between the architectures can

largely be explained by changes in the disk, using:

$$\text{disk volume} \propto C_x r^2 \quad \& \quad \text{disk inertia} \propto C_x r^4$$

The primary differentiating factor is the axial lengths. The longer axial length of the mixed and radial turbines is the reason for their higher inertia and lower power density compared to the axial architectures when comparing the same locations in the design space.

The mixed flow turbines presented here have a fixed radius ratio and cone angle (constrained). This sets a large portion of the axial length of the architecture. This results in mixed flow turbines with larger axial length than their radial turbine counterparts, resulting in significantly higher inertia and lower power density. The high volume and inertia of these architectures can be significantly improved by blending these architectures towards axial topologies.

Figure 7.3 implies that the mixed flow architectures have higher inertia than radial turbines, which is indeed the case for this particular set of designs when the comparison is made with the same mean radius. However, the comparison of radial and mixed flow turbines in literature (relating to turbochargers) is typically done for turbines with equivalent inlet casing radius and equal axial lengths. In this scenario, mixed flow turbines will have lower inertia than radial turbines, particularly if the radial turbine is unscalloped. This is one of the key advantages of mixed flow architectures especially when being used as turbochargers.

Cost trends

Predicting the exact cost of a turbine from initial development all the way through to production is highly complex and depends on a multitude of factors such as application, material, production method, use of blade cooling and design features. A full cost analysis considering all these factors is outside the scope of this thesis. However, it is still useful to discuss potential cost trends relating to geometry through out the design space. Pelz and Metzler [42] worked on the cost optimisation for small hydro power plants. The authors suggested minimising the power specific investment cost which scaled with machine volume. For the current work, it would therefore scale with the non dimensional power density. Based on this argument, Figure 7.3 would suggest that designs with higher duty flow coefficients are cheaper. This seems likely considering that these designs would require less material to manufacture and would have lower blade counts, resulting in reduced production costs.

Making direct cost comparisons of the different architectures would require further study and again is outside the scope of this thesis, however a number of observations have been made given the limited information. Axial turbines perform well at high duty flow coefficients and could have the lowest potential cost for a given application. As mentioned before, axial turbines could be structurally limited to lower blade speeds than that of the other architectures. If this is the case, smaller radial and mixed flow turbines can be used, to reduce cost. In addition to

this, radial and mixed flow turbines tend to have lower blade counts than axial turbines, further reducing the manufacturing cost.

Parallelization and staging (serialization)

Due to the vast nature of the design parameter space, the author of this thesis choose to focuses on the rotors of the different architectures. In some sense, this only represents half a stage. The degree to which staging or parallelization affects the shape of the design space has not been analysed in this thesis and therefore will not be discussed. However, It is still useful to discuss how these design choices can be used to move designs around a Balje chart to help maximise efficiency of the overall system.

Fluid flow systems share some commonalties with direct current electrical circuits. Staging/serialization in turbomachinery is somewhat analogous to placing electrical components in series, for example, placing cells, (compressors or pumps) or resistors, (turbines) in series which will split the voltage rise (or drop) between the components.

In turbo machinery this relates to splitting the net specific enthalpy(head in hydraulic systems) change per stage. If this is done with a constant blade speed and an equal share of the change, this will reduce the loading coefficient of the stages relative to the single stage as follows.

$$\Psi_{multistage} = \frac{\Psi_{single\ stage}}{n_{stages}}$$

Using duty parameters ψ and ϕ_D as opposed to D_s and N_s , has additional advantages of simplifying the movement around the charts from staging or parallelization. Staging, using loading coefficient as the vertical duty parameter, results in a purely vertical movement on the Balje charts as illustrated in figure 7.4. Since both the specific speed and diameter are functions of changes in enthalpy or head, staging shifts both these parameters at the same time.

Parallelization is far less common in turbomachinery being only found in some particularly niches areas. One example is found in single shaft turbopumps for rocket engines. Parallelization is sometimes used in these systems to reduce the specific speed (duty flow coefficient) of the individual liquid oxygen pumps. This eases the matching requirements of the three turbomachine types (fuel pump, oxidiser pump, turbine) which are being run on the same shaft.

Parallelization in turbo machinery is analogous to running circuits in parallel. Instead of current the mass flow is split up between the machines, thus lowering the duty flow coefficient.

$$\phi_{par} = \frac{\phi_{no\ par}}{n_{par}}$$

This results in a purely horizontal movement in a Balje chart using duty flow coefficient as illustrated in figure7.4.

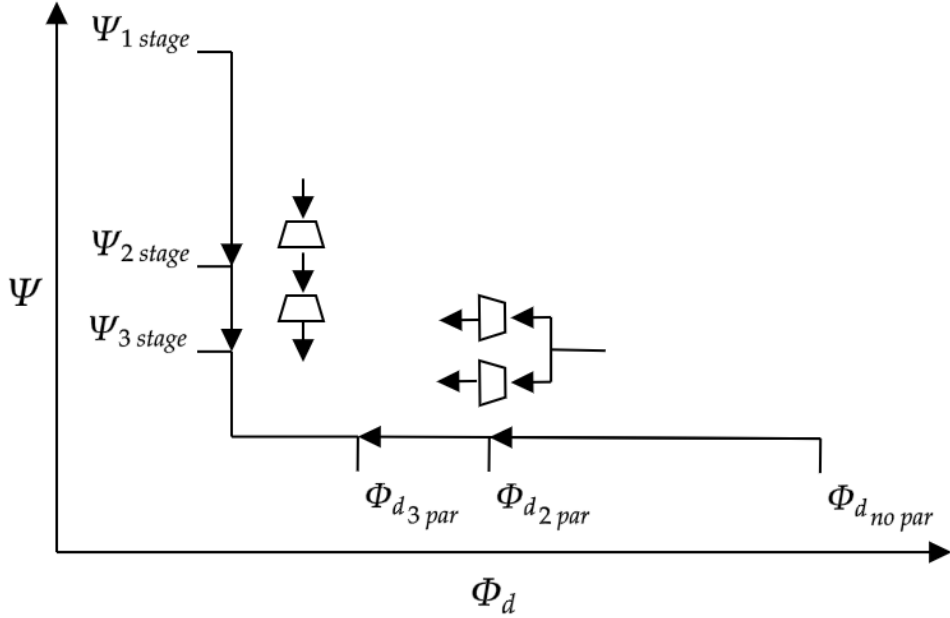


Fig. 7.4 Illustration of how parallelization and staging shifts duty flow parameters across a (Φ_D, Ψ) style Balje chart

7.4 Combined diffuser turbine performance

The choice of efficiency definitions, such as total to total or total to static used in design and optimisation, depends on whether or not the kinetic energy of the flow exiting that particular stage is being utilised. The total to total isentropic efficiency should be chosen when the exit kinetic energy is being used. Examples of this include when there is a subsequent turbine stage down stream of the first, or if the flow is being optimally used for propulsion. An example where the exit kinetic energy is not used would be a single stage turbine without a diffuser. In this scenario, the total to static isentropic efficiency is used. However, the choice is not immediately clear for scenarios where the exit kinetic energy is partially being used. For example, where a single turbine stage is coupled to an imperfect diffuser. A definition of efficiency between the total and static is required to shed light on the matter.

A combined efficiency would logically be defined as follows.

$$\eta_{com} = \frac{h_{01} - h_{02}}{h_{01} - h_{s3}} \quad (7.1)$$

Where subscript 3 reference the diffuser exit. This can then be written in terms of the total to total and total to static efficiencies.

$$\eta_{com} = \frac{\eta_{tt}}{1 + \left(\frac{\eta_{tt}}{\eta_{ts}} - 1 \right) (1 - C_r)} \quad (7.2)$$

where C_r is the diffuser recovery factor defined as.

$$C_r = \frac{V_3^2}{V_2^2} - 1$$

Equation 7.2 shows that the combined efficiency reduces to the total to total efficiency for perfect recovery and reduces to the total to static for zero recovery.

Figure 7.5 illustrates the variation in the overall efficiency of a set of axial turbines with varying local flow coefficients and diffuser recovery factors. The red line traces out the optimal flow coefficients over the range of recovery factors. It can be seen that the combined performance characteristics increase from the total to static to the total to total when increasing the recovery factor from zero to one. The optimal flow coefficient tracks with an initially steep gradient, and then turns to higher flow coefficients as recovery increases. The increasing diffuser performance reduces the exit loss. This increases the combined efficiency, and as a result the balance point between the entropy based loss mechanisms and the exit loss is established at higher flow coefficients. Accompanied with this shift in optimal local flow coefficient is a flattening of the curve. In other words, the sensitivity to changes in efficiency with changes in design flow coefficient decreases. Therefore, the performance gain by tracking the optima is marginal when compared to designing for optimal total to static performance while still using a diffuser.

Tracking the design optima also comes with an additional risk. If the diffuser underperformed, designs to the right of the optimal total to static would suffer greater performance loss. This would likely be the case when operating off design. It is the opinion of the author that it makes sense to design close to total to static efficiency optima and use a diffuser as this carries less risk. Alternatively, some of the diffusion being done by the diffuser can be achieved in the stage itself by reducing the meridional velocity ratio. This comes with the additional advantage of a more compact system, but can come with increased entropy based loss.

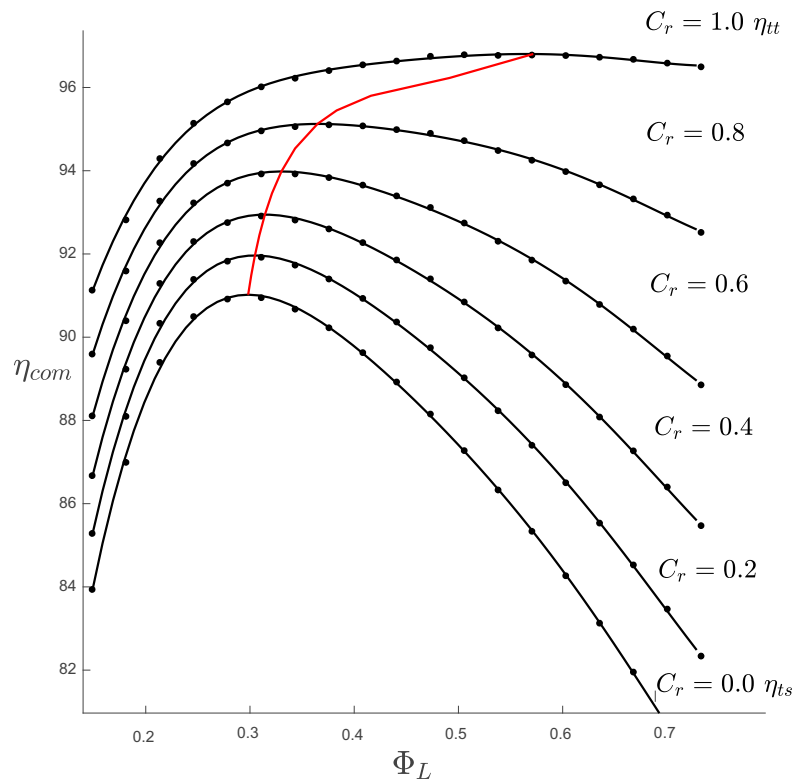


Fig. 7.5 Illustrating effects that varying diffuser recovery factor has on combined turbine-diffuser efficiency for various design flow coefficients. The red line marks the track of the optimal design flow coefficients

7.5 Conclusion

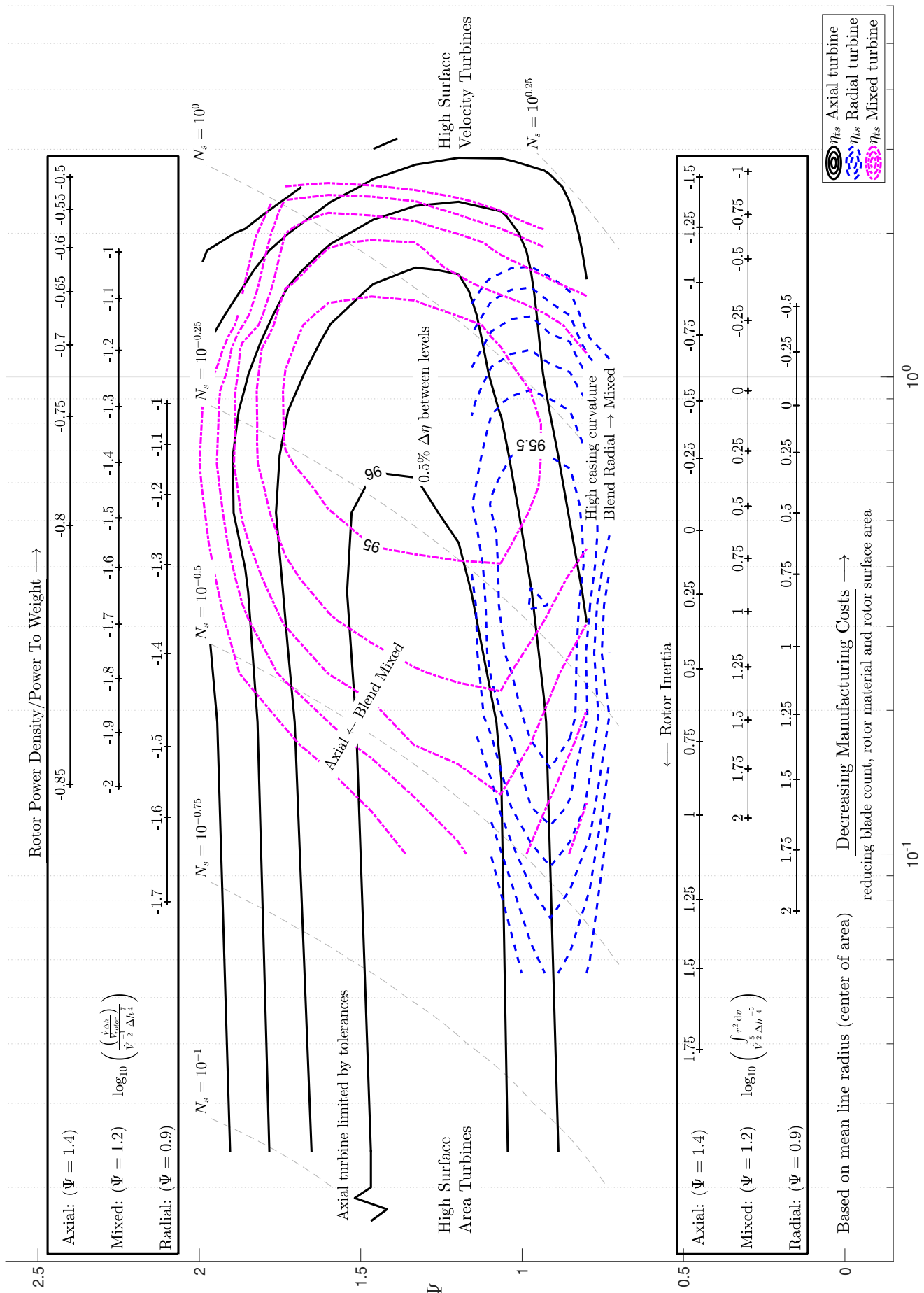


Fig. 7.6 Combined total to total Balje diagram

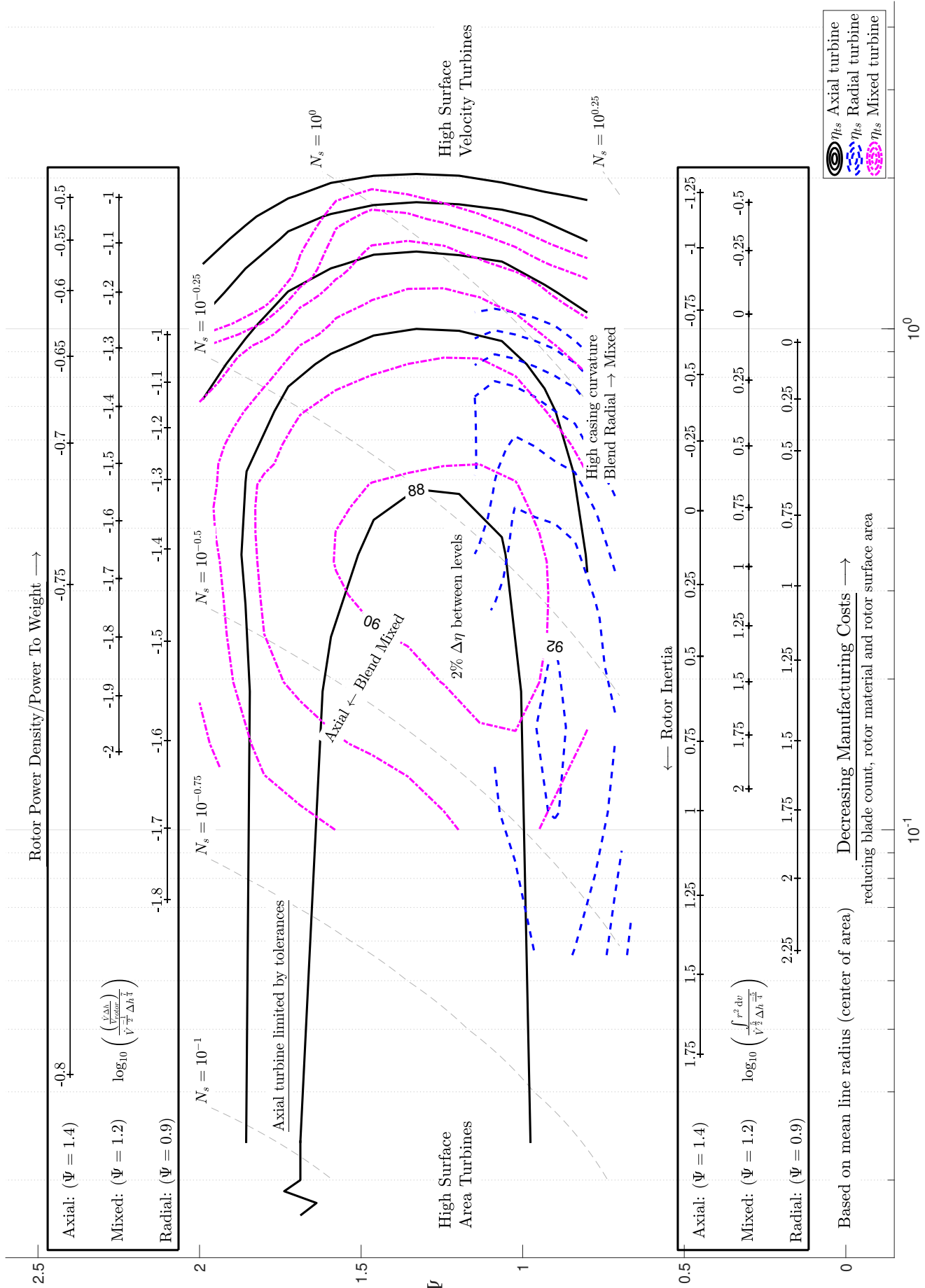


Fig. 7.7 Combined total to static Balje diagram

The primary objective of this thesis was to develop a unified preliminary design framework for turbines, use this framework to map design parameter spaces using modern tools and then to explain the shape of these design parameter spaces. The result of which will allow designers to make more informed decisions about architecture type, design parameters, speed and sizing.

Balje and Smith charts have been successfully constructed for axial, radial and mixed flow turbine rotor blades using RANS. It has been shown that the duty flow and loading coefficients (as suggested by Casey [12]) are a particularly useful duty level parameters, which can be used along side specific speed and diameter, for characterising the aerodynamic nature of turbines throughout the design space.

As with the past research on design parameter spaces of turbines, the results and conclusions of this thesis need to be taken in the context of the limitation of the tools on which they were built. Baljes and Rohlik's charts were largely produced using correlations which are limited by parameter range and architecture from which they were derived. To improve on this, a RANS solver was used to map the design spaces but this will inevitably introduce artefacts of its own.

Figure 7.6 and 7.7 depict rotor only Balje diagrams for total to total, total to static applications respectively and visually summarise many of the key results of this thesis, which are as follows:

- The duty flow coefficient essentially represents the mass/volume flow capacity of a turbomachine relative to its size and speed. The relative mass/volume flow, (ϕ_D) is set by meridional velocity, (ϕ_L) and inlet flow area, ($(\frac{A_{in}}{r_n^2})$) in non-dimension forms. Both these parameters vary through out the Balje chart to set the duty flow. The changes in non-dimensional mass/volume flow at higher duty flow coefficients is largely driven by increasing local flow coefficient and the changes at lower duty flow is driven by decreasing non-dimensional inlet area, (more so for axial turbines). There is an additional advantage to using a Φ_D, Φ framework, movement of duty parameters due to multi-staging or parallelisation are made simple and intuitive. Staging in this framework produces pure vertical movements (changes only in the loading coefficients) and parallelisation produces pure horizontal movements (changes only in the duty flow coefficients). In a N_s, D_s framework this is not the case, as specific speed and diameter are functions of both mass/volume flow and change in specific enthalpy.
- Chapters 4 through to 6 show that the rough trends of the design parameter spaces (mapped using RANS) can, by in large, be explained by surface dissipation, where the entropy generated at the surface is proportional to the cube of surface velocity (at the edge of the boundary layer, relative or otherwise). This can be written as:

$$\frac{\dot{S}T}{\rho} \propto \int^{A_{tot}} V^3 da = A_{tot} \bar{V}^3 \quad (7.3)$$

The total surface area A_{tot} and surface area average of the cubic surface velocity $\overline{V^3}$ can then be used to describe the nature of the lossy region of the design space. However, since surface dissipation does not include the mixing loss associated with leakage, secondary kinetic energy and flow separation, it significantly under predicts the total loss.

The CFD used was a reasonably simplistic RANS method, further more, transition was not modelled, since the dissipation coefficient can highly depend on the state of the boundary layer, it is likely that this trend will be significantly affected by variations in location and nature of transition, particularly at lower Reynolds numbers.

- A universal trend across all architectures was found. Turbines with high duty flow coefficient have characteristically high surface velocities and turbines with lower values of duty flow coefficient are characterised by high surface area. The high surface velocity of design at high duty flow is a consequence of the increasing local flow coefficient which is required to pass the extra mass/volume through the turbine. Examples of axial, radial and mixed flow turbines were compared throughout the design space. These examples showed significantly large differences in the balance between area and surface velocity. Axial turbines tended to have high surface velocities and low surface area, whereas radial turbines had significantly lower surface velocities and higher surface area. The lower surface velocities of the radial turbines was attributed to a combination of longer blade passages, low local flow coefficients and centrifugal loading. It was shown that shifting loading from the relative acceleration term to the centrifugal term decreases relative passage velocities. Not only is reduced velocity useful for reducing surface dissipation, it can be used to delay chocking at higher Mach numbers.
- Axial turbines have the broadest range across the design space and both constrained mixed flow and radial turbines sit inside the axial range. Axial turbines did not show a performance boundary at lower duty flow coefficients (tested to $\phi_D = 10^{-3}$). In the presented work, the geometric features that come about due to manufacturing limitations, such as tip clearance and trailing edge thickness, were scaled with the mean radius and therefore with the passage. Manufacturing tolerances tend to be absolute and therefore loss mechanisms relating to these, such as trailing edge and tip leakage losses, will increase. Blade thicknesses will also likely need to be increased, pushing up blade surface area and with that the profile loss. This suggests that the left hand performance boundary for axial architectures is set partly by these tolerance limits.

For fixed duty (mass flow and power), shifting designs to lower duty flow coefficients will reduce the blade's Reynolds numbers relative to other positions in the design space, as the surface velocity and blade cords are reducing, (axial architectures). The work presented in this thesis was done with fully turbulent boundary layers at high Reynolds numbers and hence will show a low sensitivity to Reynolds numbers changes across the design

space. However for low Reynolds number applications (Low rotational Reynolds number), Low Reynolds effects will first begin to emerge at lower duty flow, which will ultimately affect the shape of the space in this region. Conversely, turbines in this study had low Mach numbers which resulted in low sensitively to the small Mach number variation across the design space. As previously shown turbines at high duty coefficients have characteristically higher velocities and therefore Mach number effects will first emerge here.

The total and static efficiency of axial turbines drop off at high duty flow coefficients. All mechanisms contribute to the drop in performance. The characteristically high velocities of these designs result in high profile and end wall surface dissipation loss. The leakage loss also increases due to a combination of increased over tip driving pressure and higher velocities with which the leakage flow is mixing. The high velocities of these designs are a consequence of the high local flow coefficients, which is required to pass the relatively high mass flow through the turbine. The exit loss scales with the square of the local flow coefficient and hence the exit loss is also high in this region. The exit loss can be decreased by reducing meridional velocity ratio which is particularly useful for axial architectures and can help bring their total to static performance inline with that of radial and mixed flow architectures. Axial architectures presented in this work are shown to have significantly lower rotor inertia and higher power density than the other architectures when being compared at the same duty parameters, (ϕ_D, ψ) . Note, that for all machines both rotor inertia and power density improve with increasing duty flow coefficient.

- Radial turbines are restricted to low loading coefficients as a result of radial blade fibres. This constrains the inlet metal angle to zero and hence radial turbines at higher loading suffer increased loss due to incidence. It must be noted that this was not reflected by the surface dissipation contours as this is likely driven by increasing secondary flow.

The performance of these architectures drops off at both high and low duty flow coefficients. The drop in efficiency at low duty flow coefficient is caused primarily by a high end wall surface loss, most of which comes from the casing due to relatively high absolute velocities, Therefore shrouding could be beneficial for this region of the design space. Rohlik [46] showed a similar trend but seemingly overestimates the loss. This likely stems from the aspect ratio term in the rotor loss model that was used by Rohlik. The profile loss was shown to be low in this region and is due do to the low surface velocity which in part, is due to the large fraction of centrifugal loading. Rohlik's model also suggests that a significant proportion of the loss at low duty flow coefficients is due to a rise in leakage loss. Instead, it was found that the leakage loss, (according to the CFD) was relatively weak at low duty flow. This behaviour was attributed to the increasing length of the radial

section, in which scraping of the relative casing boundary layer has a strong effect, as well as the reduced velocities with which the leakage flow is mixing.

As with axial turbines, the drop in performance of radial turbines at high duty flow coefficients, was again shown to be driven by all loss mechanisms. Rohlik's model under predicts the drop off when being compared to the CFD. For example, the leakage loss model used by Rohlik predicted decreasing loss, whereas the numerical solution suggests that it increases. As with axial turbines the high leakage, profile and end wall dissipation loss is largely driven by the high surface velocities which is characteristic of designs in this region of the design space.

The higher surface velocities are in part due to increasing local flow coefficient and radius ratio, the latter because there is less available space for a reduction in radius. As a consequence, radial turbines at high duty flow coefficient have a lower centrifugal component of loading. The change in loading is therefore transferred back to the relative acceleration loading and hence the passage velocities increase.

The endwall loss was shown to rise dramatically at particularly high values of duty flow coefficient and was a result of flow separation which occurred at the casing. The high through flow area of the designs in this region leaves little space in which the casing can turn the flow in the axial direction. At some point, the radius of curvature at the casing is too low and the flow separates, dramatically increasing loss. It must be noted that this sharp increase in loss was not captured by surface dissipation. This particular performance boundary can be extended to higher duty flow by relaxing the design constraints used in this thesis and spread some of the casing curvature into the volute, however, this will require more detailed design and somewhat blurs the lines between mixed and radial turbines.

- Early designs of mixed flow architectures showed considerable limitations in maximum loading throughout the design. This was a result of a vortex like structure caused by a separation close to the rotor inlet at the hub suction surface corner.

A low pressure region was found in this corner section of the turbine and the adverse pressure gradient downstream of this is a significant factor in driving the separation. The low pressure region is a consequence of the high rake angle, which leans the suction surface towards the hub. Additionally, the high Coriolis force seems to amplify the problem significantly. A simple fillet-like end wall treatment was shown to help disrupt the formation of the separation and open up the design space to significantly higher loading coefficients, increasing the operable range of mixed flow architectures. Unlike previous method for suppressing this flow feature, the fillet-like endwall treatment did not require detailed and targeted design work and functioned robustly through out the design space.

- A constrained mixed flow Balje chart (with radial blade fibres) was mapped out with fixed radius ratios and cone angles. High-performing mixed flow designs sit at higher duty flow coefficients to radial architectures and extend to higher loading coefficients as well, but still sit inside the range of axial turbines. The faster drop in performance with loading when compared to axial architectures was attributed to a sharper increase in surface area due to increasing rake angles. Like radial architectures, the performance drop off at low duty flow coefficients is due to high end wall dissipation, which is a result of large amounts of end wall surface area. The effects of varying cone angle and radius ratio were tested. It was shown that mixed flow architectures sitting at low duty flow and high loading should be blended towards axial designs. This will improve performance by reducing surface area.

As with both axial and radial architectures the performance drops off at high duty flow coefficients which is driven by all loss mechanisms. That being said, the range is extended to higher duty flow coefficients than radial architectures. This was attributed to the larger radius of curvature as a result of the lower cone angles.

- A unified set of low order models for profile, end wall and tip leakage were compared to the decoupled loss mechanisms from the CFD. The profile loss model used was a modification of an approach used by Denton [26]. Instead of the square velocity distribution used by Denton, thin aerofoil theory was used to form a velocity distribution which was more characteristic of the architectural type. This was used to calculate the surface dissipation assuming a fixed dissipation coefficient. The model proved to be robust with good agreement with the CFD for all architectures, but will likely lose accuracy under more complex conditions (low Reynolds numbers, transitional boundary layers and flow separations due to high diffusion factors). The end wall loss was calculated by adding a loss from secondary flow and end wall surface dissipation. The end wall surface dissipation was calculated by assuming a linear variation in velocity from suction to pressure surface. The secondary flow loss model used was a modification of an approach used by Coull [18] which drew from work done by Came and Marsh [8] and Hawthorne [33]. In this model, the secondary flow loss is calculated from a vorticity amplification factor which is function of flow angles, difference in transit times between suction and pressure surface and inlet to exit velocity ratio. The approach was modified to include the effects of meridional curvature and aspect ratio. The meridional curvature correction is a modification to the vorticity amplification factor, which was actually derived for a curved rectangular duct and proved to correlate well with the change in performance with curvature as predicted by the CFD. Over all the model had mixed results. It functioned well for the axial Smith chart and less so for the axial Balje chart, where it preformed poorly at low loading and high duty flow coefficients. It functioned reasonably well for the mixed Smith and radial Balje chart but broke down completely for the mixed Balje chart.

The linear relationship with the aspect ratio term ($\frac{p_m \cos \beta_2}{h}$) seemed to be the cause of the issues. Unfortunately, no absolute conclusion can be drawn for the leakage loss model (also Denton [26]) as a likely interaction with end wall flow interfered when attempting to decouple the mechanisms. Despite this, the model does capture some of the trends. It functioned well for the radial Balje chart and it does predict an increase in loss at higher duty and local flow coefficients at lower loading for all charts. While these models require further development, they can serve as a starting point to develop a fully unified low order model for meanline design, based on physical understanding.

Design charts leveraging similitude are powerful tools during the early stages of design, allowing engineers to make informed decisions on machine sizing and architecture type. A unified design methodology/framework has been presented in this thesis with accompanying charts. However, due to the vast and high dimensional nature of the turbine design parameter space, there were necessary limitations to these charts. In addition to not optimising every design parameter, (including blade count), the detailed geometry itself is not optimised. On top of this, relatively simplistic CFD was used for modelling and estimating performance. That being said, many of the conclusion drawn from the RANS calculations related to changes in surface area and velocity, which should be captured well by RANS. However, the behaviour of more complex aspects of the loss mechanism such as the onset of separation, tip leakage in general, boundary layers states and so one, require more sophisticated modelling to correctly resolve.

With the recent advances in machine learning and computational resources available to engineers ever increasing, the ability to continuously produce maps with fewer design limitations and with better modelling is possible. The author of this thesis does not want engineers to heavily rely on the charts produced here, but should see them more as motivation and a framework to form more detailed versions of their own. This area of the field of turbines has seen little research since Balje's [4] work in 1981, (with the exception of Casey et al.,[48], [45] on compressors). Instead, these critical design charts should be continuously updated to include the state of the art designs and modelling techniques.

Alternatively, a more modern approach could be to use the data sets that would otherwise be used to create design charts, to train machine learning algorithms (a simple fully-connect deep neural net would likely suffice) to approximate a continuous high dimensional design parameter space. This then could be used to speed up the preliminary design process by allowing engineers to quickly select optimal meanline parameters given a range of design constraints. This concludes the thesis, the author would like to thank the reader for their time and interest in this work.

References

- [1] Abidat, M. (1991). *Design and Testing of Highly Loaded Mix Flow Turbine*. Phd, University of London.
- [2] Baines, N. C. and Concepts ETI, G. B. (1998). *A Meanline Prediction Method for Radial Turbine Efficiency*.
- [3] Balje, E. (1962). Study on Design Criteria and Matching of Turbomachines: Part A—Similarity Relations and Design Criteria of Turbines. *ASME*, 83:20.
- [4] Balje, O. E. (1981). Turbomachines : a guide to design, selection, and theory.
- [5] Brandvik, T. and Pullan, G. (2009). An accelerated 3D Navier-Stokes solver for flows in turbomachines. page 11.
- [6] Brear, M. J., Hodson, H. P., Gonzalez, P., and Harvey, N. W. (2001). Pressure Surface Separations in Low Pressure Turbines: Part 2 of 2 — Interactions With the Secondary Flow. In *Volume 1: Aircraft Engine; Marine; Turbomachinery; Microturbines and Small Turbomachinery*. American Society of Mechanical Engineers.
- [7] Brear, M. J., Hodson, H. P., and Harvey, N. W. (2002). Pressure Surface Separations in Low-Pressure Turbines—Part 1: Midspan Behavior. *Journal of Turbomachinery*, 124(3):393–401.
- [8] Came, P. M. and Marsh, H. (1974). Secondary Flow in Cascades: Two Simple Derivations for the Components of Vorticity. *Journal of Mechanical Engineering Science*, 16(6):391–401.
- [9] Cao, T., Xu, L., Yang, M., and Martinez-Botas, R. F. (2014). Radial Turbine Rotor Response to Pulsating Inlet Flows. *Journal of Turbomachinery*, 136(7):71003.
- [10] Carr, L. W. (1978). A Computer Program for Calculating Laminar and Turbulent Boundary Layers for Two-Dimensional Time-Dependent Flows. *Nasa technical reports*, page 62.
- [11] Casey, M. (2008). Radial Turbomachinery Design. In *Cambridge Turbomachinery Course*, volume 2, page 3. Cambridge university.
- [12] Casey, M. and Robinson, C. (2008). A New Streamline Curvature Throughflow Method for Radial Turbomachinery. page 12.
- [13] Chen, H. and Baines, N. C. (1994). The aerodynamic loading of radial and mixed-flow turbines. *International Journal of Mechanical Sciences*, 36(1):63–79.
- [14] Cordier, O. (1953). Ähnlichkeitsbedingungen für Strömungsmaschinen. *BWK Bd*, 6.
- [15] Coull, J. and Clark, C. (2019). Secondary Flow Generation In Axial Turbines, Prepublication.

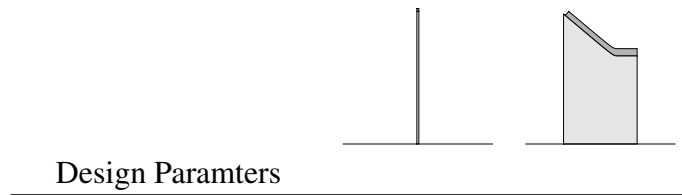
- [16] Coull, J., Clark, C., and Vazquez, R. (2019). The sensitivity of turbine cascade endwall loss to inlet boundary layer thickness. *Journal of the Global Power and Propulsion Society*, 3:OEYMDE.
- [17] Coull, J. and Hodson, H. P. (2012a). (PDF)Predicting the Profile Loss of High-Lift Low Pressure Turbines. *Journal of Turbomachinery*, 134:14.
- [18] Coull, J. D. (2017). Endwall Loss in Turbine Cascades. *Journal of Turbomachinery*, 139(8):81004.
- [19] Coull, J. D. and Atkins, N. R. (2014). The Influence of Boundary Conditions on Tip Leakage Flow. American Society of Mechanical Engineers Digital Collection.
- [20] Coull, J. D. and Hodson, H. P. (2011). Blade Loading and its Application in the Mean-Line Design of Low Pressure Turbines. page 12.
- [21] Coull, J. D. and Hodson, H. P. (2012b). Predicting the Profile Loss of High-Lift Low Pressure Turbines. *Journal of Turbomachinery*, 134(2).
- [22] Dambach, R. (2000). Tip Leakage Flow: A Comparison between Small Axial and Radial Turbines. *Professional Engineering Publishing*, page 10.
- [23] Dambach, R. and Hodson, H. P. (2001). Tip Leakage Flow in a Radial Inflow Turbine with Varying Gap Height. *Journal of Propulsion and Power*, 17(3):644–650.
- [24] Dawes, W. N. (1990). A Comparison of Zero and One Equation Turbulence Modelling for Turbomachinery Calculations. In *Volume 1: Turbomachinery*, page V001T01A093, Brussels, Belgium. American Society of Mechanical Engineers.
- [25] Denton, J. and Pullan, G. (2012). A Numerical Investigation Into the Sources of Endwall Loss in Axial Flow Turbines. In *Volume 8: Turbomachinery, Parts A, B, and C*, pages 1417–1430, Copenhagen, Denmark. American Society of Mechanical Engineers.
- [26] Denton, J. D. (1993). Loss Mechanisms in Turbomachines. In *Volume 2: Combustion and Fuels; Oil and Gas Applications; Cycle Innovations; Heat Transfer; Electric Power; Industrial and Cogeneration; Ceramics; Structures and Dynamics; Controls, Diagnostics and Instrumentation; I*, page V002T14A001, Cincinnati, Ohio, USA. ASME.
- [27] Denton, J. D. (2010). Some Limitations of Turbomachinery CFD. In *Volume 7: Turbomachinery, Parts A, B, and C*, pages 735–745, Glasgow, UK. ASME.
- [28] Denton, J. D. and Dawes, W. N. (1998). Computational fluid dynamics for turbomachinery design. *Proceedings of the Institution of Mechanical Engineers, Part C: Journal of Mechanical Engineering Science*, 213(2):107–124.
- [29] Denton, J. D. and Miller, R. J. (2008). Loss Mechanisms. In *Cambridge Turbomachinery Course*, number 1, page 3. Cambridge university.
- [30] Epple, P., Durst, F., and Delgado, A. (2011). A theoretical derivation of the Cordier diagram for turbomachines. *Proceedings of the Institution of Mechanical Engineers, Part C: Journal of Mechanical Engineering Science*, 225(2):354–368.
- [31] Evans, K. R. and Longley, J. P. (2017). Clocking in Low-Pressure Turbines. *Journal of Turbomachinery*, 139(101003).

- [32] Glassman, A. J. (1976). Computer program for design analysis of radial-inflow turbines. *Nasa technical*, page 66.
- [33] Hawthorne, W. R. (1955). Rotational flow through cascades part1. The components of vorticity. *The Quarterly Journal of Mechanics and Applied Mathematics*, 8(3):266–279.
- [34] Heyes, F. J. G., Hodson, H. P., and Dailey, G. M. (1992). The Effect of Blade Tip Geometry on the Tip Leakage Flow in Axial Turbine Cascades. *Journal of Turbomachinery*, 114(3):643–651.
- [35] Huntsman, I. (1993). *An investigation of radial inflow turbine aerodynamics*. Ph.D., University of Cambridge.
- [36] Johnson, M. W. (1978). Secondary Flow in Rotating Bends. *Journal of Engineering for Power*, 100(4):553–560.
- [37] Kammeyer, J., Natkaniec, C., and Seume, J. R. (2010). Tip Leakage in Small Radial Turbines: Optimum Tip-Gap and Efficiency Loss Correlations. pages 391–401. American Society of Mechanical Engineers Digital Collection.
- [38] Kulfan, B. M. (2008). Universal Parametric Geometry Representation Method. *Journal of Aircraft*, 45(1):142–158.
- [39] Moore, J. and Tilton, J. S. (1988). Tip Leakage Flow in a Linear Turbine Cascade. *Journal of Turbomachinery*, 110(1):18–26.
- [40] Ong, J., Miller, R. J., and Uchida, S. (2012). The Effect of Coolant Injection on the Endwall Flow of a High Pressure Turbine. *Journal of Turbomachinery*, 134(5).
- [41] Padzillah, M. H. (2014). *Experimental and Numerical Investigation of an Automotive Mixed Flow Turbocharger Turbine under Pulsating Flow Conditions*. PhD thesis.
- [42] Pelz, P. F. and Metzler, M. (2013). Optimization of power-specific investment cost for small hydropower.
- [43] Reid, K., Denton, J., Pullan, G., Curtis, E., and Longley, J. (2008). The Effect of Stator-Rotor Hub Sealing Flow on the Mainstream Aerodynamics of a Turbine. pages 789–798. American Society of Mechanical Engineers Digital Collection.
- [44] Roberts, Q. D. and Denton, J. D. (2015). Loss Production in the Wake of a Simulated Subsonic Turbine Blade. American Society of Mechanical Engineers Digital Collection.
- [45] Robinson, C., Casey, M., and Woods, I. (2011). An integrated approach to the aero-mechanical optimisation of turbo compressors. page 43.
- [46] Rohlik, H. E. (1968). Analytical determination of radial inflow turbine design geometry for maximum efficiency. Technical report.
- [47] Rosic, B., Denton, J. D., and Curtis, E. M. (2008). The Influence of Shroud and Cavity Geometry on Turbine Performance: An Experimental and Computational Study—Part I: Shroud Geometry. *Journal of Turbomachinery*, 130(4).
- [48] Rusch, D. and Casey, M. (2013). The Design Space Boundaries for High Flow Capacity Centrifugal Compressors. *Journal of Turbomachinery*, 135(3):31035.

- [49] Schlichting, H. and Gersten, K. (2016). *Boundary-Layer Theory*. Springer, New York, NY, 9th ed. 20 edition.
- [50] Serafino, A. (2015). Fluid-Dynamics Of The Orc Radial Outflow Turbine. page 10.
- [51] Smith, S. F. (1965). A Simple Correlation of Turbine Efficiency. *The Aeronautical Journal*, 69(655):467–470.
- [52] Smyth, J. (2021). *Selecting a compressor meridional topology: axial, mixed, radial*. PhD thesis, University of Cambridge.
- [53] Tyacke, J. C. and Tucker, P. G. (2015). Future Use of Large Eddy Simulation in Aero-engines. *Journal of Turbomachinery*, 137(8).
- [54] Whitfield, A. S. L. i. E. (1990). *Design of Radial Turbomachines*. Longman, Harlow, Essex, 01 edition edition.
- [55] Xu, L. and Cao, T. (2018). Mixed flow turbine separation.
- [56] Yang, B. and Martinez-Botas, R. (2019). TURBODYNA: Centrifugal/Centripetal Turbomachinery Dynamic Simulator and its Application on a Mixed Flow Turbine. page 13.
- [57] Yaras, M. I. and Sjolander, S. A. (1992). Effects of Simulated Rotation on Tip Leakage in a Planar Cascade of Turbine Blades: Part I—Tip Gap Flow. *Journal of Turbomachinery*, 114(3):652–659.
- [58] Zangeneh-Kazemi, M., Dawes, W. N., and Hawthorne, W. R. (1988). Three Dimensional Flow in Radial-Inflow Turbines. In *Volume 1: Turbomachinery*, page V001T01A046, Amsterdam, The Netherlands. American Society of Mechanical Engineers.

Appendix A

Additional Table Data



Design Parameters

Ψ	1.7	1.7
Ψ_{cen}	0.0	0.22
Ψ_{rac}	0.25	0.03
Ψ_{ake}	1.45	1.45
Φ_D	0.085	0.10
Φ_L	0.60	0.39
R_r	1.000	0.750
<hr/>		
Mechanical properties		
Blade number	715	31
$\log_{10} P_V^*$	-0.85	-2.21
$\log_{10} I_V^*$	1.30	2.39
<hr/>		
Total to Total		
η_{tt}	95.5	91.0
A_{tot}^*	11.8	78.8
$\overline{V^3}_{tot}^*$	0.88	0.51
<hr/>		
Profile loss		
$\Delta\eta_{pro}$	2.5	4.2
A_{pro}^*	9.8	36.6
$\overline{V^3}_{pro}^*$	0.92	0.70
<hr/>		
End wall loss		
$\Delta\eta_{end}$	2.2	6.0
A_{end}^*	1.93	42.20
$\overline{V^3}_{end}^*$	0.75	0.35
<hr/>		
Tip leakage loss		
$\delta\eta_{tip}$	0.3	1.3
A_{tip}^*	0.048	0.138
\dot{M}_{tip}^*	0.010	0.005
$\overline{V^2}_{cas}^*$	0.73	0.84

Table A.1 turbine comparison for point D



Design Parameters		
Ψ	1.7	1.7
Ψ_{cen}	0.0	0.22
Ψ_{rac}	0.25	0.03
Ψ_{ake}	1.45	1.45
Φ_D	0.93	0.94
Φ_L	0.72	0.48
R_r	1.0	0.75
Mechanical properties		
Blade number	76	21
$\log_{10} P_V^*$	-0.731	-1.315
$\log_{10} I_V^*$	-0.469	0.118
Total to Total		
η_{tt}	95.5	95.0
A_{tot}^*	9.46	23.57
$\frac{V^3}{V^3}_{tot}$	1.17	1.01
Profile loss		
$\Delta\eta_{pro}$	2.7	3.2
A_{pro}^*	7.80	18.86
$\frac{V^3}{V^3}_{pro}$	1.22	1.13
End wall loss		
$\Delta\eta_{end}$	2.0	3.2
A_{end}^*	1.65	4.71
$\frac{V^3}{V^3}_{end}$	0.91	0.53
Tip leakage loss		
$\Delta\eta_{tip}$	0.5	0.5
A_{tip}^*	0.038	0.07
\dot{M}_{tip}^*	0.012	0.022
$\frac{V^2}{V^2}_{cas}$	1.04	1.34

Table A.2 turbine comparison for point E



Design Paramters

Ψ	1.7	1.7
Ψ_{cen}	0.0	0.22
Ψ_{rac}	0.25	0.03
Ψ_{ake}	1.45	1.45
Φ_D	3.2	2.8
Φ_L	1.2	0.95
RR	1.0	0.75

Mechanical properties

<i>Bladenumber</i>	32	12
$\log_{10} P_V^*$	-0.45	-0.85
$\log_{10} I_V^*$	-1.62	-0.87

Total to Total

η_{tt}	93.0	92.0
A_{tot}^*	5.12	9.73
$\overline{V^3}_{tot}^*$	3.05	1.85

Profile loss

$\Delta\eta_{pro}$	4.0	3.5
A_{pro}^*	3.98	7.39
$\overline{V^3}_{pro}^*$	3.29	2.02

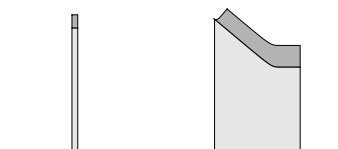
End wall loss

$\Delta\eta_{end}$	3.7	4.0
A_{end}^*	1.13	2.33
$\overline{V^3}_{end}^*$	2.19	1.31

Tip leakage loss

η_{tip}	1.0	2.0
A_{tip}^*	0.020	0.028
\dot{M}_{tip}^*	0.011	0.016
$\overline{V^2}_{cas}^*$	2.405	2.458

Table A.3 turbine comparison for point F



Design Parameters		
Ψ	1.7	1.7
Φ_D	0.274	0.261
Φ_L	0.46	0.36
RR	1.0	0.75

Mechanical properties		
Blade number	234	28
$\log_{10} P_V^*$	-0.77	-1.8
$\log_{10} I_V^*$	0.4	1.4

Total to Static		
$\Delta\eta_{ts}$	88.5	89.5
η_{tt}	95.80	93.72
A_{tot}^*	14.83	49.95
$\frac{A_{tot}^*}{V_{tot}^{3*}}$	0.62	0.32

Table A.4 turbine comparison for point C



Design Parameters		
Ψ	1.6	1.6
Φ_D	1.7	1.7
Φ_L	0.66	0.57
RR	1.000	0.750

Mechanical properties		
<i>Bladenumber</i>	55	16
$\log_{10} P_V^*$	-0.54	-1.1
$\log_{10} I_V^*$	-1.08	-0.25

Total to Static		
η_{ts}	82.0	83.0
η_{tt}	95.0	94.5
A_{tot}^*	10.18	21.25
$V^3_{tot}^*$	0.99	0.60

Table A.5 turbine comparison for point D

Appendix B

Additional plots

B.1 numerical error axial

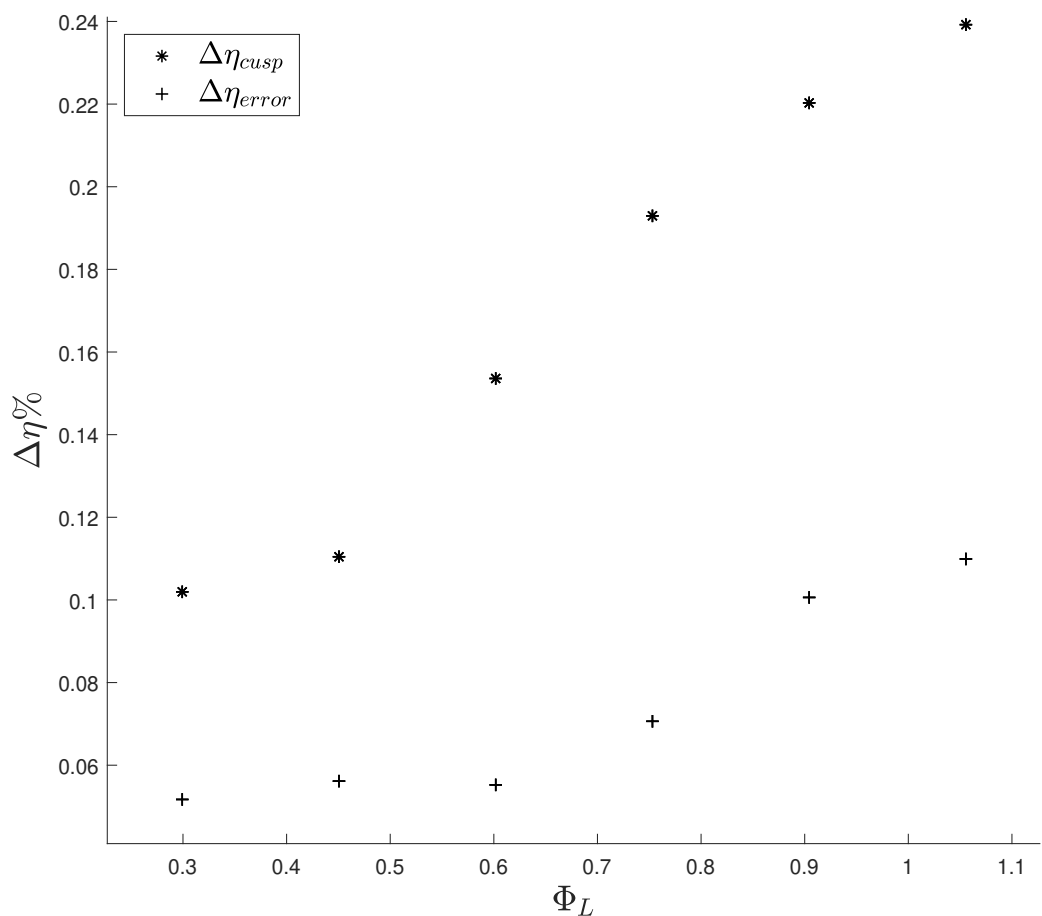


Fig. B.1 lost efficiency due to numerical error and cusp

B.2 Axial Smith

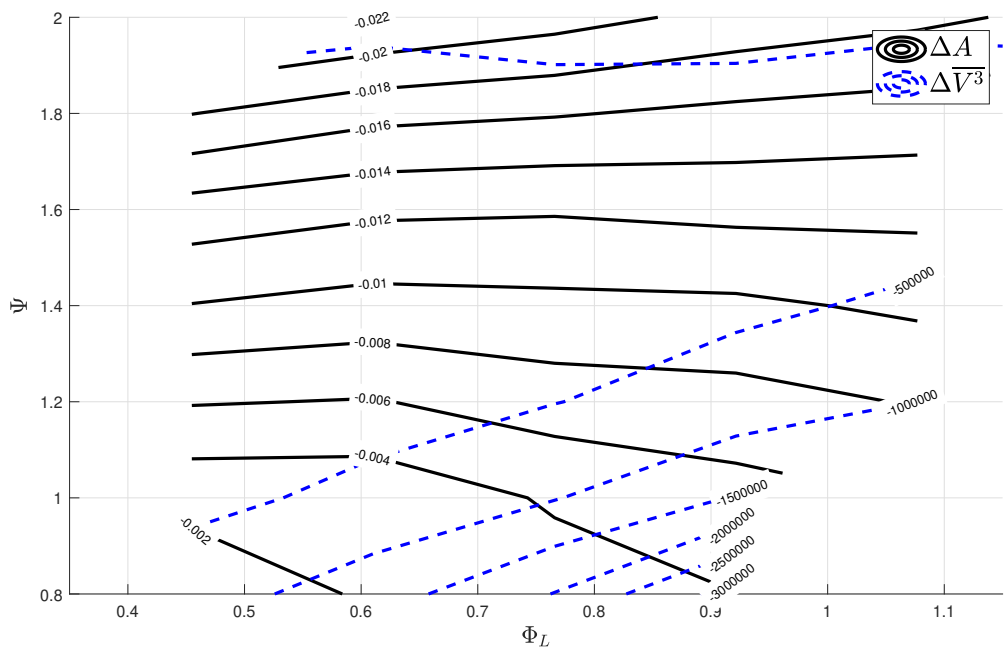


Fig. B.2 Change in area and average surface velocity cube with - 10 degrees exit swirl

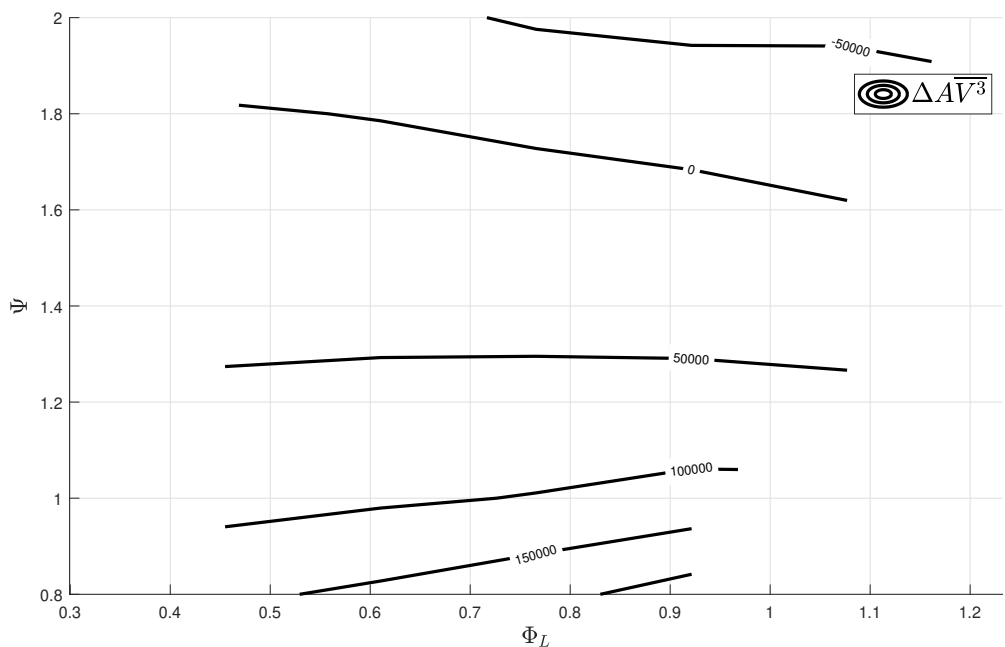


Fig. B.3 Change in surface dissipation with - 10 degrees exit swirl

B.3 Axial Balje

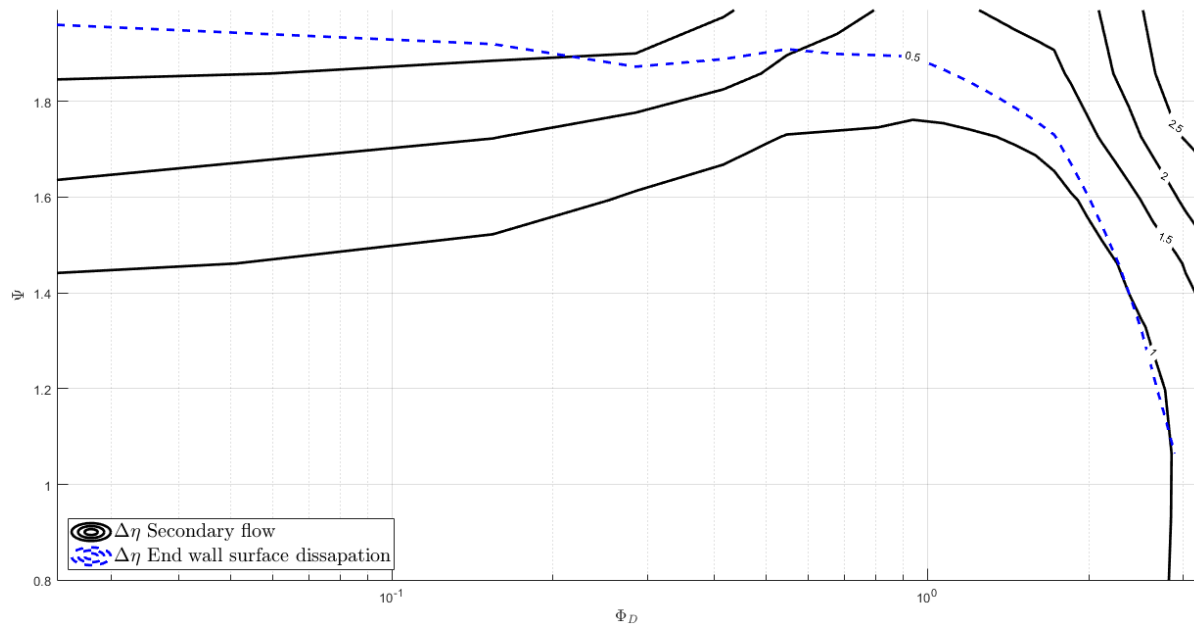


Fig. B.4 End wall dissipation and secondary flow components of loss

B.4 Radial total to static

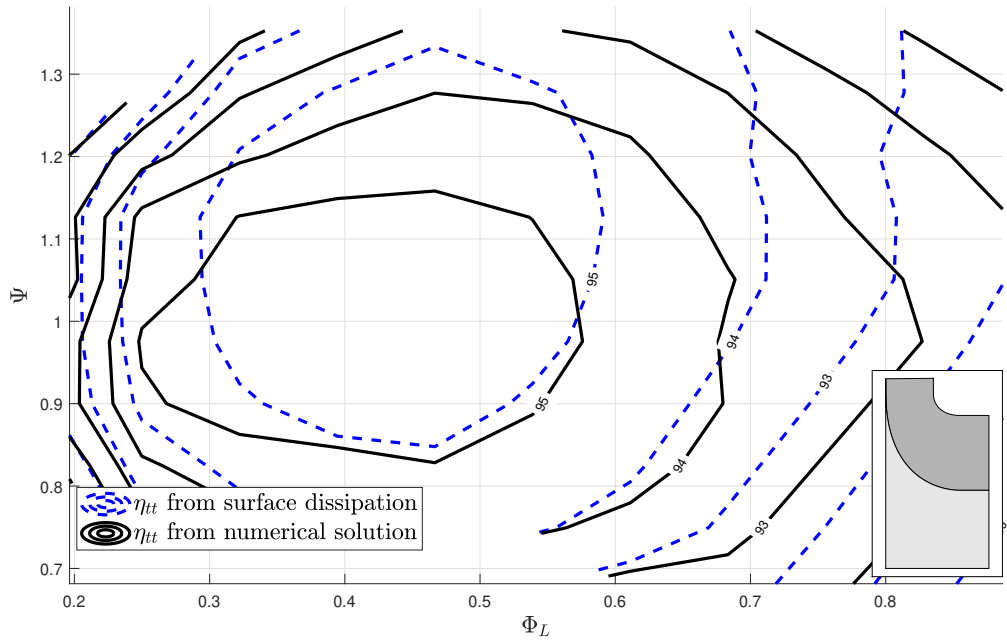


Fig. B.5 Radial Total to static with $C_d = 0.006$

B.5 Radial total to static

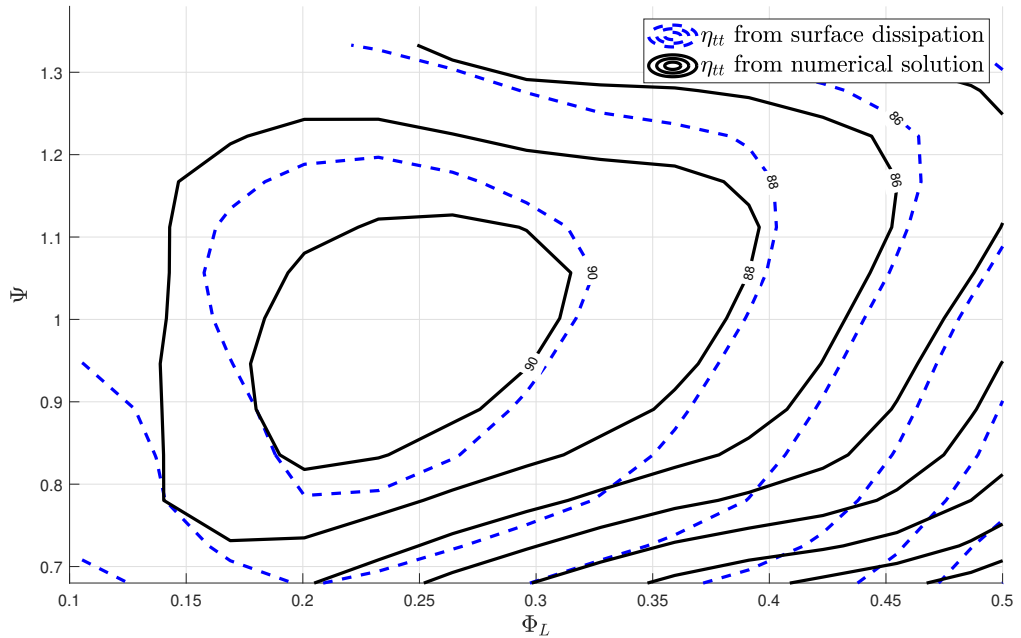
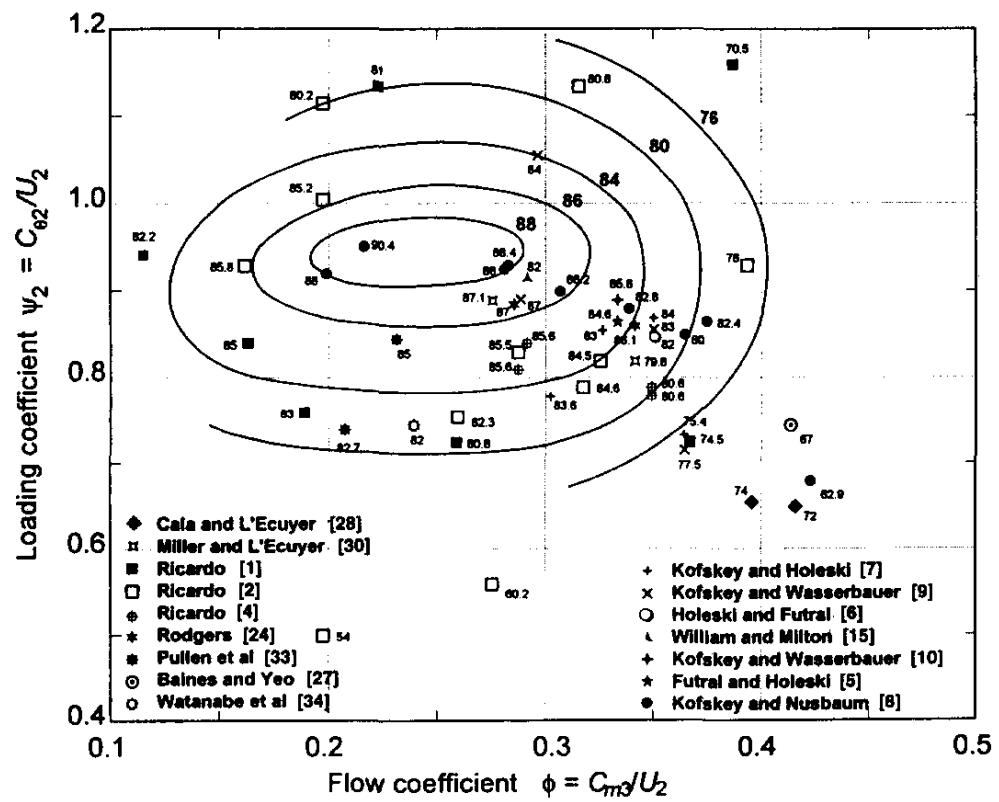


Fig. B.6 Radial Total to static with $C_d = 0.006$

B.6 Radial total to static Chen and Baines



Correlation of blade loading and flow coefficients for radial turbines. Data points and contours show total-to-static isentropic efficiency (%).

B.7 Radial total to static

B.8 Mixed turbine profile surface area and velocity distribution

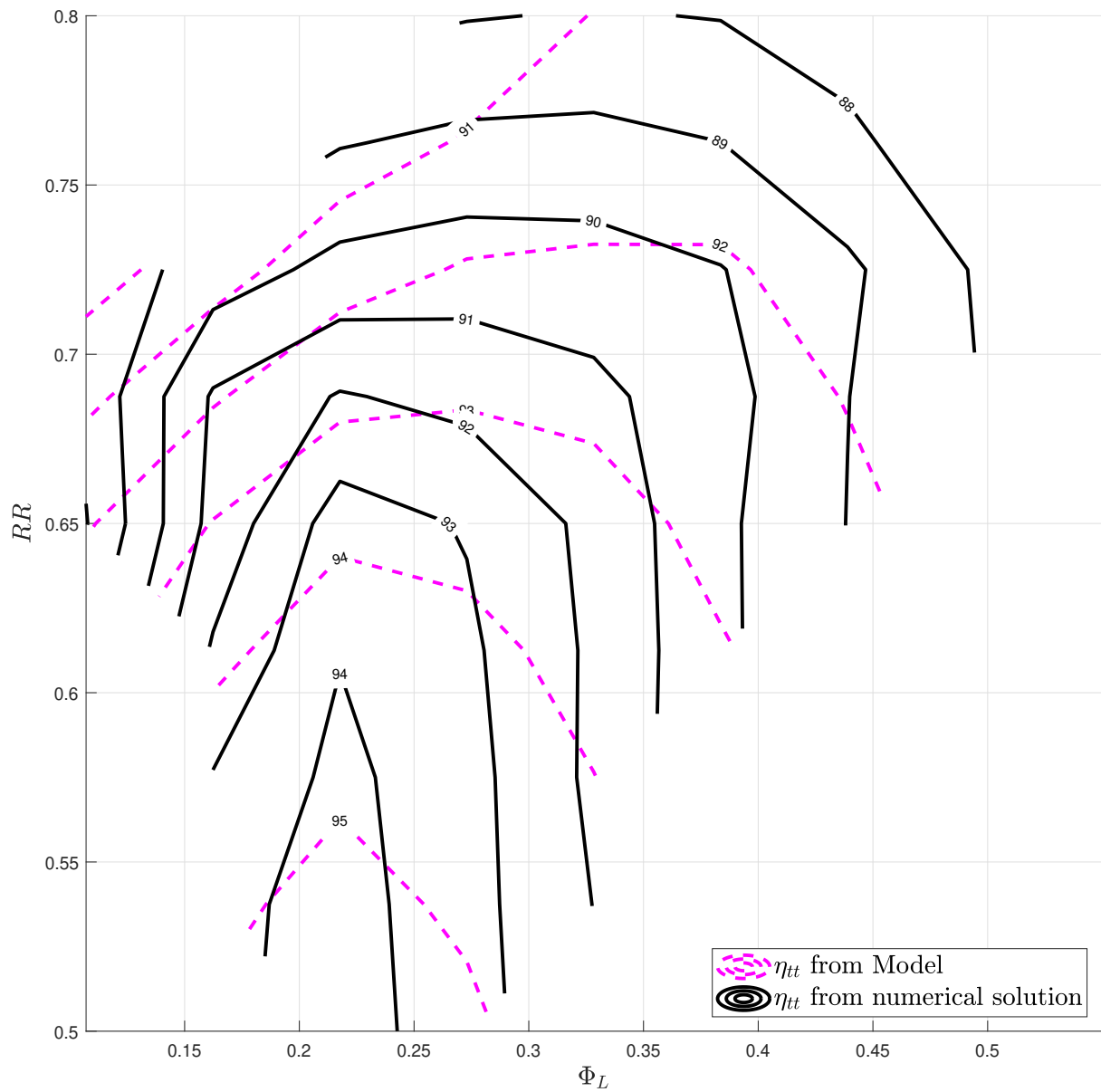


Fig. B.7 Comparison of Model and numerical solution with varying radius ratio and local flow coefficient

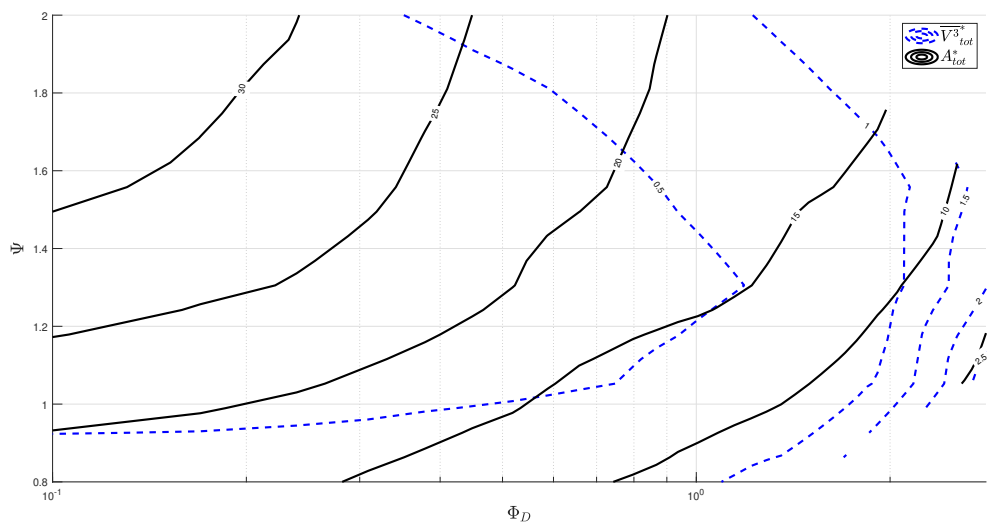


Fig. B.8 profile surface area and velocity distribution

B.9 Mixed turbine secondary and surface end wall dissipation loss

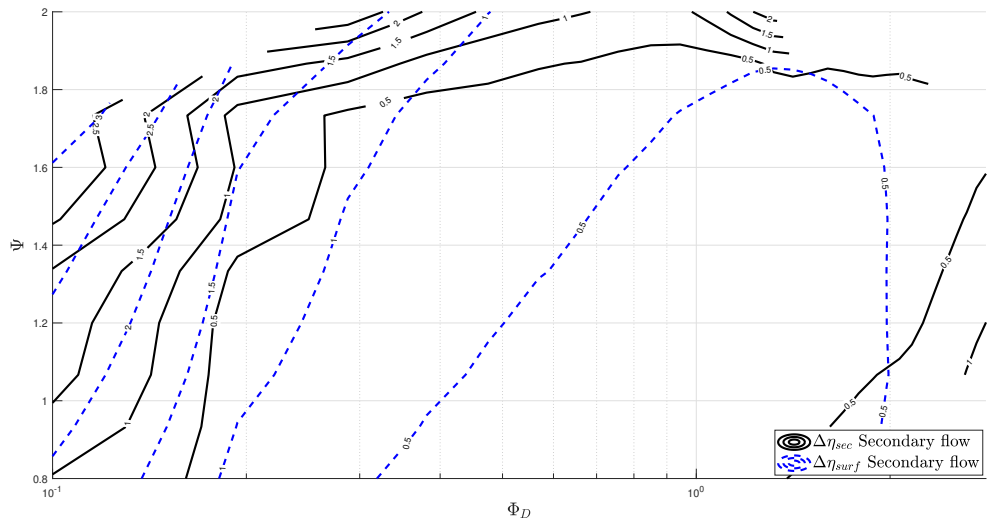


Fig. B.9 Mixed turbine secondary and end wall surface dissipation loss

Appendix C

Method for calculating reduced static pressure(compressible) and isentropic velocity

Reduced / Rotary static Temperature and Pressure

Starting from rothalpy

$$h_{0_{rot}} = h_{0_{rel}} - \frac{\Omega^2 r^2}{2C_p} \quad (\text{C.1})$$

Defining a rothalpy stagnation temperature

$$T_{0_{rot}} \equiv \frac{h_{0_{rot}}}{C_p}$$

and using

$$T_{0_{rel}} = T + \frac{W^2}{2C_p}$$

The following form of equation C.1 can be written

$$T_{0_{rot}} = T - \frac{\Omega^2 r^2}{2C_p} + \frac{W^2}{2C_p}$$

a reduced/rotary static temperature can then be defined as follows

$$T_{rot} \equiv T - \frac{\Omega^2 r^2}{2C_p}$$

Finally

$$T_{0_{rot}} = T_{rot} + \frac{W^2}{2C_p} \quad (\text{C.2})$$

Isentropic Mach Number

Using Isentropic relation we can calculate reduced/rotary static/stagnation pressures

$$P_{rot} = P \left(\frac{T_{rot}}{T} \right)^{\frac{\gamma}{\gamma-1}}$$

$$P_{0_{rot}} = P_0 \left(\frac{T_{0_{rot}}}{T_0} \right)^{\frac{\gamma}{\gamma-1}}$$

Both $P_{0_{rot}}, T_{0_{rot}}$ are invariant with radius and frame.

Using an isentropic relation and Equation C.2 a isentropic Mach number can be calculated.

$$M_{isen} = \sqrt{\frac{2 \left(\left(\frac{P_{rot}}{P_{0_{rot}}} \right)^{\frac{1-\gamma}{\gamma}} - 1 \right)}{\gamma - 1}} \quad (\text{C.3})$$

where

$$M_{isen} = \frac{W}{\sqrt{\gamma R T_{rot}}} \quad (\text{C.4})$$

Appendix D

Vorticity Amplification Factor For A Curved Rectangular Duct

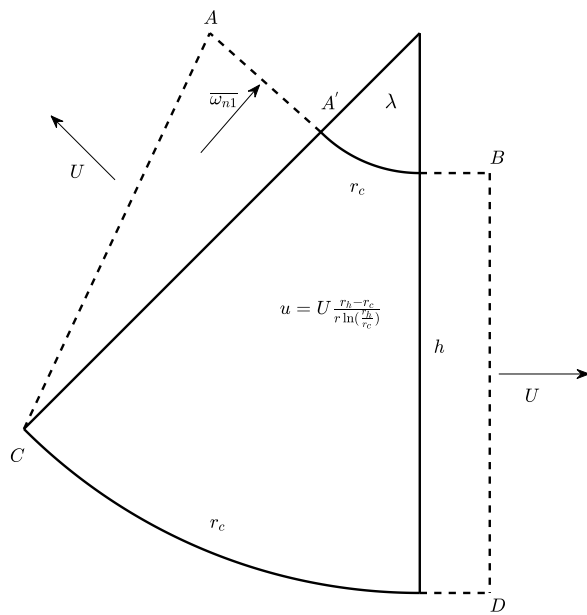


Fig. D.1 Model diagram

From Kelvins circulation theory

$$\Gamma_{AC} = \Gamma_{BD}$$

Considering only the stream normal component of vorticity.

$$x_{AA'} \bar{\omega}_{n1} \Delta z = h \bar{\omega}_2 \Delta z$$

where Δz is the width of the duct. Defining a vorticity amplification as

$$AF \equiv \frac{\bar{\omega}_2}{\bar{\omega}_1} = \frac{x_{AA'}}{h} \quad (\text{D.1})$$

Where $L_{AA'}$ can be calculated by tracing a material plane sitting in the fluid backwards in time from BD to AC . The flow velocity is higher on the AB streamline and flow length is shorter than that of the CD streamline which leads to the material point travelling the length $L_{AA'}$ from A' to A (backwards in time) by the time the corresponding material point reaches C .

$$L_{AA'} = U\Delta t \quad (\text{D.2})$$

The distance $L_{AA'}$ between AA' is set by the difference in the transit time of a streamline travelling from A' to B and C to D .

$$\Delta t = t_{CD} - t_{A'B}$$

Which can be written as

$$\Delta t = \frac{\lambda r_h}{u_h} - \frac{\lambda r_c}{u_c} \quad (\text{D.3})$$

The velocity in the bent section is modelled to take the form of a free vortex as follows

$$u = U \frac{r_h - r_c}{r \ln(\frac{r_h}{r_c})}$$

which using $h = r_h - r_c$ can be rewritten as

$$u = U \frac{h}{r \ln(1 + \frac{h}{r_c})} \quad (\text{D.4})$$

Substituting D.4, D.3 and D.2 into D.1

$$\frac{U\Delta t}{h} = \frac{\lambda \ln(1 + \frac{h}{r_c})}{h^2} [(r_c + h)^2 - r_c^2]$$

Which simplifies to

$$AF = \lambda \ln \left(1 + \frac{h}{r_c} \right) \left(2 \frac{r_c}{h} + 1 \right) \quad (\text{D.5})$$

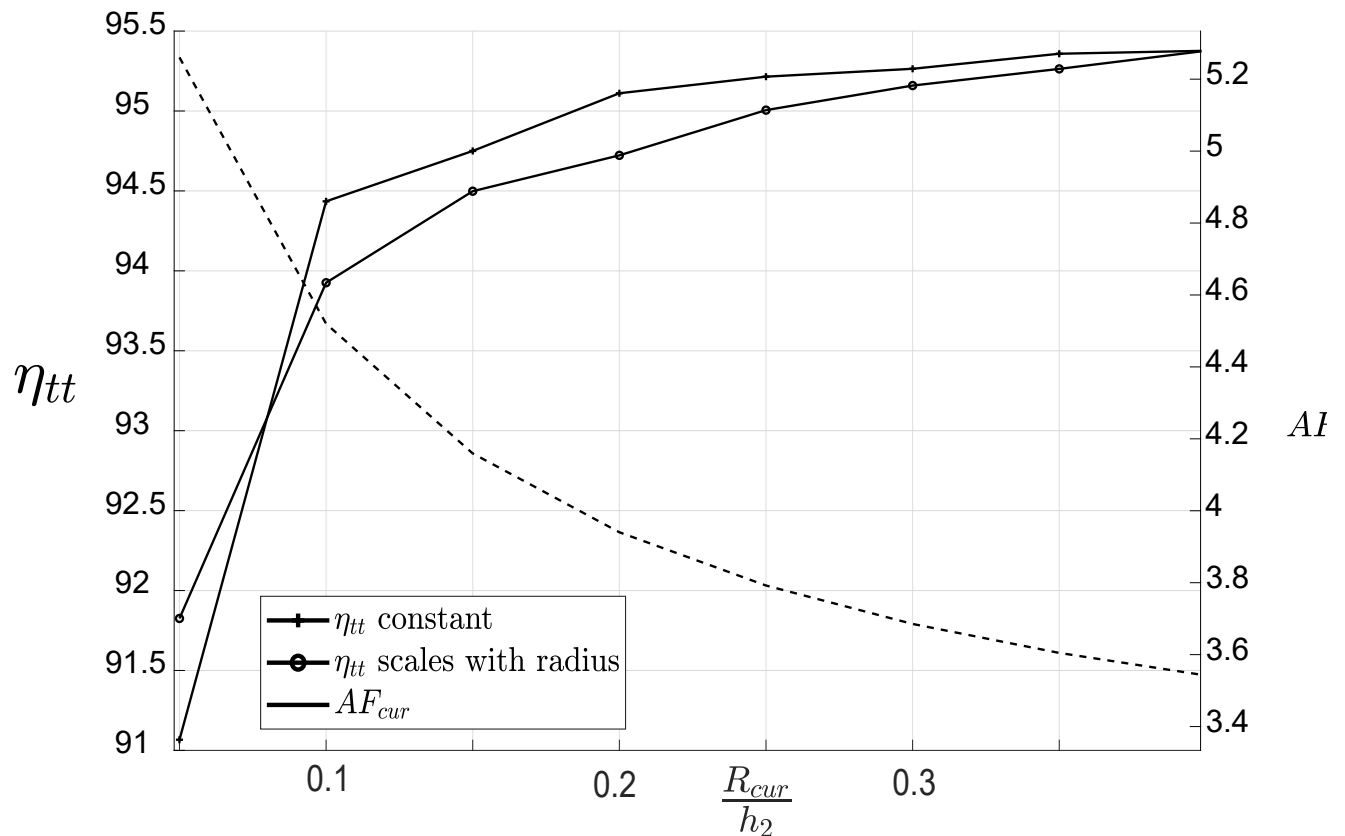


Fig. D.2 total to total efficiency vs Non dimensional radius of curvature

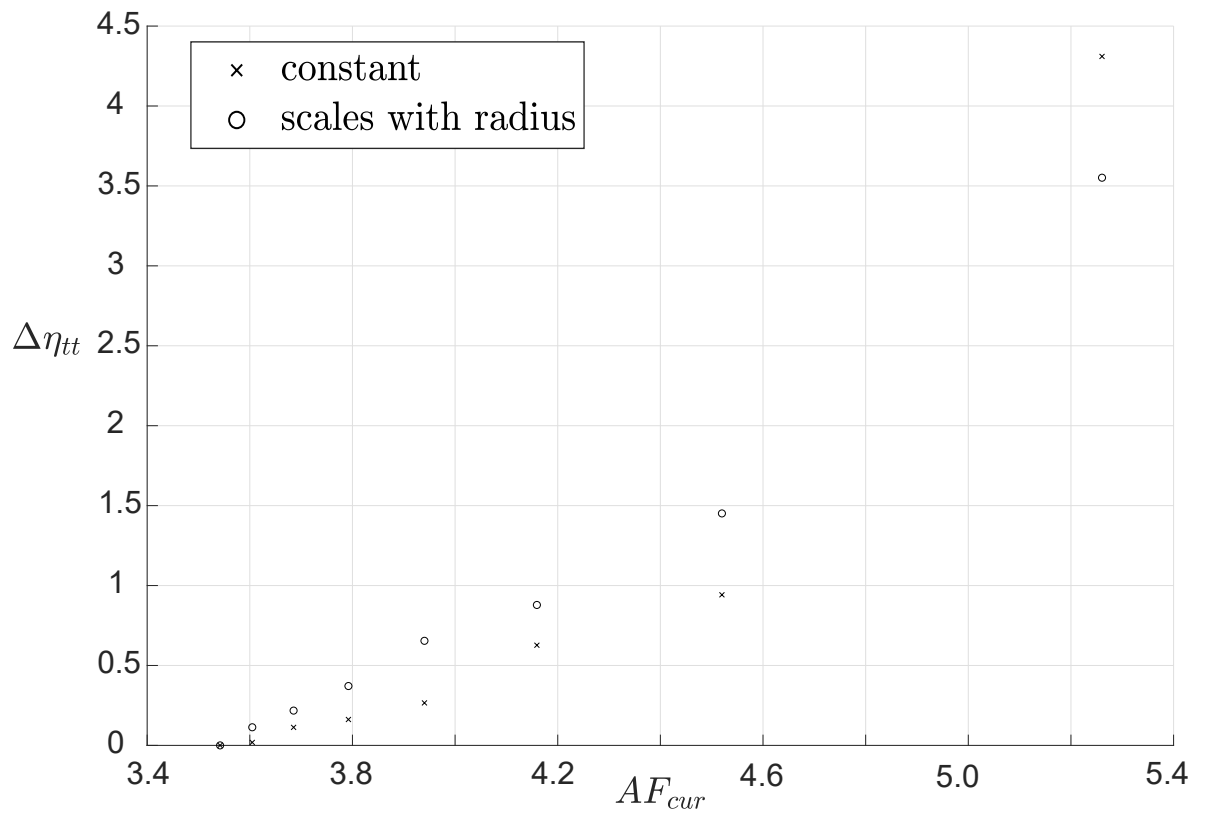


Fig. D.3 Change in total to total efficiency vs curvature amplification factor

Appendix E

Curvature pressure gradient Factor

The goal is to characterise the adverse pressure gradient of the curved duct in figure D.1. The gradient comes about as the flow decelerates from the peak velocity(which occurs at the apex) to the mean velocity down stream. From Bernoulli the change in pressure is.

$$\Delta p = \frac{1}{2}\rho \left(u_c^2 - U^2 \right)$$

The Distance in which this change in pressure occurs depends on the down stream conditions but likely scales with r_c .

so a characteristic pressure gradient can be defined as

$$\frac{\Delta p}{r_c} = \frac{\frac{1}{2}\rho \left(u_c^2 - U^2 \right)}{r_c}$$

non-dimentionalising this with $\frac{1}{2}\rho U^2$ and h

$$\frac{\Delta ph}{\frac{1}{2}\rho U^2 r_c} = \frac{h \left(\left(\frac{u_c}{U} \right)^2 - 1 \right)}{r_c}$$

substituting in equation D.4

$$FC \equiv \frac{\Delta ph}{\frac{1}{2}\rho U^2 r_c} = \frac{h}{r_c} \left(\left(\frac{h}{r_c} \right)^2 \ln \left(1 + \frac{h}{r_c} \right)^{-2} - 1 \right)$$

$$FC = \frac{\left(\frac{h}{r_c} \right)^3}{\ln \left(1 + \frac{h}{r_c} \right)^2} - \frac{h}{r_c} \quad (\text{E.1})$$

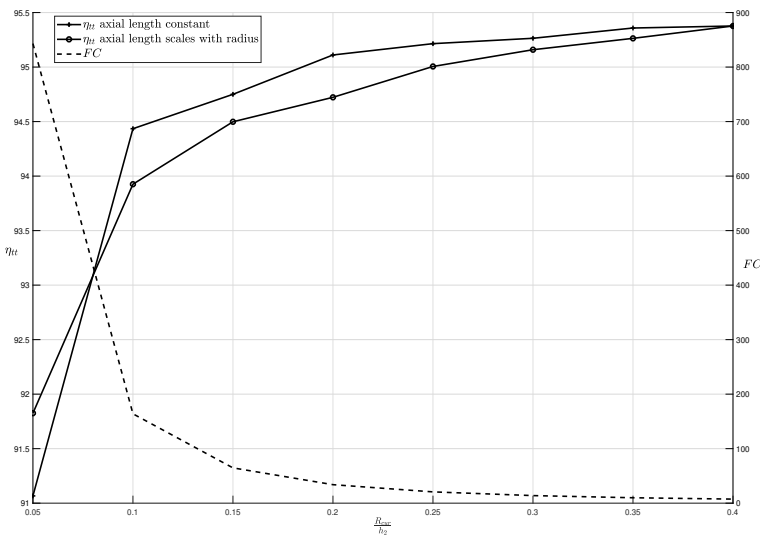


Fig. E.1 total to total efficiency vs Non dimensional radius of curvature

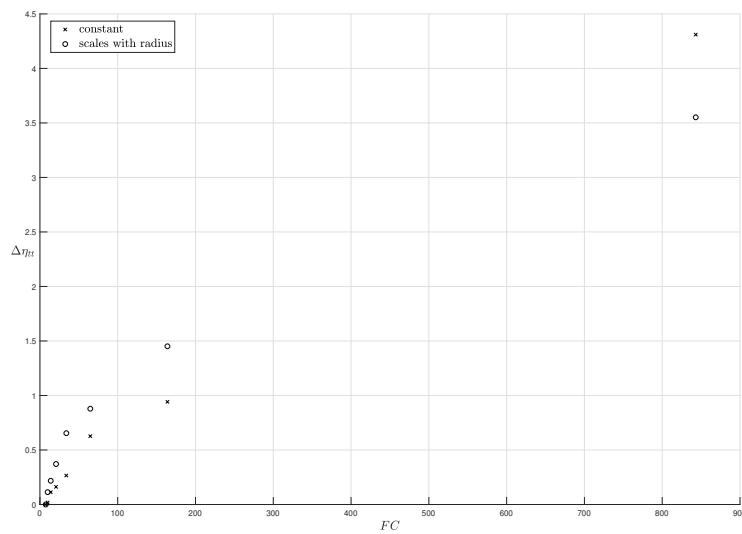


Fig. E.2 Change in total to total efficiency vs curvature pressure gradient factor

Appendix F

Circulation vs Flow angles

The pitch to suction surface length ratio is calculated by equating the change in angular momentum of the flow to the force torque supplied by the blade. Starting from the change in angular momentum of the flow

$$T = \dot{m}(r_1 V_{\theta_1} - r_2 V_{\theta_2})$$

Which in the relative frame is

$$\frac{T}{\dot{m}} = r_1(U_1 + W_{\theta_1}) - r_2(U_2 + W_{\theta_2})$$

Rearranging to

$$\frac{T}{\dot{m}} = (r_1 U_1 - r_2 U_2) + (r_1 W_{\theta_1} - r_2 W_{\theta_2}) \quad (\text{F.1})$$

Noting that the first term on the right hand side of equation F.1 represent the centrifugal loading. Now taking out r_1 and V_{m_1} as a common factor.

$$\frac{T}{\dot{m}} = r_1 V_{m_1} \left(\frac{U_1}{V_{m_1}} \left(1 - \frac{r_2}{r_1} \frac{U_2}{U_1} \right) + \frac{W_{\theta_1}}{V_{m_1}} - \frac{r_2}{r_1} \frac{V_{m_2}}{V_{m_1}} \frac{W_{\theta_2}}{V_{m_2}} \right)$$

Which then simplifies to

$$T = \dot{m} r_1 V_{m_1} \left(\frac{1 - R^2}{\phi_L} + \tan \beta_1 - R V R \tan \beta_2 \right) \quad (\text{F.2})$$

Drawing from Thin aerofoil theory , the rotor blade can be modelled as a thin vortex sheet embedded in the flow, The force on a section of the blade is derived from the Kutta–Joukowski theorem, which relates the lift per unit length produced by an aerofoil to its circulation as follows.

Note the theory is based on an assumption of incompressible flow.

$$L = \rho V \Gamma$$

Where V the velocity is perpendicular to the lift generated. From this a small element of torque can be written as.

$$\Delta T = rh\rho V_m \Delta \Gamma$$

Where h is the local span of the stream tube in question and r is the local radius. The meridional velocity V_m is used because the force in the tangential direction is required. This can then be written in terms of the circulation distribution multiplied by a small element of surface length.

$$\Delta T = rh\rho V_m \gamma \Delta s \quad (\text{F.3})$$

where γ is the local vorticity per unit length such that $\gamma(s) = \frac{d\Gamma}{ds}$. The Total torque can then be calculated by integrating equation F.3 along the length of the blade

$$T = \rho \int_0^{S_{tot}} rhV_m \gamma ds \quad (\text{F.4})$$

Equation F.4 and equation F.2 are then equated and continuity is used $\dot{m} = h_1 p_1 V_{m1} \rho$, where p is the pitch and then rearranging. leads to

$$\frac{\int_0^{S_{tot}} rhV_m \gamma ds}{r_1 h_1 p_1 V_{m1}^2} = \frac{1 - R^2}{\phi_L} + \tan \beta_1 - R V R \tan \beta_2$$

Then using $\frac{r}{r_1} = \frac{p}{p_1}$ (constant blade count) The left hand side can then be written as.

$$\frac{1}{p_1 V_{m1}} \int_0^{S_{tot}} \frac{p}{p_1} \frac{h}{h_1} \frac{V_m}{V_{m1}} \gamma ds = \dots$$

then using incompressible continuity $\frac{p}{p_1} \frac{h}{h_1} \frac{V_m}{V_{m1}} = 1$

$$\frac{1}{p_1 V_{m1}} \int_0^{S_{tot}} \gamma ds = \frac{\Gamma}{p_1 V_{m1}} = \dots$$

Then using the definition of circulation coefficient $C_o = \frac{\Gamma}{W^2 S_{tot}}$ and $V_2 = \frac{V_{m2}}{\cos \beta_2}$

$$\frac{V_{m2}}{V_{m1}} \frac{S_{tot}}{p_1} \frac{C_o}{\cos \beta_2} = \dots$$

Which can then be rearranged to

$$C_o = \frac{p_1}{S_{tot}} \frac{\cos \beta_2}{VR} \left(\frac{1-R^2}{\phi_L} + \tan \beta_1 - R VR \tan \beta_2 \right) \quad (\text{F.5})$$

or using $\frac{1}{\phi} = \tan \alpha_1 - \tan \beta_1$

$$C_o = \frac{p_1}{S_{tot}} \frac{\cos \beta_2}{VR} \left(\overbrace{(1-R^2)(\tan \alpha_1 - \tan \beta_1)}^{Centrifugal} + \overbrace{\tan \beta_1 - R VR \tan \beta_2}^{Tangential} \right) \quad (\text{F.6})$$

which can be decomposed into two terms

$$C_{o_{cen}} = \frac{p_1}{S_{tot}} \frac{\cos \beta_2}{VR} \overbrace{(1-R^2)(\tan \alpha_1 - \tan \beta_1)}^{Centrifugal}$$

$$C_{o_{tan}} = \frac{p_1}{S_{tot}} \frac{\cos \beta_2}{VR} \overbrace{\tan \beta_1 - R VR \tan \beta_2}^{Tangential}$$

Appendix G

Velocity difference equation

This section of the appendix shows how the equation used to predict the difference between the suction and pressure surface velocities used in the model, is derived.

Similarly to appendix F the angular momentum equation is used in conjunction with thin aerofoil theory where by we imagine the flow is acted upon by a thin vortex sheet in the middle of the passage.

Starting with momentum equation.

$$T = \dot{m}(r_1 V_{\theta_1} - r_2 V_{\theta_2})$$

Which in the relative frame can be written as

$$\frac{T}{\dot{m}} = \omega(r_2^2 - r_1^2) + r_2 W_{\theta_2} - r_1 W_{\theta_1} \quad (\text{G.1})$$

Now the effect of a small element of the vortex sheet (Δs long) on the local change in angular momentum is considered such that.

$$\begin{aligned} r_1 &= r \\ r_2 &= r + \frac{dr}{ds} \Delta s \\ r_1 W_{\theta_1} &= r W_{\theta} \\ r_2 W_{\theta_2} &= r W_{\theta} + \frac{d(r W_{\theta})}{ds} \Delta s \end{aligned}$$

substituting these into equation G.1 and dropping Δs^2 terms.

$$\frac{\Delta T}{\dot{m}} = \left(\omega \frac{d(r^2)}{ds} + \frac{d(r W_{\theta})}{ds} \right) \Delta s$$

again the small element of torque is derived using the Kutta–Joukowski theorem.

$$\Delta T = rh\rho V_m \gamma \Delta s$$

and using the contention equation $\dot{m} = hpV_m \rho$

$$\frac{rh\rho V_m \gamma \Delta s}{hpV_m \rho} = (\omega \frac{d(r^2)}{ds} + \frac{d(rW_\theta)}{ds}) \Delta s$$

which simplifies to

$$\gamma(s) = \frac{p}{r} \left(\omega \frac{d(r^2)}{ds} + \frac{d(rW_\theta)}{ds} \right)$$

ΔV in terms of $\gamma(s)$ can be derived by calculating the circulation of the small element.

$$\int \gamma(s) ds = \oint V ds$$

$$\gamma(s) \Delta s = \left((\bar{W} + \frac{1}{2} \Delta W) - (\bar{W} - \frac{1}{2} \Delta W) \right) \Delta s$$

$$\gamma(s) = \Delta W(s)$$

Finally

$$\Delta W(s) = \frac{p}{r} \left(\omega \frac{d(r^2)}{ds} + \frac{d(rW_\theta)}{ds} \right)$$

Appendix H

Velocity Triangle

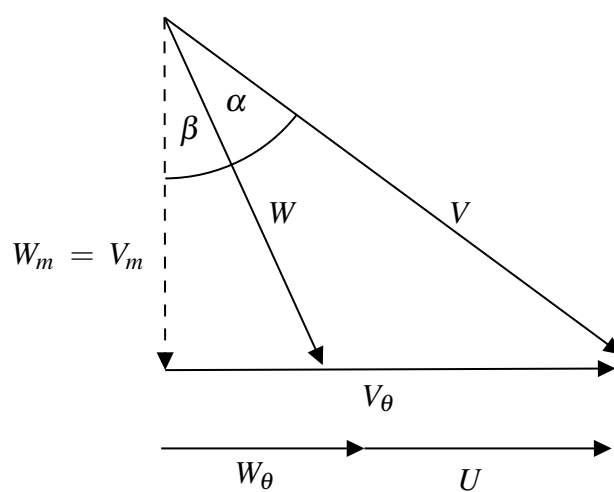


Fig. H.1 Velocity triangles